Order, Motion and Relaxation in Radical Pair Compass Magnetoreception

Susannah Worster

Worcester College

University of Oxford



A thesis submitted in partial fulfilment of the requirements for the degree

of

Doctor of Philosophy

in

Physical and Theoretical Chemistry

Physical and Theoretical Chemistry Laboratory

Hilary Term 2018

Order, Motion and Relaxation in Radical Pair Compass Magnetoreception

Susannah Worster, Worcester College

A thesis submitted in partial fulfilment of the requirements for the degree of Doctor of Philosophy in Physical and Theoretical Chemistry.

Hilary Term 2018

Abstract

Traditionally, biological systems are thought to be governed by classical, rather than quantum behaviour. In the warm, aqueous environment of a cell, the thermal energy $k_{\mathrm{B}}T$ is much larger than the spacing of quantum energy levels and there are many processes, such as molecular motion, that can rapidly destroy delicate quantum coherences. An exception may be the remarkable ability of birds to navigate using the Earth's pervasive but extremely weak magnetic field; an ability that is thought to depend on the spin-selective reactions of photochemically-generated radical pair species.

Despite substantial (although inconclusive) evidence pointing towards a radical pair mechanism of avian magnetoreception, whether, and how, spin coherence can be maintained long enough to produce a field-dependent compass signal remains a key question. It becomes even more critical in light of recent work, presented in this thesis, showing that coherence lifetimes > 10 μs reveal 'spiky' features in the compass signal that could explain the astonishing precision of the avian compass and its sensitivity to radiofrequency noise. In the first half of this thesis, two different models are used to explore the resilience of the compass to restricted rotational motion of individual radicals, with a focus on the flavin and tryptophan radicals in the proposed magnetoreceptor, cryptochrome. Fast, highly constrained motion is found to be crucial for the flavin radical, whilst the tryptophan radical can be allowed greater motional freedom, in keeping with its position near the surface of the protein. However, even in an optimised system, very little compass information is likely to survive in the presence of realistic relaxation, suggesting that our current understanding of the radical-pair mechanism may be incomplete.

Chapter 7 investigates how relaxation effects could be exploited to probe the function of cryptochrome. An experiment in which relaxation rates are locally enhanced by the presence of the biomimetic, superparamagnetic nanoparticle magnetoferritin is proposed and assessed. This experiment could provide much-needed evidence for the identity of the magnetoreceptor, allowing for more focused investigation of the compass mechanism.

Finally, the requirements for highly restricted motion and long-range ordering of the magnetoreceptors make the radical pair compass inherently sensitive to polarized light. This is potentially problematic because natural variations in skylight polarization could compromise detection of the magnetic field. A combination of algebraic and biological arguments are used to demonstrate how unwanted information can be filtered out of the compass signal by taking the ratio of signals from two neighbouring cells related by a 180° rotation about their line-of-sight. The combination of magnetic field patterns from the two cells additionally helps to pinpoint a precise heading.

Publications

The work in this thesis has formed the basis of several publications, listed below:

- The work in chapter 4 feeds into ref. [61]: "The Quantum Needle of the Avian Magnetic Compass", published in *Proceeding of the National Academy of Sciences of the United States of America* (2016). This paper also includes work by co-authors Hamish Hiscock, Daniel Kattnig, Charlotte Steers, Ye Jin, David Manolopoulos, Henrik Mouritsen and Peter Hore, which is summarised in this thesis but not discussed in detail.

- The majority of the work in chapter 5, along with some of chapter 4, may be found in ref. [150]: "Spin relaxation of radicals in cryptochrome and its role in avian magnetoreception", published in *The Journal of Chemical Physics* (2016). Co-authors Daniel Kattnig and Peter Hore provided assistance in developing the methods and discussing the results, as well as comments on the manuscript.

- Sections of chapter 6 have been published in an edited form in ref. [165]: "A light-dependent magnetoreception mechanism insensitive to light intensity and polarization", which appears in *The Journal of the Royal Society, Interface* (2017). Biological insight, discussion of the results and comments on the manuscript were provided by co-authors Henrik Mouritsen and Peter Hore.

Original versions of many of the figures in these papers have been included in this thesis. Where this is the case, it has been indicated in the relevant figure caption.

Acknowledgements

Thanks must first go to my supervisor, Peter Hore, who has guided me through four years of DPhil research. Thank you for suggesting such interesting projects for me to work on and for all your advice and encouragement.

The work in this thesis has also been supported by the members of the Hore group. Particular thanks go to Daniel Kattnig for hours of help (and several pages of code) figuring out the best way to handle very stubborn linear systems and correctly adjust my Redfield theory equations. Second, thanks to Benedict Graves, whose masters' thesis was the foundation for the work on polarized light presented in chapter 6. Thanks to Hamish Hiscock, my DPhil 'twin', whose discovery of 'spikes' in our first year has had a huge influence on the direction and focus of this thesis; to Jakub Sowa for many discussions about MATLAB and linear solvers, and to Thomas Player, for willingly proof-reading all the long equations, always being ready to talk through problems and helping me reinstate a regular tea-time!

Extending beyond the Hore group, I would like to thank the groups of Henrik Mouritsen (Oldenburg) and Ilia Solov'yov (Odense) for many interesting and inspiring talks and conversations at the regular OOO meetings. I would especially like to thank Henrik Mouritsen, Arndt Meyers and Anja Günther for helping me understand the biological context and application of my abstract, theoretical work. Their input was particularly invaluable for the work in chapter 6, along with insightful comments on the structure and suitability of double cones from the reviewers of our paper (in the Journal of the Royal

Society, Interface).

Similarly, I am very grateful for discussions with members of the Mackenzie and Timmel groups (Oxford) about the practicalities of measuring a magnetic field effect on nanoparticle-radical pair complexes.

I would also like to thank my tutors, Grant Ritchie and Martin Galpin, for getting me into Physical Chemistry as an undergraduate, for continuing to look out for me as a graduate and for offering me the opportunity to do some teaching - I have really enjoyed the experience.

Outside the office, thanks to all the friends who have kept me company during my DPhil, especially to Naomi Saunders for her friendship and singing through six years of living together, and to Liam Young for his limitless supply of stories and for sharing my love of ballroom dancing - you've kept me sane!

Likewise, thank you to my family for all the love, friendship, teasing and support you have given me my whole life. More specifically, thank you to my mum for her help with proof-reading; to my dad and Caroline for all the 'maths chat', and to Lizzie and Katherine for helping me learn about 'bird psychology' and how vision works.

Finally, to Mark Bourne, my wonderful husband-to-be, thank you for your professional advice on geomagnetism, spherical projections and data analysis and your shining example of how to do a DPhil. But more than that, thank you for your support - even during your years 'across the Pond', you have been there every single day to encourage me, listen to all my grumbles and all my ideas and (however unknowingly!) offer me huge amounts of inspiration. I couldn't have done it without you.

Contents

1 Introduction **1**

1.1 The radical pair mechanism 6

1.2 The magnetite hypothesis 11

1.3 Cryptochrome: the candidate magnetoreceptor 13

1.4 Aims 17

2 Theoretical background **19**

2.1 Spin 19

2.2 Magnetic interactions 24

2.2.1 Zeeman interaction 24

2.2.2 Hyperfine interactions 25

2.2.3 Interelectron interactions 27

2.3 Density matrix formalism 29

2.3.1 Correlation and Entanglement 31

2.4 Singlet yield calculations 33

2.4.1 The Liouville Von-Neumann equation 34

2.4.2 Singlet yield in Hilbert space 35

2.4.3 Singlet yield in Liouville space 36

3 Modelling techniques **40**

3.1 Modelling rotations 40

3.1.1 Euler angles 40

3.1.2 Rotation matrices . . . 42
3.1.3 Spherical tensor operators . . . 43
3.1.4 Wigner matrices . . . 46
3.1.5 Clebsch-Gordan coefficients . . . 48
3.2 Modelling relaxation . . . 50
3.2.1 The two-site model . . . 50
3.2.2 Redfield theory . . . 57

4 Preliminary relaxation calculations 64
4.1 Application of the two-site model . . . 67
4.1.1 Treating larger spin systems . . . 69
4.1.2 Preconditioners . . . 72
4.2 One-spin systems . . . 73
4.3 Two-spin systems . . . 79
4.3.1 Spike-producing radical pairs . . . 79
4.3.2 The 'toy' radical pair . . . 83
4.3.3 Spike-fitting . . . 86
4.3.4 Optimising hyperfine interactions. . . . 89
4.4 Larger spin systems . . . 94
4.5 Conclusions . . . 97

5 Realistic modelling of relaxation 101
5.1 Introducing realistic rotations into the Hamiltonian . . . 102
5.1.1 Adjusted Redfield superoperator . . . 103
5.2 Analytical spectral densities for diffusion in a uniaxial potential . . . 106
5.3 Validating the Redfield approach . . . 114
5.4 Small model systems . . . 116
5.4.1 Optimisation principles . . . 119
5.5 Flavin-tryptophan radical pair . . . 121

5.6 Extension to biaxial potentials . . . 126
5.6.1 Defining the potentials . . . 127
5.6.2 Calculating correlation functions . . . 128
5.6.3 Motion of flavin and tryptophan . . . 131
5.7 Conclusions . . . 134

6 Interaction of the compass with polarized light 136
6.1 Skylight polarization . . . 136
6.2 Polarization vision and polarization sensitivity . . . 138
6.2.1 The photoselection effect . . . 138
6.3 Birds' eyes . . . 139
6.3.1 Known mechanisms of polarization sensitivity . . . 142
6.3.2 Can birds perceive polarized light? . . . 146
6.3.3 The problem with polarization sensitivity . . . 148
6.4 Geometric requirements . . . 151
6.4.1 Relative orientation of magnetoreceptor cells . . . 151
6.4.2 Orientation of magnetoreceptor molecules . . . 157
6.5 Visualising the signal . . . 159
6.5.1 Reference frames . . . 159
6.5.2 Simulation method . . . 164
6.5.3 Directional information . . . 169
6.5.4 Cross conditions . . . 176
6.6 Cell disorder . . . 178
6.6.1 Introducing disorder . . . 178
6.6.2 The effect of disorder . . . 180
6.7 Realising the separation mechanism . . . 185
6.7.1 Immobilizing the magnetoreceptors . . . 185
6.7.2 Potential pitfalls . . . 187
6.8 Alternative mechanisms . . . 188

6.9 Conclusions 190

7 Testing the cryptochrome hypothesis 193

7.1 Proposed experiment 194

7.2 Magnetic materials: some definitions 195

7.3 Biological applications of magnetic nanoparticles 199

7.4 Application of the two-site model 203

7.4.1 Néel relaxation 203

7.4.2 Brownian motion 205

7.5 Determining the criteria for the nanoparticle 206

7.6 Candidate nanoparticles 214

7.7 Practical considerations 221

7.7.1 Biogenic nanoparticles 223

7.7.2 Suggested preliminary experiments 225

7.8 Conclusions 233

8 Conclusions 235

A Hyperfine interaction tensors 272

B Calculating Euler angles to position hyperfine interactions 280

C Recipe for magnetoferritin 283

Chapter 1

Introduction

The Earth has a natural magnetic field, generated by a "self-exciting dynamo process" [1] in which the magnetic field is coupled to and maintained by convective motion of electrically-conducting iron-nickel alloy in the fluid outer core [2]. The simplest description of the geomagnetic field is as a geocentric magnetic dipole. It provides a pervasive, global reference grid that is potentially invaluable to any creature with a need to navigate over long distances.

In reality, the Earth's field is more complex than the simple geocentric dipole model. First, the geomagnetic poles (the poles of the best-fit geocentric dipole) do not coincide with the measured magnetic poles (the points on the Earth's surface at which the magnetic field lines are vertical - also referred to as dip poles). Second, neither the geomagnetic nor magnetic dip poles coincide with the geographic poles (figure 1.1) and over a geologically short time (1000s of years) perform a random walk about the Earth's rotation axis (which defines geographic North and South) [2]. Currently[1], magnetic North (the magnetic dip pole in the northern hemisphere) lies at 86.39° latitude and −169.80° longitude [3]. From a navigational perspective, the discrepancy between magnetic and geographic North is advantageous as it provides information about longitudinal position [4, 5].

[1] Values from International Geomagnetic Reference Field for 2020.

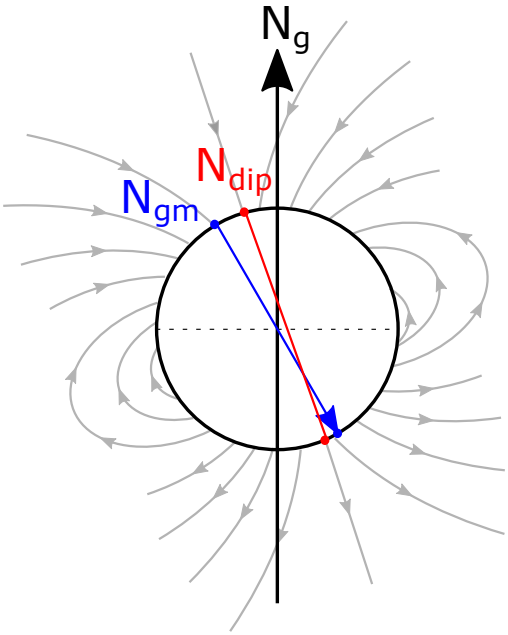


Figure 1.1: Schematic representation of the geomagnetic field. Approximately 90% of the field can be represented by a geocentric dipole (blue), whose poles are the geomagnetic North (N_{gm}) and South poles. The geomagnetic poles are a theoretical construct describing the underlying dipole model. The physical magnetic North pole detected by a compass is the North magnetic dip pole (N_{dip}). Note that the labels North and South refer to the hemisphere in which the pole is found. The magnetic field lines (currently) go in to the magnetic North pole (whereas they conventionally come out of the North pole of a bar magnet). Deviations from the geocentric dipole model mean that the dip poles are not necessarily antipodal, nor do they have to coincide with the geomagnetic poles. Neither N_{gm} or N_{dip} coincides with geographic North (N_g), which lies on the rotation axis of the Earth. Over time, the magnetic poles perform a random walk around the geographic poles.

Traditionally, the direction of the geomagnetic field at a point on the surface is described by two angles: inclination and declination. The inclination of the field is the angle measured downwards from the horizontal tangent at the surface to the field vector. Declination measures the angle between True North (the direction along the Earth's surface towards geographic North) and the field vector projected onto the horizontal plane. Illustrations of these two angles can be found in figure 6.9 on page 161. Within the dipole model of the field, inclination is strongly linked to geographical latitude, whilst declination can be used to determine longitude.

Approximately 10% of the natural field cannot be described by a geocentric dipole field

[2]. Eddy currents in the turbulent fluid flow of the outer core generate more complex features in the field [2], which can be modelled by combinations of higher order spherical harmonics. In combination with magnetic 'anomalies', produced by magnetic minerals in the Earth's crust [1], these more complex features could serve as landmarks in a magnetic 'map'. The strength of the Earth's field also varies, spatially and temporally, in the range $22 - 67\mu$T at the surface, providing an additional source of potential magnetic landmarks.

The wealth of navigational information available from the Earth's field (in all weathers and regardless of the time of day) means that magnetic compasses have been used throughout human history, dating back as far as 200 BC, when the Chinese created compasses using naturally occurring magnetic lodestone (magnetite) [6]. However, the use of a magnetic compass is not limited to humans. Since the 1960s ([7] and [8], cited in [4]), it has been known that many birds (likely all migratory birds [4]), have a magnetic compass sense that they use alongside other visual and olfactory cues [9–11] to guide them on long-distance migrations. This magnetic compass is tuned to a narrow functional window around the natural magnetic field intensity [12] but can be adapted to different ranges over the course of a few hours [13, 14]. An astonishing number of other animals have subsequently been shown to have a magnetic sense [13], from magnetotactic bacteria [15, 16] to cockroaches [17] to wood mice [18, 19]. Migratory birds, and European robins (*Erithacus rubecula*) in particular, have, however, remained a key model organism in the study of animal magnetoreception.

Over the past 50 years, the avian magnetic compass has been extensively studied and characterised. Although some tracking studies have been carried out on wild birds to determine migratory routes and flight behaviour, the majority of studies of the magnetic compass have been performed using an Emlen funnel set-up [20, 21]. In this simple experiment, birds are placed into a funnel lined with scratch-sensitive paper. During the migratory season, birds display 'migratory restlessness' ([22], cited in [4]), increased activity levels around dusk, and will try to escape the funnel in their preferred migratory direc-

tion. Birds can be exposed to different conditions within the funnels and their preferred direction is determined by counting the scratches left on the paper and identifying the direction with the most scratches. This is preferably carried out using carefully controlled, double-blinded procedures. Groups of birds can then be characterised as 'disoriented' (randomly oriented) or 'oriented' in a particular direction.

Early experiments showed that, unlike man-made magnetic-mineral based compasses, birds did not distinguish between North and South but rather between 'poleward' and 'equator-ward' [23]. This type of compass is termed an 'inclination' compass, in contrast to our usual 'polarity' compasses. Other animals, including honeybees [24] and lobsters [25], do possess a polarity compass, suggesting that more than one mechanism may exist for animal magnetoreception. To date, two key mechanisms have been proposed and will be discussed below.

Further differences from magnetic-mineral compasses became apparent when it was discovered that the avian magnetic compass is light-dependent [26]. Moreover, the compass is wavelength-dependent, with blue-green light between 424-565 nm being required for the birds to orient themselves [26, 27]. However, although birds are unable to orient if they are kept completely in the dark or under red light, recent research has suggested that the key magnetosensitive step of the compass mechanism may be able to occur in the dark, following periods of light exposure [28]. If true, this suggests a multi-step mechanism for the compass and provides interesting information about the timescales of various steps.

In 2000, the combination of these properties prompted serious investigation [29] into a mechanism proposed over 20 years previously - the radical pair mechanism. It proposed that the Earth's field could be detected via its influence on the coherent spin dynamics of a short-lived, photo-induced radical pair reaction intermediate [30, 31]. After computational models had confirmed that the radical pair could, in theory, explain the observed properties of the avian compass, researchers looked for further experimental proof of the mechanism. In 2004, it was proposed that the key feature of the radical pair mecha-

nism, the coherent, field-dependent interconversion of singlet and triplet states, could be disrupted by applying a radio-frequency (RF) field that would induce additional, field-independent, transitions [32, 33]. The same paper included the first of several demonstrations of the effect on birds, which became disoriented when exposed to RF fields at the Larmor frequency of a free electron in the local geomagnetic field [33, 34]. The result was initially taken as decisive evidence for the radical pair mechanism, as well as proof that in one of the radicals, the unpaired electron was isolated from interaction with any magnetic nuclei [35]. However, careful attempts to replicate the study later failed to find any disorientation under narrow-band, Larmor-frequency fields [36], and instead noticed that the birds became significantly disoriented by very weak, broadband radiofrequency noise produced by human activity and electrical devices around the experimental site [36, 37]. Although RF disorientation is still frequently used as a diagnostic test for a radical-pair compass (e.g. [19, 28, 38, 39]), the conflicting findings have created huge controversy over the exact RF conditions needed to affect the compass, the implication of existing results in identifying the magnetosensitive radical pair and the necessary steps that need to be taken to perform sufficiently well-controlled orientation experiments [40]. One clear conclusion can, however, be drawn. For the radical pair mechanism, as we currently understand it, to be affected by weak RF fields, the radical pair must have a significantly longer coherence lifetime than previously estimated [41, 42]. The feasibility of long-lived coherence in a biological magnetoreceptor will be a major theme of this thesis.

Alongside the drive to uncover the physical mechanism of magnetoreception, research has also been ongoing to understand how birds process and use magnetic information. By observing levels of gene activation in different parts of the brain, it has been shown that magnetic information is processed in an area of the forebrain called Cluster N [11, 43, 44]. Cluster N is a small part of the visual pathway and indirectly receives information from the retinal ganglion cells. The high level of activity in this specific part of the visual system during magnetic orientation suggests that birds may, in some sense, 'see' the magnetic field, perhaps as features modifying or overlaying their 'normal' vision [11].

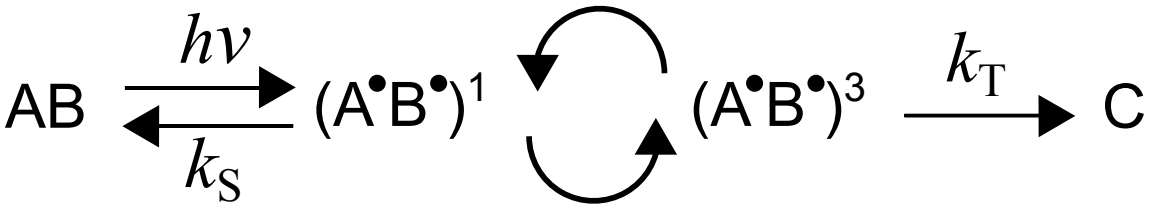


Figure 1.2: Reaction scheme for the radical pair mechanism. k_S and k_T are the rate constants for spin-selective reactions from the singlet and triplet states respectively.

Moreover, it suggests that there is scope for magnetic compass information to interact, whether constructively or destructively, with the birds' vision and even with other visual compasses, such as the sun or star compass. From this perspective, it is particularly interesting that birds appear to calibrate their magnetic compass from the pattern of skylight polarization at dawn and dusk [45–49], allowing them to correct for shifting and variation in the magnetic field over time. It is not known whether birds perceive the magnetic field and polarization patterns as a single visual impression or as separate cues that are each interpreted in the context of the other. However, behavioural experiments have begun to probe the interaction of polarized light with the magnetic compass [50]. Chapter 6 of this thesis considers how the two stimuli might combine to form an image and the implications of separating conflicting signals on the ordering of magnetosensitive cells and receptors.

1.1 The radical pair mechanism

Magnetic fields have been known since the 1970s [51–54] to affect the outcome of reactions involving radical pair intermediates. This dependency is described by the radical pair mechanism, summarised in figure 1.2.

Radicals are reactive, often short-lived, species containing an unpaired electron. They are usually formed in pairs by electron transfer or homolytic bond-breaking. In the avian compass, radical pairs are thought to be formed by photoexcitation of the magnetorecep-

tor, followed by a fast electron transfer that separates the excited electron from its hole and prevents the molecule from instantly returning to the ground state [29, 55]. Hence, the compass requires light to operate and, moreover, requires light at a wavelength that matches the absorption spectrum of the chromophore in the magnetoreceptor. Neither of these experimentally observed properties can be easily explained by a mineral-based compass.

Conservation of spin means that, immediately following the photoexcitation, the molecule is in a singlet state, in which the two unpaired electron spins are arranged antiparallel to each other. If the subsequent electron transfer is very rapid, as is thought to be the case for the avian magnetoreceptor (see section 1.3), spin will continue to be preserved and the radical pair will be generated in a pure singlet state. An initial singlet state is assumed for all the calculations in this thesis. It is not, however, a requirement for a radical pair compass [56].

If the initial state is not an eigenstate of the spin Hamiltonian describing the radical pair, the system will evolve over time, oscillating regularly between the singlet and triplet states at a frequency (or superposition of frequencies) determined by the magnetic interactions present in the radicals. The pattern of oscillations is modulated by the interaction of the unpaired electrons with an external magnetic field (the Zeeman interaction - see section 2.2.1), as shown in figure 1.3. This creates a magnetic field dependence in the state of the radical pair intermediate. In the presence of anisotropic interactions within the radical (e.g. anisotropic hyperfine interactions) the Zeeman interaction will perturb the system more strongly or weakly depending on the direction of the field relative to the quantization axis set by the internal interactions. This gives the reaction a directional dependence that allows it to provide compass information.

Magnetic information is captured by spin-selective reactions of the radical pair. Due to the requirement for electrons to be paired in an orbital (the Pauli principle), the radical pair can only recombine from the singlet state. The longer the radical pair spends in the singlet state during the mixing period, the more chance it has of recombining and

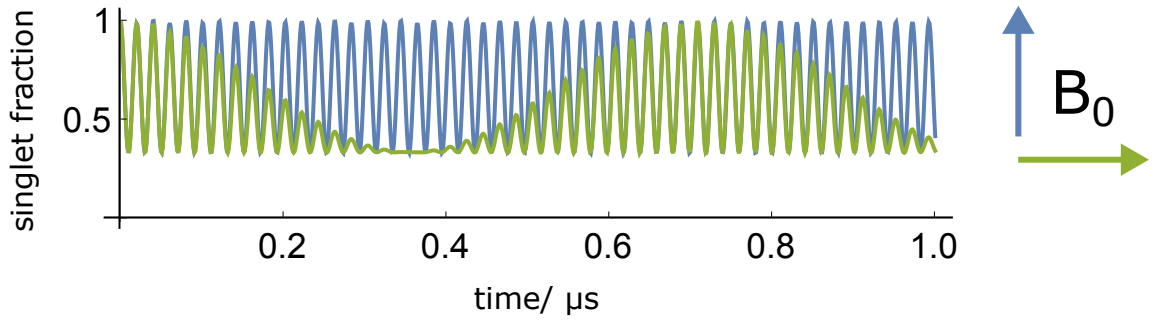


Figure 1.3: Singlet/triplet evolution under different directions of the external field ($B_0 = 50$ μT). The radical pair contains a single spin-1/2 nucleus with hyperfine tensor $[-0.0989, 0.0039, 0.0; 0.0039, -0.0881, 0.0; 0.0, 0.0, 1.7658]$ mT. The direction of the external field is measured relative to the z-axis of this interaction.

the higher will be the ratio of ground state to other products. In this work, it will be assumed that the radical pair has just two reaction pathways: recombination from the singlet state or a further spin-selective reaction of the triplet state to form some other product termed the 'signalling state'. In reality, the reaction scheme is likely to be more complex, possibly even involving multiple radical pair intermediates [28, 57]. However, as the true reaction scheme is not known, the simple model in figure 1.2 is used to capture the essential behaviour of the system.

In addition to the requirement for at least one spin-selective reaction, a radical pair must fulfil a number of other criteria if it is to form the basis of a compass (reviewed in [58] and [59]). First, the radical pair must contain at least one hyperfine interaction (section 2.2.2) between an unpaired electron and a magnetic nucleus in the molecule (e.g. ^{1}H, ^{14}N). Without this crucial interaction, there can be no singlet/triplet mixing and the radical pair will remain in a stationary (singlet) eigenstate of the Hamiltonian. If the compass is to respond to the *direction* of the Earth's field, rather than just its intensity, the radical pair must furthermore contain a source of anisotropy. This is frequently assumed to come from the hyperfine interactions [55], which are often anisotropic and therefore combine differently with different directions of the external field to alter the rate of inter-system crossing. However, other sources, such as electron-electron interactions or anisotropy in the g-tensor, are also possible [58].

The need for anisotropy implies a degree of ordering and immobilisation of the radical pairs. If each radical pair had a completely random orientation, any anisotropy in the signal produced by a single radical pair would disappear when averaged over all the pairs in a receptor cell. Equally, anisotropy will be averaged away if the radical pair is allowed to tumble freely inside the cell. Moreover, without a known orientation for the radical pairs, the signal cannot be meaningfully interpreted in terms of the appropriate heading of the bird. It has been suggested that a directional compass signal could be derived from a disordered ensemble of radical pairs using polarized light to selectively photoexcite a subset of radical pairs with similar orientations inside a well-defined distribution [60]. This arrangement, however, reduces the signal intensity relative to a situation where all radical pairs can be excited and contribute to the signal. It also still requires that the molecules maintain a fixed orientation for the duration of the reaction.

The other consequence of radical pair motion is that it has the potential to drive spin relaxation. At first sight, it is surprising that the outcome of a chemical reaction should be affected by an interaction as weak as that of the radical electrons with the Earth's ≈ 50 μT field, where the interaction energy is six orders of magnitude smaller than the thermal energy ($k_{\mathrm{B}}T$) at room temperature. However, this thermodynamic argument only applies to systems at equilibrium. Upon formation, the radical pair, in a pure singlet state, is very far from its equilibrium configuration (25%S, 75%T) and hence can be influenced by tiny interactions [59]. Once the radical pair has relaxed to equilibrium, the reaction will no longer generate information about the direction of the external field. This creates several criteria for the radical pair. First, relaxation should ideally be slow, which reinforces the idea that radical motion should be restricted. Second, the lifetime of the radical pair must be carefully balanced with the relaxation rate. If the radicals react or recombine too quickly, there will not be sufficient time for the anisotropy of the signal to emerge. On the other hand, if they react too slowly, the system will relax to equilibrium and any field-dependent signal that has built up will be increasingly diluted by the field-independent signal that arises at equilibrium. It has previously been estimated

that the optimum lifetime for the radical pair would be around 1 μs [58], which maximises anisotropy and minimises the effects of relaxation. However, recent work, discussed in chapter 4, has suggested that, under the right conditions, longer radical pair lifetimes could offer advantages in terms of compass precision [61].

The lifetime of the radical pair is closely linked to the physical separation of the two radicals, which influences the rates of forward and backward electron transfer. It also, critically, determines the strength of electron-electron dipolar and exchange interactions. At a centre-to-centre distance of 2.0 ± 0.2 nm, the effects of dipolar and exchange interactions on the outcome of the reaction have been shown to approximately cancel [62]. This separation is also likely to be compatible with a recombination lifetime of 1 μs [58].

To date, the radical pair mechanism remains the most convincing mechanism for the magnetic compass in migratory birds. It offers a clear explanation for the inability of the compass to detect magnetic polarity and the need for specific wavelengths of light. Changes to the signal as the radical pair interacts with fields of different strengths accounts for the ability of birds to adapt to orienting in field intensities outside their usual functional window - they simply need to learn a new pattern or respond to an unfamiliar intensity of the usual pattern. Deactivation of the compass by RF fields provides powerful evidence for a radical pair mechanism, where additional transitions induced by the RF field obscure the dependence of the singlet yield on the rate of S/T transitions induced by the Earth's field.

However, a number of questions remain unanswered about the ability of the radical pair mechanism to fully explain all aspects of the compass. The issue of relaxation and whether coherence can be preserved for long enough to observe a usable compass signal has long been cited as a 'stumbling block' for the radical pair mechanism [63]. The problem is exacerbated by studies of RF effects on animal orientation. Although RF experiments provide the strongest evidence in favour of the radical pair mechanism, the fact that even incredibly weak noise fields appear to disable the compass implies much longer radical pair lifetimes than previously estimated [40]. It is not known why birds might have evolved

an apparently unnecessary sensitivity to such weak fields or whether it is possible to have a sufficiently long-lived *coherent* radical pair in a noisy biological setting.

The second barrier to achieving a strong compass signal is the amount of available light. Although the compass requires light to function, most of the commonly studied species of birds are night-migratory and appear to be able to use their compass even in extremely low light levels (0.0003 lux, reported in [47]) [59]. Intuitively, the ability to function under such conditions seems to imply a more highly anisotropic signal that can be resolved using smaller numbers of radical pairs [64]. The important question is again whether an adequately strong signal can be derived from the radical pair mechanism, taking into account the potentially detrimental effects of relaxation.

Furthermore, it has been unclear from previous simulations whether the radical pair mechanism could give rise to a sufficiently precise compass. Tracking experiments and tests of orientation in very high or low inclination fields imply that the birds' compass is precise to within around 5° [36, 65, 66], whereas simulations of the radical pair mechanism show very little difference in the singlet yield when the field direction is altered by 5° [29, 67, 68].

Finally, a major barrier to understanding the radical pair mechanism is the lack of an unambiguously identified magnetoreceptor (and radical pair). Currently, the strongest candidate is the blue-light photoreceptor, cryptochrome, which will be discussed in section 1.3.

1.2 The magnetite hypothesis

The second major hypothesis invoked to explain animal magnetosensitivity is a magnetite mechanism, which is based on the central idea that the compass utilises particles of single-domain biogenic magnetite. Like common man-made compasses, any compass system based on single-domain magnetite will be sensitive to the polarity of the magnetic

field. Several permutations of the magnetite mechanism have been proposed [69, 70]. The simplest proposal is that the compass consists of a chain of single-domain magnetite particles bound to a mechano-sensitive, trans-membrane ion channel. As the chain of particles rotates to align itself in the Earth's field, it opens or closes the channel. The probability of Ca^{2+} ions passing through the channel to generate an action potential depends on how open the channel is and therefore on the direction of the field. In other variations, the channel is indirectly opened by the single domain particles via their interaction with intermediary chemical reactions or nearby superparamagnetic particles.

Magnetite-based compasses have been proposed for several animals, including bees [24], trout [71] and pigeons [72], which appear to be sensitive to polarity. Remagnetization experiments on bees have shown that the animals changed their preferred orientation relative to the natural geomagnetic field after exposure to a strong, pulsed magnetic field [73]. This behaviour would be consistent with a change in the direction of the permanent magnetic moment of a single domain particle acting as a 'compass needle'.

Iron structures in animal cells are frequently reported as possible magnetoreceptors [71, 72, 74]. None, however, has been confirmed as playing a role in magnetoreception [75, 76] and many have later been shown to be contaminants [70]. The search for a magnetoreceptive particle is hampered by the frequent presence of contaminants, the lack of a 100% accurate method of staining [75], and the fact that the particles could be located in any of the many billions of cells in the body, lots of which contain iron for completely separate purposes [59, 70, 77]. For example, iron-containing cells in the upper beaks of birds, now known to be macrophages [76, 78], were long thought to form part of the magnetosensory pathway [72, 79].

For migratory birds, a purely magnetite-based compass is no longer considered a feasible hypothesis. However, there are still suggestions that magnetic particles might exist as the basis of a map sense, used in tandem with a radical pair based compass [59, 80]. The possibility of magnetic particles forming part of an amplification mechanism for the radical pair mechanism has also recently been postulated in several different forms [81, 82].

1.3 Cryptochrome: the candidate magnetoreceptor

In their seminal paper investigating the radical pair mechanism in the context of avian magnetoreception, Ritz *et al.* made the insightful suggestion that the magnetically-sensitive radical pair could be produced by blue-light photoreceptor proteins called cryptochromes [29]. Eighteen years later, cryptochrome is still considered the most viable candidate for a radical pair magnetoreceptor.

Cryptochromes are closely related to DNA photolyases [83, 84] - a family of proteins that repair UV-damaged DNA. They are widespread throughout the plant and animal kingdoms and are thought to be involved in a range of blue-light dependent signalling pathways [85, 86]. Different varieties of cryptochromes may be loosely categorized as either plant cryptochromes, animal cryptochromes or DASH-cryptochromes [87] (a distinct group, most closely resembling animal cryptochromes [84]). Despite a relatively high level of diversity in their DNA sequences, a few key structural features are preserved across the cryptochrome family. All cryptochromes and photolyases share a highly conserved N-terminal domain and a similar three-dimensional structure for the main body of the protein (the 'photolyase homology region', PHR) [84, 88]. The topological similarity is thought to belie shared energy and electron transfer pathways, which demand precise separations and orientations of key components [88]. Within the PHR lies an essential flavin cofactor, responsible for absorbing blue light [86], and a triad of tryptophan residues, which form an electron transfer pathway for photoreduction of the flavin [89, 90]. In animal cryptochromes, a tryptophan tetrad, rather than a triad, is observed [91, 92]. The most variable part of the cryptochrome structure is an extended C-terminal tail, of varying lengths, which is not present in photolyases. This tail is thought to underlie a number of specific functions for different cryptochromes [84, 86], such as triggering a signalling pathway [93].

Despite their structural similarity to DNA photolyases, cryptochromes do not show pho-

tolyase activity. Plant cryptochromes influence the way that the plant responds to light by extending its roots, lengthening its stem and putting out flowers [85–87, 94]. In animals, type I and type II cryptochromes act, respectively, as photoreceptors and transcriptional repressors in the process of entraining the circadian clock in response to daily variations in light levels [84, 95, 96]. Some animals, including chickens, zebrafish and migratory birds, possess an additional type of cryptochrome, CRY4, for which the functional role is still unknown [94, 95].

To date there is no direct evidence for the involvement of cryptochrome in avian magnetoreception. Nor is it known which, if any, of the four cryptochromes found in birds (CRY1a, CRY1b, CRY2 and CRY4 [84]) might form part of the compass. There is, however, a growing body of experimental data to support a cryptochrome magnetoreceptor.

Knockdown experiments on *Drosophila* (fruit flies) have shown that naive and trained responses to a magnetic field in a binary-choice maze are CRY-dependent [97]. Exposure to magnetic fields also alters the length of the circadian period and induces hyperactivity in a CRY-dependent manner in *Drosophila* [98] and in cockroaches [17]. In addition to behavioural assays, electrophysiology experiments have demonstrated magnetic field effects on neuronal firing in response to blue-light activation of CRY [99]. In both behavioural and electrophysiological experiments, the observed magnetic field effects were seen to disappear when mutations were introduced into the C-terminal tail (thought to participate in signal transduction) but not when the terminal Trp was replaced with a redox-inactive residue. These observations are not necessarily transferable to migratory birds, where genetic studies are significantly more challenging, although they provide valuable information about the behaviour and role of CRY *in vivo*. In particular, the agreement between different assays offers good evidence that cryptochrome plays a role in magnetoreception, whilst the effects of introducing point mutations help to elucidate the important, active parts of the CRY structure. However, although they suggest a role for cryptochrome in magnetoreception, the experiments offer no information about

what that role might be and, crucially, whether cryptochrome might produce the magnetically sensitive radical pair. More recent genetic studies of *Drosophila* have indicated that CRY-dependent climbing behaviour is disrupted by weak radiofrequency fields [98, 100]. Thus, we might expect that a cryptochrome-based compass would also be susceptible to radiofrequency noise, as observed in behavioural experiments. So far, the results of these rf-field experiments have not been independently repeatable.

All four avian cryptochromes have been found in retinal cells, as would be expected for a light-dependent compass. Moreover, they have been found potentially associated with ordered structures within the cell that could offer a way of partially immobilizing populations of cryptochromes [101], as required for the radical pair mechanism (see above). CRY1a has been found in UV photoreceptor cones, where it is observed in ordered bands alongside layered membrane discs in the outer segment [102]. Meanwhile, CRY1b is located in retinal ganglion cells and the inner segments of photoreceptor cells [102–105], which also contain ordered membrane structures [106]. During night-time magnetic orientation, CRY1 co-localizes with neuronal activity markers in ganglion cells [103]. Furthermore, the amount of CRY1 in the ganglion cells is seasonally variable and the strongest expression occurs during the migratory season [105].

Perhaps most interestingly, CRY4, whose function is currently unknown, has recently been found in double cones, where it also shows increased expression during the migratory season [107]. Double cones have been postulated [59] as the ideal location for a magnetoreceptor as the output of receptors in different orientations in the two member cones could be compared to filter out unwanted light intensity and polarization effects. Double cones are found in abundance across the whole avian retina and their purpose is unclear [59].

Studies of cryptochrome in vitro have revealed that it has many of the properties needed for it to function as a radical pair magnetoreceptor. Most importantly, cryptochrome forms radical pairs under blue light illumination. In its oxidized groundstate, the flavin cofactor (FAD) absorbs strongly around 360 nm (UV) and 450 nm (blue) [57]. Photoexci-

tation increases its oxidation potential, triggering a series of sequential electron transfers along the Trp triad/tetrad, from a terminal tryptophan or tyrosine residue [90]. The radical forms of flavin ($FAD^{\bullet -}$, $FADH^{\bullet}$ and $FADH^{-}$) all absorb most strongly in the UV region, around 350 nm and below 300 nm. $FAD^{\bullet -}$ also has a relatively strong, broad absorption from $450 - 650$ nm. Absorption in this ranges photoreduces $FAD^{\bullet -}$ to FAD^{-} [108], which, it has been suggested, could act as a storage species for light-independent radical pair formation at a later time [28].

The radical pair formed varies between different cryptochromes. Garden warbler CRY1a (*gw*CRY1a) initially forms a radical pair between $FADH^{\bullet}$ and $Trp^{\bullet}$ with a lifetime on the order of a millisecond. This may be followed by slower electron transfer from a nearby tyrosine to form a $TyrO^{\bullet}$ radical [109]. In *Arabidopsis thaliana* CRY1 (*At*CRY1) [110] and chicken CRY4 [111], the third tryptophan in the triad donates an electron to form [$FAD^{\bullet -}$ $TrpH^{\bullet +}$]. Fast electron transfer means that the radical pair is produced in a singlet state [110, 112]. A secondary radical pair, [$FADH^{\bullet}$ $Trp^{\bullet}$] is subsequently formed by protonation/deprotonation reactions. The primary radical pair survives for about 10 μs before reacting to make the secondary radical pair or recombining to the ground state (from the singlet state) [89, 110]. A model photocycle for *At*CRY1 is shown in figure 1.4. In this work, I will take [$FAD^{\bullet -}$ $TrpH^{\bullet +}$] as a model for the magnetically sensitive radical pair.

Magnetic field effects have been measured on [$FAD^{\bullet -}$ $TrpH^{\bullet +}$] in *At*CRY1 in fields as low as 1 mT [110], demonstrating that, in principle, cryptochrome could form the basis of a compass. However, for the avian compass to work, there would need to be discernible magnetic field effects at much weaker fields. It is conceivable that cryptochrome could respond more strongly to weaker fields *in vivo*, where the proteins may be immobilized and ordered by fine-tuned protein interactions. There is currently no technique for probing the behaviour of cryptochrome *in vivo*, although experiments are being developed to sensitively image magnetic field effects on over-expressed proteins in cell cultures [113].

It is also possible that a bird cryptochrome might have evolved to optimise the identity

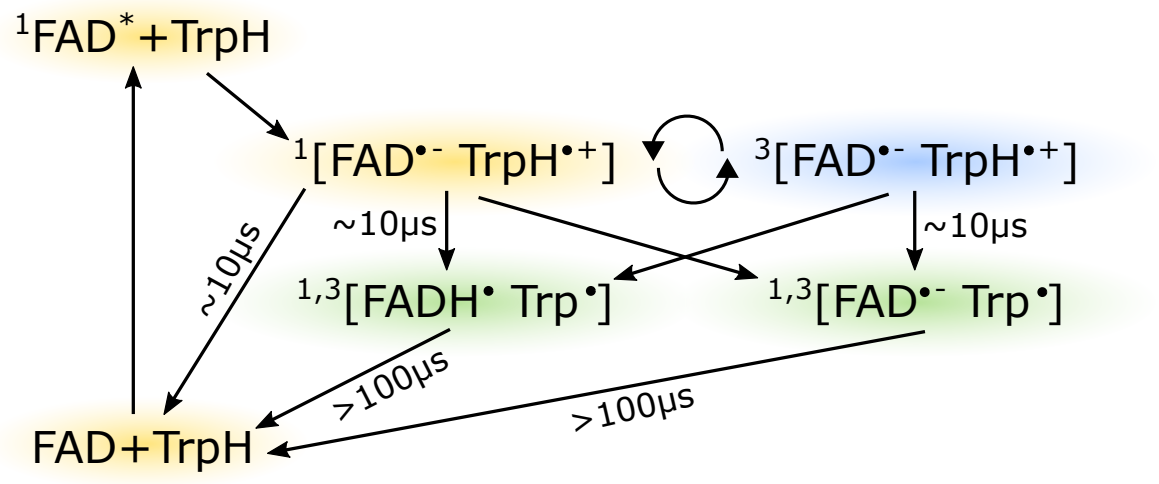


Figure 1.4: Photocycle for *At*CRY1 [110]. The first radical pair, [FAD$^{\bullet-}$ TrpH$^{\bullet+}$] is thought to impart magnetosensitivity.

and kinetics of the radical pair for magnetoreception. The difficulty of expressing the bird cryptochromes with FAD correctly bound has hindered potential explorations of the specific conditions in which a radical pair might be formed [59, 109]. Moreover, recent work has shown that the key amino acid residues used to bind FAD in *Dm*CRY1 may be missing from many of the avian CRY1a and CRY2 proteins that have previously been isolated and studied, resulting in poor binding affinities [114]. By contrast, chicken CRY4 shows good flavin binding, supporting the suggestion that it may be the most likely avian cryptochrome to act as a magnetoreceptor.

The lack of any definitive evidence that cryptochrome produces the magnetically sensitive radical pair and the inability to carry out detailed studies of avian cryptochromes under realistic conditions are both significant barriers in ongoing research into the avian magnetic compass.

1.4 Aims

There are many questions in the field of avian magnetoreception that are currently out of the reach of current experimental techniques. However, it is possible to investigate these

questions theoretically. Computational modelling of cryptochrome and the radical pair mechanism can never completely replace direct measurement but it can provide insights that can guide the interpretation and design of further experiments. In this thesis, I will use spin dynamical simulations of a radical pair magnetoreceptor to look at three outstanding problems:

1. As stated above, the question of whether spin coherence in cryptochrome can be preserved long enough to detect the Earth's weak magnetic field has long been a stumbling block for the radical pair mechanism. Although spectroscopic studies can probe the motion and relaxation times of cryptochrome *in vitro*, they cannot replicate biological conditions. They are also hindered by the difficulty of obtaining samples of bird cryptochromes. In chapters 4 and 5, I will report investigations of optimal conditions for preserving coherence, with a particular focus on relaxation caused by restricted rotational motion of the two radicals within the cryptochrome molecule. I will also look at the effect of relaxation in model systems designed to represent cryptochrome.

2. It is already known that a high degree of order is needed for the compass to function correctly. This has implications for the way that the compass might interact with polarized light, which selectively excites molecules with a particular orientation. The effect of polarized light on the magnetic compass has recently been under experimental investigation. In chapter 6, I will explore ways of arranging highly ordered ensembles of magnetoreceptors to avoid any conflict of polarized light and magnetic cues.

3. Indisputable identification of the magnetoreceptor would mark a significant step forward in the quest to understand radical pair magnetoreception and the avian compass. In chapter 7 I will use ideas about the effect of spin relaxation on the compass (from chapters 4 and 5) to propose and design an experiment to convincingly test the hypothesis that cryptochrome is the avian magnetoreceptor.

Chapter 2

Theoretical background

2.1 Spin

The radical pair mechanism makes use of one of the fundamental properties of electrons: their spin. Spin is an intrinsic angular momentum; it is a purely quantum mechanical property that is not associated with any actual physical rotation but it obeys all the rules of a classical angular momentum.

Spin is a vector quantity with a magnitude $\sqrt{s(s+1)}\hbar$ and a direction described by its projection $m_s\hbar$ onto a chosen axis, as shown in figure 2.1. The magnitude is quantized by the spin quantum number s and its value can be found using the operator

$$\hat{S}^2 \left|s, m_s\right\rangle = s(s+1)\hbar^2 \left|s, m_s\right\rangle . \tag{2.1}$$

In contrast to classical angular momenta, the spin quantum number is able to adopt half-integer as well as integer values ($s = 0, 1/2, 1, 3/2 \cdots$). Electrons are spin-1/2 ($s = 1/2$). The magnetic nuclei considered in this thesis are ^{1}H, which has $s = 1/2$ and ^{14}N, which has $s = 1$.

The direction of the spin angular momentum vector is quantized by the spin projection

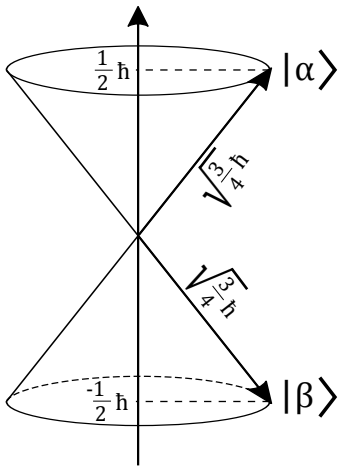


Figure 2.1: Quantization of spin angular momentum for a spin-1/2 particle. The magnitude of the angular momentum vector is $\sqrt{s(s+1)}\hbar = \sqrt{3/4}\hbar$. The vector is projected onto a quantization axis (usually the z axis) with a projection of $m_s\hbar = \pm\hbar/2$. Once the projection onto the z axis is measured, the projection onto the x and y axes can no longer be defined.

quantum number m_s, which can take the $2s+1$ values, $s, s-1, \cdots -s$. An electron therefore has two possible spin states: $|\alpha\rangle = |s = 1/2, m_s = 1/2\rangle$ and $|\beta\rangle = |s = 1/2, m_s = -1/2\rangle$. The quantization axis (or projection axis) is usually taken as the z axis, with the projection of the spin onto this axis being given by

$$\hat{S}_z \left|s, m_s\right\rangle = m_s\hbar \left|s, m_s\right\rangle . \tag{2.2}$$

Once the projection axis has been set (by measurement), the projection of the spin onto the two perpendicular axes (x and y axes) can no longer be determined, according to the cyclically symmetric commutation rules

$$[\hat{S}_z, \hat{S}_x] = i\hbar\hat{S}_y, \tag{2.3}$$

$$[\hat{S}_x, \hat{S}_y] = i\hbar\hat{S}_z, \tag{2.4}$$

$$[\hat{S}_y, \hat{S}_z] = i\hbar\hat{S}_x. \tag{2.5}$$

These non-zero commutators mean that eigenstates of $\hat{S}_z$ are not eigenstates of $\hat{S}_x$ and $\hat{S}_y$, which consequently drive transitions between the eigenstates. Specifically, $\hat{S}_x$ and $\hat{S}_y$

combine to form the raising and lowering operators

$$\hat{S}_{\pm} = \hat{S}_x \pm i\hat{S}_y, \tag{2.6}$$

which step the spin state up and down between m_s levels, according to

$$\hat{S}_{\pm} \left|s, m_s\right\rangle = \sqrt{s(s+1) - m_s(m_s \pm 1)}\hbar \left|s, m_s \pm 1\right\rangle. \tag{2.7}$$

The building blocks for matrix representations of spin operators systems are the Pauli matrices σ_q, such that

$$\boldsymbol{S}_q = \frac{\hbar}{2}\sigma_q, \tag{2.8}$$

where $\boldsymbol{S}_q$ is the matrix representation of $\hat{S}_q$ in an $\{\left|\alpha\right\rangle, \left|\beta\right\rangle\}$ basis. The Pauli matrices for a spin-1/2 particle are

$$\sigma_x = \begin{pmatrix} 0 & 1 \\ 1 & 0 \end{pmatrix}, \qquad \sigma_y = \begin{pmatrix} 0 & -i \\ i & 0 \end{pmatrix}, \qquad \sigma_z = \begin{pmatrix} 1 & 0 \\ 0 & -1 \end{pmatrix}. \tag{2.9}$$

For a spin-1 particle, the spin matrices are

$$\sigma_x = \begin{pmatrix} 0 & \frac{1}{\sqrt{2}} & 0 \\ \frac{1}{\sqrt{2}} & 0 & \frac{1}{\sqrt{2}} \\ 0 & \frac{1}{\sqrt{2}} & 0 \end{pmatrix}, \qquad \sigma_y = \begin{pmatrix} 0 & -i\frac{1}{\sqrt{2}} & 0 \\ i\frac{1}{\sqrt{2}} & 0 & -i\frac{1}{\sqrt{2}} \\ 0 & i\frac{1}{\sqrt{2}} & 0 \end{pmatrix}, \qquad \sigma_z = \begin{pmatrix} 1 & 0 & 0 \\ 0 & 0 & 0 \\ 0 & 0 & -1 \end{pmatrix}. \tag{2.10}$$

Spin operators for larger systems are constructed by taking the Kronecker product of the Pauli matrices for each spin. For example, for a three-spin system, the operator corresponding to the projection of the first spin along the z axis is

$$\boldsymbol{S}_{1,z} = \sigma_z \otimes \mathbb{I}_{2s_2+1} \otimes \mathbb{I}_{2s_3+1}, \tag{2.11}$$

where $\mathbb{I}_n$ is the n-dimensional identity matrix. The Kronecker product, represented by

the symbol $\otimes$, is defined by

$$\begin{pmatrix} a_{11} & a_{12} \\ a_{21} & a_{22} \end{pmatrix} \otimes \begin{pmatrix} b_{11} & b_{12} \\ b_{21} & b_{22} \end{pmatrix} = \begin{pmatrix} a_{11}b_{11} & a_{11}b_{12} & a_{12}b_{11} & a_{12}b_{12} \\ a_{11}b_{21} & a_{11}b_{22} & a_{12}b_{21} & a_{12}b_{22} \\ a_{21}b_{11} & a_{21}b_{12} & a_{22}b_{11} & a_{22}b_{12} \\ a_{21}b_{21} & a_{21}b_{22} & a_{22}b_{21} & a_{22}b_{22} \end{pmatrix}. \tag{2.12}$$

It is a bilinear, associative, non-commutative operation and also has the property that

$$(A \otimes B)(C \otimes D) = (AC) \otimes (BD). \tag{2.13}$$

This last property is particularly useful when it comes to constructing the product operators (e.g. $S_z\hat{L}_z$) that appear in multi-spin interaction Hamiltonians (see section 2.2). The matrix representation of a product operator is defined by

$$\mathbf{S_q L_r} = \sigma_q \otimes \sigma_r \otimes \mathbb{I}_n, \tag{2.14}$$

where S is the first spin in the system (e.g. electron 1), L is the second spin (e.g. electron 2), $q, r = x, y, z$ and n is the sum of the dimensions of the spin operators of all the remaining spins in the system (e.g. magnetic nuclei in the radical pair). Using equation (2.13),

$$\begin{aligned} \mathbf{S_q L_r} =& ((\sigma_q \otimes \mathbb{I})(\mathbb{I} \otimes \sigma_r)) \otimes (\mathbb{I}_n), & (2.15) \\ =& (\sigma_q \otimes \mathbb{I}_{2l+1} \otimes \mathbb{I}_n)(\mathbb{I}_{2s+1} \otimes \sigma_r \otimes \mathbb{I}_n), & (2.16) \\ =& \boldsymbol{S}_{\mathrm{q}} \times \boldsymbol{L}_{\mathrm{r}}, & (2.17) \end{aligned}$$

which means that product operator matrices can be formed by taking the matrix product of the one-spin operator matrices.

The outcome of a radical pair reaction depends not on the spin state of the individual electrons but rather the spin state of the whole radical pair i.e. the total spin angular mo-

mentum of the two coupled electron spins. The spin states of a total angular momentum $\boldsymbol{S} = \boldsymbol{s}_1 + \boldsymbol{s}_2$ are defined by their spin quantum numbers S, the possible values of which are given by the Clebsch-Gordan series:

$$S = s_1 + s_2, s_1 + s_2 - 1, \cdots, |s_1 - s_2|. \tag{2.18}$$

Each state, described by the quantum number S has $2S + 1$ sublevels, labelled by the total projection quantum number M_s. A radical pair (which has two spin-1/2 electrons) can either have $S = 0$, known as the singlet state, or $S = 1$, known as the triplet state. The singlet state $|S_0\rangle$ has just one sublevel with $M_s = 0$, corresponding to an antiparallel arrangement of the two spins. The triplet state has three sublevels, $|T_+\rangle$, $|T_0\rangle$ and $|T_-\rangle$, corresponding to $M_s = +1$, 0 and -1 respectively. Before the photoexcitation that forms the radical pair, the two electrons are paired in an orbital with opposite spins (according to the Pauli principle) and hence $S = 0$. Spin is conserved during the photoexcitation and, if it is fast enough, during the initial electron transfer, meaning that the radical pair is produced in a singlet state. By the same argument, the radical pair can only recombine back to the ground state from its singlet state.

The spin wavefunctions for the radical pair spin states are

$$|S_0\rangle = \frac{1}{\sqrt{2}}(|\alpha\beta\rangle - |\beta\alpha\rangle) \tag{2.19}$$

$$|T_+\rangle = |\alpha\alpha\rangle \tag{2.20}$$

$$|T_0\rangle = \frac{1}{\sqrt{2}}(|\alpha\beta\rangle + |\beta\alpha\rangle) \tag{2.21}$$

$$|T_-\rangle = |\beta\beta\rangle\,. \tag{2.22}$$

2.2 Magnetic interactions

2.2.1 Zeeman interaction

The avian magnetic compass depends on the interaction between the unpaired electron spins and the Earth's magnetic field, known as the Zeeman interaction. The spin of an unpaired electron is associated with a magnetic moment

$$\boldsymbol{\mu} = \gamma_{\mathrm{e}} \boldsymbol{S}, \tag{2.23}$$

where $\mathbf{S}$ is the spin angular momentum vector and γ_{e} the gyromagnetic ratio of the electron. This magnetic moment interacts with an external field $\boldsymbol{B}$ with an energy

$$E = -\boldsymbol{\mu} \cdot \boldsymbol{B}. \tag{2.24}$$

Consequently, the Hamiltonian for the Zeeman interaction is

$$\hat{H}_{\mathrm{zee}} = -\gamma_{\mathrm{e}} \boldsymbol{B} \cdot \hat{\boldsymbol{S}}. \tag{2.25}$$

In the reference frame of the radical pair molecule,

$$\hat{\boldsymbol{S}} = \begin{pmatrix} \hat{S}_x \\ \hat{S}_y \\ \hat{S}_z \end{pmatrix} \qquad \text{and} \qquad \boldsymbol{B} = B_0 \begin{pmatrix} \sin\theta\cos\phi \\ \sin\theta\sin\phi \\ \cos\theta \end{pmatrix}, \tag{2.26}$$

where B_0 is the strength of the Earth's field and θ and ϕ are, respectively, polar and azimuthal angles describing the orientation of the Earth's field relative to the molecular z axis. Hence, for the radical pair

$$\hat{H}_{\mathrm{zee}} = -\gamma_{\mathrm{e}} B_0 \left((\hat{S}_z + \hat{L}_z)\cos\theta + (\hat{S}_x + \hat{L}_x)\sin\theta\cos\phi + (\hat{S}_y + \hat{L}_y)\sin\theta\sin\phi \right), \tag{2.27}$$

where $\hat{S}_q$ and $\hat{L}_q$ are the spin operators for the two electrons. The frequency $\gamma_e B_0$ is the Larmor frequency ω_e of the free electron in the Earth's magnetic field, which describes the rate at which the electron spins precess around the magnetic field vector.

Providing that both radicals experience the same magnetic field (as is assumed in equation (2.27)), the initial singlet state is an eigenfunction of the Zeeman Hamiltonian. Therefore, the field on its own cannot induce singlet-triplet interconversion. It can, however, modulate the rate of inter-system crossing driven by other interactions.

The gyromagnetic ratio of each electron is

$$\gamma_e = \frac{ge}{2m_e}, \tag{2.28}$$

where m_e is the mass and e the charge on the electron. The constant g is the g-factor of the electron. In some cases, strong spin-orbit coupling can change the value of g or even make it anisotropic (in which case, g is represented by a tensor rather than a scalar). A difference in the g-factors of the electrons means that they experience slightly different magnetic fields and hence precess at different rates, creating a pathway for singlet-triplet interconversion. This is known as the Δg-mechanism. However, for the organic radicals in cryptochrome, the g-factors of both electrons are essentially isotropic and equal to the value for a free electron.

2.2.2 Hyperfine interactions

The driving force for inter-system crossing in the radical pair mechanism is the presence of hyperfine interactions between the unpaired electrons and any magnetic nuclei in the radicals. Hyperfine interactions also frequently act as a source of anisotropy in the compass.

The hyperfine Hamiltonian is[1]

$$\hat{H}_{\mathrm{HFI}} = \hat{\boldsymbol{S}} \cdot \boldsymbol{A} \cdot \hat{\boldsymbol{I}}, \tag{2.30}$$

where the hyperfine tensor $\boldsymbol{A}$ can be divided into isotropic (a) and anisotropic ($\boldsymbol{T}$) components that arise from different sources [115].

The isotropic hyperfine interaction,

$$\hat{H}_{\mathrm{iso}} = a\hat{\boldsymbol{S}} \cdot \hat{\boldsymbol{I}}, \tag{2.31}$$

comes from the Fermi contact interaction, which can be thought of as the interaction between the electron spin and the magnetic field inside the nucleus. The isotropic coupling,

$$a = \frac{8\pi}{3}\gamma_{\mathrm{e}}\gamma_{\mathrm{n}}\hbar^2|\psi(0)|^2, \tag{2.32}$$

is therefore only non-zero if there exists some electron density at the nucleus ($|\psi(0)|^2$). The strength of the isotropic coupling also depends on the electron gyromagnetic ratio γ_{e} (equation (2.28)) and the nuclear gyromagnetic ratio $\gamma_{\mathrm{n}} = g_{\mathrm{n}}e/2m_{\mathrm{n}}$.

The anisotropic hyperfine interaction is the result of the dipolar interaction between the magnetic moments of the electron and nuclear spins outside the nucleus (where the nuclear spin may be treated as a point dipole). The size of the anisotropic coupling is found by averaging the dipolar Hamiltonian,

$$\hat{H}_{\mathrm{dip}} = \gamma_{\mathrm{e}}\gamma_{\mathrm{n}}\hbar^2 \left(\frac{3(\hat{\boldsymbol{I}} \cdot \boldsymbol{r})(\hat{\boldsymbol{S}} \cdot \boldsymbol{r})}{r^5} - \frac{\hat{\boldsymbol{I}} \cdot \hat{\boldsymbol{S}}}{r^3} \right) \tag{2.33}$$

over the spatial wavefunction to give [115]

$$T_{ij} = \gamma_{\mathrm{e}}\gamma_{\mathrm{n}}\hbar^2 \left\langle \psi \left| \frac{3r_i r_j - \delta_{ij}r^2}{r^5} \right| \psi \right\rangle; \qquad i,j = x,y,z. \tag{2.34}$$

[1] A note on notation: The dot product in equation (2.30) can be equivalently written as a sum of product operator terms.

$$\hat{\mathbf{S}} \cdot \mathbf{A} \cdot \hat{\mathbf{I}} = \sum_{p,q} A_{pq} S_p \hat{I}_q \tag{2.29}$$

The vector $\boldsymbol{r}$ describes the position of the electron relative to the centre of the magnetic nucleus with which it is interacting.

The anisotropic hyperfine tensor is traceless, indicating that the interaction will be averaged to zero by fast tumbling of the molecule in solution. The effect of molecular tumbling on the anisotropy of the compass signal, which arises from the anisotropy of the hyperfine interactions, will be explored in chapters 4 and 5.

Previous work has found that, for a 1-nucleus radical pair, an optimally anisotropic compass signal is achieved when the hyperfine tensor has axial anisotropy ($T_{xx} = T_{yy} \neq T_{zz}$) with $T_{zz} = 2a$ [68]. The traceless nature of the anisotropic hyperfine tensor means that when $T_{zz} = 2a$, $A_{xx} = A_{yy} = 0$.

The hyperfine tensors used in this thesis were calculated by Ilya Kuprov. They are published in reference [68] and are listed in appendix A.

2.2.3 Interelectron interactions

As well as interacting with nuclear spins, the unpaired electron spins can interact with each other.

Two electron spins have a dipolar interaction analogous to the one that generates the anisotropic component of the hyperfine tensor. The dipolar Hamiltonian is

$$\hat{H}_{\text{dipolar}} = D(r)\left((\hat{S}_z\cos\varepsilon + \hat{S}_x\sin\varepsilon)^2 - \frac{1}{3}\hat{S}^2\right), \tag{2.35}$$

where ε is the angle between the molecular z axis and the axis joining the two electron spins [62]. The strength of the dipolar coupling $D(r)$ falls away rapidly with distance (r) according to

$$D(r) = -\frac{3\mu_0\gamma_e^2\hbar^2}{8\pi r^3}. \tag{2.36}$$

The electron spins are also coupled by an exchange interaction with the Hamiltonian

$$\hat{H}_{\text{ex}} = -J(r)(\hat{S}^2 - \hat{\mathbb{I}}). \tag{2.37}$$

The exchange interaction is usually assumed to decay exponentially according to

$$J(r) = J_0 \exp(-\beta r), \tag{2.38}$$

where the constant β is positive and J_0 can be either positive or negative.

If either the dipolar or the exchange interaction are larger than the external field B_0, they reduce the compass sensitivity by lifting zero field degeneracies that would otherwise have been lifted by the Zeeman interaction with the Earth's field [62, 116]. At a 1.9 nm separation inside the cryptochrome protein [58], the exchange and dipolar interactions between the flavin and tyrptophan radicals are unlikely to be weaker than the Zeeman interaction with the Earth's field. However, the effects of the two interactions will approximately cancel out if either of the conditions

$$D \approx 6J \qquad \text{or} \qquad D \approx -3J \tag{2.39}$$

are met [62]. These conditions are thought to be satisfied for the flavin-tryptophan radical pair with a separation of $1.8 - 2.2$ nm.

Coupling the two radicals via exchange or dipolar interactions significantly increases the difficulty of simulating the spin dynamics of the reaction, thus limiting the size of the spin system that can be treated. Based on the observation above, that exchange and dipolar interactions in cryptochrome may cancel each other out, electron-electron interactions will be neglected from all the calculations in this thesis.

However, we cannot conclude that these interactions have no role to play in the compass. Recent work has shown that modulating exchange and dipolar interactions via electron-hopping along the Trp triad or fluctuations in the protein conformation may provide a

mechanism for enhancing the compass signal [117].

2.3 Density matrix formalism

A system in a pure state can be described by a wavefunction

$$|\psi\rangle = \sum_i c_i |\phi_i\rangle , \tag{2.40}$$

where $\{\phi_i\}$ are a set of orthonormal basis states that span the Hilbert space.

However, in many realistic situations, such as thermal equilibrium, the system exists in a statistical mixture of pure states. We cannot know the exact make-up of the system but, rather, can describe the probability that any particular state is occupied. In these cases it is more convenient to use an alternative representation of the system: the density matrix.

The density matrix is a matrix representation of the density operator

$$\hat{\rho} = |\psi\rangle \langle\psi| . \tag{2.41}$$

It has elements

$$\rho_{ij} = \langle\phi_i|\hat{\rho}|\phi_j\rangle = c_i c_j^* . \tag{2.42}$$

From equation (2.42), it can easily be shown that the density matrix, like all quantum operator matrices, is hermitian:

$$\rho_{ij} = \langle\phi_i|\psi\rangle \langle\psi|\phi_j\rangle = \langle\phi_j|\psi\rangle^* \langle\psi|\phi_i\rangle^* = \rho_{ji} * . \tag{2.43}$$

The products of coefficients that make up the elements of the density matrix contain a lot of important information about the system. For example, the diagonal elements of

the density matrix

$$\rho_{ii} = c_i c_i^* = c_i c_i^* \langle \phi_i | \phi_i \rangle = | \langle \phi_i | \psi \rangle |^2 \tag{2.44}$$

give the probability of the system being found in the basis state ϕ_i. For this reason the diagonal elements of the density matrix are referred to as 'populations'. They are always real and in the range [0,1], consistent with their definition as probabilities. The off-diagonal elements, which describe the evolution of coherent superpositions, are termed 'coherences' and have complex values.

Products of coefficients are also crucial for determining the expectation values of the operators that describe the physical properties of a system. Using a wavefunction notation, the expectation value of an operator $\hat{A}$ is

$$\langle \hat{A} \rangle = \langle \psi | \hat{A} | \psi \rangle \,. \tag{2.45}$$

Expanding the wavefunction as a linear combination of basis states gives

$$\langle \hat{A} \rangle = \left\langle \sum_i c_i \phi_i \middle| \hat{A} \middle| \sum_j c_j \phi_j \right\rangle \tag{2.46}$$

$$= \sum_{ij} c_i^* c_j A_{ij}. \tag{2.47}$$

Using the definition of the density matrix in equation (2.42)

$$\langle \hat{A} \rangle = \sum_{ij} \rho_{ji} A_{ij} = \sum_j (\rho A)_j = \mathrm{Tr}(\rho \mathbf{A}) = \mathrm{Tr}(\mathbf{A} \rho). \tag{2.48}$$

Thus, using the density matrix, the expectation value of an operator can be simply calculated for pure and mixed states.

A system in a pure state $|\psi\rangle$ has a 100% chance of being found in that state. Its density matrix therefore has one non-zero element, equal to 1, in the eigenbasis of the spin Hamiltonian. By contrast, a mixed state will have several non-zero diagonal elements, which add up to 1 (as the system certainly exists in some state). These non-zero elements

represent the probability of each state existing in a statistical ensemble. The density matrix consequently has the property

$$\mathrm{Tr}(\rho^2) = \begin{cases} 1 & \text{pure state} \\ < 1 & \text{mixed state.} \end{cases} \tag{2.49}$$

Note that the trace is invariant under a similarity transform so equation (2.49) holds regardless of the basis set of the density matrix.

2.3.1 Correlation and Entanglement

At thermal equilibrium, states are populated according to the Boltzmann distribution, such that the diagonal elements of the density matrix are

$$\rho_{ii} = \frac{\exp(-\epsilon_i / k_\mathrm{B} T)}{q} \tag{2.50}$$

where ϵ_i is the energy of state i relative to the lowest energy state and q is the molecular partition function

$$q = \sum_i \exp(-\epsilon_i / k_\mathrm{B} T). \tag{2.51}$$

For a radical pair in the Earth's magnetic field, the energy splitting between states is so small compared to the thermal energy (see Introduction) that, to a good approximation, all states are equally populated and the density matrix is

$$\rho = \begin{pmatrix} \frac{1}{4} & 0 & 0 & 0 \\ 0 & \frac{1}{4} & 0 & 0 \\ 0 & 0 & \frac{1}{4} & 0 \\ 0 & 0 & 0 & \frac{1}{4} \end{pmatrix} \otimes \frac{\mathbb{I}_M}{M}, \tag{2.52}$$

where $\mathbb{I}$ is the identity matrix and M is the number of nuclear spin states.

The presence of diagonal density matrix elements different from the Boltzmann values indicates the presence of spin correlation, where spins have a greater than equilibrium probability of pointing in the same direction along the quantization axis. Correlation is a physical property of the system and exists independent of the basis set that is used to describe it.

Correlation along an axis that isn't the quantization axis is known as 'coherence'. It appears in the density matrix as non-zero off-diagonal elements that cause the system to oscillate between basis states. The existence of coherence *is* basis-set-dependent. Coherence in the singlet-triplet basis set ($\{|\mathrm{S}_0\rangle, |\mathrm{T}_0\rangle, |\mathrm{T}_+\rangle, |\mathrm{T}_-\rangle\}$) is essential for the radical pair mechanism, where the Earth's field is detected via its influence on the rate of coherent oscillations between the singlet and triplet states. Relaxation processes reduce the amount of coherence in a system by returning it to its equilibrium configuration where there are no correlations of any kind.

Entanglement describes the curious quantum behaviour of multiple-spin (in this case two-spin) systems that cannot be described as the product of their one-spin components. The wavefunction of a non-entangled pure state can be written

$$|\psi\rangle = \sum_{ij} c_{ij} |i_1\rangle \otimes |j_2\rangle , \tag{2.53}$$

where $|i_1\rangle$ and $|j_2\rangle$ are basis states for spin 1 and spin 2, respectively, and $c_{ij} = c_i c_j$. States that cannot be separated in this way are entangled.

Entanglement is harder to spot for mixed states, which are considered separable (not entangled) if their density matrix can be decomposed as

$$\rho = \sum_{ij} a_{ij} \rho_i^{(1)} \rho_j^{(2)}, \tag{2.54}$$

where $\rho_i^{(1)}$ and $\rho_j^{(2)}$ describe mixed states of spin 1 and spin 2 and $\sum_{ij} a_{ij} = 1$.

An entangled pair of spins has the remarkable property that the spin of one particle

depends on the spin of the other particle. Therefore, measurement of one spin instantly fixes the quantum state of the other spin. The singlet state, in which the radical pair is initially formed, is maximally entangled and it was originally thought that entanglement might play an important role in the radical pair compass. However, it has subsequently been shown that an anisotropic compass signal can still be produced by a radical pair formed in an initial non-entangled state [56, 118].

2.4 Singlet yield calculations

The most important property of the radical pair reaction is the singlet yield (or equivalently, the yield of triplet product), which directly quantifies the information that is available for the bird to use, even whilst it remains unclear how or if they might use it. All the investigations in this thesis will focus on how various factors influence the singlet yield and the way that it changes as a function of field direction.

The fractional yield of singlet product can be calculated using a simple rate equation to describe the reaction of the radical pair from its singlet state:

$$\frac{d\Phi_{\mathrm{S}}(t)}{dt} = k_{\mathrm{S}}[S(t)]; \tag{2.55}$$

$$\Phi_{\mathrm{S}} = \Phi_{\mathrm{S}}(\infty) = \int_0^\infty k_{\mathrm{S}}[S(t)]dt. \tag{2.56}$$

Equation (2.56) shows that the singlet yield is proportional to an integral over the amount $[S(t)]$ of singlet radical pair state present at any time during the reaction. This amount depends on the total number of radical pairs still remaining, modulated by the probability P_{S} that those radicals pairs exist in the singlet state. If it is assumed that singlet and triplet radical pairs are both removed, at the same rate ($k_{\mathrm{S}} = k_{\mathrm{T}} = k$), by first-order

reactions, then [119]

$$[S(t)] = P_{\mathrm{S}}(t)\exp(-kt), \tag{2.57}$$

$$\Phi_{\mathrm{S}} = k\int_0^\infty P_{\mathrm{S}}(t)\exp(-kt)dt. \tag{2.58}$$

The probability of a radical pair existing in the singlet state is calculated by taking the trace of the density matrix $\hat{\rho}(t)$ with the singlet projection operator,

$$\hat{P}^{\mathrm{S}} = |\mathrm{S}\rangle\langle\mathrm{S}| \tag{2.59}$$

$$= \frac{\hat{\mathbb{I}}}{4} - \hat{\mathbf{S}}_{\mathrm{A}}\cdot\hat{\mathbf{S}}_{\mathrm{B}}, \tag{2.60}$$

according to

$$P_{\mathrm{S}}(t) = \mathrm{Tr}[\hat{\rho}(t)\hat{P}^{\mathrm{S}}]. \tag{2.61}$$

2.4.1 The Liouville Von-Neumann equation

The first step in calculating the singlet yield produced by the radical pair reaction is to track the spin state of the radical pair over the course of the reaction. This is done using the Liouville-von Neumann equation, which describes the evolution of the density matrix through time. The Liouville-von Neumann equation can be derived directly by differentiating equation (2.41) with respect to time:

$$\frac{d\hat{\rho}}{dt} = \frac{d|\psi\rangle}{dt}\langle\psi| + |\psi\rangle\frac{d\langle\psi|}{dt}. \tag{2.62}$$

Substituting in the time-dependent Schrödinger equation,

$$\frac{d|\psi\rangle}{dt} = -i\hat{H}|\psi\rangle, \tag{2.63}$$

and its hermitian conjugate, gives

$$\frac{d\hat{\rho}}{dt} = -i\hat{H}\left|\psi\right\rangle\left\langle\psi\right| + i\left|\psi\right\rangle\left\langle\psi\right|\hat{H} \tag{2.64}$$

$$= -i(\hat{H}\hat{\rho} - \hat{\rho}\hat{H}) \tag{2.65}$$

$$= -i[\hat{H}, \hat{\rho}]. \tag{2.66}$$

To follow the step-by-step time evolution of the density matrix, it can be more convenient to use the integrated form of the Liouville-von-Neumann equation (equation (2.66)). If $\hat{H}$ is time-independent, this is

$$\hat{\rho}(t) = \exp(-i\hat{H}t)\hat{\rho}(0)\exp(i\hat{H}t). \tag{2.67}$$

Assuming that the radical pair is produced in a pure singlet state, the initial density matrix $\rho(0)$ is

$$\hat{\rho}(0) = \frac{\hat{P}^{\mathrm{S}}}{M}, \tag{2.68}$$

where M is the number of nuclear spin states.

2.4.2 Singlet yield in Hilbert space

In Hilbert space, the probability of the radical pair existing in the singlet state can be propagated through time using the integrated form of the Liouville-von Neumann equation (equation (2.67)). Substituting equations (2.67) and (2.68) into equation (2.61) gives

$$P_{\mathrm{S}}(t) = \frac{1}{M}\mathrm{Tr}[\exp(-i\hat{H}t)\hat{P}^{\mathrm{S}}\exp(i\hat{H}t)\hat{P}^{\mathrm{S}}], \tag{2.69}$$

which, in the eigenbasis of $\hat{H}$ is

$$P_{\mathrm{S}}(t) = \frac{1}{M}\mathrm{Tr}[A\exp(-iht)A^{-1}\hat{P}^{\mathrm{S}}A\exp(iht)A^{-1}\hat{P}^{\mathrm{S}}], \tag{2.70}$$

where A is the matrix of (orthonormal) eigenvectors of $\hat{H}$ and $h = A\hat{H}A^{-1}$ is a diagonal matrix whose entries are the eigenvalues ω_n.

Using the invariance of the trace under cyclic permutation[2], equation (2.70) can be rewritten as

$$P_{\mathrm{S}}(t) = \frac{1}{M}\mathrm{Tr}[\exp(-iht)A^{-1}\hat{P}^{\mathrm{S}}A\exp(iht)A^{-1}\hat{P}^{\mathrm{S}}A], \tag{2.71}$$

where $A^{-1}\hat{P}^{\mathrm{S}}A = \hat{P}^{\mathrm{S}'}$ is the singlet projection operator in the eigenbasis of $\hat{H}$.

A simplified expression for the singlet probability can be found by considering the individual matrix elements in the trace:

$$P_{\mathrm{S}}(t) = \frac{1}{M}\sum_{nm}\exp(-iht)_{nn}P^{\mathrm{S}'}_{nm}\exp(iht)_{mm}P^{\mathrm{S}'}_{mn} \tag{2.72}$$

$$= \frac{1}{M}\sum_{nm}\exp(i(\omega_m - \omega_n)t)|P^{\mathrm{S}'}_{mn}|^2. \tag{2.73}$$

Finally, substituting into equation (2.58) gives [119]

$$\Phi_{\mathrm{S}} = \frac{1}{M}\sum_{mn}|P^{\mathrm{S}'}_{mn}|^2\frac{k^2}{k^2+\omega^2_{mn}}, \tag{2.74}$$

where $\omega_{mn} = \omega_m - \omega_n$. Equation (2.74) states that the singlet yield is reduced by the presence of coherences between states with singlet character that are far apart in energy. Even in weak fields, the Zeeman interaction lifts degeneracies between states (i.e. increases $|\omega_{mn}|$), allowing the coherences in $P^{\mathrm{S}'}$ to oscillate and reducing their contribution to the singlet yield. This is the Low Field Effect [119].

2.4.3 Singlet yield in Liouville space

Using the Hilbert space Liouville-von Neumann equation, the rate of change of any element of the density matrix depends only on its current value and the value of any matrix

[2] $\mathrm{Tr}(ABC) = \sum_i(ABC)_{ii} = \sum_{ij}A_{ij}(BC)_{ji} = \sum_{ijk}A_{ij}B_{jk}C_{ki} = \sum_{ijk}B_{jk}C_{ki}A_{ij} = \sum_{jk}B_{jk}(CA)_{kj} = \sum_j(BCA)_{jj} = \mathrm{Tr}(BCA)$.

elements with which it is directly linked (i.e. that are in the same row or column). The change in the population of a state depends only the coherences in which that state is involved. It does not depend directly on the population of any other state, although population may indirectly transfer from one state to another via shared coherences. This is illustrated by considering a simple two-state system. The Liouville-von Neumann equation, in matrix form, is

$$\begin{pmatrix} \frac{d\rho_{11}}{dt} & \frac{d\rho_{12}}{dt} \\ \frac{d\rho_{21}}{dt} & \frac{d\rho_{22}}{dt} \end{pmatrix} = -i \begin{pmatrix} H_{11} & H_{12} \\ H_{21} & H_{22} \end{pmatrix} \begin{pmatrix} \rho_{11} & \rho_{12} \\ \rho_{21} & \rho_{22} \end{pmatrix} + i \begin{pmatrix} \rho_{11} & \rho_{12} \\ \rho_{21} & \rho_{22} \end{pmatrix} \begin{pmatrix} H_{11} & H_{12} \\ H_{21} & H_{22} \end{pmatrix}. \tag{2.75}$$

The rate of change of the population in state 1,

$$\frac{d\rho_{11}}{dt} = -iH_{12}\rho_{21} + iH_{21}\rho_{12}, \tag{2.76}$$

for example, does not depend directly on the population of state 2.

However, time-dependent perturbations such as molecular motion, chemical exchange and electron hopping, which may drive spin relaxation, create new pathways for population and coherence transfer between different elements of the density matrix. To describe these processes properly, every element of ρ must be able to contribute to the rate of change of every other element. That is, we should be able to write

$$\frac{d\rho_{11}}{dt} = a\rho_{11} + b\rho_{21} + c\rho_{12} + d\rho_{22}. \tag{2.77}$$

This is achieved by working in Liouville space, sometimes known as 'operator space'. In Hilbert space, states are represented by vectors and are acted on by matrix operators. In Liouville space, it is operators that are represented by vectors and matrices are used to represent 'superoperators': operators that act on operators.

The Liouville space Liouville-von Neumann equation is

$$\frac{d\hat{\rho}}{dt} = -\hat{\hat{L}}\hat{\rho}. \tag{2.78}$$

In equation (2.78), the Hilbert space density matrix operator has been row-wise flattened into the column vector

$$\hat{\rho} = \begin{pmatrix} \rho_{11} \\ \rho_{12} \\ \rho_{21} \\ \rho_{22} \end{pmatrix}. \tag{2.79}$$

It evolves under the action of the superoperator $\hat{\hat{L}}$ (indicated by a double hat), which has the form

$$\hat{\hat{L}} = \begin{pmatrix} L_{1111} & L_{1112} & L_{1121} & L_{1122} \\ L_{1211} & L_{1212} & L_{1221} & L_{1222} \\ L_{2111} & L_{2112} & L_{2121} & L_{2122} \\ L_{2211} & L_{2212} & L_{2221} & L_{2222} \end{pmatrix}, \tag{2.80}$$

where L_{ijkl} can be though of as the rate of transfer from element ρ_{kl} to ρ_{ij}.

The superoperator $\hat{\hat{L}}$ contains several parts, each incorporating different processes. Unitary evolution under the Hamiltonian is captured by simply converting the Hilbert space commutator $i[\hat{H}, \hat{\rho}]$ (equation (2.66)) into the Liouville space *commutation superoperator*

$$i\hat{\hat{H}} = i(\hat{H} \otimes \hat{I} - \hat{I} \otimes \hat{H}^{\mathrm{t}}), \tag{2.81}$$

where $\hat{I}$ is the identity operator and $\hat{H}^{\mathrm{t}}$ is the transpose of $\hat{H}$.

The reaction and recombination of the radical pair can also be included in $\hat{\hat{L}}$ using a reaction superoperator

$$\hat{\hat{K}} = -\frac{1}{2}k_{\mathrm{S}}(\hat{P}^{\mathrm{S}} \otimes \hat{I} + \hat{I} \otimes (\hat{P}^{\mathrm{S}})^{\mathrm{t}}) - \frac{1}{2}k_{\mathrm{T}}(\hat{P}^{\mathrm{T}} \otimes \hat{I} + \hat{I} \otimes (\hat{P}^{\mathrm{T}})^{\mathrm{t}}), \tag{2.82}$$

where the triplet projection operator $\hat{P}^{\mathrm{T}} = \hat{\mathbb{I}} - \hat{P}^{\mathrm{S}}$. Equation (2.82) follows the Haberkorn model [120], which has been experimentally demonstrated to provide an accurate description of spin-selective kinetics [121].

Finally, relaxation processes can be included in equation (2.78) by adding a relaxation term into $\hat{\hat{L}}$. The elements of a relaxation superoperator describe the rates of transfer between elements of the density matrix due to the process (e.g. molecular motion) inducing the relaxation. The structure of the relaxation matrix will be discussed in more detail in chapter 3.

Equation (2.78) is a first-order differential equation that can be solved to give

$$\hat{\rho}(t) = \exp(-\hat{\hat{L}}t)\hat{\rho}(0). \tag{2.83}$$

Hence,

$$[S(t)] = \langle \hat{P}^{\mathrm{S}}| \exp(-\hat{\hat{L}}t)|\hat{\rho}(0)\rangle \,. \tag{2.84}$$

Substituting into equation (2.56) gives

$$\Phi_{\mathrm{S}} = k_{\mathrm{S}} \int_0^\infty \langle \hat{P}^{\mathrm{S}}| \exp(-\hat{\hat{L}}t)|\hat{\rho}(0)\rangle \, dt \tag{2.85}$$

$$= k_{\mathrm{S}} \langle \hat{P}^{\mathrm{S}}| \int_0^\infty \exp(-\hat{\hat{L}}t)|\hat{\rho}(0)\rangle \, dt \tag{2.86}$$

$$= k_{\mathrm{S}} \langle \hat{P}^{\mathrm{S}}|\hat{\hat{L}}^{-1}|\hat{\rho}(0)\rangle \tag{2.87}$$

for the singlet yield.

Chapter 3

Modelling techniques

This chapter introduces some of the standard tools that are used in this thesis. The specific ways in which they are employed and adapted will be described in later chapters alongside the results of the corresponding calculations.

3.1 Modelling rotations

For almost all the work in this thesis, it is important to be able to mathematically model rotations. By rotating radical pairs, cells, birds' heads, external magnetic moments etc. we can introduce (geometric and energetic) disorder - both static and, in the case of modelling relaxation processes, dynamic.

3.1.1 Euler angles

Rotations are most intuitively visualised by turning through an angle α around a given axis. However, it can be inconvenient to keep defining arbitrary rotation axes - particularly when describing the rotational motion of a molecule that could, in theory, pivot around any axis. In much of this thesis, rotations will instead be described using an Euler angle decomposition, which makes use of the fact that any rotation can be described by no more

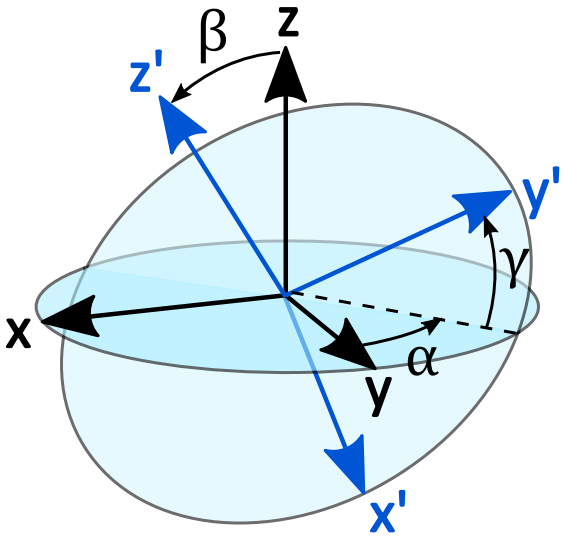


Figure 3.1: Any rotation can be decomposed into a set of 3 successive rotations: a rotation through an angle γ around the z axis, a rotation through β around the original y axis and a rotation through α around the original z axis. In this figure, the original axis system is shown in black and the rotated axis system in blue.

than three parameters - in this case, by three successive rotations around a fixed set of axes. The angles parameterising these three rotations are called Euler angles [122].

There are several different conventions for defining Euler angles, depending on the choice of the fixed rotation axes and whether one considers active rotations of the object or passive rotations of the coordinate frame. I will use a convention of active, extrinsic rotations where the object undergoes three successive rotations around the original coordinate frame axes [123, 124]. Under this convention, any rotation can be decomposed into

1. a rotation by $0 \leq \gamma \leq 2\pi$ around the z axis,
2. a rotation by $0 \leq \beta \leq \pi$ around the original y axis, and
3. a rotation by $0 \leq \alpha \leq 2\pi$ around the original z axis,

such that $R(\alpha, \beta, \gamma) = R_z(\alpha)R_y(\beta)R_z(\gamma)$. This sequence of rotations is illustrated in figure 3.1.

(It is worth noting that the same rotation can be achieved in an intrinsic fashion by rotating through α around the z axis, then through β around the new y axis and finally

through γ around the new z axis [122].)

Using Euler angles to characterize a rotation can be problematic as they are not a valid parameterisation of the $SO(3)$ rotation group [123]. Consequently, singularities arise at $\beta = 0$ and $\beta = \pi$, which can be difficult to handle. In particular, it is not always easy, or possible, to extract a set of Euler angles from a rotation matrix or from an alternative (e.g. angle-axis) description of the rotation. Appendix B describes the procedure used to deal with exactly this problem when attempting to extract sets of Euler angles from hyperfine interaction tensors.

3.1.2 Rotation matrices

Mathematically, rotations are implemented using a transformation or rotation matrix, which describes a mapping of the object or vector from its original to its rotated position. Rotation matrices have the important properties that they are always orthogonal (meaning that $\mathbf{R}^t = \mathbf{R}^{-1}$) and have a determinant of 1.

Rotation matrices can be defined in a number of different ways, depending on how the rotation is described. I will use two separate definitions throughout the course of this thesis.

For sets of rotations that occur around the same well-defined axis, the most intuitive approach is to describe each one by its angle of rotation. For an anticlockwise rotation through α degrees around an axis specified by the unit vector (u_x, u_y, u_z), the rotation matrix is given by Rodrigues' formula: [125]

$$\mathbf{R}(\alpha) = \mathbb{I} + \tilde{u}\sin(\alpha) + \tilde{u}^2(1 - \cos(\alpha)), \tag{3.1}$$

where $\mathbb{I}$ is the identity matrix and

$$\tilde{\mathbf{u}} = \begin{pmatrix} 0 & -u_z & u_y \\ u_z & 0 & -u_x \\ -u_y & u_x & 0 \end{pmatrix} \qquad \tilde{\mathbf{u}}^2 = \begin{pmatrix} -u_z^2 - u_y^2 & u_x u_y & u_x u_z \\ u_x u_y & -u_z^2 - u_x^2 & u_y u_z \\ u_x u_z & u_y u_z & -u_y^2 - u_x^2 \end{pmatrix}. \quad (3.2)$$

Substituting equation (3.2) into equation (3.1) gives the following explicit equation for the rotation matrix:

$$\mathbf{R} = \begin{pmatrix} \cos(\alpha) + u_x^2(1-\cos(\alpha)) & u_x u_y(1-\cos(\alpha)) - u_z \sin(\alpha) & u_x u_z(1-cos(\alpha)) + u_y \sin(\alpha) \\ u_x u_y(1-\cos(\alpha)) + u_z \sin(\alpha) & \cos(\alpha) + u_y^2(1-\cos(\alpha)) & u_y u_z(1-\cos(\alpha)) - u_x \sin(\alpha) \\ u_x u_z(1-\cos(\alpha)) - u_y \sin(\alpha) & u_y u_z(1-\cos(\alpha)) - u_x \sin(\alpha) & \cos(\alpha) + u_z^2(1-\cos(\alpha)) \end{pmatrix}. \quad (3.3)$$

In cases where the rotation is more easily described using an Euler angle decomposition, the rotation matrix can be built up by multiplying the angle-axis rotation matrices for each sucessive rotation step described in section 3.1.1:

$$\mathbf{R}(\alpha,\beta,\gamma) = \mathbf{R}_z(\alpha)\mathbf{R}_y(\beta)\mathbf{R}_z(\gamma); \quad (3.4)$$

$$= \begin{pmatrix} \cos\alpha & -\sin\alpha & 0 \\ \sin\alpha & \cos\alpha & 0 \\ 0 & 0 & 1 \end{pmatrix} \begin{pmatrix} \cos\beta & 0 & \sin\beta \\ 0 & 1 & 0 \\ -\sin\beta & 0 & \cos\beta \end{pmatrix} \begin{pmatrix} \cos\gamma & -\sin\gamma & 0 \\ \sin\gamma & \cos\gamma & 0 \\ 0 & 0 & 1 \end{pmatrix}; \quad (3.5)$$

$$= \begin{pmatrix} \cos\alpha\cos\beta\cos\gamma - \sin\alpha\sin\gamma & -\cos\alpha\cos\beta\sin\gamma - \sin\alpha\cos\gamma & \cos\alpha\sin\beta \\ \sin\alpha\cos\beta\cos\gamma + \cos\alpha\sin\gamma & -\sin\alpha\cos\beta\sin\gamma + \cos\alpha\cos\gamma & \sin\alpha\sin\beta \\ -\sin\beta\cos\gamma & \sin\beta\sin\gamma & \cos\beta \end{pmatrix}. \quad (3.6)$$

3.1.3 Spherical tensor operators

Many of the contributions to the spin Hamiltonian involve the interaction between two spins (e.g. the hyperfine interaction between an electron spin and a nuclear spin). As-

suming, for simplicity, an isotropic interaction, these terms have the form of a dyadic cartesian tensor

$$\mathbf{T} = a\mathbf{LS} = a \begin{pmatrix} L_x S_x & L_x S_y & L_x S_z \\ L_y S_x & L_y S_y & L_y S_z \\ L_z S_x & L_z S_y & L_z S_z \end{pmatrix}; \tag{3.7}$$

$$T_{ij} = L_i S_j. \tag{3.8}$$

Rank 2 tensors, such as the one in equation (3.8), transform under rotation according to [126]

$$T'_{ij} = \sum_{i'j'} R_{ii'} R_{jj'} T_{i'j'} = \sum_{i'j'} R_{ii'} L_{i'} R_{jj'} S_{j'}. \tag{3.9}$$

Given the potential complexity of the rotation matrices (equation (3.6)), this is clearly a possible but laborious task. A less demanding approach is to decompose the tensor into irreducible representations that have a predictable and well-defined behaviour under rotation.

Dyadic Cartesian tensors may be reduced according to [126]

$$T_{ij} = T_{ij}^{(0)} + T_{ij}^{(1)} + T_{ij}^{(2)} \tag{3.10}$$

$$= \frac{\mathbf{L}\cdot\mathbf{S}}{3}\delta_{ij} + \frac{L_i S_j - L_j S_i}{2} + \left(\frac{L_i S_j + L_j S_i}{2} - \frac{\mathbf{L}\cdot\mathbf{S}}{3}\delta_{ij} \right). \tag{3.11}$$

$T_{ij}^{(0)}$ has one independent component and, like a scalar, is invariant under rotation. $T_{ij}^{(1)}$ is an antisymmetrized vector product and transforms like a vector under rotations. It has three independent components. Finally, $T_{ij}^{(2)}$ is a symmetrized, traceless vector product and transforms under rotations according to equation (3.9). It has five independent components, such that

$$T^{(2)} = \sum_i T_i^{(2)}. \tag{3.12}$$

The purpose of rewriting the tensor $\mathbf{T}$ as a sum of irreducible tensors is that the tensors

$\{T_m^{(j)}\}$ form a basis that block-diagonalises the rotation matrix. Under rotation, each $T_m^{(j)}$ will only transform into one of the other $2j+1$ basis functions of the same rank.

The generators of the rotation group can be identified as the three angular momentum operators $\hat{J}_x$, $\hat{J}_y$ and $\hat{J}_z$ [123]. Thus, the Euler angle rotation matrix in equation (3.6) can be generated using the relation [122]

$$R(\alpha, \beta, \gamma) = \exp(-i\alpha J_z) \exp(-i\beta J_y) \exp(-i\gamma J_z). \tag{3.13}$$

All three operators commute with the $\hat{J}^2$ total angular momentum operator and consequently the eigenfunctions of $\hat{J}^2$ form an irreducible representation of the SO(3) rotation group and have a well-defined behaviour under rotation operators [123].

The eigenfunctions of $\hat{J}^2$ are spherical harmonics, some of which are listed in table 3.1 and they have all the properties required to form the $\{T_m^{(j)}\}$ basis. Irreducible spherical tensor operators of rank j are defined as being a set of $2j+1$ operators that transform under rotation in the same way as spherical harmonics (and therefore angular momentum eigenstates) [126, 127]. They can be found from the spherical harmonics by replacing the cartesian vectors $\{\boldsymbol{x}, \boldsymbol{y}, \boldsymbol{z}\}$ with the angular momentum operators $\{L_x, L_y, L_z\}$, as shown in table 3.1.

The irreducible spherical tensor operators can be used to rewrite any two-spin interaction according to [123]

$$\hat{\mathbf{L}} \cdot \mathbf{A} \cdot \hat{\mathbf{S}} = a_0^{(0)} \hat{T}_0^{(0)} + \sum_{m=-1}^{1} a_m^{(1)} \hat{T}_m^{(1)} + \sum_{m=-2}^{2} a_m^{(2)} \hat{T}_m^{(2)}, \tag{3.14}$$

Table 3.1: Rank-0 and rank-2 spherical harmonics and irreducible spherical tensor operators [101, 123].

l	m	$Y_{lm}(x,y,z)$	$\hat{T}_m^{(l)}$ one spin	$\hat{T}_m^{(l)}$ two spins
0	0	$\sqrt{\frac{1}{4}\pi}$	$\hat{E}$	$\hat{E}$
2	2	$\sqrt{\frac{15}{32\pi}}\frac{(x+iy)^2}{r^2}$	$\frac{1}{2}\hat{L}_+^2$	$\frac{1}{2}\hat{L}_+\hat{S}_+$
2	1	$-\sqrt{\frac{5}{8\pi}}\frac{(x+iy)z}{r^2}$	$-\frac{1}{2}(\hat{L}_z\hat{L}_+ + \hat{L}_+\hat{L}_z)$	$-\frac{1}{2}(\hat{L}_z\hat{S}_+ + \hat{L}_+\hat{S}_z)$
2	0	$\sqrt{\frac{5}{16\pi}}\frac{2z^2-x^2-y^2}{r^2}$	$\sqrt{\frac{2}{3}}(\hat{L}_z^2 - \frac{1}{4}(\hat{L}_+\hat{L}_- + \hat{L}_-\hat{L}_+))$	$\sqrt{\frac{2}{3}}(\hat{L}_z\hat{S}_z - \frac{1}{4}(\hat{L}_+\hat{S}_- + \hat{L}_-\hat{S}_+))$
2	-1	$\sqrt{\frac{15}{8\pi}}\frac{(x-iy)z}{r^2}$	$\frac{1}{2}(\hat{L}_z\hat{L}_- + \hat{L}_-\hat{L}_z)$	$\frac{1}{2}(\hat{L}_z\hat{S}_- + \hat{L}_-\hat{S}_z)$
2	-2	$\sqrt{\frac{15}{32\pi}}\frac{(x-iy)^2}{r^2}$	$\frac{1}{2}\hat{L}_-^2$	$\frac{1}{2}\hat{L}_-\hat{S}_-$

where

$$a_0^{(0)} = a = \frac{-(A_{XX} + A_{YY} + A_{ZZ})}{\sqrt{3}} \qquad \text{Isotropic component} \tag{3.15}$$

$$a_0^{(2)} = \mathrm{Ax} = \frac{2A_{ZZ} - (A_{XX} + A_{YY})}{\sqrt{6}} \qquad \text{Axiality} \tag{3.16}$$

$$a_{\pm 2}^{(2)} = \mathrm{Rh} = \frac{A_{XX} - A_{YY}}{2} \qquad \text{Rhombicity} \tag{3.17}$$

The first rank terms in equation (3.14) are very small and have never been observed so they are usually neglected altogether.

3.1.4 Wigner matrices

Irreducible spherical tensor operators form a good operator basis for the Hamiltonian as they transform under rotations in the same way as spherical harmonics, which block-diagonalise any rotation matrix. The constituent blocks of a rotation matrix (defined as in equation (3.6)), in a spherical harmonic basis, are termed Wigner rotation matrices

[122, 123]. The matrix elements of $R(\alpha, \beta, \gamma)$,

$$\mathfrak{D}^{(l)}_{m,m'}(\alpha, \beta, \gamma) = \langle Y_{l,m}|R(\alpha, \beta, \gamma)|Y_{lm'}\rangle\,, \tag{3.18}$$

are called Wigner functions.

Using Wigner functions, the effect of any rotation on the irreducible spherical tensor operators can be written as [123, 127]

$$R(\alpha, \beta, \gamma)\hat{T}^{(l)}_m = \sum_{m'=-l}^{l} \hat{T}^{(l)}_{m'}\mathfrak{D}^{(l)}_{m',m}(\alpha, \beta, \gamma). \tag{3.19}$$

This provides an efficient means of calculating the effect of rotations on the spin Hamiltonian, which is made up of interactions that can be expressed in terms of irreducible spherical tensors operators, as described in section 3.1.3.

Furthermore, their relationship to spherical harmonics means that Wigner functions have a very well-defined behaviour under the angular momentum operators [127, 128]:

$$\hat{L}^2\mathfrak{D}^{(l)}_{m,n}(\alpha, \beta, \gamma) = l(l+1)\mathfrak{D}^{(l)}_{m,n}(\alpha, \beta, \gamma); \tag{3.20}$$

$$\hat{L}_z\mathfrak{D}^{(l)}_{m,n}(\alpha, \beta, \gamma) = n\mathfrak{D}^{(l)}_{m,n}(\alpha, \beta, \gamma); \tag{3.21}$$

$$\hat{L}_\pm\mathfrak{D}^{(l)}_{m,n}(\alpha, \beta, \gamma) = \sqrt{l(l+1) - n(n\pm 1)}\mathfrak{D}^{(l)}_{m,n\pm 1}(\alpha, \beta, \gamma). \tag{3.22}$$

In reference [128] (extensively followed in chapter 5), these relationships are used to derive an analytical solution to a rotational diffusion equation describing internal rotational motion of the radicals.

The full Wigner functions $\mathfrak{D}^{(l)}_{m,m'}(\alpha, \beta, \gamma)$ can be expressed in terms of a limited number of reduced functions, the Wigner "small-*d*" functions $d^{(l)}_{m,m'}(\beta)$, that depend only on the angle β:

$$\mathfrak{D}^{(l)}_{m,m'}(\alpha, \beta, \gamma) = e^{-im\alpha}d^{(l)}_{m,m'}(\beta)e^{-im'\gamma}. \tag{3.23}$$

The Wigner *d*-functions are tabulated in a number of standard angular momentum text-

Table 3.2: Formulae for the rank-0, rank-1 and rank-2 $d^{(l)}_{m,m'}(\beta)$ functions [122].

$d^{(0)}_{0,0}$	1
$d^{(1)}_{1,1} = d^{(1)}_{-1,-1}$	$\cos^2(\frac{\beta}{2})$
$d^{(1)}_{1,-1} = d^{(1)}_{-1,1}$	$\sin^2(\frac{\beta}{2})$
$d^{(1)}_{0,1} = d^{(1)}_{-1,0} = -d^{(1)}_{0,-1} = -d^{(1)}_{1,0}$	$\frac{\sin(\beta)}{\sqrt{2}}$
$d^{(1)}_{0,0}$	$\cos(\beta)$
$d^{(2)}_{2,2} = d^{(2)}_{-2,-2}$	$\cos^4(\frac{\beta}{2})$
$d^{(2)}_{2,1} = -d^{(2)}_{1,2} = -d^{(2)}_{-2,-1} = -d^{(2)}_{-1,-2}$	$-\frac{1}{2}\sin(\beta)(1+\cos(\beta))$
$d^{(2)}_{2,0} = d^{(2)}_{0,2} = d^{(2)}_{-2,0} = -d^{(2)}_{0,-2}$	$\sqrt{\frac{3}{8}}\sin^2(\beta)$
$d^{(2)}_{2,-1} = -d^{(2)}_{-1,2} = -d^{(2)}_{-2,1} = -d^{(2)}_{1,-2}$	$\frac{1}{2}\sin(\beta)(-1+\cos(\beta))$
$d^{(2)}_{2,-2} = d^{(2)}_{-2,2}$	$\sin^4(\frac{\beta}{2})$
$d^{(2)}_{1,1} = d^{(2)}_{-1,-1}$	$\frac{1}{2}(2\cos(\beta)-1)(1+\cos(\beta))$
$d^{(2)}_{1,0} = d^{(2)}_{0,1} = -d^{(2)}_{-1,0} = -d^{(2)}_{0,-1}$	$\sqrt{32}\sin(\beta)\cos(\beta)$
$d^{(2)}_{1,-1} = d^{(2)}_{-1,1}$	$\frac{1}{2}(2\cos(\beta)+1)(1-\cos(\beta))$
$d^{(2)}_{0,0}$	$\frac{1}{2}(3\cos^2(\beta)-1)$

books e.g. refs. [122, 127, 129]. The rank-0, rank-1 and rank-2 $d^{(l)}_{m,m'}(\beta)$ are listed in table 3.2. However, in most cases, I have calculated the Wigner functions using the *wigner.m* package from the Spinach library [130].

3.1.5 Clebsch-Gordan coefficients

Two angular momenta, $\mathbf{J}_1$ and $\mathbf{J}_2$, described by the quantum numbers j_1 and j_2 with projections m_1 and m_2, combine or couple together according to the rules of vector addi-

tion. Consequently, the resulting total angular momentum **J** may have a range of different magnitudes and projections (parameterised by the quantum numbers j and m, respectively). The probability of the resultant angular momentum having specific values of j and m is characterised by a Clebsch-Gordan coefficient $C^{jm}_{j_1 m_1 j_2 m_2}$ [127], such that coupled and uncoupled representations of the system are related by [129]

$$|j, j_1, j_2, m\rangle = \sum_{m_1, m_2} C^{jm}_{j_1 m_1 j_2 m_2} |j_1, j_2, m_1, m_2\rangle . \tag{3.24}$$

The value of j must lie in the range $|j_1 - j_2|, |j_1 - j_2| + 1, \cdots j_1 + j_2$, whilst m, which satisfies $|m| \leq j$, is equal to $m_1 + m_2$. If these conditions are not met, $C^{jm}_{j_1 m_1 j_2 m_2}$ will be zero. Consequently, the value of m is often not explicitly specified and in some references the coefficient $C^{jm}_{j_1 m_1 j_2 m_2}$ is written $C(j_1, j_2, j; m_1, m_2)$ [129].

Clebsch-Gordan coefficients are ubiquitous in angular momentum theory and have many useful properties. Crucially for this thesis, they are related to integrals over products of Wigner functions. In a realistic description of internal rotational motion of the radicals, it is necessary to integrate over continuous distributions of possible orientations of the moving radical. Doing this within the Wigner matrix formalism is made possible using the relation

$$C^{c\gamma}_{a\alpha b\beta} C^{c\gamma'}_{a\alpha' b\beta'} = \frac{2c+1}{8\pi^2} \int \mathfrak{D}^a_{\alpha\alpha'}(\Omega) \mathfrak{D}^b_{\beta\beta'}(\Omega) \mathfrak{D}^{c*}_{\gamma\gamma'}(\Omega) d\Omega. \tag{3.25}$$

Using equation (3.25), complex integrals can be replaced by previously calculated standard coefficients (calculated using the *clebsch_gordan.m* routine in the Spinach library [130]). The number of coefficients that need to be calculated can be reduced by exploiting two of the (many) symmetry properties of the Clebsch-Gordan coefficients [127]:

$$C^{c\gamma}_{a\alpha b\beta} = (-1)^{a+b-c} C^{c-\gamma}_{a-\alpha b-\beta} \tag{3.26}$$

$$= (-1)^{a+b-c} C^{c\gamma}_{b\beta a\alpha}. \tag{3.27}$$

3.2 Modelling relaxation

3.2.1 The two-site model

Relaxation is driven by incoherent evolution under a time-dependent perturbing Hamiltonian. In this thesis, the Hamiltonian is perturbed either by motion of one of the radicals or, in chapter 7, by the fluctuating magnetic field produced by a nearby nanoparticle. To model the relaxation induced by these processes, we need a way of describing the time-dependence of the Hamiltonian.

The evolution of a system (or, more accurately, the evolution of its density matrix) may be described by the Liouville von-Neumann equation (section 2.4.1). From the integrated form of equation (2.78),

$$\rho(t) = \exp(-\hat{\hat{L}}t)\rho(0), \tag{3.28}$$

where $\hat{\hat{L}}$ is time-independent, we can define an evolution operator

$$\hat{U}(t) = \exp(-\hat{\hat{L}}t). \tag{3.29}$$

When molecular motion (or a nanoparticle) is introduced, the Hamiltonian and hence $\hat{\hat{L}}$ becomes time-dependent. Conceptually the simplest way to think about the time-dependence is to imagine that, at random time-intervals, $\hat{\hat{L}}$ jumps between discrete, defined values: initially $\hat{\hat{L}} = \hat{\hat{L}}_0$, then at time t_1 it suddenly switches to $\hat{\hat{L}}_1$ etc., as illustrated in figure 3.2. For subsequent periods of evolution, the evolution operators multiply together such that

$$\hat{U}(t) = \hat{U}(t-h)\hat{U}(h). \tag{3.30}$$

For a random process, we cannot know the sequence of jumps that $\hat{\hat{L}}$ will make, but we can consider the probability of different evolution pathways using a 'tree' diagram, as in figure 3.2. The evolution operator corresponding to a specific sequence of jumps (one

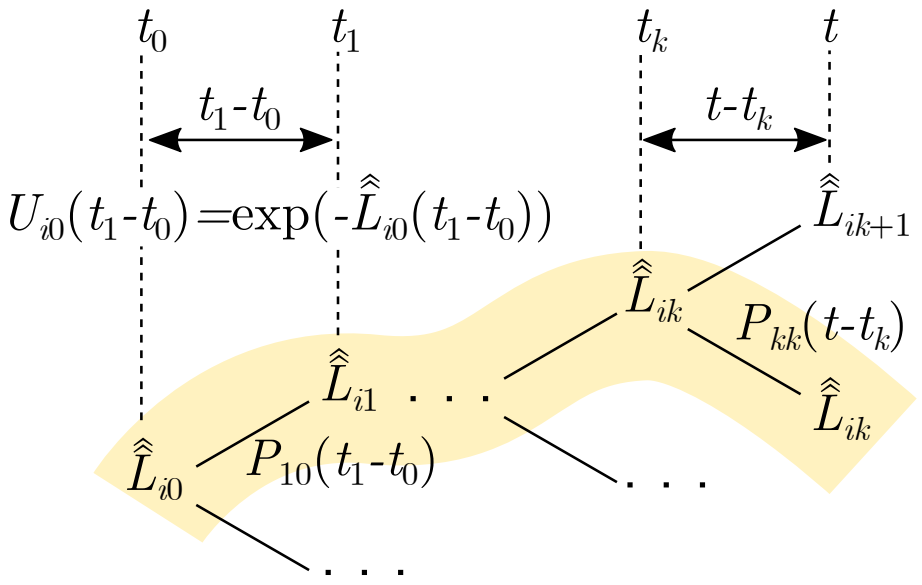


Figure 3.2: Probability tree for a Markov process, where the system jumps between different sites or values at random times. The branch of the tree described by equation 3.31 is highlighted in yellow. $P_{10}(t_1 - t_0)$ is the probability that the system remains in site i_0 for a length of time $t_1 - t_0$ before jumping to site i_1. During that time, the system is described by the Liouville superoperator $\hat{\hat{L}}_{i0}$ and evolves under the evolution operator $\hat{U}_{i0}$.

branch of the 'tree'), weighted by the probability of that sequence occurring is [131]

$$\begin{aligned} P \times \hat{U} =& P_{i_k,i_k}(t-t_k)\hat{U}_{i_k}(t-t_k) \times P_{i_k,i_{k-1}}(t_k-t_{k-1})\hat{U}_{i_{k-1}}(t_k-t_{k-1}) \times \cdots \\ & \cdots \times P_{i_1,i_0}(t_1-t_0)\hat{U}_{i_0}(t_1-t_0), \end{aligned} \tag{3.31}$$

where $\hat{U}_{i_k}(t) = \exp(-\hat{\hat{L}}_k t)$ is the evolution operator corresponding to the k^{th} value of $\hat{\hat{L}}$ and $P_{j,i}(t)$ is the probability that the system jumps from $\hat{\hat{L}}_i$ to $\hat{\hat{L}}_j$ between time t and $t + dt$. The probability of observing a transition depends on the length of the observation period.

The full evolution operator for a time period t is simply the weighted average over all the 'branches' of the probability tree:

$$\hat{U}(t) = \sum P \times \hat{U}. \tag{3.32}$$

The stochastic jump process describing the changes to $\hat{\hat{L}}$ can be thought of as a Markov process [132], in which the probability of any given jump occurring depends only on the current value of $\hat{\hat{L}}$ and is independent of the path taken to reach that value (i.e. independent of what jumps have occurred previously). The transition probability, $P_{j,i}(t)$, defined above, has two important properties. First, according to the Chapman-Kolmogorov equation [131, 132],

$$P_{j,i}(t) = \sum P_{j,m}(h) P_{m,i}(t-h), \tag{3.33}$$

the probability of jumping from state i to j in time t is the product of the probabilities of doing two jumps via an intermediate state m in the same time (as in the tree diagram in figure 3.2).

Second, it is assumed that the transition probability can be written (within negligible error) in terms of a constant transition rate γ as [131]

$$P_{j,i}(t) = \gamma_{j,i} t + O(t) \tag{3.34}$$

where $O(t)$ is a quantity that is small compared to (and, importantly, tends to zero faster than) t.

By definition, the transition rate from one state to itself is zero, as no transition is occurring. Therefore,

$$\gamma_{jj}(t) = 0. \tag{3.35}$$

However, conservation of probability means that [131]

$$P_{jj}(t) = 1 - \gamma_j t + O(t), \tag{3.36}$$

where $\gamma_j = \sum_k \gamma_{k,j}$ is the sum over the probabilities of all possible transitions.

Using the arguments above, the evolution operator for a system evolving under $\hat{\hat{L}}_j$ during

the time interval $t-h$ to t can be written

$$\hat{U}_j(t) = \underbrace{\exp(-\hat{\hat{L}}_j h)}_{=\hat{U}_j(h)} \sum_i P_{j,i}\hat{U}_i(t-h), \tag{3.37}$$

where $\hat{U}_i(t-h)$ is defined by equation (3.32) (with only branches ending in state i included on the probability tree). When the time period h is small, the exponential term can be approximated by the first two terms of its Taylor expansion. The summation can also be split into terms with $i = j$ and $i \neq j$, allowing equation to be rewritten as

$$\hat{U}_j(t) = (1 - \hat{\hat{L}}_j h)\left[\sum_{j\neq i} P_{j,i}(h)\hat{U}_i(t-h) + P_{jj}(h)\hat{U}_j(t-h)\right]. \tag{3.38}$$

Substituting in equations (3.34) and (3.36) gives

$$\hat{U}_j(t) - \hat{U}_j(t-h) = (-\hat{\hat{L}}_j - \gamma_j)h\hat{U}_j(t-h) + \sum_i \gamma_{j,i} h\hat{U}_i(t-h) + O(h) \tag{3.39}$$

(where terms in h^2 have been subsumed into $O(h)$). Dividing by h and taking the limit $h \to 0$ produces a differential equation for $\hat{U}_j(t)$ [131]:

$$\frac{d\hat{U}_j(t)}{dt} = \left(-\hat{\hat{L}}_j - \gamma_j\right)\hat{U}_j(t) + \sum_i \gamma_{j,i}\hat{U}_i(t). \tag{3.40}$$

Equation (3.40) can be written in matrix form as

$$\frac{d\hat{U}(t)}{dt} = (\mathbf{\Lambda} + \mathbf{\Xi})\,\hat{U}(t), \tag{3.41}$$

where $\mathbf{\Lambda}$ and $\mathbf{\Xi}$ are both $(NM) \times (NM)$ matrices with N equal to the number of sites in the jump process and M the dimension of the Liouville space for a single site. $\mathbf{\Lambda}$ is a

block diagonal matrix;

$$\mathbf{\Lambda} = \begin{pmatrix} \hat{\hat{L}}_{i_1} & 0 & 0 & \\ 0 & \hat{\hat{L}}_{i_2} & 0 & \cdots \\ 0 & 0 & \hat{\hat{L}}_{i_3} & \\ & \cdots & & \end{pmatrix}, \tag{3.42}$$

whilst

$$\mathbf{\Xi} = \mathbf{\Gamma} \otimes \mathbb{I}_M, \tag{3.43}$$

where $\Gamma_{ij} = \gamma_{ij}$ and $\Gamma_{jj} = -\gamma_j$.

The density matrix vector

$$\rho = \begin{pmatrix} \rho_1 \\ \rho_2 \\ \rho_3 \\ \cdots \end{pmatrix}, \tag{3.44}$$

evolves in the same way as the evolution operator $\hat{U}$ and thus it is possible to write

$$\frac{d\rho(t)}{dt} = (\mathbf{\Lambda} + \mathbf{\Xi})\,\rho(t). \tag{3.45}$$

Equation (3.45) is the stochastic Liouville equation [131].

From the structure of equation (3.42), it is clear that the size of the matrices $\mathbf{\Lambda}$ and $\mathbf{\Xi}$ grows rapidly with the number of sites that are sampled. In this thesis, I use a model where the radical pair samples just two different environments, in a manner analogous to the two-site chemical exchange models commonly used in NMR studies. In chapter 4, the two environments correspond to two possible orientations of the primary radical, providing an approximate picture of the effect of internal rotational motion of the radical pair. In chapter 7, the radical pair remains static but is exposed to two different external magnetic fields emanating from a nearby nanoparticle, in an accurate model of the particle's Neel relaxation behaviour.

For a two-site model, Γ takes the simple form [133]

$$\Gamma = \begin{pmatrix} -m\mathbb{I} & m\mathbb{I} \\ m\mathbb{I} & -m\mathbb{I} \end{pmatrix}, \tag{3.46}$$

where it is assumed that transitions between the sites occur with equal probability in either direction.

Equation (3.45) thus becomes

$$\begin{aligned} \begin{bmatrix} \dot{\rho}_1 \\ \dot{\rho}_2 \end{bmatrix} &= \begin{bmatrix} \hat{\hat{L}}_1 - m\mathbb{I} & m\mathbb{I} \\ m\mathbb{I} & \hat{\hat{L}}_2 - m\mathbb{I} \end{bmatrix} \begin{bmatrix} \rho_1 \\ \rho_2 \end{bmatrix} \\ &= -\hat{\hat{L}} \begin{bmatrix} \rho_1 \\ \rho_2 \end{bmatrix} \end{aligned} \tag{3.47}$$

where the Liouville superoperator for each site,

$$\hat{\hat{L}}_i \rho(t) = -i[\hat{H}_i, \rho(t)] - \frac{k_{\mathrm{S}}}{2}\left\{\hat{P}^{\mathrm{S}}, \rho(t)\right\} - \frac{k_{\mathrm{T}}}{2}\left\{\hat{P}^{\mathrm{T}}, \rho(t)\right\}, \tag{3.48}$$

contains the unitary evolution under the hyperfine interactions in that site and the reactions of the singlet and triplet states. The brackets $[\cdots]$ denote the commutator and $\{\cdots\}$ the anticommutator operation. The rates of the singlet and triplet reactions are given by k_{S} and k_{T}, respectively.

The singlet yield is calculated, according to equation (2.87), as

$$\Phi_{\mathrm{S}} = k_{\mathrm{S}} \sum_{i=1}^{N_{\mathrm{sites}}} \langle \hat{P}^{\mathrm{S}} | x_i \rangle, \tag{3.49}$$

$$= k_{\mathrm{S}} \sum_{i=1}^{N_{\mathrm{sites}}} \mathbf{P}^{\mathrm{S}} \cdot \boldsymbol{x}_{\mathrm{i}}, \tag{3.50}$$

where N_{sites} is the number of sites in the model (in equation (3.47), $N_{\mathrm{sites}} = 2$). The

vectors $\boldsymbol{x}_{\mathrm{i}}$ together form the solution to

$$x = \begin{pmatrix} x_1 \\ x_2 \\ \vdots \\ x_{N_{\mathrm{sites}}} \end{pmatrix} = \hat{\hat{L}}^{-1} \left|\rho(0)\right\rangle, \tag{3.51}$$

or, equivalently,

$$\hat{\hat{L}} \begin{pmatrix} x_1 \\ x_2 \\ \vdots \\ x_{N_{\mathrm{sites}}} \end{pmatrix} = \begin{pmatrix} \rho_1(0) \\ \rho_2(0) \\ \vdots \\ \rho_{N_{\mathrm{sites}}}(0) \end{pmatrix}.^{1} \tag{3.52}$$

In equation (3.52), each $\rho_i(0)$ is the Liouville space density matrix vector of the initial state, normalized by the number of sites N_{sites}:

$$\rho_i(0) = \frac{\rho(0)}{N_{\mathrm{sites}}}. \tag{3.53}$$

Gaussian elimination

The matrix $\hat{\hat{L}}$ in equation (3.47) is an $N \times N$ matrix with

$$N = 2 \times \left(\sum_i (2I_i + 1) \right)^2, \tag{3.54}$$

where I_i is the magnetic quantum number of spin i. The coupling between spins in each site, and between the two sites, additionally means that the matrix is very poorly conditioned. As the number of magnetic nuclei in the radical pair is increased, the problem quickly becomes computationally intractable. However, the size of the matrix can be reduced by a factor of four by carrying out the first step of a gaussian elimination,

[1] For small spin systems, this linear system is easily solved using the MATLAB 'backslash' functionality.

transforming

$$\begin{bmatrix} A & B \\ C & D \end{bmatrix} \begin{bmatrix} x_u \\ x_l \end{bmatrix} = \begin{bmatrix} a \\ b \end{bmatrix} \tag{3.55}$$

$$\tag{3.56}$$

to

$$\begin{bmatrix} A & B \\ 0 & D - CA^{-1}B \end{bmatrix} \begin{bmatrix} x_u \\ x_l \end{bmatrix} = \begin{bmatrix} a \\ b - CA^{-1}a \end{bmatrix} \tag{3.57}$$

The solution vector, x, can then be found in two steps. First, x_l is found by solving the reduced linear system

$$(D - CA^{-1}B)x_l = b - CA^{-1}a. \tag{3.58}$$

The solution can then be substituted back into the top line of equation (3.57):

$$Ax_u - Bx_l = a \tag{3.59}$$

to find x_u.

Further, more specific, techniques to reduce the size of computations are discussed in chapters 4 and 7.

3.2.2 Redfield theory

Although it can be a useful first approximation, molecular motion is rarely well described by considering only two sites and extending the approach to more sites is often impractical. It quickly becomes more convenient to turn to a master equation approach where the evolution of the density matrix is described by a set of coupled linear differential equations (one for each density matrix element). In Redfield theory (also known as Bloch-Redfield-

Table 3.3: Converting between the Interaction and Schrödinger pictures of Quantum Mechanics.

	Interaction	Schrödinger
state $\|\Psi(t)\rangle$	$e^{i\hat{H}_0^S t}\|\Psi_S(t)\rangle$	$e^{-i\hat{H}^S t}\|\Psi_S(0)\rangle$
operator $A(t)$	$e^{i\hat{H}_0^S t}A^S e^{-i\hat{H}_0^S t}$	constant
density $\rho(t)$	$e^{i\hat{H}_0^S t}\rho^S(t)e^{-i\hat{H}_0^S t}$	$e^{-i\hat{H}_0^S t}\rho^S(0)e^{i\hat{H}_0^S t}$

Wangsness theory), a master equation is derived using the principles of second-order perturbation theory [134] (but also see references [115, 135, 136]). It is designed to treat the effects of a weak, random perturbation on the evolution of a system. In this case, the perturbation is the modulation of weak local magnetic interactions by motion of the individual radicals.

As with all perturbation approaches, the first step is to divide the Hamiltonian into a time-independent part, describing the unitary evolution of the system, and a time-dependent part, describing the perturbation:

$$\hat{H} = \hat{H}_0 + \hat{H}_1(t). \tag{3.60}$$

The evolution of the system is described by the Liouville-von Neumann equation (section 2.4.1), which, for convenience, is written in the Interaction picture as

$$\frac{d\rho^{\mathrm{I}}(t)}{dt} = i\left[\rho^{\mathrm{I}}(t), \hat{H}_1^{\mathrm{I}}(t)\right], \tag{3.61}$$

where ρ^{I} and $H_1^{\mathrm{I}}(t)$ are, respectively, the density matrix and perturbation Hamiltonian in the Interaction picture (see table 3.3).

(To understand the origin of equation (3.61), consider that the Interaction picture density

matrix is related to the Schrödinger picture by

$$\rho^{\mathrm{I}}(t) = \exp\left(i\hat{H}_0 t\right) \rho(t) \exp\left(-i\hat{H}_0 t\right). \tag{3.62}$$

Differentiating gives

$$\frac{d\rho(t)}{dt} = i\left[\rho(t), \hat{H}_0\right] + \exp\left(-i\hat{H}_0 t\right) \frac{d\rho^{\mathrm{I}}(t)}{dt} \exp\left(i\hat{H}_0 t\right). \tag{3.63}$$

Equating equation (3.63) to the Liouville-von Neumann equation in the Schrödinger picture,

$$\frac{d\rho(t)}{dt} = i\left[\rho(t), \hat{H}_0 + \hat{H}_1(t)\right], \tag{3.64}$$

gives

$$i\left[\rho(t), \hat{H}_1(t)\right] = \exp\left(-i\hat{H}_0 t\right) \frac{d\rho^{\mathrm{I}}(t)}{dt} \exp\left(i\hat{H}_0 t\right) \tag{3.65}$$

$$\frac{d\rho^{\mathrm{I}}(t)}{dt} = \exp\left(i\hat{H}_0 t\right) i\left[\rho(t), \hat{H}_1(t)\right] \exp\left(-i\hat{H}_0 t\right) \tag{3.66}$$

$$= i\left[\rho^{\mathrm{I}}(t), \hat{H}_1^{\mathrm{I}}(t)\right] \tag{3.67}$$

as required.)

Integrating equation (3.61) gives an explicit expression for the density matrix at time t:

$$\rho^{\mathrm{I}}(t) = \rho^{\mathrm{I}}(0) + i\int_0^t \left[\rho^{\mathrm{I}}(t'), \hat{H}_1^{\mathrm{I}}(t')\right] dt'. \tag{3.68}$$

An improved solution, equivalent to second-order time-dependent perturbation theory, is then obtained by substituting equation (3.68) back into the integral on the right hand

side;

$$\rho^{\mathrm{I}}(t) = \rho^{\mathrm{I}}(0) + i\int_0^t \left[\left(\rho^{\mathrm{I}}(0) + i\int_0^{t'} \left[\rho^{\mathrm{I}}(t''), \hat{H}_1^{\mathrm{I}}(t'')\right] dt''\right), \hat{H}_1^{\mathrm{I}}(t')\right] dt' \tag{3.69}$$

$$= \rho^{\mathrm{I}}(0) + i\int_0^t \left[\rho^{\mathrm{I}}(0), \hat{H}_1^{\mathrm{I}}(t')\right] dt' + (i)^2 \int_0^t \int_0^{t'} \left[\left[\rho^{\mathrm{I}}(t''), \hat{H}_1^{\mathrm{I}}(t'')\right], \hat{H}_1^{\mathrm{I}}(t')\right] dt'' dt'. \tag{3.70}$$

Differentiating equation (3.70) then gives

$$\frac{d\rho^{\mathrm{I}}(t)}{dt} = i\left[\rho^{\mathrm{I}}(0), \hat{H}_1^{\mathrm{I}}(t)\right] - \int_0^t \left[\left[\rho^{\mathrm{I}}(t'), \hat{H}_1^{\mathrm{I}}(t')\right], \hat{H}_1^{\mathrm{I}}(t)\right] dt'. \tag{3.71}$$

To account for the random nature of the perturbation, the average is taken over an ensemble of systems, all starting from the same point at $t = 0$ but experiencing different perturbations. Two assumptions are made about the perturbation:

1. The perturbation is random, meaning that $\hat{H}_1^{\mathrm{I}}(t)$ does not depend on $\rho^{\mathrm{I}}(0)$.
2. The perturbation has a zero time-average. This is equivalent to saying that the ensemble average over the perturbation is zero.

Applying these assumptions to the first term in equation (3.71) immediately simplifies the problem. Working in a basis of states (labelled by the four independent indices α, α', β and β') that diagonalises $\hat{H}_0$, a generalised matrix element of this term can be expressed as

$$\langle\alpha| i[\rho^{\mathrm{I}}(0), H_1^{\mathrm{I}}(t)] |\alpha'\rangle = i\sum_\beta \langle\alpha|\rho^{\mathrm{I}}(0)|\beta\rangle \langle\beta|\hat{H}_1^{\mathrm{I}}(t)|\alpha'\rangle - \langle\alpha|\hat{H}_1^{\mathrm{I}}(t)|\beta\rangle \langle\beta|\rho^{\mathrm{I}}(0)|\alpha'\rangle \tag{3.72}$$

Assumption 1 means that each braket on the right-hand side of equation (3.72) can be averaged separately, whilst assumption 2 implies that the ensemble average over each term containing $\hat{H}_1^{\mathrm{I}}(t)$ will be zero. Therefore,

$$\frac{d\rho^{\mathrm{I}}(t)}{dt} = -\int_0^t \left[\left[\rho^{\mathrm{I}}(t'), \hat{H}_1^{\mathrm{I}}(t')\right], \hat{H}_1^{\mathrm{I}}(t)\right] dt'. \tag{3.73}$$

Before the ensemble average of the second term of equation (3.71) is taken, a change of variables $t' \to t - \tau$ is used to relate variables depending on t and t'. This gives

$$\int_0^t dt' = -\int_t^0 d\tau = \int_0^t d\tau \tag{3.74}$$

$$\frac{d\rho^{\mathrm{I}}(t)}{dt} = -\int_0^t \left[\left[\rho^{\mathrm{I}}(t-\tau), \hat{H}_1^{\mathrm{I}}(t-\tau)\right], \hat{H}_1^{\mathrm{I}}(t)\right] d\tau \tag{3.75}$$

$$\begin{aligned} = -\int_0^t \Big(&\rho^{\mathrm{I}}(t-\tau)\hat{H}_1^{\mathrm{I}}(t-\tau)\hat{H}_1^{\mathrm{I}}(t) - \hat{H}_1^{\mathrm{I}}(t-\tau)\rho^{\mathrm{I}}(t-\tau)\hat{H}_1^{\mathrm{I}}(t) \\ &- \hat{H}_1^{\mathrm{I}}(t)\rho^{\mathrm{I}}(t-\tau)\hat{H}_1^{\mathrm{I}}(t-\tau) + \hat{H}_1^{\mathrm{I}}(t)\hat{H}_1^{\mathrm{I}}(t-\tau)\rho^{\mathrm{I}}(t-\tau)\Big) d\tau. \end{aligned} \tag{3.76}$$

Again considering a generalised matrix element, the ensemble average can be taken over each component of the product terms separately to produce

$$\begin{aligned} \frac{d\rho^{\mathrm{I}}_{\alpha\alpha'}(t)}{dt} = -\int_0^t \sum_{\beta\beta'} \Big(&\rho^{\mathrm{I}}_{\alpha\beta}(t-\tau) g^{\mathrm{I}}_{\beta\beta'\beta'\alpha'}(\tau) - \rho^{\mathrm{I}}_{\beta\beta'}(t-\tau) g^{\mathrm{I}}_{\alpha\beta\beta'\alpha'}(\tau) \\ &- \rho^{\mathrm{I}}_{\beta\beta'}(t-\tau) g^{\mathrm{I}}_{\beta'\alpha'\alpha\beta}(\tau) + \rho^{\mathrm{I}}_{\beta'\alpha'}(t-\tau) g^{\mathrm{I}}_{\beta\beta'\alpha\beta}(\tau)\Big) d\tau, \end{aligned} \tag{3.77}$$

where $g_{\alpha\alpha'\beta\beta'}(\tau) = \overline{\hat{H}_{\alpha\alpha'}(t-\tau)\hat{H}_{\beta\beta'}(t)}$ is defined as the correlation function.

Equation (3.76) describes a non-Markovian system, in which the change in the density matrix at any time t depends on the value of the density matrix at all previous times $(t-\tau)$. However, coupling the system to its environment damps the system and destroys knowledge of previous states. Redfield theory relies on the key assumption that the damping is efficient enough that correlation functions decay to zero in times much less than t and the change in the density matrix only depends on its current value, such that $\rho^{\mathrm{I}}(t-\tau)$ can be replaced by $\rho(t)$ and the upper limit of the integral can be approximated as infinity:

$$\begin{aligned} \frac{d\rho^{\mathrm{I}}_{\alpha\alpha'}(t)}{dt} = -\int_0^\infty \sum_{\beta\beta'} \Big(&\rho^{\mathrm{I}}_{\alpha\beta}(t) g^{\mathrm{I}}_{\beta\beta'\beta'\alpha'}(\tau) - \rho^{\mathrm{I}}_{\beta\beta'}(t) g^{\mathrm{I}}_{\alpha\beta\beta'\alpha'}(\tau) \\ &- \rho^{\mathrm{I}}_{\beta\beta'}(t) g^{\mathrm{I}}_{\beta'\alpha'\alpha\beta}(\tau) + \rho^{\mathrm{I}}_{\beta'\alpha'}(t) g^{\mathrm{I}}_{\beta\beta'\alpha\beta}(\tau)\Big) d\tau. \end{aligned} \tag{3.78}$$

This is the Markov approximation and it limits the applicability of Redfield theory.

Using the relationships in table 3.3 to transform back into the Schrödinger picture, equation (3.78) becomes

$$\frac{d\rho_{\alpha\alpha'}(t)}{dt} = -i\left[\hat{H}_0, \rho(t)\right]_{\alpha\alpha'} - \int_0^\infty \sum_{\beta\beta'} \Big(\rho_{\alpha\beta}(t)e^{i\omega_{\beta\beta'}\tau} g_{\beta\beta'\beta'\alpha'}(\tau) - \rho_{\beta\beta'}(t)e^{i\omega_{\alpha\beta}\tau} g_{\alpha\beta\beta'\alpha'}(\tau) - \rho_{\beta\beta'}(t)e^{i\omega_{\beta'\alpha'}\tau} g_{\beta'\alpha'\alpha\beta}(\tau) + \rho_{\beta'\alpha'}(t)e^{i\omega_{\beta\beta'}} g_{\beta\beta'\alpha\beta}(\tau)\Big) d\tau \quad (3.79)$$

$$= -i\left[\hat{H}_0, \rho(t)\right]_{\alpha\alpha'} - \sum_{\beta\beta'} \Big(\rho_{\alpha\beta}(t)J_{\beta\beta'\beta'\alpha'}(\omega_{\beta\beta'}) - \rho_{\beta\beta'}(t)J_{\alpha\beta\beta'\alpha'}(\omega_{\alpha\beta}) - \rho_{\beta\beta'}(t)J_{\beta'\alpha'\alpha\beta}(\omega_{\beta'\alpha'}) + \rho_{\beta'\alpha'}(t)J_{\beta\beta'\alpha\beta}(\omega_{\beta\beta'})\Big) d\tau, \quad (3.80)$$

where $\omega_{\alpha\alpha'} = E_\alpha - E_{\alpha'}$, and integrating over the correlation functions has produced a quantity

$$J_{\alpha\alpha'\beta\beta'}(\omega_{\alpha\alpha'}) = \int_0^\infty e^{-i\omega_{\alpha\alpha'}\tau} g_{\alpha\alpha'\beta\beta'}(\tau) d\tau, \quad (3.81)$$

whose real part is the spectral density [135].

To complete the derivation of the Redfield master equation, some adjustments are made to the indexing so that the density matrix elements can be factorised out of the right hand side of the equation. In the first term in the integral, a factor $\delta_{\alpha\beta}$ is introduced and the indices β and β' are relabelled as $\beta \to \beta'$ and $\beta' \to \gamma$. The new index γ is summed over to prevent the equation being changed mathematically. Similarly, in the last term in the integral a factor $\delta_{\alpha'\beta'}$ is included with $\beta' \to \beta$ and $\beta \to \gamma$. The final master equation is

$$\frac{d\rho_{\alpha\alpha'}(t)}{dt} = -i\left[\hat{H}_0, \rho(t)\right]_{\alpha\alpha'} - \sum_{\beta\beta'} R_{\alpha\alpha'\beta\beta'}\rho_{\beta\beta'} \quad (3.82)$$

with the elements of the relaxation (or Redfield) superoperator defined by

$$R_{\alpha\alpha'\beta\beta'} = \left(\sum_\gamma \delta_{\alpha\beta}J_{\beta'\gamma\gamma\alpha'}(\omega_{\beta'\gamma}) - J_{\alpha\beta\beta'\alpha'}(\omega_{\alpha\beta}) - J_{\beta'\alpha'\alpha\beta}(\omega_{\beta'\alpha'}) + \sum_\gamma \delta_{\alpha'\beta'}J_{\gamma\beta\alpha\gamma}(\omega_{\gamma\beta})\right). \quad (3.83)$$

Secular approximation

If, after equation (3.78), only the perturbation Hamiltonian $\hat{H}_1$ is transformed to the Schrödinger picture, the Redfield master equation can be derived for the density matrix in the interaction picture as

$$\frac{d\rho^{\mathrm{I}}_{\alpha\alpha'}(t)}{dt} = -\sum_{\beta\beta'} R_{\alpha\alpha'\beta\beta'}\rho^{\mathrm{I}}_{\beta\beta'}(t)e^{i(\omega_{\beta\beta'}-\omega_{\alpha\alpha'})t}. \tag{3.84}$$

From equation (3.84), it is possible to make the secular approximation that high frequency oscillatory terms (terms with large $\omega_{\beta\beta'} - \omega_{\alpha\alpha'}$) can be discarded [115, 134, 137]. This turns equation (3.84) into a coarse-grained derivative over time-intervals that are long compared to the period of the free motion of the system.

Although these terms disappear naturally if the whole equation is converted to the Schrödinger picture, as in the initial derivation, manually discarding them in this way produces a much sparser relaxation matrix $\mathbf{R}$, which allows larger calculations to be performed.

Chapter 4

Preliminary relaxation calculations

In theoretical studies of the radical pair mechanism of magnetoreception, it has been common to assume static, perfectly ordered radicals and to ignore the effects of molecular motion. However, in a real system, some degree of motion is unavoidable. It affects the radical pair compass in three main ways: by driving relaxation, introducing effective static disorder (in the case of very slow motion), and by altering the size or shape of the (effective) interactions experienced by the electrons.

Although they did not explicitly consider motion of the radicals, there have been several efforts to assess the impact of static disorder on the compass. Intuitively, the more disordered an ensemble of radical pairs, the harder it should be to relate the resulting, averaged signal to the orientation of the bird, thus reducing the precision of the compass. However, the effect is not as damaging as might be expected and it is estimated that the compass could still function if the distribution of orientations in an ensemble of radical pairs had a standard deviation of $34 - 50^\circ$ or less [64, 101, 106, 138]. Furthermore, only one degree of orientational freedom needs to be restricted [106]. The wide range of upper bounds on the disorder arises largely because of the number of unknown parameters in

such a calculation: the number of receptors being averaged over, the detection threshold and the target precision of the compass.

It has been suggested that the necessary degree of ordering could be achieved by embedding the magnetoreceptors in a membrane or by tethering them to membrane-bound proteins or elements of the cytoskeleton [101, 106, 139]. Stacks of membrane discs within the outer segments of photoreceptor cells are thought to be a particularly promising location for binding receptors in an ordered fashion [60, 106, 140]. However, there is no clear evidence that the candidate magnetoreceptor, cryptochrome, binds particularly to any of these structures. Even assuming that cryptochrome is tethered in an oriented manner, some level of disorder is unavoidable. This can be compensated for, up to a point, by increasing the number of receptors, reducing the required sensitivity or precision of the compass or by optimising the radicals to produce the most anisotropic signal [64].

Many studies have indeed looked for the optimum hyperfine interactions to maximise the signal in a static system. They have shown that the most anisotropic signals are produced by radical pairs with a highly asymmetric distribution of hyperfine interactions between the two radicals, up to the limit where one radical contains no hyperfine interactions at all [35, 62, 67, 141]. For radical pairs of this type, the anisotropy of the signal is boosted further if the largest hyperfine interaction has an axial shape with $A_x = A_y = 0$ [68]. Radical pairs that maximize anisotropy are the most robust against static disorder and variability in the hyperfine interactions (due to e.g. slight differences in the way the radicals are bound) [68, 142]. In cryptochrome, the flavin radical contains a dominant axial hyperfine interaction with a nitrogen nucleus (N5) that has very small (although non-zero) A_x and A_y components [68]. It therefore appears to be well-suited to forming one half of a radical pair compass. However, the only biological radical with no hyperfine interactions that has been suggested to form part of the compass is a superoxide radical [35], which is likely to relax extremely rapidly [59].

Whilst the effects of static disorder are fairly well characterised in model radical pair systems, there has been almost no (but see [101]) attempt to examine the impact of

dynamic disorder. Similarly, little study has been made of spin relaxation in these systems, although it has long been identified as a potential problem.

Most previous attempts to treat relaxation have introduced the process phenomenologically, using Lindblad operators [143–146]. Such studies have established that relaxation is generally detrimental and will reduce the sensitivity of the compass. However, processes that generate *correlated* noise can drive dephasing in such a way that it amplifies, rather than destroys, the compass signal [144]. An example is reversible electron hopping between different sites in the Trp triad, which modulates the distance between the two radicals and hence the strength of electron-electron exchange and dipolar interactions [117].

Phenomenological descriptions of relaxation offer information about the possible effects but say nothing about the physical sources of relaxation or how much relaxation might be expected in any given system. At the other end of the scale, relaxation has been studied using molecular dynamics simulations, which start from a physical description of the system and can be used to work out how much relaxation is caused by particular motions. In combination with spin dynamics simulations, this approach has been used to show that, in *At*CRY1, librational motion of the flavin radical and fluctuations in the dihedral angle between the ring system and side chain of the tryptophan radical both drive efficient spin relaxation [147]. Again, when the flavin radical is paired with a radical containing no hyperfine interactions, the compass displays greater immunity to the effects of relaxation.

The molecular dynamics approach also comes with limitations. Firstly, it relies on knowing the structure of the protein being modelled. This is particularly problematic as structures have not been solved for any of the four bird cryptochromes [59]. Investigations are therefore limited to studying cryptochromes from other species, which may be missing subtle variations that allow the compass to work. Furthermore, many molecular dynamics simulations are carried out on proteins in isolation or in a solvent continuum [92, 107], without treating the possibility that interactions between the protein and its cellular

environment might alter its internal dynamics [147, 148].

The work in this chapter and chapter 5 aims to fill the gap between Lindblad and molecular dynamics approaches to relaxation and the effects of molecular motion. Two different models of molecular motion are used, in combination with spin dynamics simulations, to explore the effects of different types of motion on the compass and determine the conditions that must be met if cryptochrome is to act as a viable magnetoreceptor. I will focus on the effect of librational motion of the two radicals, as this type of motion is particularly common and has already been shown to be a potential source of efficient relaxation [147]. Lau *et al.* have already started to address this question for rigid-body rotational motion of the whole cryptochrome protein. They demonstrated that the impact of motionally-induced relaxation depended on the amplitude and speed of the motion, the lifetime of the radical pairs and the size of the hyperfine interactions, concluding that an acceptable compass signal could be maintained with "medium-amplitude fluctuations" and a "motional correlation time longer than about a quarter of the radical pair lifetime" [101]. I will extend this work to consider the internal rotations of individual radicals and to treat larger systems and a greater range of parameter values.

This chapter contains preliminary calculations, using a very simplified model of the motion to explore the general trends observed by Lau *et al.* over a range of parameter values.

4.1 Application of the two-site model

The two-site model, introduced in section 3.2.1, was used to gain an initial understanding of the effects of internal motion on the radical pair compass. Although instantaneous hopping between just two sites is not a realistic description of most internal rotations, the simplicity of the model allowed a wide range of parameters to be explored and the results will be used to guide more specific investigation using Redfield theory in chapter 5.

In this model, the system evolves under a spin Hamiltonian of the form

$$\begin{aligned}\hat{H} =&\gamma_{\mathrm{e}} B_0[(\hat{S}_{1z} + \hat{S}_{2z})\cos\theta + (\hat{S}_{1x} + \hat{S}_{2x})\sin\theta\cos\phi \\ &+ (\hat{S}_{1y} + \hat{S}_{2y})\sin\theta\sin\phi] + \sum_{n,i} \hat{\mathbf{S}}_i \cdot \mathbf{A}_{i,n} \cdot \hat{\mathbf{I}}_{i,n},\end{aligned} \tag{4.1}$$

where the term in square brackets represents the Zeeman interaction of the radical pair with the external field B_0 (section 2.2.1) and the final term is the hyperfine interaction between the unpaired electrons and any magnetic nuclei in the radicals (2.2.2). The orientation of B_0 (in the coordinate frame of the radical pair) is described by the polar and azimuthal angles θ and ϕ. The vector operator $\hat{\mathbf{I}}_{i,n}$ is the n^{th} nuclear spin coupled to electron i, whilst $\hat{\mathbf{S}}_1$ and $\hat{\mathbf{S}}_2$ are the spin operators for the two unpaired electrons. The i^{th} electron and n^{th} nuclear spin are coupled together by the (3×3) hyperfine interaction tensor $\mathbf{A}_{i,n}$.

In each site the Hamiltonian is indirectly altered by rotation of one of the radicals. For the moving radical, the hyperfine tensors are rotated through an angle, $\pm\beta$ around an axis (u_x, u_y, u_z) in the molecular frame, using an angle-axis rotation matrix (section 3.1.2). In most cases, the rotation axis is chosen as the x-axis (1,0,0), the y-axis (0,1,0) or an axis halfway between the two in the xy-plane $(1/\sqrt{2}, 1/\sqrt{2}, 0)$.

The initial singlet state is described by the density matrix

$$\rho(0) = P^{\mathrm{S}}/M,$$

where P^{S} is the singlet projection operator (defined in 2.59). The number of nuclear spin states M is calculated as

$$M = N_{\text{sites}} \times \prod_i (2I_i + 1), \tag{4.2}$$

where I_i is the spin quantum number of nucleus i. The factor N_{sites} accounts for the increased size of the Liouville space needed to describe multiple sites (see equation (3.53)). In this chapter $N_{\text{sites}} = 2$ but in later chapters, other values will be used.

It is assumed that the singlet and triplet reactions occur at the same rate ($k_{\mathrm{S}} = k_{\mathrm{T}} = k$), such that

$$\frac{k_{\mathrm{S}}}{2}\left\{\hat{P}^{\mathrm{S}}, \rho(t)\right\} + \frac{k_{\mathrm{T}}}{2}\left\{\hat{P}^{\mathrm{T}}, \rho(t)\right\} = k\rho(t). \tag{4.3}$$

This is not necessarily the case in the avian compass although measurements of *At*CRY suggest that they may be of a similar order of magnitude [110]. However, the assumption is thought not to obscure the essential physics of the system [62] and, as it greatly simplifies calculations, will therefore be used throughout the rest of this thesis.

The two-site model in equation (3.47) can now be written more specifically as

$$\begin{bmatrix}\dot{\rho}_1\\ \dot{\rho}_2\end{bmatrix} = \begin{bmatrix}-i\hat{\hat{H}}_1 - (m+k)\mathbb{I} & m\mathbb{I}\\ m\mathbb{I} & -i\hat{\hat{H}}_2 - (m+k)\mathbb{I}\end{bmatrix}\begin{bmatrix}\rho_1\\ \rho_2\end{bmatrix}, \tag{4.4}$$

$$= -\hat{\hat{L}}\begin{bmatrix}\rho_1\\ \rho_2\end{bmatrix}. \tag{4.5}$$

4.1.1 Treating larger spin systems

[1]Using equation (4.4) with equations (3.50) and (3.52), calculations involving more than around 3 nuclei quickly become prohibitively expensive in terms of the time or memory cost of solving $\hat{\hat{L}}x = |\hat{\rho}(0)\rangle$. As described in section 3.2.1, the size of the calculation can be reduced by first carrying out one step of a gaussian elimination. However, the most effective rearrangement of $\hat{\hat{L}}$ depends on the conditions being simulated.

Slow motion regime

When molecular motion is slow, the system is best described by considering the two sites separately. The original Liouville superoperator in equation (4.4), is rearranged directly,

[1]The methods of rearranging and preconditioning the linear system, described in this section, were originally proposed by Dr. Daniel Kattnig.

as described by equation (3.57), to give

$$\begin{bmatrix} \hat{\hat{L}}_1 + m\mathbb{I} & -m\mathbb{I} \\ 0 & \hat{\hat{L}}_2 + m\mathbb{I} - (m\mathbb{I})(\hat{\hat{L}}_1 + m\mathbb{I})^{-1}(m\mathbb{I}) \end{bmatrix} \begin{bmatrix} x_u \\ x_l \end{bmatrix} = \begin{bmatrix} \rho(0) \\ \rho(0) - (m\mathbb{I})(\hat{\hat{L}}_1 + m\mathbb{I})^{-1}\rho(0) \end{bmatrix}, \tag{4.6}$$

where $\hat{\hat{L}}_i = i\hat{\hat{H}}_i + k\mathbb{I}$.

The lower half,

$$x_l = \left(\hat{\hat{L}}_2 + m\mathbb{I} - (m\mathbb{I})(\hat{\hat{L}}_1 + m\mathbb{I})^{-1}(m\mathbb{I})\right)^{-1} \left(\rho(0) - (m\mathbb{I})(\hat{\hat{L}}_1 + m\mathbb{I})^{-1}\rho(0)\right) \tag{4.7}$$

is solved using an iterative solver (BICGSTAB[2]) with an initial guess $x_l = (\hat{\hat{L}}_2 + m\mathbb{I})^{-1}(\rho(0) - (m\mathbb{I})(\hat{\hat{L}}_1 + m\mathbb{I})^{-1}\rho(0))$.

To minimise the expense of calculating and storing the required operator matrices, $\hat{\hat{L}}_1$ and $\hat{\hat{L}}_2$ are constructed in the eigenbasis of $\hat{H}_1$ and $\hat{H}_2$, respectively. The main diagonal of each of the resulting diagonal matrices can be stored as vectors, reducing the memory requirement to the Hilbert space rather than the Liouville space dimensions. The diagonal matrices are, furthermore, trivial to invert and the necessary matrix multiplications can be implemented by element-wise operations.

In addition, the matrix $\mathbf{M} = (\hat{\hat{L}}_2 + m\mathbb{I} - (m\mathbb{I})(\hat{\hat{L}}_1 + m\mathbb{I})^{-1}(m\mathbb{I}))$ is not passed directly to the BICGSTAB solver, which would require $\mathbf{M}^{-1}$ to be calculated explicitly and stored in full. Instead the solver is provided with a function that calculates the result of applying $\mathbf{M}$ to the estimated solution vector in each iteration of the algorithm. In this way, $\mathbf{M}$ can be applied in a stepwise fashion, keeping $\hat{\hat{L}}_1$ and $\hat{\hat{L}}_2$ in their diagonal forms and converting between the two eigenbases between steps where necessary:

1. Transform estimated solution vector into the eigenbasis of $\hat{H}_1$.

2. Multiply vector by constant m.

[2]A BICGSTAB solver is provided in MATLAB.

3. Multiply by $(\hat{\hat{L}}_1 + m\mathbb{I})^{-1}$. As $(\hat{\hat{L}}_1 + m\mathbb{I})$ is diagonal in this eigenbasis, it can be stored in vector form and the inverse operation can be implemented as an element-wise division.

4. Multiply vector by constant m.

5. Transform estimated solution vector into the eigenbasis of $\hat{H}_2$.

6. Subtract from $(\hat{\hat{L}}_2 + m\mathbb{I})$. This can again be carried out as element-wise multiplication of two vectors.

Once x_l has been calculated, x_u is found using

$$x_u = (\hat{\hat{L}}_1 + m\mathbb{I})^{-1} (\rho(0) + m x_l) . \tag{4.8}$$

Fast motion regime

When the hopping frequency is very large, the system evolves under the influence of the average hyperfine interaction for the two sites. Before the gaussian elimination step the system is converted from $Lx = |\rho(0)\rangle$ to $VLV^T Vx = V|\rho(0)\rangle$ where

$$V = \begin{bmatrix} -1/\sqrt{2} & 1/\sqrt{2} \\ 1/\sqrt{2} & 1/\sqrt{2} \end{bmatrix} \otimes \mathbb{I}. \tag{4.9}$$

This places the average Hamiltonian, $\hat{H}_{av} = (\hat{H}_1 + \hat{H}_2)/2$, on the main diagonal block, along with the large rate constant m:

$$\begin{gathered} \frac{1}{2} \begin{bmatrix} \Sigma + 4m\mathbb{I} & \Delta \\ \Delta & \Sigma \end{bmatrix} \begin{bmatrix} 0 \\ y \end{bmatrix} = \begin{bmatrix} 0 \\ \sqrt{2}\rho(0) \end{bmatrix}; \\ \Sigma = L_1 + L_2, \qquad \Delta = L_2 - L_1. \end{gathered} \tag{4.10}$$

Minimising the number of large off-diagonal components makes the matrix easier to precondition (section 4.1.2) and hence to solve.

The gaussian elimination step produces

$$\frac{1}{2}\begin{bmatrix} \Sigma + 4m\mathbb{I} & \Delta \\ 0 & \Sigma - \Delta(\Sigma + 4m\mathbb{I})^{-1}\Delta \end{bmatrix}\begin{bmatrix} 0 \\ y \end{bmatrix} = \begin{bmatrix} 0 \\ \sqrt{2}\rho(0) \end{bmatrix}; \tag{4.11}$$

The solution vector, $x = y/\sqrt{2}$, is found by iteratively solving the bottom line,

$$(\Sigma - \Delta(\Sigma + 4m\mathbb{I})^{-1}\Delta)x_l = 2\rho(0), \tag{4.12}$$

in the eigenbasis of the average Hamiltonian, using an initial guess of $x = 4\Sigma^{-1}\rho(0)$.

The upper half of the solution vector $x_u = x_l$, so the singlet yield is

$$\Phi_{\mathrm{S}} = 2k_{\mathrm{S}}\mathbf{P}^{\mathrm{S}} \cdot \mathbf{x}_l.^{3} \tag{4.13}$$

4.1.2 Preconditioners

The speed of the BICGSTAB iterative solver can be drastically improved by the use of a preconditioner. Ideally, a preconditioner should provide a good approximation of the matrix inverse and be cheap to calculate [149].

When solving in the fast motion regime (equation (4.11)), the matrix, $\mathbf{M} = (\Sigma - \Delta(\Sigma + 4m\mathbb{I})^{-1}\Delta)$ is strongly diagonally dominant in the eigenbasis of the average Hamiltonian. A Jacobi preconditioner, $\mathbf{P} = (\mathrm{diag}(\mathbf{M}))^{-1}$, which is the cheapest possible preconditioner to calculate, is therefore perfectly sufficient.

[3] Note that the factor of 2 in equation (4.13) can be introduced at a variety of points in the calculation. My code, for example, multiplies $\rho(0)$ by 2 before solving the linear system and then calculates $\Phi_{\mathrm{S}} = k_{\mathrm{S}}\mathbf{P}^{\mathrm{S}} \cdot \mathbf{x}_l$.

In the slow motion regime, switching between the eigenbases of $\hat{H}_1$ and $\hat{H}_2$ introduces larger off-diagonal elements, which must be accounted for in forming the preconditioner. The best preconditioner was found to be a polynomial preconditioner.

A polynomial preconditioner approximates the inverse of a matrix $\mathbf{M} = \mathbb{I} - \mathbf{B}$ as a polynomial expansion of the form

$$\mathbf{M}^{-1} = \sum_{k=0}^{\infty} \mathbf{B}^k, \tag{4.14}$$

which converges when the spectral radius (largest absolute eigenvalue) of $(\mathbb{I} - \mathbf{B})$ is less than one. As with the calculation of the matrix-vector product described above, the polynomial preconditioner does not have to be calculated directly but can be passed to the BICGSTAB solver as a function $f(x) = \mathbf{M}^{-1}x$. Within this function $\mathbf{M}$ and x are first mutiplied by $(\hat{\hat{L}}_2 + m\mathbb{I})^{-1}$, such that $\mathbf{M}$ is in the form required for the polynomial expansion: $\mathbf{M} = \mathbb{I} - (\hat{\hat{L}}_2 + m\mathbb{I})^{-1}(m\mathbb{I})(\hat{\hat{L}}_1 + m\mathbb{I})^{-1}(m\mathbb{I})$ (see equation (4.6)).

As before, advantage is taken of the diagonal nature of $\hat{\hat{L}}_1$ and $\hat{\hat{L}}_2$ to implement each matrix inversion and multiplication as element-wise operations between two vectors, minimising storage and computation demands.

4.2 One-spin systems

In this section, initial observations about the effects of motion are made by considering a radical pair with a single spin-1/2 nucleus in one of the radicals (hereafter referred to as R_1). Unless otherwise stated, the hyperfine tensor of the single magnetic nucleus is taken to be

$$A = \begin{pmatrix} 0 & 0 & 0 \\ 0 & 0 & 0 \\ 0 & 0 & 1.5 \end{pmatrix} \text{ mT}, \tag{4.15}$$

which is similar to the hyperfine tensor of N5 in the $FAD^{\bullet-}$ radical in cryptochrome.

Figure 4.1(a) shows the singlet yield profile (the singlet yield as a function of θ) for this model radical pair. Due to the cylindrical symmetry of the hyperfine tensor, ϕ can be set to zero without loss of generality. The singlet yield varies approximately sinusoidally with θ, as has been observed in previous theoretical studies [29, 55, 101]. The sensitivity of the compass is directly related to magnitude of the difference in the singlet yield at different field directions. This will be referred to as the singlet yield anisotropy:

$$\Delta\Phi_{\mathrm{S}} = \phi_{\mathrm{S}}^{\mathrm{max}} - \phi_{\mathrm{S}}^{\mathrm{min}}. \tag{4.16}$$

The predictable shape of the singlet yield profile means that, in this case, the anisotropy can be calculated from

$$\Delta\Phi_{\mathrm{S}} = \phi_{\mathrm{S}}(0^{\circ}) - \phi_{\mathrm{S}}(90^{\circ}). \tag{4.17}$$

For the radical pair described above, with $k = 10^6$ s^{-1}, the anisotropy is 0.25 in the absence of any motion.

Figure 4.1(b) illustrates the effect on $\Delta\Phi_{\mathrm{S}}$ of allowing R_1 to hop between two sites rotated by $\pm 5^{\circ}$ about the x-axis, as a function of the hopping rate. The most noticeable effect of the motion is that it drives spin relaxation, which is fastest when the hopping rate m is around 10^8 s^{-1} (a similar magnitude to the energy scale of the Hamiltonian). In this region, the singlet yield anisotropy is reduced, corresponding to the singlet yield tending towards its equilibrium value of 0.25 for all field directions. This is expected as the relaxation rate is known to be proportional to both the squared amplitude of the fluctuations driving the relaxation and the spectral density $J(\omega)$:

$$\text{rate} \propto J(\omega)|\Delta B|^2. \tag{4.18}$$

It has previously been predicted that 1 μs would be the optimum recombination lifetime $(1/k)$ for a radical pair compass, as it is the shortest lifetime in which the maximum singlet yield can build up, thereby minimizing the time in which relaxation can occur [58]. This

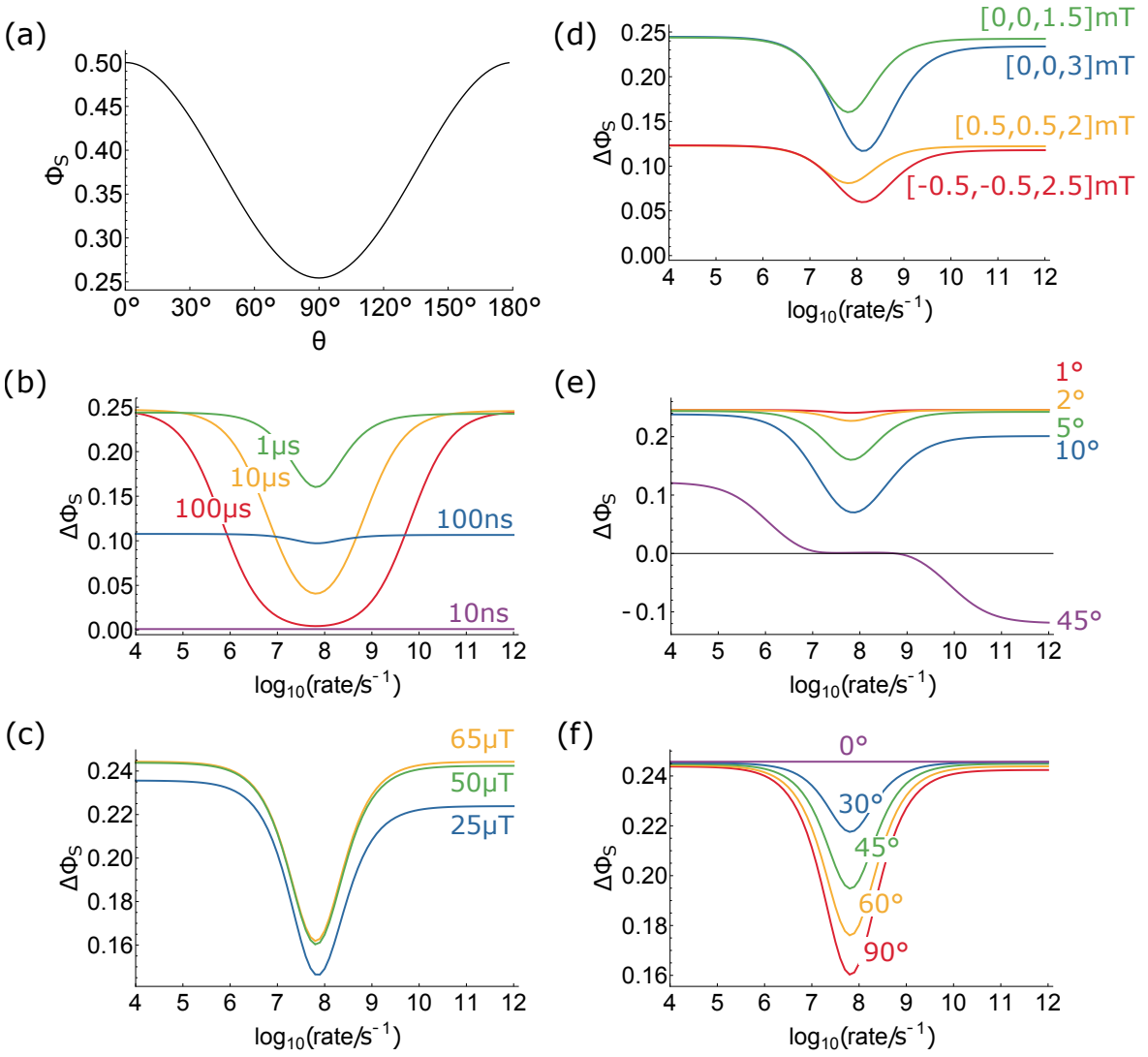


Figure 4.1: Factors affecting the singlet yield anisotropy of the one-spin model radical pair described in the text. (a) Singlet yield profile of the static radical pair with a 1 μs lifetime in a 50 μT field. (b-f) Singlet yield anisotropy as a function of the hopping frequency m with different (b) radical pair recombination lifetimes ($1/k$); (c) external field strengths (B_0); (d) hyperfine tensors; (e) hopping angles ($\pm\beta$) and (f) rotation axes ($[\sin(\alpha), 0, \cos(\alpha)]$), as labelled on the graphs. Unless otherwise indicated, the radical pair containing the hyperfine interaction hops $\pm 5°$ around the x-axis ($[1, 0, 0]$); the radical pair recombination lifetime is 1 μs; the external field strength is 50 μT and the hyperfine tensor has principal components $[0, 0, 3a]$, with $a = 0.5$ mT.

point is demonstrated by observing the effect of different radical pair recombination rates (different lifetimes) in figure 4.1(b). When $k > 10^6$ s^{-1} (the radicals have a lifetime < 1 μs), the singlet yield anisotropy is noticeably smaller at the plateau values (very fast or very slow hopping, which induces little to no relaxation). Conversely, as the recombination rate is reduced below 10^6 s^{-1}, the plateau values remain constant but the singlet yield anisotropy is more significantly reduced by relaxation around the region $m = 10^8$ s^{-1}.

It might be expected that the anisotropy would develop more rapidly in the singlet yield in the presence of a stronger external field, allowing for shorter radical pair lifetimes to reduce the damaging effects of relaxation. However, figure 4.1(c) shows that within the natural range of field strengths for the Earth's magnetic field, this is an essentially negligible effect.

Similarly, increasing the size of the hyperfine interactions, particularly the size of the anisotropic component, might be expected to increase the singlet yield anisotropy. In fact, it is the shape rather than the size of the hyperfine tensors that appears to have the most influence. The limiting singlet yield anisotropy, in the absence of relaxation, may be calculated using the result from Timmel *et al.* (1998) that

$$\Phi_{\mathrm{S}}(k \to 0) = \frac{1}{M} \sum_{m=1}^{4M} {}^{*} \sum_{n=1}^{4M} {}^{*} |P^{S}_{mn}|^2, \tag{4.19}$$

where the asterisks indicate that only terms for which $\omega_{mn} = E_m - E_n = 0$ (i.e. states m and n are degenerate) are included in the sum. Varying the T_{zz}/a ratio shows that, for this one-nucleus system, the singlet yield anisotropy peaks at a value of 0.25 for $T_{zz}/a = 2$ and then decreases towards a value of 0.125 as the ratio increases or decreases (see figure 4.2(a)). Due to the traceless nature of the anisotropic HFI, the ratio $T_{zz}/a = 2$ forces the transverse components of the hyperfine coupling to be zero. Changing the size of the hyperfine coupling also changes the limiting value but, as shown in figure 4.2(b), this is a much smaller effect.

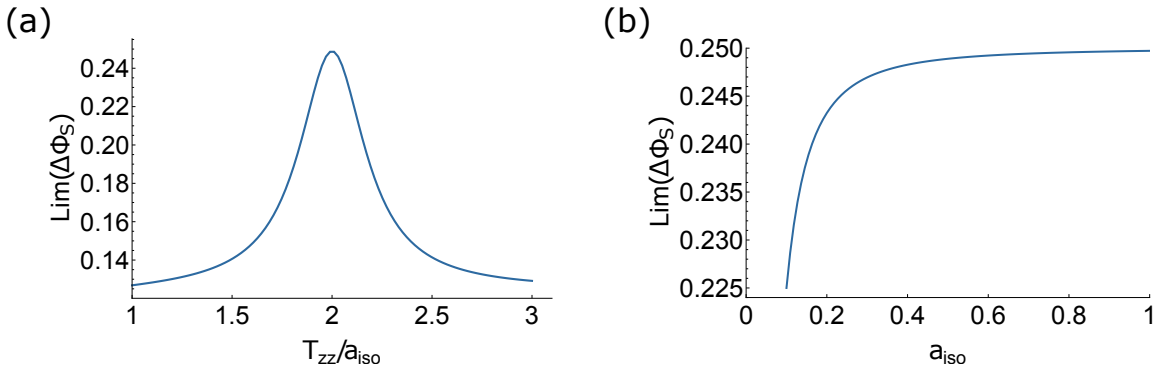


Figure 4.2: (a) Change in the limiting singlet yield anisotropy as a function of the shape of the hyperfine tensor, parameterised by T_{zz}/a_{iso}. The isotropic component $a_{\mathrm{iso}} = 0.5$ mT. (b) Change in the limiting singlet yield anisotropy as a function of the size of the hyperfine tensor, parameterised by a_{iso}. The shape of the tensor is fixed with $T_{zz}/a_{\mathrm{iso}} = 2$.

Figure 4.1(d) demonstrates that, in the limit of fast or slow motion, the singlet yield anisotropy is smaller for radical pairs where T_{zz}/a deviates significantly from the optimum value of 2, even when the hyperfine tensor is larger or more anisotropic. However, increasing the size of the hyperfine tensor results in faster relaxation due to larger fluctuations in the interaction as the radical moves (equation (4.18)). Changing the size of the hyperfine interactions also, necessarily, changes the energy level spacings and hence the hopping frequency at which the fastest relaxation is induced.

The magnitude of magnetic fluctuations, and hence the relaxation rate, is likewise increased by allowing the radical to hop through a larger angle between sites (figure 4.1(e)). Due to the symmetry of this particular radical pair, the axis around which the radical hops is also significant. Figure 4.1(f) shows that as the rotation axis is brought closer to the symmetry axis of the radical, more anisotropy is preserved at $m = 10^8$ s^{-1}, where relaxation should be fastest. When the rotation axis and the symmetry axis are aligned, the hopping motion has no effect on the hyperfine tensor and no relaxation is observed.

When m is small, the modulations are essentially 'frozen out', spin relaxation is slow, and the observed singlet yield profile corresponds to that for a system with static disorder. As the radical is rotated through larger angles, the principal axis of the hyperfine interaction

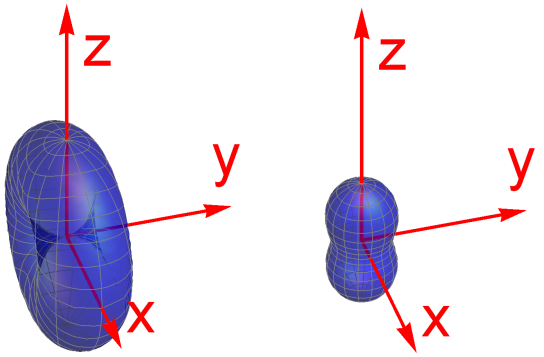


Figure 4.3: Effective hyperfine interaction when the [0,0,1.5] mT tensor is averaged over 45° hopping in the two-site model (left) vs. isotropic rotation in a $\sin^2\beta$ potential of the type introduced in chapter 5, with an average deviation of 45°. The blue surfaces represent the strength of the hyperfine interaction as a function of the angles θ and ϕ. They are calculated by projecting the hyperfine tensor into a spherical polar coordinate system to create a set of parametric equations for 3D plotting: Surface $= (qAq) \cdot q$ with $q = (\sin\theta\cos\phi, \sin\theta\sin\phi, \cos\theta)$.

is less well-aligned with the z-axis of the electron spins and the singlet yield anisotropy is reduced.

By contrast, high frequency modulations make the two sites indistinguishable on the time-scale of the spin evolution and the radical pair evolves under the influence of the average of the hyperfine interactions in each site. Spin relaxation is, again, slow and $\Delta\Phi_S$ plateaus at its limiting value for the averaged hyperfine tensor, which is not necessarily the same as the unmodulated hyperfine interaction. Again, as the moving radical hops through larger angles, the singlet yield anisotropy is reduced, this time because non-zero A_{yy} are introduced into the effective hyperfine tensor. Thus the effective interaction has a less optimum shape.

At very large hopping angles, the singlet yield anisotropy is severely reduced and even becomes negative. This behaviour was not observed by Lau *et al.* (2010) and indicates a breakdown in the two-site model. In reality, rather than sampling just two sites, the moving radical would sample a continuous range of orientations in three dimensions. As the motion becomes less restrained, the radical would sample more orientations but still be statistically aligned more along one axis than the others. In the two-site model, when

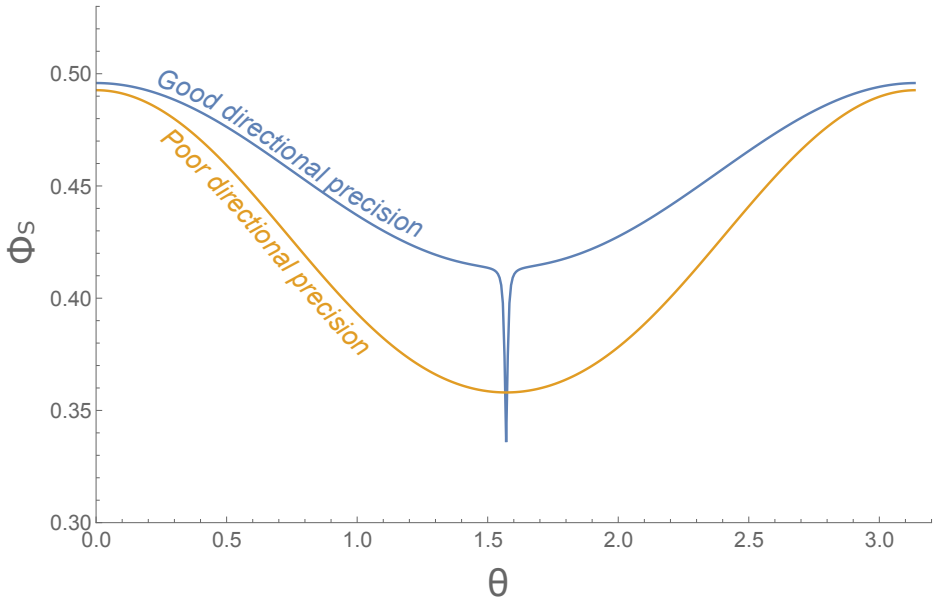


Figure 4.4: Spiky features in the singlet yield, as seen in the blue trace, offer more precise directional information than the smoothly varying singlet yield profiles seen in previous theoretical studies (orange).

β reaches 45°, the projection of the hyperfine interaction onto the y and z axes is the same in both sites (i.e. every site sampled by the radical). The resulting hyperfine tensor (shown in figure 4.3) looks very different from the effective tensor that might result from averaging over more realistic motion. The two-site model therefore cannot offer a reliable picture of what happens when the radical is free to move through larger angles.

4.3 Two-spin systems

4.3.1 Spike-producing radical pairs

The majority of previous theoretical studies have, for computational simplicity, focused on model radical pair systems containing a single nuclear spin and with a 1 μs lifetime. For such radical pairs, the singlet yield has a characteristically smooth, approximately sinusoidal dependence on the external field direction (see figure 4.4). However, prolonging the recombination (and coherence) lifetime results in sharp features, or spikes, appearing

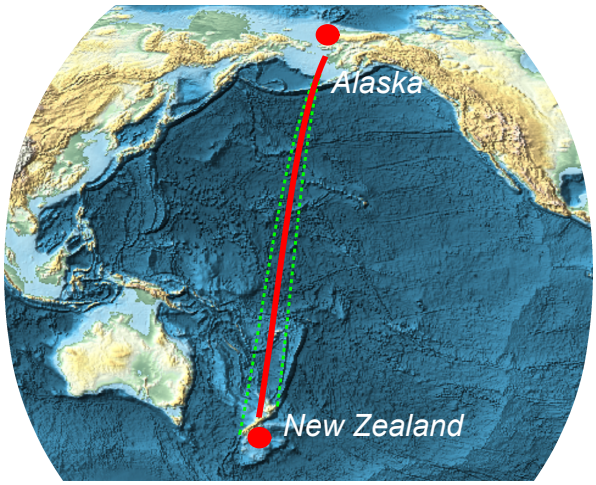


Figure 4.5: Migratory route of the bar-tailed godwit (solid red line) and the range of acceptable error (dashed green lines).

in the singlet yield of a number of multi-spin radical pairs (figure 4.4), including the flavin-tryptophan radical pair [61]. These spiky features could go a long way towards explaining the apparent precision of the avian magnetic compass.

The exact precision of the avian magnetic compass is hard to determine from simple observation of the preferred directions of the birds in an Emlen funnel experiment. The first indication of a high precision compass comes from the long-distance migration paths of certain birds. The migratory route of the bar-tailed godwit (figure 4.5), for example, takes it across the Pacific Ocean from Alaska to New Zealand [65]. There is little to no land along the route to act as landmarks and a misjudged bearing would result in the birds missing their narrow target and falling into the sea. The required precision is about 7.5°.

Adherence to precise migratory routes may be achieved by integrating information from a number of sources, such as the position of the stars and sun. Further evidence for the high precision of the magnetic compass comes from more controlled studies of the ability of birds to orient under near-vertical [66] or near-horizontal fields [36] (mimicking the conditions at the poles and equator, respectively). At the poles and equator, there is a symmetry in the magnetic information available to the bird that makes it impossible to

determine a correct bearing. Consequently, in Emlen funnel experiments, birds are completely disoriented under fields with 0° or 90° inclination. If the compass were infinitely precise, any small shift away from 0° or 90° inclination would break the symmetry and restore orientation ability. However, birds remain disoriented at 88° [66]. At 5° and 85° birds are once again able to orient, suggesting a precision of 5° for the compass. It is unclear how this could be achieved using the sinusoidal patterns in figure 4.1(a), whereas a sharp spike could pick out a precise direction, rather like a compass needle.

Spikes arise when radical pair spin states with different singlet character are efficiently mixed at avoided crossings of energy levels. For this situation to occur, the radical pair must fulfil 3 criteria.

The first requirement is the existence of an avoided crossing. Avoided crossings are formed when two states are coupled by a weak perturbation $\hat{W}$ that introduces small off-diagonal terms into the Hamiltonian:

$$\hat{H} = \begin{pmatrix} E_1 & 0 \\ 0 & E_2 \end{pmatrix} \tag{4.20}$$

$$\hat{H} + \hat{W} = \begin{pmatrix} E_1 & W \\ W & E_2 \end{pmatrix}. \tag{4.21}$$

The eigenstates of the perturbed system contain a dependence on the elements of the perturbation, which prevents the two states from ever becoming degenerate:

$$E_{\pm} = \frac{1}{2}(E_1 + E_2) \pm \frac{1}{2}\sqrt{(E_1 - E_2)^2 + 4|W|^2}. \tag{4.22}$$

This is illustrated in figure 4.6.

In spike-producing radical pairs, the perturbation is created by the presence of small, but non-zero, A_{xx} and A_{yy} components in the hyperfine tensor, which introduce small off-diagonal elements into $\hat{H}_{\text{hfi}}$. This is the first requirement for observing spikes.

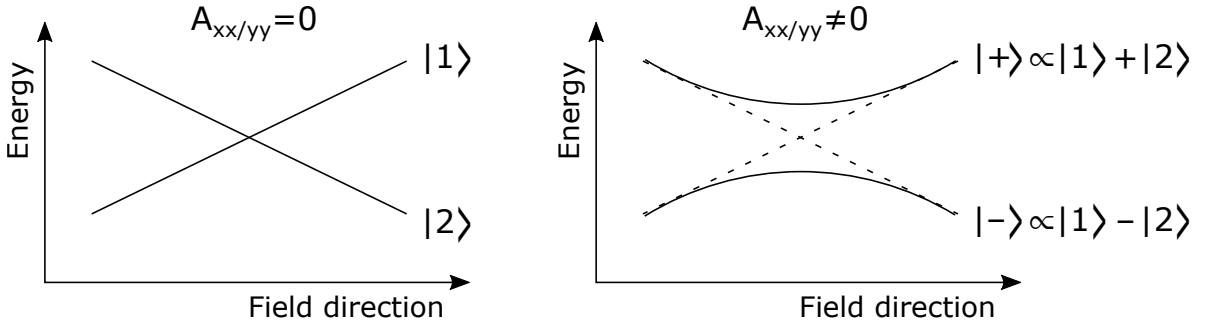


Figure 4.6: Small A_{xx} and A_{yy} elements in the hyperfine tensor couple pairs of states. The perturbation prevents the energy levels from ever becoming degenerate, creating an avoided crossing. The states listed on the right-hand picture describe the system in the middle of the avoided crossing.

The eigenstates of $(\hat{H} + \hat{W})$ are coherent superpositions of the eigenstates of $\hat{H}$. As the system evolves in time, it oscillates between the constituent unperturbed states at a frequency that depends on the energy gap between them. At the avoided crossing, the energy gap between the coupled states is extremely small and hence the coherence evolves very slowly. The second requirement for observing a spike is that the radical pair has a long (coherence) lifetime, in order to observe the effect of the slow evolution at the avoided crossing. This is reflected in equation (2.74), which demonstrates that off-diagonal terms (coherences) only contribute significantly to the singlet yield when the energy gap ω_{mn} is small compared to the rate constant k. As the lifetime of the radical pair increases (k gets smaller), the off-diagonal terms get smaller (compared to the unperturbed case where the states are degenerate), creating a larger dip (spike) in the singlet yield (see figure 4.7). The minimum recombination lifetime required to observe spikes appears to be on the order of 10 μs - an order of magnitude larger than the optimum lifetime identified for 'non-spiky' radical pairs.

The final requirement for observing a spike is that the coupled states have a different singlet yield character (so that the evolution of the coherences corresponds to S/T inter-conversion). It can be shown (reference [61]) that this will only occur if the counter-radical contains at least one hyperfine interaction with a non-zero z-component.

Consideration of these spikes adds a new dimension to the search for optimum conditions

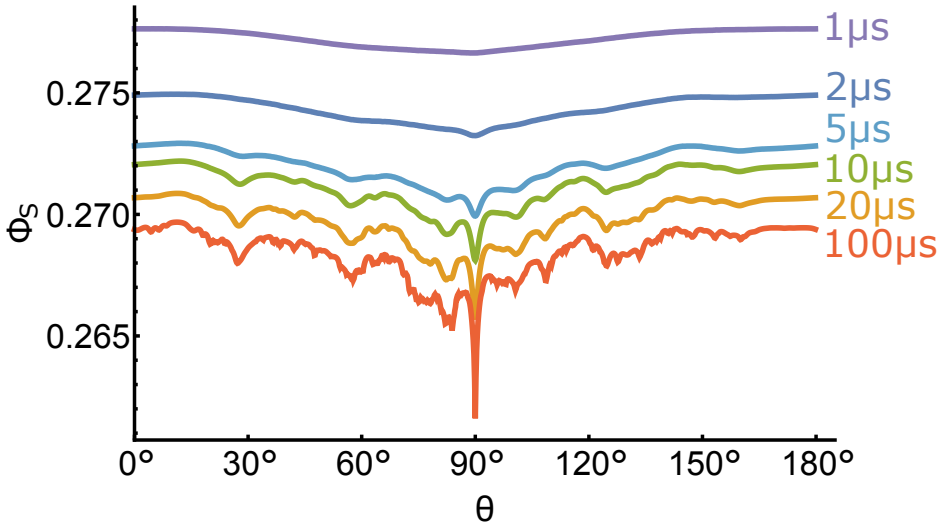


Figure 4.7: Increasing the lifetime of the radical pair allows more time to observe the effect of coherent oscillations between states at the avoided crossing. The data used in this figure was calculated by Hamish Hiscock for a flavin-tryptophan radical pair in a 50 μT field.

for compass function. Not only is a large singlet yield anisotropy required to maximise the sensitivity of the compass, but the sharpness of the spike must also be maintained to maximise the compass precision. The requirement for long-lived coherence also increases the susceptibility of the compass to relaxation (see section 4.2) and adds further importance to the question of how much relaxation can be tolerated.

4.3.2 The 'toy' radical pair

To investigate the effect of molecular motion on the spikes a two-spin model radical pair was designed[4] that would capture the fundamental behaviour of the spikes, whilst still being computationally tractable [61]. This toy radical pair is described below and illustrated in fig. 4.8.

[4] 'Toy' model designed by Hamish Hiscock

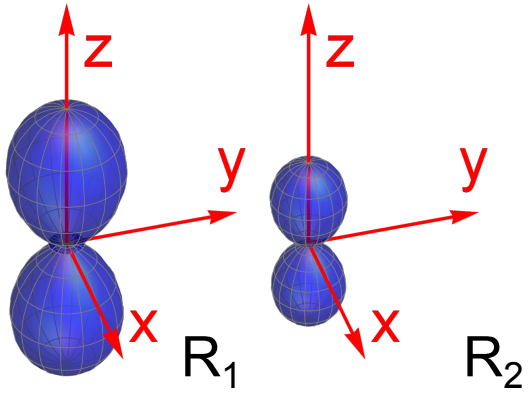


Figure 4.8: Two-spin model radical pair. The blue surfaces represent the strength of the hyperfine interaction as a function of the angles θ and ϕ, as described for figure 4.3.

Radical:	R_1	R_2
Type:	spin-1	spin-1
HFI:	$\begin{bmatrix} -0.0989 & 0 & 0 \\ 0 & -0.0989 & 0 \\ 0 & 0 & 1.7569 \end{bmatrix}$ mT	$\begin{bmatrix} 0 & 0 & 0 \\ 0 & 0 & 0 \\ 0 & 0 & 1.0812 \end{bmatrix}$ mT
	Based on N5 in FAD.	Chosen so that the whole system mimics FAD-Trp.

The general effects of molecular motion were investigated by introducing 10° hops ($\beta = 5°$) of the radical R_1 around the axis $u = (1/\sqrt{2}, 1/\sqrt{2}, 0)$. Figure 4.9 shows the singlet yield profile, as a function of θ, over a range of different hopping rates. In the example shown, the recombination rate constant, k, was set to 10^4 s^{-1} to allow a long enough lifetime (100 μs) for a strong spike to emerge in the singlet yield whilst minimising the potential for relaxation.

The basic relaxation behaviour of this two-spin radical pair is very similar to that displayed by the one spin radical pairs described in section 4.2. Maximum relaxation occurs when the frequency of the hopping is close to the energy scale of the Hamiltonian ($m \approx 10^8$ s^{-1}), with the system relaxing efficiently towards equilibrium (25% singlet, 75% triplet) at all field directions.

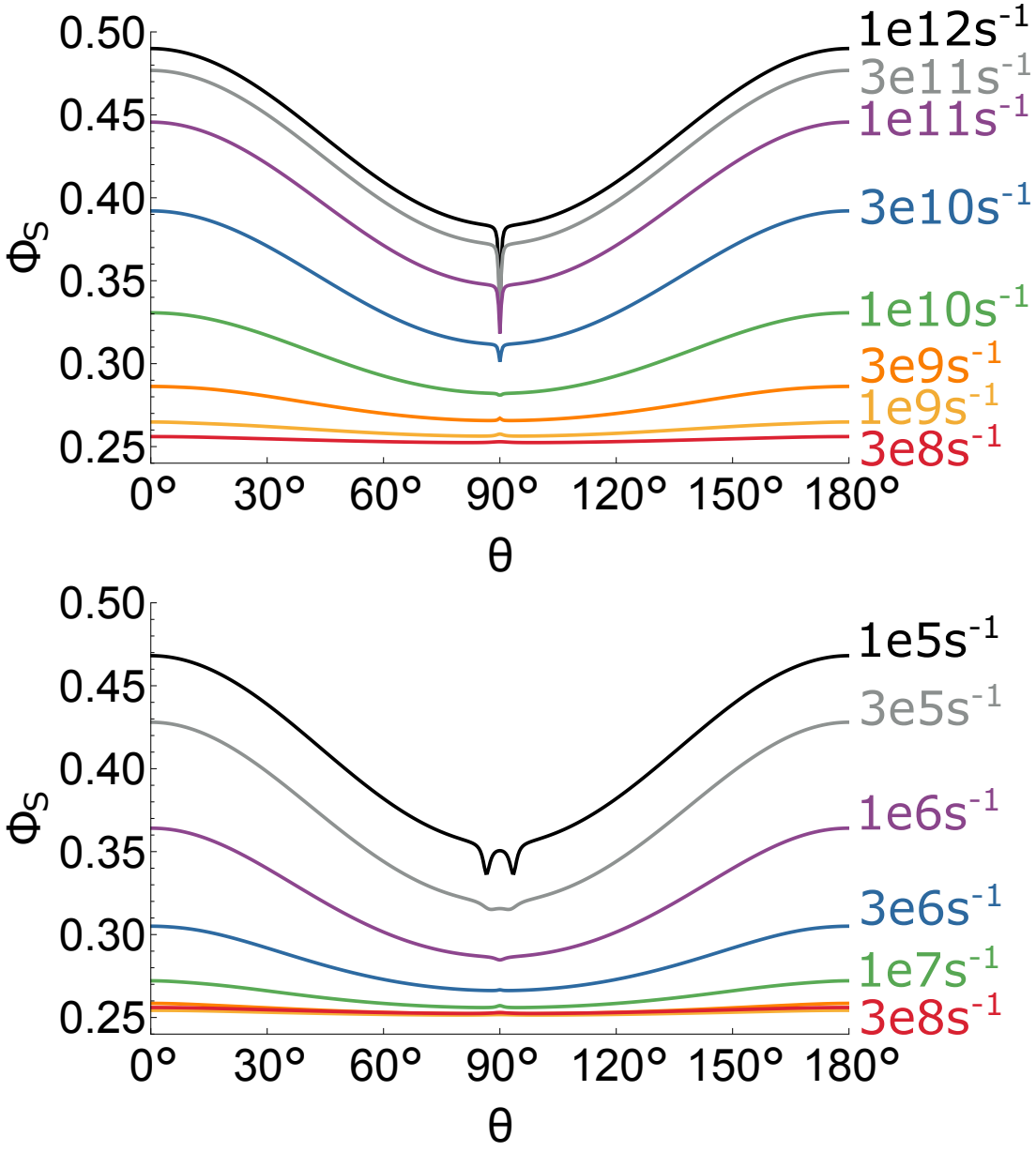


Figure 4.9: Relaxation of the 'toy' radical pair (figure 4.8). R_1 undergoes 10° hops (i.e. $\beta = 5°$) around the axis halfway between the x and y axes, with rate constants, m between 1×10^5 s^{-1} and 1×10^{12} s^{-1} as indicated. The traces for $m = 1 \times 10^8$ s^{-1} and $m = 3 \times 10^7$ s^{-1} in the lower graph lie under that of $m = 3 \times 10^8$ s^{-1}. $k = 10^4$ s^{-1} and $B_0 = 50$ μT.

In the slow motion regime ($m \approx 10^5$ s^{-1}), relaxation is slow but the spike is affected by the static disorder experienced by the system as a result of the 'frozen out' motion. In this simple two-site model, the spike is split into two smaller spikes, corresponding to each of the two sites in the model. However, in reality, a moving radical would sample many more than two orientations and hence very slow rotations are expected to result in spike-broadening rather than spike-splitting. This compromises the precision of the compass.

In the fast motion regime ($m \approx 10^{12}$ s^{-1}), the interactions at the two sites are effectively averaged and the singlet yield profile for the static system was recovered. As the hopping frequency is decreased from $m = 10^{12}$ s^{-1} to $m = 10^9$ s^{-1}, the difference in singlet yield between the base and the tip of the spike is rapidly reduced and the sharp signal becomes less pronounced. However, the width of the spike does not change significantly in this region, meaning that only the sensitivity, and not the directional precision of the avian compass would be affected by relaxation due to 'fast' rotations.

4.3.3 Spike-fitting

To confirm the observation that fast molecular motion has no impact on the width of the spike, functions were fitted to the singlet yield profile to numerically evaluate the width, height and position of the spike under various conditions. The fitting was performed using the *Fit* and *FindFit* functionalities in Mathematica.

As the functional form of the spike was not known, the spike was extracted from the total singlet yield profile by fitting a $\cos^2\theta$ function to the background and subtracting the result from the data (figure 4.10(a,b)). This initial fitting worked very well for fast and slow motion but not for intermediate hopping rates, where the background was flattened out by relaxation. However, this region was not of interest as the spike had already disappeared.

Once extracted, both Gaussian (figure 4.10(c)) and Lorentzian (figure 4.10(d)) curves were

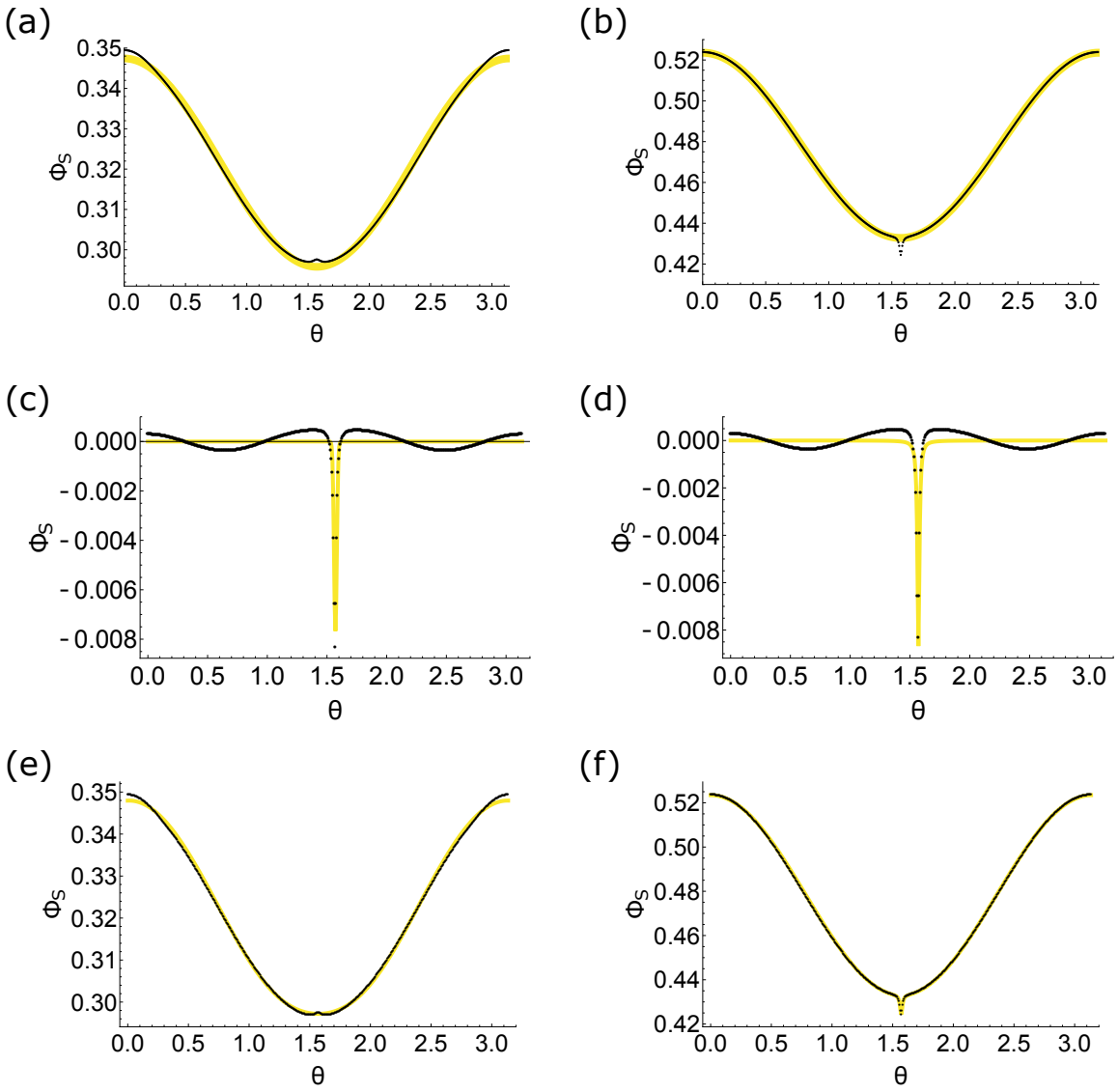


Figure 4.10: Stages of fitting. Singlet yields (shown in black) are calculated for the toy radical pair with a 10 μs recombination lifetime. (a,b) Fitting the broad background to a $\cos^2\theta$ function (yellow) for (a) $m = 10^9$ s^{-1} and (b) $m = 10^{12}$ s^{-1}. (c,d) Fitting the spike (black), with background subtracted, to (c) a Gaussian or (d) a Lorentzian function (yellow) for $m = 10^{12}$ s^{-1}. (e,f) Fitting the full singlet yield profile (black) to equation (4.23) (yellow) for (e) $m = 10^9$ s^{-1} and (f) $m = 10^{12}$ s^{-1}.

fitted to the spike. The Lorentzian function provided the better fit, with the Gaussian function consistently underestimating the full height of the peak.

Assuming a Lorentzian spike, the whole singlet yield profile can be fitted in one go to a function with the form:

$$F(\theta) = c + d\cos^2(\theta) + \frac{-sa^2}{(\theta - b)^2 + a^2}, \tag{4.23}$$

which is the sum of a $\cos^2\theta$ background and a Lorentzian peak, centred at b, with height s and full width at half maximum $2a$. The parameter d gives the height of the background curve, whilst c is the value of the singlet yield at $\theta = 0$. The full fit is shown in figure 4.10(e,f).

Although this function does not perfectly capture the shape of the profile around the base of the spike, it still provides an extremely good fit for the fast motion regime. When the spike disappears around $m = 3 \times 10^9$ s^{-1}, the fitting parameters become harder to interpret as both components of the function are used to create the broad background curve.

Figure 4.11 shows the variation in each of the fitting parameters (a, b, s, c, d) as the hopping rate increases from $m = 10^9$ s^{-1} to $m = 10^{12}$ s^{-1}. The breakdown of the fitting procedure at smaller m values is clear from the abrupt jump in b away from what should be a constant value of $\pi/2$. The value of a, which parameterises the width of the spike (FWHM) is also invariant with hopping rate. This emphasises that the shape of the singlet yield profile cannot be explained purely by a simple two-site chemical exchange models, where the peak width should decrease with faster exchange between the two sites.

Figure 4.12 shows that, in addition, the spike is attenuated faster than the background as the hopping frequency is decreased towards $m = 10^8$ s^{-1}. The heights quoted are the values of s and d, given as a fraction of their value at $m = 10^{12}$ s^{-1}. There are two possible explanations for this. It could be that the spike is simply less robust against spin relaxation than the anisotropy of the background curve. Alternatively, the pattern

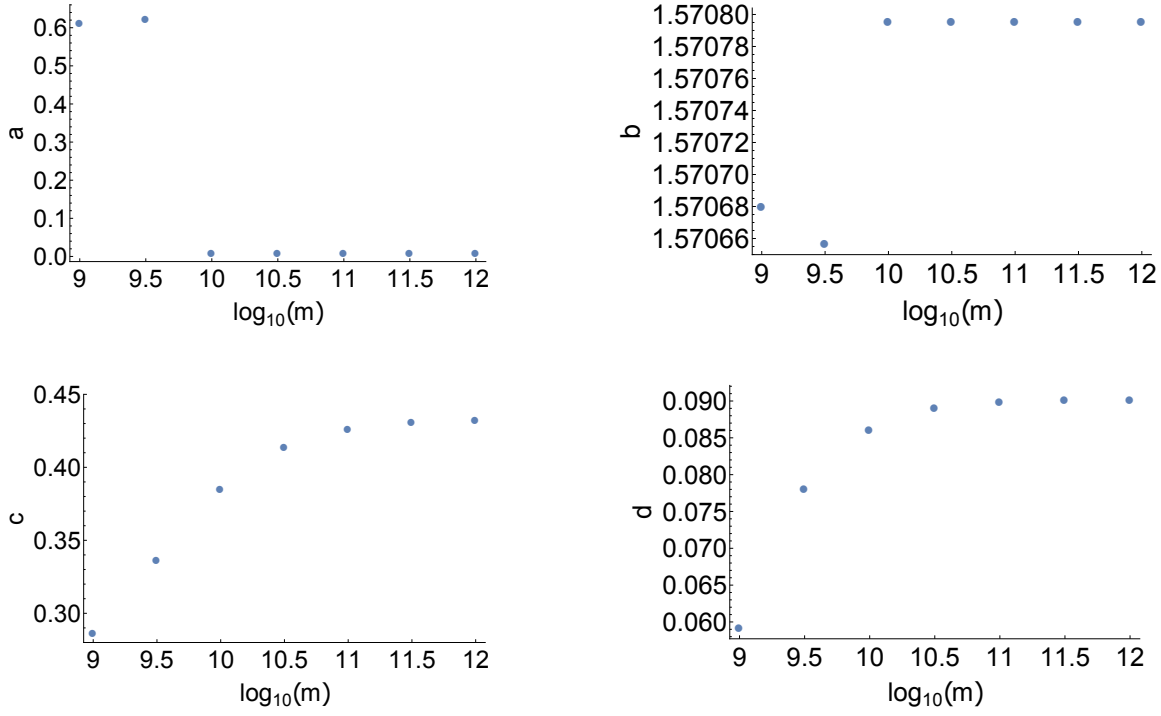


Figure 4.11: Variation of fitting parameters (equation (4.23)) with hopping rate for the toy radical pair with a 10 μs lifetime.

observed in figure 4.12 might reflect the fact that the spike is primarily due to the shape of the hyperfine interactions in the moving radical, whereas the broad background is created by the interactions in the stationary radical and is therefore less susceptible to relaxation.

4.3.4 Optimising hyperfine interactions.

It has previously been shown that, for a one-spin system, the anisotropy of the compass signal is maximized when $T_{zz}/a_{\text{iso}} = 2$, such that the full hyperfine tensor only has one non-zero component, pointing along the z axis. Given this fixed optimum shape, the size of the hyperfine tensor can still be adjusted by increasing the size of all components of the hyperfine tensor in proportion. Increasing the size of the hyperfine tensor increases the amount of anisotropy in the system, which is reflected in an increase in the anisotropy of the singlet yield. However, when molecular motion is introduced into the model, a

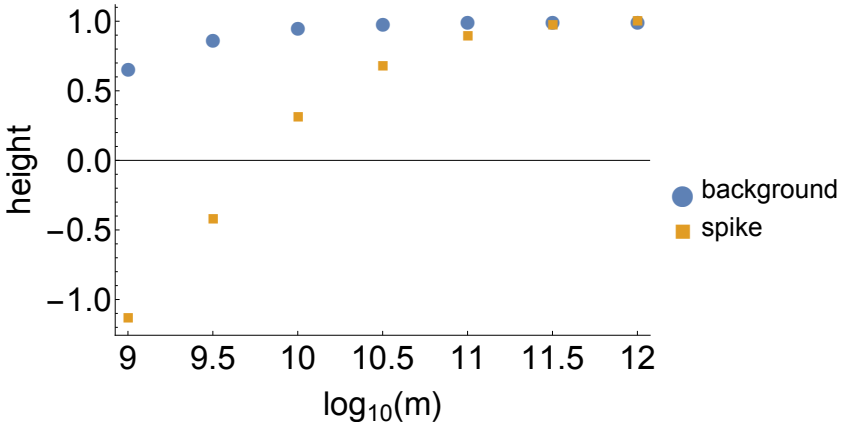


Figure 4.12: Decay of the background anisotropy and the length of the spike for the toy radical pair with a 10 μs lifetime.

Table 4.1: Example systems used to investigate how the size and shape of a hyperfine interaction alters the magnetic signal produced by the radical pair. All components of the hyperfine interactions A_{qq}, the isotropic component a_{iso} and the axiality $\Delta A = 2A_{zz} - (A_{xx} + A_{yy})$ are given in mT.

		$A_{xx} = A_{yy}$	A_{zz}	ΔA	a_{iso}	A_{zz}/A_{xx}
1	Original system	−0.1	1.8	3.8	0.53	−18
2	Double a_{iso}	0.43	2.33	3.8	1.06	5.42
3	Double ΔA	−0.73	3.07	7.6	0.53	−4.21
4	Double A_{zz}	−0.1	3.6	7.4	1.13	−36
5	Double A_{xx}	−0.2	1.8	4.0	0.47	−9
6	Double all components	−0.2	3.6	7.6	1.33	−18
7	Halve all components	−0.05	0.9	1.9	0.27	−18
8	Change sign of A_{xx}	0.1	1.8	3.4	0.67	18

larger hyperfine interaction also increases the rate of relaxation (see equation (4.18)). To maximise the sensitivity of the compass, a balance must be achieved between these two effects.

For the spin systems considered in this section, an additional factor is producing and maintaining a sharp, narrow spike. A small number of preliminary calculations were carried out to determine a set of design principles for optimising the spike. Starting from the 'toy' radical pair introduced in section 4.3.2, the overall size and shape of the hyperfine interaction in R_1 were systematically varied, along with the size of individual components. The set of systems included in the investigation is listed in table 4.1, along with a description of how they relate to the original 'toy' system.

Based on observations of one-spin systems, increasing the isotropic component (case 2) or the anisotropy (case 3) of the hyperfine tensor might be expected to improve the compass. However, figure 4.13 does not show any noticeable increase in the amplitude of the spike or the background curve for case 2 or 3. Rather, the change in the shape of the hyperfine tensor (characterized by the A_{zz}/A_{xx} ratio) results in a broader, less precise spike in both cases.

Cases 4 - 6 illustrate the result of increasing either the A_{zz} or the A_{xx} and A_{yy} components of the tensor by comparable amounts. Figure 4.13 shows that changes to all components alter the shape of the spike, with larger A_{zz} values giving a broader spike and larger A_{xx} a narrower spike. These data suggest that the shape of the spike might be dictated by the ratio A_{zz}/A_{xx}.

This hypothesis can be tested by comparing cases 1, 7 and 8. Although the sizes of the interactions in case 7 are twice as large as those in case 1 and four times the size of those in case 8, the singlet yield profile is identical in all three cases. The shape of the hyperfine interaction, defined by the ratio $A_{zz}/A_{xx/yy}$, is therefore the crucial parameter for optimising the spin system. Comparison with system 9 shows that changing the relative signs of A_{zz} and A_{xx} also has no effect on the compass.

The fitting procedure in section 4.3.3 was used to search for the optimum shape of the hyperfine interaction in R_1. Figure 4.14 shows how the length and width of the spike vary with the size of the components of the hyperfine tensor. The most striking feature is that the values of both parameters increase in the same direction, making it impossible to simultaneously optimise the compass precision and sensitivity. This implies that the 'best' spikes would have the maximum tolerable width (minimum necessary precision), in order to optimise the sensitivity. Birds can detect the axis of the Earth's magnetic field with a precision between 2° and 5° [36, 65, 66]. For a spike with full width $2a \leq 5°$, the principal components of the hyperfine tensor in R_1 need to satisfy $A_{zz}/A_{xx} \geq 6.5$. There is, however, no reason to expect that this inequality would hold for larger spin systems.

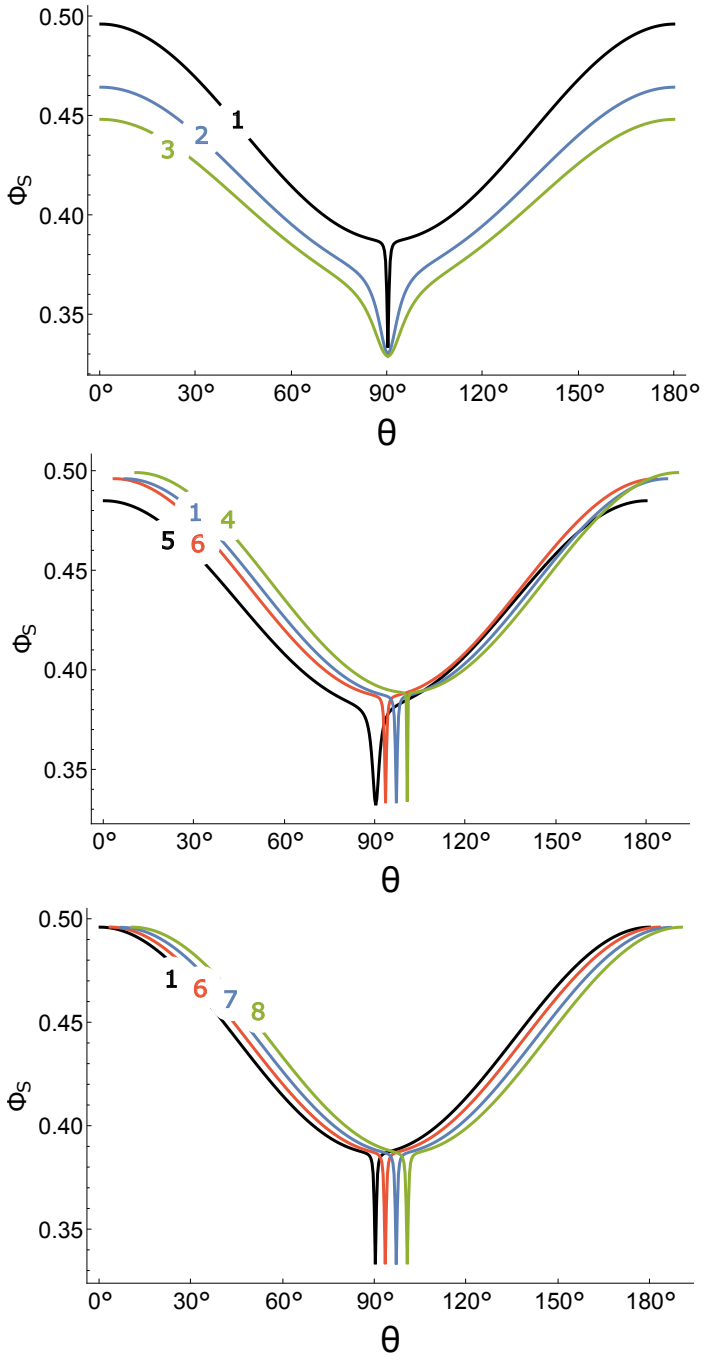


Figure 4.13: Comparing the size and shape of the spike produced by cases 1-8 in table 4.1. $k = 10^4$ s^{-1}; $B_0 = 50$ μT. Some of the traces in the lower panels have been offset horizontally for clarity. In reality, the spike is always centred on $\theta = 90°$.

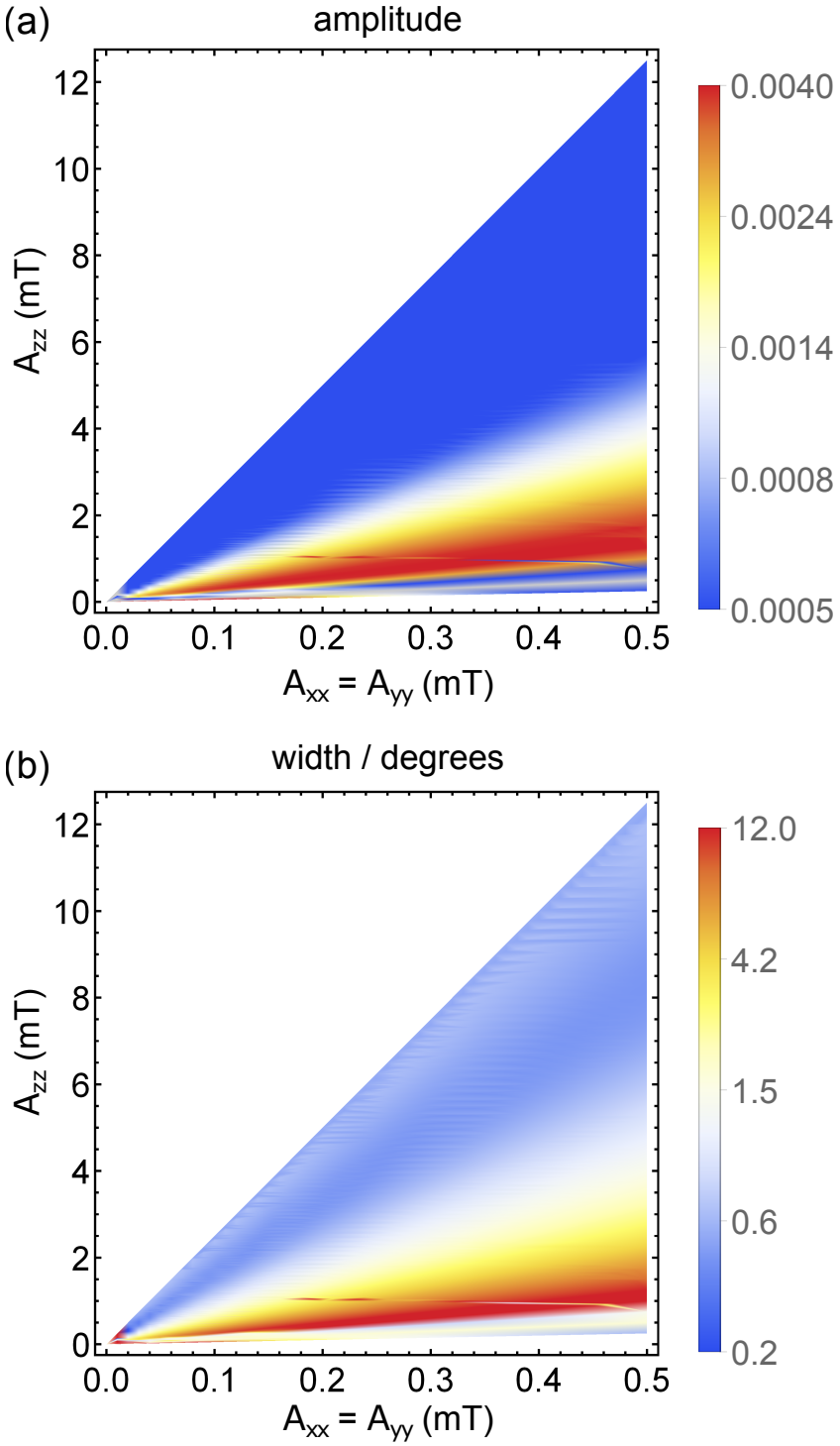


Figure 4.14: Spike amplitude (a) and width (b) as a function of the principal components of the hyperfine tensor in the primary radical. Each radical in the pair contains a single spin-1 nucleus. The primary radical has hyperfine components $[A_{xx}, A_{yy}, A_{zz}]$. The secondary radical has hyperfine components $[0, 0, 1.0812]$ mT. $k = 10^5$ s^{-1}. The external field strength is 50 μT and the field is applied in the yz plane of the primary radical such that $\phi = \pi/2$. Both radicals are static. The solid black lines indicate a spike width of $2a = 5°$. [*Figure published as figure 2 in Ref. [150].*]

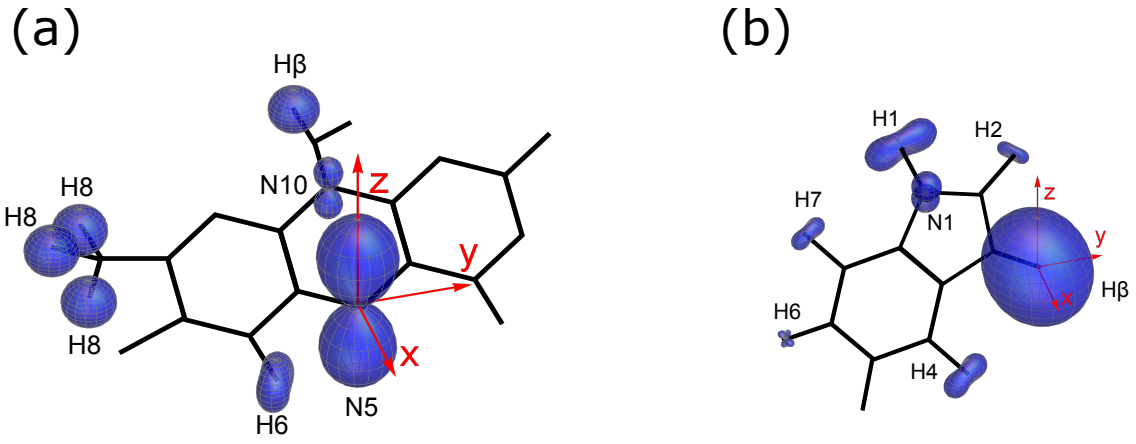


Figure 4.15: Largest 7 hyperfine interactions in (a) $FAD^{\bullet-}$ and (b) $TrpH^{\bullet+}$.

Although the size of the hyperfine interactions appears to play no role in shaping the compass signal in a static radical pair, larger hyperfine interactions do lead to faster relaxation when hopping motion of the radical is included. The ability of molecular motion to redefine the desirable qualities of the hyperfine interactions is explored in section 5.4.1 using a more realistic model of molecular motion.

4.4 Larger spin systems

Calculations were performed on a number of larger model systems to verify that the trends observed in section 4.3 were maintained for more realistic radical pairs. Using the methods described in section 4.1.1 it was possible to model spin systems containing up to eight nuclei.

In section 4.3 it was shown that in the slow motion regime ($m \leq 10^8$ s^{-1}) the compass precision is compromised by the presence of effective static disorder. Consequently, in this section, I only consider motion with $m \geq 10^9$ s^{-1}. Internal motions, which are the focus of this study, are likely to fall within this higher frequency range. For example, at room temperature in aqueous solution, flavin mononucleotide tumbles with a correlation time of around 155 ps [151, 152].

The potential consequences of flavin motion were investigated using a model spin system in which the moving radical R_1 contained the seven largest hyperfine interactions from the $FAD^{\bullet-}$ radical: N5, N10, H6, H8 ($\times 3$) and Hβ (see Appendix A). A pictorial representation of these interactions is given in figure 4.15(a). It was paired with a counter-radical R_2 containing a single spin-1/2 nucleus with the hyperfine interaction of the R_2 radical in the 'toy' system introduced in section 4.3.2. This system will be referred to as the [$FAD^{\bullet-}$ $Y^{\bullet}$] radical pair.

Figure 4.16 shows the effect of 10° hops ($\beta = 5°$) of the $FAD^{\bullet-}$ radical around the y axis. Qualitatively the same relaxation behaviour is observed for this flavin-based system as for the two-spin toy system, with faster relaxation occurring as the hopping rate tends towards $m = 10^8$ s^{-1}. As the system relaxes towards equilibrium, the spike decreases in length but maintains its narrow width.

Also in agreement with the 'toy' model, the spike is initially stronger (longer), when a slower recombination rate ($k = 10^4$ s^{-1} in figure 4.16(a) vs. $k = 10^5$ s^{-1} in figure 4.16(b)) allows more time for it to develop. However, a longer-lived radical pair is also more susceptible to relaxation and for $m \leq 10^{10}$ s^{-1}, a larger spike is visible for the faster recombination rate $k = 10^5$ s^{-1} than the slower recombination rates favoured in a static system.

Furthermore, following the suggestions in section 4.3.4, a longer (albeit wider) spike can be produced with the faster radical recombination rate by doubling the A_{xx} and A_{yy} components of the N5 interaction in the $FAD^{\bullet-}$ radical (figure 4.16(c)). Although, clearly, we cannot change the hyperfine interactions in the natural protein, this is an interesting observation as the small change is likely within the range of error in the DFT calculations used to generate the hyperfine tensors in Appendix A. The implication is that the hyperfine interactions in cryptochrome are potentially more optimal than they appear in the calculations performed here.

The flavin radical, bound in the centre of the protein, is likely to have more restricted

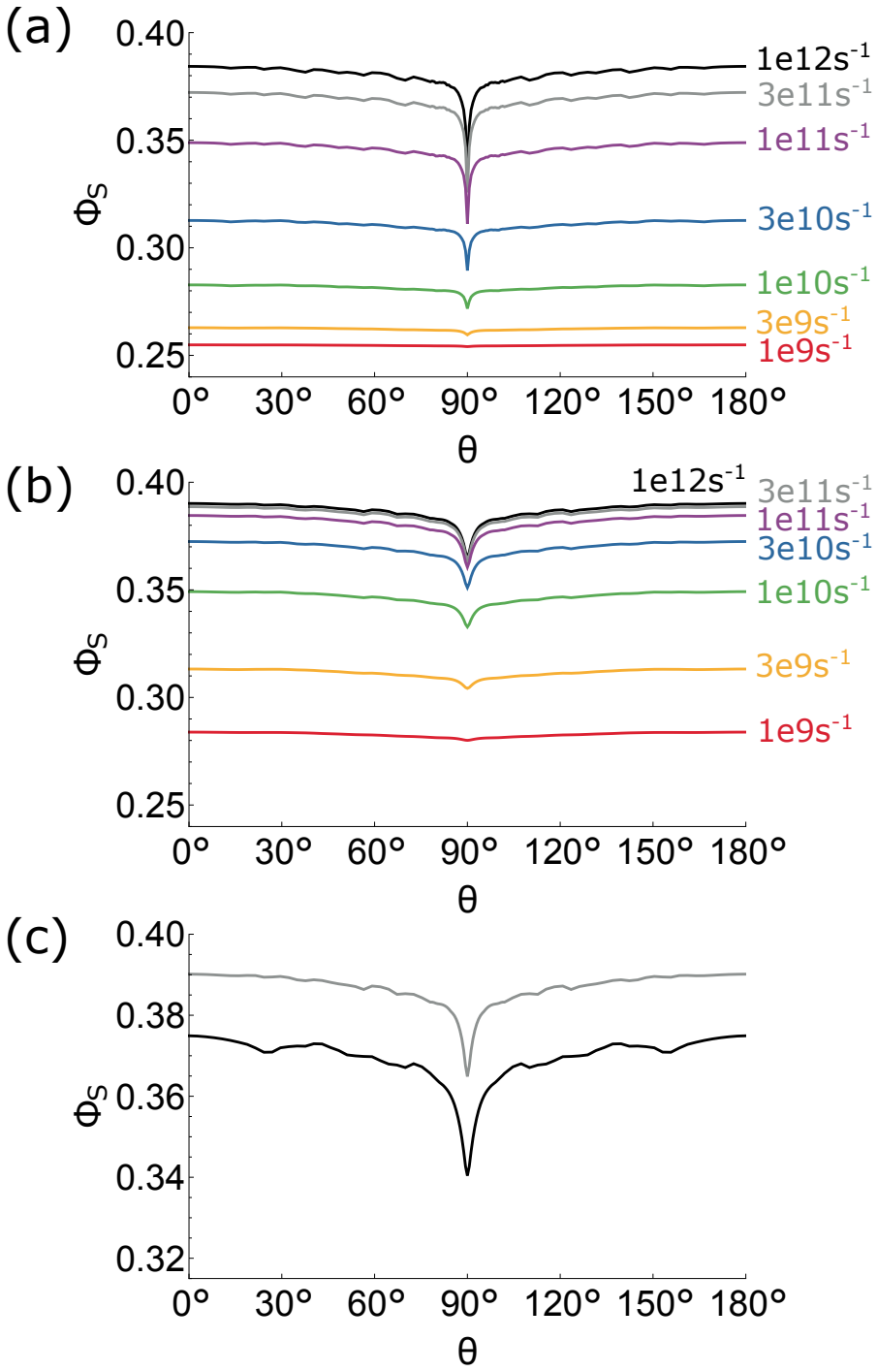


Figure 4.16: Relaxation of the [FAD$^{\bullet-}$ Y$^{\bullet}$] radical pair with (a) a 100 μs recombination lifetime ($k = 10^4$ s^{-1}); (b) a 10 μs recombination lifetime ($k = 10^5$ s^{-1}). The FAD$^{\bullet-}$ undergoes 10° hops ($\beta = 5°$) around the y axis. The hopping rates (m) are indicated on the graph. (c) The effect of doubling the A_{xx} and A_{yy} components in the FAD$^{\bullet-}$ radical. The original radical is shown in grey and the altered version in black. The hopping rate $m = 10^{12}$ s^{-1} and the recombination lifetime is 10 μs.

motion than the tryptophan radical at the surface of the protein. To investigate the effect of tryptophan motion an [$X^\bullet$ $TrpH^{\bullet+}$] model was used. The $X^\bullet$ radical (R_1) was made up of a single spin-1 nucleus with hyperfine components $[A_{xx}, A_{yy}, A_{zz}] = [-0.1002, -0.0868, 1.7569]$ mT (i.e. N5 from $FAD^{\bullet-}$), whilst the R_2 radical contained the seven largest hyperfine interactions from the $TrpH^{\bullet+}$ radical (Appendix A and figure 4.15(b)).

The effect of 10° hopping of $TrpH^{\bullet+}$ is illustrated in figure 4.17. For comparison, the result of 10° $X^\bullet$ hopping is included on the same graph. Although motion of $TrpH^{\bullet+}$ causes the anisotropy of the broad background to disappear more quickly, it also attenuates the spike noticeably slower. Furthermore, relaxation is slower overall when $TrpH^{\bullet+}$ is chosen as the moving radical.

For flavin-based radical pairs, the curved shape of the broad background is thought to be largely due to the properties of the counter-radical, whilst the spike is primarily a product of the hyperfine interactions in the flavin radical. It therefore appears that the motion of each radical most strongly relaxes the part of the singlet yield profile that it is responsible for producing. This observation is discussed further in chapter 5.

4.5 Conclusions

Using a two-site hopping model, analogous to two-site chemical exchange, the work in this chapter has produced some preliminary guidelines that will inform further investigations in later chapters.

Calculations on small model systems have shown that relaxation induced by internal rotations of the magnetoreceptor is fastest when the motion induces fluctuations in the local magnetic field on a 100 ns - 1 ns time-scale. The rate of relaxation increases when larger amplitude motions are permitted and the moving radical contains more anisotropic hyperfine interactions. Both observations are easily explained by the proportionality

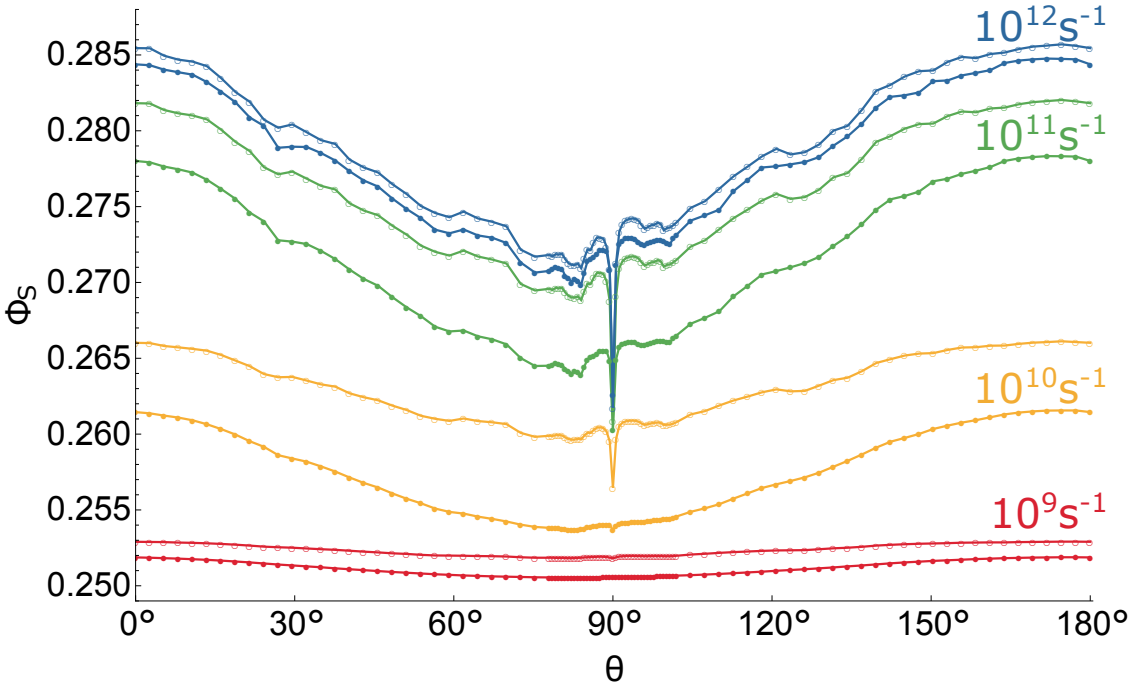


Figure 4.17: Effect of R_1 vs. R_2 hopping. R_1 contains the N5 nucleus from the $FAD^{\bullet-}$ radical. R_2 contains the 7 largest hyperfine interactions from the $TrpH^{\bullet+}$ radical. Filled circles correspond to hopping of R_1 and empty circles to hopping of R_2. The moving radical performs 10° hops around the y axis. The hopping rates (m) are indicated on the graph. The recombination lifetime is 100 μs ($k = 10^4$ s^{-1}).

of relaxation rate to the squared amplitude of the fluctuations driving the relaxation (equation 4.18)).

For particularly large motions, the two-site model produces some anomalous results as a consequence of the highly-limited sampling of molecular orientations. The more sophisticated model in chapter 5 will provide a more realistic view of the effect of less restricted motion.

On the basis of equation (4.18), relaxation should be faster in the presence of a weaker external field where fluctuations in the hyperfine interactions are correspondingly larger in relation to the Zeeman interaction. This is indeed what is observed but the effect is close to negligible over the range of natural field strengths. Therefore, for the rest of this thesis, the external field strength will always be taken as 50 μT - a value in the middle of

the natural range.

To minimize the detrimental effects of relaxation, motion of the radicals should ideally be highly restricted and either very fast or very slow compared to the time-scale of the coherent evolution of the spin system. Any hyperfine interactions within the radicals should preferably have only small components perpendicular to the rotation axis of the radical to minimize the size of fluctuations that might induce relaxation. However, this is not always compatible with optimising the shape of the hyperfine interactions to maximise singlet yield anisotropy. This is a prime example of why motion must be considered when deriving criteria for an optimised radical pair compass. A balance between the two effects must be found to maximize the compass sensitivity. This is explored in more detail in chapter 5.

Similarly, it has been acknowledged in previous work that a balance must be struck between slow radical recombination to allow time for a strong anisotropic signal to emerge and fast recombination to minimize the time over which relaxation can take effect. These effects are clearly illustrated by the one-spin models in this chapter. The optimum recombination lifetime was originally estimated to be on the order of 1 μs. However, prolonging the lifetime of more complex radical pairs could be the key to unlocking detailed features ('spikes') in the singlet yield that offer superior directional information. In this chapter a quintessential 'toy' model has been introduced that captures the behaviour of the spikes whilst allowing for easy computation. A fitting procedure was also developed to allow for quantitative investigation of the spikes. Characterisation of the toy model shows that the dimensions of the spikes depend on the shape rather than the size of the hyperfine interactions in the radicals, although size still plays a key role in determining their relaxation properties.

In particular, increasing the ratio $A_{zz}/A_{xx/yy}$ increases the length and width of the spikes, allowing them to be observed even with shorter radical pair lifetimes. For this reason, in all remaining chapters 'the toy model' will refer to a more optimal version of the model introduced in this chapter, with the two radicals described by

Radical:	R_1	R_2
Type:	spin-1	spin-1
HFI:	$\begin{bmatrix} -0.2 & 0 & 0 \\ 0 & -0.2 & 0 \\ 0 & 0 & 1.7569 \end{bmatrix}$ mT	$\begin{bmatrix} 0 & 0 & 0 \\ 0 & 0 & 0 \\ 0 & 0 & 1.0812 \end{bmatrix}$ mT

The effect of motion on the toy radical pair, within the two-site hopping model, showed similar trends to one-spin model systems. However, two striking features emerged. First, in the fast motion regime, the spike width was independent of the hopping rate, although its length was rapidly attenuated as a result of fast relaxation of the background as the hopping rate was decreased towards $m = 10^9$ s^{-1}. Second, slow motion had an equivalent effect to introducing static disorder and resulted in broadening or splitting of the spike, compromising compass precision. As a consequence, chapter 5 will focus exclusively on the fast motion regime, which is less detrimental to compass precision and likely more relevant to the time-scales of internal rotations.

Finally, in this chapter I looked at relaxation in a model of the flavin-tryptophan radical pair. Assuming that spikes are an essential compass feature, the optimum radical pair lifetime appears to be on the order of 10 μs, taking into account molecular motion on a realistic time-scale. These preliminary calculations furthermore suggested that motion of the flavin radical is more detrimental to the preservation of the spike, which it is primarily responsible for producing, than the tryptophan radical. Motion of tryptophan may, therefore, have less effect on the compass. This idea is explored in more detail in chapter 5.

Chapter 5

Realistic modelling of relaxation

The calculations in the previous chapter offer some useful insights about what parameters are worth investigating and the general trends that might be expected. However, the two-site hopping model is clearly far from realistic. In this chapter, I will present a more realistic model of the motion in which the moving radical is assumed to undergo isotropic rotational diffusion within the confines of an ordering potential. Analytical spectral densities describing the motion are derived and used to construct a Redfield relaxation superoperator. This method does not simulate the exact behaviour of CRY but offers important insights about the type of motion that can be tolerated by the compass. Additionally, it can be used to explore the parameter space and identify possible opportunities for optimisation.

5.1 Introducing realistic rotations into the Hamiltonian

As in chapter 4, I consider a spin Hamiltonian containing only a Zeeman interaction and a set of hyperfine interactions. In the rotational basis (see section 3.1.4), this is

$$\hat{H} = \gamma_{\mathrm{e}}\mathbf{B_0}\cdot(\hat{\mathbf{S}}^{(1)}+\hat{\mathbf{S}}^{(2)}) + \sum_i \left(a_i \hat{\mathbf{S}}^{(1/2)}\cdot\hat{\mathbf{I}}^{(i)} + \hat{R}_{\mathrm{mol}}\hat{R}^{(i)}_{\mathrm{pos}} \sum_{m=-2}^{2} a^{(2)}_{m,i}\hat{T}^{(2)}_{m,i} \right), \tag{5.1}$$

where $\hat{\mathbf{S}}^{(1/2)}$ are the spin operators of the two electron spins and $\hat{\mathbf{I}}^{(i)}$ are the operators for the nuclear spins. The index i labels the nuclei, γ_{e} is the electron gyromagnetic ratio and $\mathbf{B_0} = [0, 0, 50]$ μT is the external magnetic field. The first two terms of equation (5.1) are isotropic and therefore invariant under rotation of the molecule. The final term is affected by molecular rotation and will be referred to in the following section as the anisotropic Hamiltonian $\hat{H}_{\mathrm{aniso}}$.

Two rotations, $\hat{R}_{\mathrm{mol}}$ and $\hat{R}^{(i)}_{\mathrm{pos}}$, are needed to describe the anisotropic hyperfine interactions in the lab frame. The first rotation $\hat{R}^{(}i)_{\mathrm{pos}}$ is applied to each hyperfine interaction individually and serves to position them in the molecular frame. The second rotation $\hat{R}_{\mathrm{mol}}$ represents the rotational diffusion of the moving radical and is applied to all the nuclei within that radical simultaneously. The rotations are effected using the Wigner rotation matrices $\mathfrak{D}^{(L)}_{mn}(\omega)$ (see section 3.1.4):

$$\hat{H}_{\mathrm{aniso}} = \sum_i \hat{R}_{\mathrm{mol}}\hat{R}^{(i)}_{\mathrm{pos}} \left(\sum_{n=-2}^{2} a^{(2)}_{n,i}\hat{T}^{(2)}_{n,i} \right) \tag{5.2}$$

$$= \sum_i \hat{R}_{\mathrm{mol}} \left(\sum_{m=-2}^{2} \hat{T}^{(2)}_{m,i}\phi_{m,i} \right) \qquad \text{all nuclei positioned in molecule} \tag{5.3}$$

$$= \sum_{i\subset\mathrm{static}} \left(\sum_{m=-2}^{2} \hat{T}^{(2)}_{m,i}\phi_{m,i} \right) + \sum_{j\subset\mathrm{moving}} \left(\sum_{m'=-2}^{2}\sum_{m=-2}^{2} \hat{T}^{(2)}_{m',j}\phi_{m,j}\mathfrak{D}^{(2)}_{m'm}(\omega_{\mathrm{mol}}) \right), \tag{5.4}$$

where

$$\phi_{m,i} = \sum_{n=-2,0,2} a^{(2)}_{n,i} \mathfrak{D}^{(2)}_{mn}(\omega_{\text{pos}}) \tag{5.5}$$

and $\hat{T}^{(2)}_{m',j}$ are the second-rank irreducible spherical tensor operators introduced in section 3.1.3.

For Redfield theory, the full Hamiltonian must be divided into time-independent ($\hat{H}_0$) and time-dependent ($\hat{H}_1(t)$) parts. Note that the average orientation of the moving radical is not time-dependent so must be subtracted from ($\hat{H}_1(t)$) and included in ($\hat{H}_0$) [153]. The two parts of the Hamiltonian are therefore

$$\begin{aligned}\hat{H}_0 = {} & \gamma_{\text{e}} \mathbf{B_0} \cdot (\hat{\mathbf{S}}^{(1)} + \hat{\mathbf{S}}^{(2)}) + \sum_k a_k \hat{\mathbf{S}}^{(1/2)} \cdot \hat{\mathbf{I}}^{(k)} \\ & + \sum_{i \subset \text{static}} \left(\sum_{m=-2}^{2} \hat{T}^{(2)}_{m,i} \phi_{m,i} \right) + \sum_{j \subset \text{moving}} \left(\sum_{m'=-2}^{2} \sum_{m=-2}^{2} \hat{T}^{(2)}_{m',j} \phi_{m,j} \left\langle \mathfrak{D}^{(2)}_{m'm}(t) \right\rangle_{\text{av}} \right); \end{aligned} \tag{5.6}$$

and

$$\hat{H}_1(t) = \sum_{j \subset \text{moving}} \left(\sum_{m'=-2}^{2} \sum_{m=-2}^{2} \hat{T}^{(2)}_{m',j} \phi_{m,j} \left[\mathfrak{D}^{(2)}_{m'm}(t) - \left\langle \mathfrak{D}^{(2)}_{m'm}(t) \right\rangle_{\text{av}} \right] \right), \tag{5.7}$$

where $\mathfrak{D}^{(2)}_{m'm}(t) = \mathfrak{D}^{(2)}_{m'm}(\omega_{\text{mol}}(t))$ describes the rotation needed for the moving radical to have an orientation described by the Euler angles ω_{mol} at time t. It will be shown in section 5.2 that $\left\langle \mathfrak{D}^{(2)}_{m'm}(t) \right\rangle_{\text{av}}$ is only non-zero when $m' = 0$ and hence the static Hamiltonian becomes

$$\begin{aligned}\hat{H}_0 = {} & \gamma_{\text{e}} \mathbf{B_0} \cdot (\hat{\mathbf{S}}^{(1)} + \hat{\mathbf{S}}^{(2)}) + \sum_k a_k \hat{\mathbf{S}}^{(1/2)} \cdot \hat{\mathbf{I}}^{(k)} \\ & + \sum_{i \subset \text{static}} \left(\sum_{m=-2}^{2} \hat{T}^{(2)}_{m,i} \phi_{m,i} \right) + \sum_{j \subset \text{moving}} \left(\sum_{m=-2}^{2} \hat{T}^{(2)}_{0,j} \phi_{m,j} \left\langle \mathfrak{D}^{(2)}_{0m}(t) \right\rangle_{\text{av}} \right). \end{aligned} \tag{5.8}$$

5.1.1 Adjusted Redfield superoperator

The Redfield master equation derived in section 3.2.2 needs adjusting to accommodate the form of the rotational basis Hamiltonian in equations (5.6) and (5.7). Picking up the

derivation from equation (3.75) (with $\hbar = 1$),

$$\frac{d\rho^I(t)}{dt} = -\int_0^t \left[\left[\rho^I(t-\tau), \hat{H}_1^I(t-\tau)\right], \hat{H}_1^I(t)\right] d\tau,$$

the Markovian approximation is made and the equation is transformed back into the Schrödinger picture to give

$$\frac{d\rho(t)}{dt} = -i\left[\hat{H}_0, \rho(t)\right] - \int_0^\infty \left[\left[\rho(t), e^{i\hat{H}_0\tau}\hat{H}_1(t+\tau)e^{-i\hat{H}_0\tau}\right], \hat{H}_1(t)\right] d\tau. \tag{5.9}$$

Substituting in the rotational basis Hamiltonian (equation (5.7)), equation (5.9) is written

$$\begin{aligned}\frac{d\rho(t)}{dt} &= -i\left[\hat{H}_0, \rho(t)\right] \\ &\quad - \int_0^\infty \Bigg[\Bigg[\rho(t), e^{i\hat{H}_0\tau} \sum_{j\subset\text{mov.}} \sum_{nn'} \phi^*_{n',j} \hat{T}^{(2)\dagger}_{n,j} \left(\mathfrak{D}^{(2)*}_{nn'}(t+\tau) - \langle \mathfrak{D}^{(2)*}_{nn'}(t+\tau)\rangle_{\text{av}}\right) e^{-i\hat{H}_0\tau}\Bigg], \\ &\qquad \sum_{i\subset\text{mov.}} \sum_{mm'} \phi_{m',i} \hat{T}^{(2)}_{m,i} \left(\mathfrak{D}^{(2)}_{mm'}(t) - \langle \mathfrak{D}^{(2)}_{mm'}(t)\rangle_{\text{av}}\right) \Bigg] d\tau; \end{aligned} \tag{5.10}$$

$$\begin{aligned}\frac{d\rho(t)}{dt} &= -i\left[\hat{H}_0, \rho(t)\right] \\ &\quad - \sum_{ij\subset\text{mov.}} \sum_{mm'nn'} \int_0^\infty \phi_{m',i}\phi^*_{n',j} g_{mm'nn'}(\tau) \left[\left[\rho(t), e^{i\hat{H}_0\tau}\hat{T}^{(2)\dagger}_{n,j} e^{-i\hat{H}_0\tau}\right], \hat{T}^{(2)}_{m,i}\right] d\tau. \end{aligned} \tag{5.11}$$

Equation (5.11) is now in the form used by Kuprov *et al.* (2007) [154], with the correlation function, $g_{mm'nn'}(\tau)$ defined by

$$g_{nmn'm'}(\tau) = \left\langle \left[\mathfrak{D}^{(2)}_{mm'}(t) - \langle \mathfrak{D}^{(2)}_{mm'}(t)\rangle_{\text{av}}\right] \left[\mathfrak{D}^{(2)*}_{nn'}(t+\tau) - \langle \mathfrak{D}^{(2)*}_{nn'}(t+\tau)\rangle_{\text{av}}\right] \right\rangle. \tag{5.12}$$

Expanding the double commutator in the integral gives

$$
\begin{aligned}
-\sum_{ij\subset\text{mov.}}\sum_{mm'nn'}\int_0^\infty \phi_{m',i}\phi^*_{n',j}g_{mm'nn'}(\tau)\left[\left[\rho(t),\ \ e^{i\hat{H}_0\tau}\hat{T}^{(2)\dagger}_{n,j}e^{-i\hat{H}_0\tau}\right],\hat{T}^{(2)}_{m,i}\right]d\tau \\
=-\sum_{ij\subset\text{mov.}}\sum_{mm'nn'}\int_0^\infty \phi_{m',i}\phi^*_{n',j}g_{mm'nn'}(\tau)\Big(\hat{T}^{(2)}_{m,i}e^{i\hat{H}_0\tau}\hat{T}^{(2)\dagger}_{n,j}e^{-i\hat{H}_0\tau}\rho(t) \\
-\hat{T}^{(2)}_{m,i}\rho(t)e^{i\hat{H}_0\tau}\hat{T}^{(2)\dagger}_{n,j}e^{-i\hat{H}_0\tau} \\
-e^{i\hat{H}_0\tau}\hat{T}^{(2)\dagger}_{n,j}e^{-i\hat{H}_0\tau}\rho(t)\hat{T}^{(2)}_{m,i} \\
+\rho(t)e^{i\hat{H}_0\tau}\hat{T}^{(2)\dagger}_{n,j}e^{-i\hat{H}_0\tau}\hat{T}^{(2)}_{m,i}\Big)d\tau \qquad (5.13)
\end{aligned}
$$

Following the steps of the derivation in section 3.2.2, the matrix elements of each individual term are

$$\langle\alpha|(1)|\alpha'\rangle = -\sum_{ij\subset\text{mov.}}\sum_{nm}\sum_{\beta\beta'}J^{ij}_{nm}(\omega_{\beta\beta'})\langle\alpha|\hat{T}^{(2)}_{m,i}|\beta\rangle\langle\beta|\hat{T}^{(2)\dagger}_{n,j}|\beta'\rangle\langle\beta'|\rho(t)|\alpha'\rangle\,, \qquad (5.14)$$

$$\langle\alpha|(2)|\alpha'\rangle = \sum_{ij\subset\text{mov.}}\sum_{nm}\sum_{\beta\beta'}J^{ij}_{nm}(\omega_{\beta'\alpha'})\langle\alpha|\hat{T}^{(2)}_{m,i}|\beta\rangle\langle\beta|\rho(t)|\beta'\rangle\langle\beta'|\hat{T}^{(2)\dagger}_{n,j}|\alpha'\rangle\,, \qquad (5.15)$$

$$\langle\alpha|(3)|\alpha'\rangle = \sum_{ij\subset\text{mov.}}\sum_{nm}\sum_{\beta\beta'}J^{ij}_{nm}(\omega_{\alpha\beta})\langle\alpha|\hat{T}^{(2)\dagger}_{n,j}|\beta\rangle\langle\beta|\rho(t)|\beta'\rangle\langle\beta'|\hat{T}^{(2)}_{m,i}|\alpha'\rangle\,, \qquad (5.16)$$

$$\langle\alpha|(4)|\alpha'\rangle = -\sum_{ij\subset\text{mov.}}\sum_{nm}\sum_{\beta\beta'}J^{ij}_{nm}(\omega_{\beta\beta'})\langle\alpha|\rho(t)|\beta\rangle\langle\beta|\hat{T}^{(2)\dagger}_{n,j}|\beta'\rangle\langle\beta'|\hat{T}^{(2)}_{m,i}|\alpha'\rangle\,, \qquad (5.17)$$

where [135]

$$J^{ij}_{nm}(\omega_{\beta\beta'}) = \sum_{n'm'}\int_0^\infty \phi_{m',i}\phi^*_{n',j}g_{mm'nn'}(\tau)e^{i\omega_{\beta\beta'}\tau}d\tau. \qquad (5.18)$$

Using the relabelling process in section 3.2.2 to factorise out $\rho_{\beta\beta'}$, the final expression for

the relaxation matrix may be written

$$R_{\alpha\alpha'\beta\beta'} = -\sum_{ij\subset\text{mov.}}\sum_{nm}\Bigg[\sum_{\gamma} J^{ij}_{nm}(\omega_{\gamma\beta})\hat{T}^{(2),\alpha\gamma}_{m,i}\hat{T}^{(2)\dagger,\gamma\beta}_{n,j}\delta_{\alpha'\beta'} - J^{ij}_{nm}(\omega_{\beta'\alpha'})\hat{T}^{(2),\alpha\beta}_{m,i}\hat{T}^{(2)\dagger,\beta'\alpha'}_{n,j} - J^{ij}_{nm}(\omega_{\alpha\beta})\hat{T}^{(2)\dagger,\alpha\beta}_{n,j}\hat{T}^{(2),\beta'\alpha'}_{m,i} + \sum_{\gamma} J^{ij}_{nm}(\omega_{\beta'\gamma})\hat{T}^{(2)\dagger,\beta'\gamma}_{n,j}\hat{T}^{(2),\gamma\alpha'}_{m,i}\delta_{\alpha\beta}\Bigg]. \tag{5.19}$$

To aid computation, the secular approximation was used to identify elements of $R_{\alpha\alpha'\beta\beta'}$ that could be set to zero (see section 3.2.2). By comparison with the exact solution, it was found that only terms with $|\omega_{\alpha\alpha'} - \omega_{\beta\beta'}| < 10^6$ Hz needed to be kept for an accurate calculation of the singlet yield.

5.2 Analytical spectral densities for diffusion in a uniaxial potential

Most of the relaxation matrix in equation (5.19) is made up of standard irreducible spherical tensor operators (see section 3.1.3). All information about the motion of the radicals is incorporated via the spectral densities $J^{ij}_{nm}(\omega)$, which, in turn, are derived from correlation functions that characterise the motion. The necessary correlation functions were calculated using the method developed by Tarroni and Zannoni (1991) to describe the rotational diffusion of asymmetric molecules in a uniaxial liquid crystal phase [128].

The authors of [128] treat molecular motion as a stochastic, Markovian process so that

the correlation functions can be written in terms of probabilities as

$$\begin{aligned} g^{LL'}_{mm'nn'}(\tau) &= \left\langle \left[\mathfrak{D}^{L}_{mm'}(\omega_0) - \langle \mathfrak{D}^{L}_{mm'}(\omega_0)\rangle_{\mathrm{av}}\right]\left[\mathfrak{D}^{L'*}_{nn'}(\omega) - \langle \mathfrak{D}^{L'*}_{nn'}(\omega)\rangle_{\mathrm{av}}\right]\right\rangle \\ &= \int\int d\omega_0 d\omega P(\omega_0)\left[\mathfrak{D}^{L}_{mm'}(\omega_0) - \langle \mathfrak{D}^{L}_{mm'}(\omega_0)\rangle_{\mathrm{av}}\right] \\ &\qquad \times P(\omega_0|\omega t)\left[\mathfrak{D}^{L'*}_{nn'}(\omega) - \langle \mathfrak{D}^{L'*}_{nn'}(\omega)\rangle_{\mathrm{av}}\right] \qquad (5.20) \\ &= \int\int d\omega_0 d\omega P(\omega_0)P(\omega_0|\omega t)\Big[\mathfrak{D}^{L}_{mm'}(\omega_0)\mathfrak{D}^{L'*}_{nn'}(\omega) - \mathfrak{D}^{L}_{mm'}(\omega_0)\,\langle \mathfrak{D}'^{L*}_{nn'}(\omega)\rangle_{\mathrm{av}} \\ &\qquad - \mathfrak{D}^{L'*}_{nn'}(\omega)\,\langle \mathfrak{D}^{L}_{mm'}(\omega_0)\rangle_{\mathrm{av}} + \langle \mathfrak{D}^{L'*}_{nn'}(\omega)\rangle_{\mathrm{av}}\,\langle \mathfrak{D}^{L}_{mm'}(\omega_0)\rangle_{\mathrm{av}}\Big], \qquad (5.21) \end{aligned}$$

where $P(\omega)$ is the equilibrium probability of finding the molecule at an orientation ω. It depends on the ordering potential $U(\omega)$ experienced by the molecule via a Boltzmann relation;

$$P(\omega) = \frac{\exp[-U(\omega)/k_BT]}{\int d\omega \exp[-U(\omega)/k_BT]}. \qquad (5.22)$$

$P(\omega_0)$ represents the probability of the molecule having the initial orientation ω_0. The integral over ω_0 gives a weighted average of the correlation function over all possible initial orientations. This means that, rather than starting from a single orientation and then spreading out, the radicals pairs in this model start from an equilibrium distribution of orientations.

Similarly, $P(\omega_0|\omega t)$ is the conditional probability of the molecule having the orientation ω at time t, given that it had orientation ω_0 at time $t = 0$.

Given that, by definition,

$$\int d\omega P(\omega_0|\omega t) = 1 \qquad (5.23)$$

and

$$\int d\omega_0 P(\omega_0)\mathfrak{D}^{L}_{mm'}(\omega_0) = \langle \mathfrak{D}^{L}_{mm'}(\omega_0)\rangle_{\mathrm{av}}\,, \qquad (5.24)$$

the correlation function can be simplified to;

$$g^{LL'}_{mm'nn'}(\tau) = \boxed{\int\int P(\omega_0)P(\omega_0|\omega t)\mathfrak{D}^{L}_{mm'}(\omega_0)\mathfrak{D}^{L'*}_{nn'}(\omega)d\omega_0 d\omega} - \langle\mathfrak{D}^{L}_{mm'}(\omega_0)\rangle_{\mathrm{av}}\langle\mathfrak{D}^{L'*}_{nn'}(\omega)\rangle_{\mathrm{av}}\,. \tag{5.25}$$

The boxed section of equation (5.25) is equation (3) of ref. [128].

The time-dependence of the correlation function now depends entirely on the way that the conditional probability evolves over time. This can be described by the differential equation ([155], cited in [128])

$$\frac{\partial P(\omega_0|\omega t)}{\partial t} = -\mathbf{LD}\left[\mathbf{L} + \mathbf{L}\frac{U(\omega)}{k_{\mathrm{B}}T}\right]P(\omega_0|\omega t), \tag{5.26}$$

where $\mathbf{L} = (L_x, L_y, L_z)$ is a dimensionless angular momentum operator and D is a diagonal diffusion tensor, whose elements give the rate of diffusion around each of the x-, y- and z-axes. To give a more intuitive picture of the motion, $\mathbf{D}$ is rewritten as

$$\mathbf{D} = \zeta\begin{pmatrix} 1+\epsilon & 0 & 0 \\ 0 & 1-\epsilon & 0 \\ 0 & 0 & \eta \end{pmatrix}, \tag{5.27}$$

where $\zeta \equiv (D_x + D_y)/2$ is the rate of 'tumbling' of the molecular z-axis, $\eta \equiv (2D_z)/(D_x + D_y)$ is the ratio between 'spinning' around the z-axis and tumbling of the z-axis and $\epsilon \equiv (D_x - D_y)/(D_x + D_y)$ is an asymmetry parameter with a value between -1 and $+1$.

Before solving equation (5.26), the authors of [128] first perform a symmetrizing transformation to ensure that the rotational diffusion operator is self-adjoint. The symmetrized equation is

$$\frac{1}{\zeta}\frac{\partial\tilde{P}(\omega_0|\omega t)}{\partial t} = \tilde{\Gamma}\tilde{P}(\omega_0|\omega t), \tag{5.28}$$

where $\tilde{P}(\omega_0|\omega t) = P^{-\frac{1}{2}}(\omega)P(\omega_0|\omega t)P^{\frac{1}{2}}(\omega_0)$ is the symmetrized conditional probability and

$$\tilde{\Gamma} = P^{-\frac{1}{2}}(\omega)\left[-\mathbf{L}\frac{\mathbf{D}}{\zeta}\left[\mathbf{L}+\mathbf{L}\frac{U(\omega)}{k_{\mathrm{B}}T}\right]\right]P^{\frac{1}{2}}(\omega) \tag{5.29}$$

is the symmetrized diffusion operator. The symmetrised version of equation (5.25) (equation (19) of ref. [128]) is

$$g^{LL'}_{mm'nn'}(\tau) = \boxed{\int\int P^{\frac{1}{2}}(\omega_0)P^{\frac{1}{2}}(\omega)\tilde{P}(\omega_0|\omega t)\mathfrak{D}^{L}_{mm'}(\omega_0)\mathfrak{D}^{L'*}_{nn'}(\omega)d\omega_0 d\omega} - \left\langle\mathfrak{D}^{L}_{mm'}(\omega_0)\right\rangle_{\mathrm{av}}\left\langle\mathfrak{D}^{L'*}_{nn'}(\omega)\right\rangle_{\mathrm{av}} \tag{5.30}$$

By expanding the conditional probability $\tilde{P}(\omega_0|\omega t)$ and the energy of the confining potential $U(\omega)$ as linear combinations of normalised Wigner functions,

$$D^{L}_{mm'}(\omega) = \sqrt{\frac{2L+1}{8\pi^2}}\mathfrak{D}^{L}_{mm'}(\omega); \tag{5.31}$$

$$\tilde{P}(\omega_0|\omega t) = \sum_{Lmm'} c_{Lmm'}(\omega_0,t)D^{L}_{mm'}(\omega); \tag{5.32}$$

$$\frac{-U(\omega)}{k_B T} = \sum_{J,q}\sqrt{\frac{8\pi^2}{2J+1}}A_{Jq}D^{J}_{0q}(\omega), \tag{5.33}$$

equation (5.28) can be cast into matrix form:

$$\frac{1}{\zeta}\frac{\partial\mathbf{c}}{\partial t} = \tilde{\mathbf{R}}\mathbf{c}(t) \tag{5.34}$$

where

$$\tilde{R}_{L'm'n',Lmn} = \langle D^{L'}_{m'n'}|\tilde{\Gamma}|D^{L}_{mn}\rangle\,. \tag{5.35}$$

For uniaxial potentials, as treated in ref. [128], $\tilde{R}$ can be arranged in a block-diagonal form, due to the fact that there is no coupling between Wigner basis functions with different values of m. Without this simplifying symmetry property, the rotational diffusion matrix is much larger and harder to solve. For that reason, most of the results presented in this

Table 5.1: Coefficients for potentials of different strengths. The mean angular deviation from the laboratory frame z axis is calculated as $\langle B\rangle = \int_0^\pi \beta\sin(\beta)\exp(-U(\beta)/k_\mathrm{B}T)d\beta/\int_0^\pi \sin(\beta)\exp(-U(\beta)/k_\mathrm{B}T)d\beta$.

A	400	100	50	27	15
$\langle\pi-\beta\rangle$(deg)	5.1	10.2	14.4	19.7	26.7
J_max	30	24	24	12	12

chapter will be for motion in a uniaxial potential of the form

$$\frac{U(\beta)}{k_\mathrm{B}T} = A\cos^2\left(\frac{\beta}{2}\right); \tag{5.36}$$

$$= \frac{A}{2}\left(D^{(0)}_{0,0}(0,\beta,0) + D^{(1)}_{0,0}(0,\beta,0)\right), \tag{5.37}$$

in which A is a positive constant that determines the gradient of $U(\beta)$. Figure 5.1 illustrates the shape of the potential. Although motion over the barrier at $\beta = 0$ is possible, the values of A are selected to be large enough that the radical moves in what is effectively a simple harmonic potential, $U(\beta)/k_\mathrm{B}T \approx A(\beta-\pi)^2/4$, centred at $\beta = \pi$. Table 5.1 lists the selected values of A, which describe a series of potentials that permit an increasing range of molecular orientations.

Each block of R (labelled by a value of m) can be diagonalised to solve equation (5.34), giving

$$\mathbf{c}^m(t) = \mathbf{X}^m e^{\zeta t\mathbf{r}^m}(\mathbf{X}^m)^T\mathbf{c}^m(0), \tag{5.38}$$

where $\mathbf{X}^m$ and $\mathbf{r}^m$ are, respectively, the eigenvectors and eigenvalues of the m^th block of R. The resulting expression for the conditional probability is

$$\tilde{P}(\omega_0|\omega t) = \frac{1}{8\pi^2}\sum\sqrt{2J+1}\sqrt{2J'+1}(\hat{X}^q)_{Jp,k}e^{t\zeta r^q_k}(\hat{X}^q)_{J'p',k}\mathfrak{D}^J_{qp}(\omega)\mathfrak{D}^{J'*}_{qp'}(\omega_0) \tag{5.39}$$

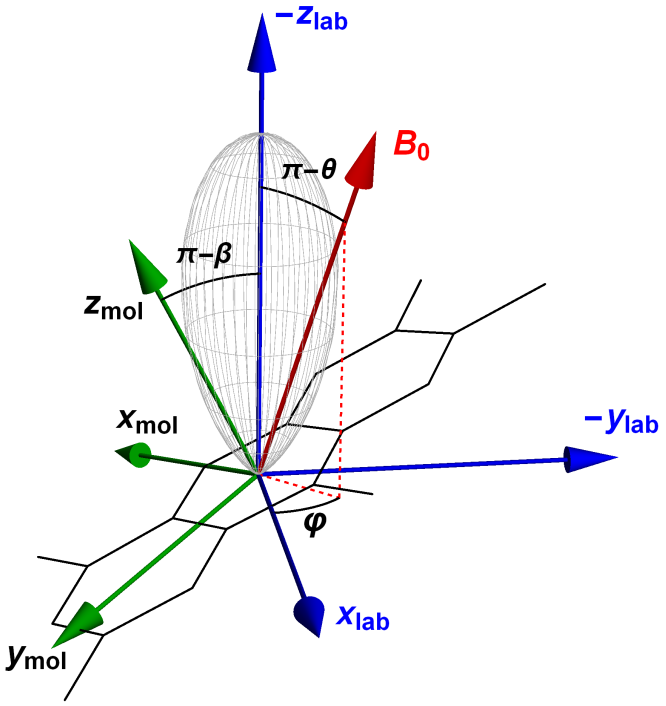


Figure 5.1: Representation of the rotational diffusion of the flavin radical with an ordering potential $U(\beta)$ of the type defined in equation (5.37), with $A = 15$. $U(\beta)$ is represented here by the grey surface; the distance from the origin to the surface is proportional to the Boltzmann weight $\exp(-U(\beta)/k_{\mathrm{B}}T)$ for the molecular z axis being oriented in that direction. The position of the molecular axes (green) in the laboratory frame (blue) is specified by the Euler angles $\omega(t) = (\alpha(t), \beta(t), \gamma(t))$. The orientation of the magnetic field (red) is given by the angles θ and ϕ. [*Figure published as part of figure 1 in Ref. [150].*]

The symmetrized conditional probability satisfies the equilibrium condition

$$\lim_{t\to\infty} \tilde{P}(\omega_0|\omega t) = P^{\frac{1}{2}}(\omega_0)P^{\frac{1}{2}}(\omega). \tag{5.40}$$

In the limit $t \to \infty$, all the exponentials in equation (5.39) decay to zero except the one containing r_0^0, the zero eigenvalue of the rotational diffusion matrix. This term becomes

$$P^{\frac{1}{2}}(\omega_0)P^{\frac{1}{2}}(\omega) = \frac{1}{8\pi^2} \sum_{J''J'''p''p'''} \sqrt{2J''+1}\sqrt{2J'''+1}(\hat{X}^{(0)})_{J''p'',0}(\hat{X}^{(0)})_{J'''p''',0}\mathfrak{D}^{J''}_{0p''}(\omega)\mathfrak{D}^{J'''*}_{0p'''}(\omega_0). \tag{5.41}$$

Substituting equations (5.40) and (5.41) into equation (5.30), the correlation function is [128]

$$
\begin{aligned}
g^{LL'}_{mm'n'}(t) &\equiv g^{LL'}_{mm'nn'}(t)\delta_{mn} \\
&= \sum_{k,J,p,J',p',J'',J'''} \frac{\sqrt{(2J+1)(2J'+1)(2J''+1)(2J'''+1)}}{(2L+1)(2L'+1)} \\
&\times (X^m)_{Jp,k}(X^m)_{J'p',k}(X^0)_{J''(m'-p),0}(X^0)_{J'''(n'-p'),0} \\
&\times C^{L,m}_{J''',0,J',m}C^{L,n'}_{J''',n'-p',J',p'}C^{L',m}_{J'',0,J,m}C^{L',m'}_{J'',m'-p,J,p}e^{t\zeta r^m_k} \\
&- \langle \mathfrak{D}^{(L)}_{mm'}(\omega_0)\rangle_{\mathrm{av}} \langle \mathfrak{D}^{(L')*}_{mn'}(\omega)\rangle_{\mathrm{av}} \qquad (5.42) \\
&= \sum_k \mathrm{F}(k,m,m',n')e^{t\zeta r^m_k} - \langle \mathfrak{D}^{(L)}_{mm'}(\omega_0)\rangle_{\mathrm{av}} \langle \mathfrak{D}^{(L')*}_{mn'}(\omega)\rangle_{\mathrm{av}} \qquad (5.43)
\end{aligned}
$$

In equation (5.42), J,J',J'',J''' are all independent indices labelling the angular momentum quantum number of the Wigner D-functions. For narrower potentials, the basis of the rotational diffusion matrix must be extended to include higher rank Wigner functions (a higher maximum J). The indices p and p' label the projection of the angular momentum for the Wigner D-function whose J-value has the corresponding number of dashes. The index k labels the eigenstates and corresponding eigenvalues of each block of the diffusion matrix. $(X^m)_{Jp,k}$ is the coefficient of the basis function $\mathfrak{D}^J_{mp}$ in the k^{th} eigenvector of the $(m)^{th}$ block of the diffusion matrix. Likewise, r^m_k is the k^{th} eigenvalue of the $(m)^{th}$ block of the diffusion matrix. $C^{J,p}_{J1,p1,J2,p2}$ are Clebsch-Gordan coefficients (see section 3.1.5).

The zero eigenvalue r^0_0 corresponds to the equilibrium distribution [128], such that when $r^m_k = r^0_0$, the first term in equation (5.42) equals $\langle \mathfrak{D}^{(L)}_{mm'}(\omega_0)\rangle_{\mathrm{av}} \langle \mathfrak{D}^{(L')*}_{mn'}(\omega)\rangle_{\mathrm{av}}$. This lengthy expression can be factorised, by inspection, into two equivalent pieces to show that

$$
\langle \mathfrak{D}^{(L)}_{0m'}(\omega)\rangle_{\mathrm{av}} = \sum \frac{\sqrt{2J+1}\sqrt{2J'+1}}{2L+1} \left(\hat{X}^{(0)}\right)_{Jp,0} \left(\hat{X}^{(0)}\right)_{J'p',0} C^{L,0}_{J',0,J,0}C^{L,m'}_{J',m'-p,J,p}. \qquad (5.44)
$$

Note that $\langle \mathfrak{D}^{(L)}_{mm'}(\omega)\rangle_{\mathrm{av}} = 0$ unless $m = 0$. As $\langle \mathfrak{D}^{(L)}_{0m'}(\omega)\rangle_{\mathrm{av}}$ can also be evaluated analyti-

cally using

$$\langle \mathfrak{D}^{(L)}_{0m'}(\omega)\rangle_{\mathrm{av}} = \int P(\omega)\mathfrak{D}^{(L)}_{0m'}(\omega)d\omega, \tag{5.45}$$

comparison of the values obtained from equation (5.44) or (5.45) was used as a means of confirming that a sufficiently large basis set had been used to form the diffusion operator matrix. Table 5.1 lists the maximum rank Wigner functions included in the basis set of each potential.

Substituting equation (5.43) into equation (5.18) and noting that the eigenvalues $r_k^{m'}$ are negative, the spectral density is

$$\begin{aligned} J^{ij}_m(\omega_{\beta\beta'}) &= J^{ij}_{mn}(\omega_{\beta\beta'})\delta_{mn} \\ &= \int_0^\infty \sum_{k,m',n'} \phi_{m',i}\phi_{n',j}F(k,m,m'n')e^{(i\omega_{\beta\beta'}+\zeta r_k^m)\tau}d\tau \\ &+ \int_0^\infty \sum_{k,m',n'} \phi_{m',i}\phi_{n',j}e^{(i\omega_{\beta\beta'}\tau)}\left\langle \mathfrak{D}_{mm'}(t)\right\rangle_{\mathrm{av}}\left\langle \mathfrak{D}^*_{mn'}(t+\tau)\right\rangle_{\mathrm{av}}d\tau. \end{aligned} \tag{5.46}$$

The second integral in equation (5.46) decays to zero, except when $\omega_{\beta\beta'} = 0$. When $\omega_{\beta\beta'} = 0$

$$J(0) = \int_0^\infty \sum_{k,m',n'} \phi_{m',i}\phi_{n',j}\left[F(k,m,m',n')e^{(\zeta r_k^m\tau)} - \left\langle \mathfrak{D}_{mm'}(t)\right\rangle_{\mathrm{av}}\left\langle \mathfrak{D}^*_{mn'}(t+\tau)\right\rangle_{\mathrm{av}}\right]d\tau. \tag{5.47}$$

As above, when $r_k^m = r_0^0 = 0$, the first term in equation (5.47) corresponds to $\langle \mathfrak{D}_{mm'}(t)\rangle_{\mathrm{av}}\langle \mathfrak{D}^*_{mn'}(t+\tau)\rangle_{\mathrm{av}}$. The expression for the zero-frequency spectral density thus becomes [156]

$$J(0) = \int_0^\infty \sum_{k,m',n'} \phi_{m',i}\phi_{n',j}F(k,m,m',n')e^{(\zeta r_k^m\tau)}d\tau; \qquad r_k^m \neq 0. \tag{5.48}$$

Therefore,

$$J_m^{ij}(\omega_{\beta\beta'}) = \sum_{k,m',n'} \frac{\phi_{m',i}\phi_{n',j}F(k,m,m',n')}{-\zeta r_k^m - i\omega_{\beta\beta'}}; \qquad r_k^m \neq 0 \text{ if } \omega_{\beta\beta'} = 0. \tag{5.49}$$

The imaginary part of $J_m^{ij}(\omega_{\beta\beta'})$ corresponds to a dynamic frequency shift that is usually very small and will therefore be neglected from these calculations [115]. The real part of J_{nm} is the spectral density, given by;

$$\mathrm{Re}(J_m^{ij}(\omega_{\beta\beta'})) = \sum_{k,m',n'} \frac{-\zeta r_k^m \phi_{m',i}\phi_{n',j}F(k,m,m',n')}{(\zeta r_k^m)^2 + (\omega_{\beta\beta'})^2}; \qquad r_k^m \neq 0 \text{ if } \omega_{\beta\beta'} = 0. \tag{5.50}$$

This expression for the spectral densities can be substituted into equation (5.51) to give a final expression for the relaxation superoperator:

$$\begin{aligned} R_{\alpha\alpha'\beta\beta'} = -\sum_{ij\subset\mathrm{mov.}}\sum_m \Bigg[& \sum_\gamma J_m^{ij}(\omega_{\gamma\beta})\hat{T}_{m,i}^{(2),\alpha\gamma}\hat{T}_{m,j}^{(2)\dagger,\gamma\beta}\delta_{\alpha'\beta'} \\ & - J_m^{ij}(\omega_{\beta'\alpha'})\hat{T}_{m,i}^{(2),\alpha\beta}\hat{T}_{m,j}^{(2)\dagger,\beta'\alpha'} \\ & - J_m^{ij}(\omega_{\alpha\beta})\hat{T}_{m,j}^{(2)\dagger,\alpha\beta}\hat{T}_{m,i}^{(2),\beta'\alpha'} \\ & + \sum_\gamma J_m^{ij}(\omega_{\beta'\gamma})\hat{T}_{m,j}^{(2)\dagger,\beta'\gamma}\hat{T}_{m,i}^{(2),\gamma\alpha'}\delta_{\alpha\beta} \Bigg]. \end{aligned} \tag{5.51}$$

5.3 Validating the Redfield approach

The derivation of the Redfield relaxation superoperator includes the key assumption that the system is well-described by Markovian dynamics, i.e. that the motional correlation time is much shorter than the time-scale for the coherent evolution of the spin system [115]. As maximum relaxation occurs when the correlation time for the motion approximately matches the time-scale of the coherent system dynamics, it is not immediately obvious that Redfield theory will be valid over the whole region of interest.

The range of applicability of Redfield theory was confirmed by comparing its results to

those in an earlier study looking at the effect of rigid-body rotations of the whole radical pair [101]. Lau *et al.* (2010) used a method of finite differencing to directly solve the rotational diffusion equation for the density matrix, within the stochastic Liouville-von Neumann equation. This method was not suitable for the current investigation as it quickly becomes unwieldy for larger spin systems and steep ordering potentials. However, it is valid for any rotational correlation time, so provides a good test of the Redfield approach.

Fig. 5.2 shows a comparison of original data from Lau *et al.* with the same data calculated using Redfield theory. Using each method, the singlet yield anisotropy (equation (4.16)) was calculated as a function of rotational correlation time for a radical pair containing a single spin-1/2 nucleus with an axial hyperfine interaction. The two radicals in the pair had a fixed relative orientation. The whole radical pair system performed rigid-body, isotropic rotational diffusion within an ordering potential with the form

$$\frac{U(\beta)}{k_{\mathrm{B}}T} = \varepsilon \sin^2(\beta) \tag{5.52}$$

$$= \frac{2\varepsilon}{3}(\mathfrak{D}^{(0)}_{0,0}(0,\beta,0) - \mathfrak{D}^{(2)}_{0,0}(0,\beta,0)). \tag{5.53}$$

For correlation times less that 10 ns, the two methods are in very good agreement. For slower rotations, Redfield theory fails to capture the decreasing relaxation rates and the expected effects of 'frozen-in' motion, which essentially introduces static disorder. However, the preliminary conclusion made in chapter 4 was that the compass precision and sensitivity could be better preserved by fast rather than slow motion. Furthermore, the types of motion we particularly wish to consider, i.e. restricted rotations of small sections of the magnetoreceptor, are likely to fall within this higher frequency range. For these reasons, this chapter will focus on motion with correlation times less than 10 ns, which is accurately described by Redfield theory.

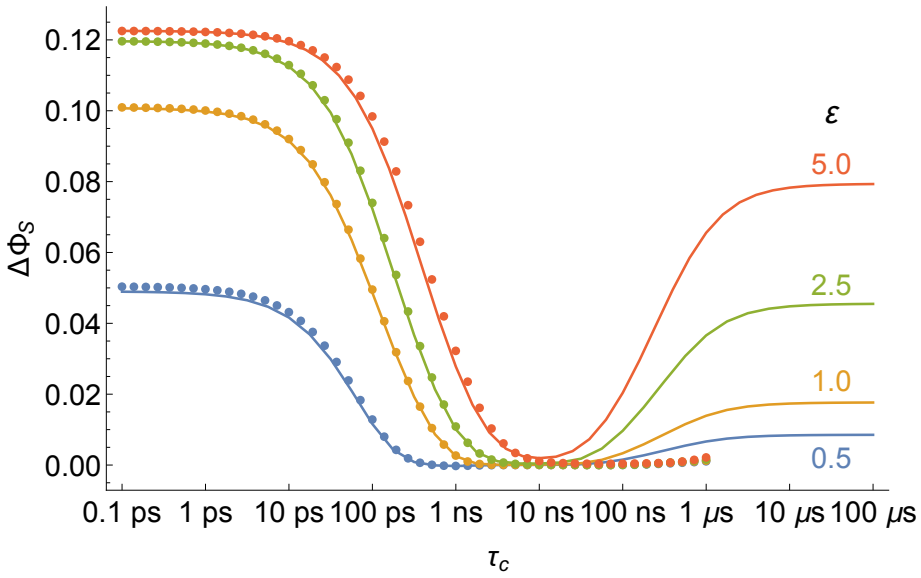


Figure 5.2: Testing the range of validity of Redfield theory (circles) by comparison with data from Lau *et al.* (2010), reference [101] (solid lines). The radical pair contained a single spin-1/2 nucleus with hyperfine tensor [0.5, 0.5, 2] mT. $B_0 = 50$ μT; $k = 10^6$ s^{-1}. [*Figure published in supplementary information of Ref. [150].*]

5.4 Small model systems

As before, the behaviour of small model systems was used to identify general trends before larger, more specific calculations were carried out. This section looks at the effect of rotational motion on the 'toy' radical pair introduced in section 4.5.

Figure 5.3 shows the effect of (restricted) isotropic rotational diffusion ($D_x = D_y = D_z = D = (6\tau)^{-1}$) of the primary radical on the singlet yield profile of this toy radical pair. The recombination lifetime of the radical pair is 10 μs, which is the minimum time required for the emergence of a noticeable spike. A longer lifetime would allow more time for spin relaxation to occur and consequently the system would relax completely to equilibrium under a wider range of conditions. Keeping the recombination lifetime as short as possible allows for a higher resolution study of how different physical conditions affect the relaxation rate.

Figure 5.3(a) shows that relaxation, which is almost complete ($\Phi_S \approx 0.25$) when $\tau = 10$ ns, becomes slower as τ is decreased to 0.1 ps. The amplitude of the broad background

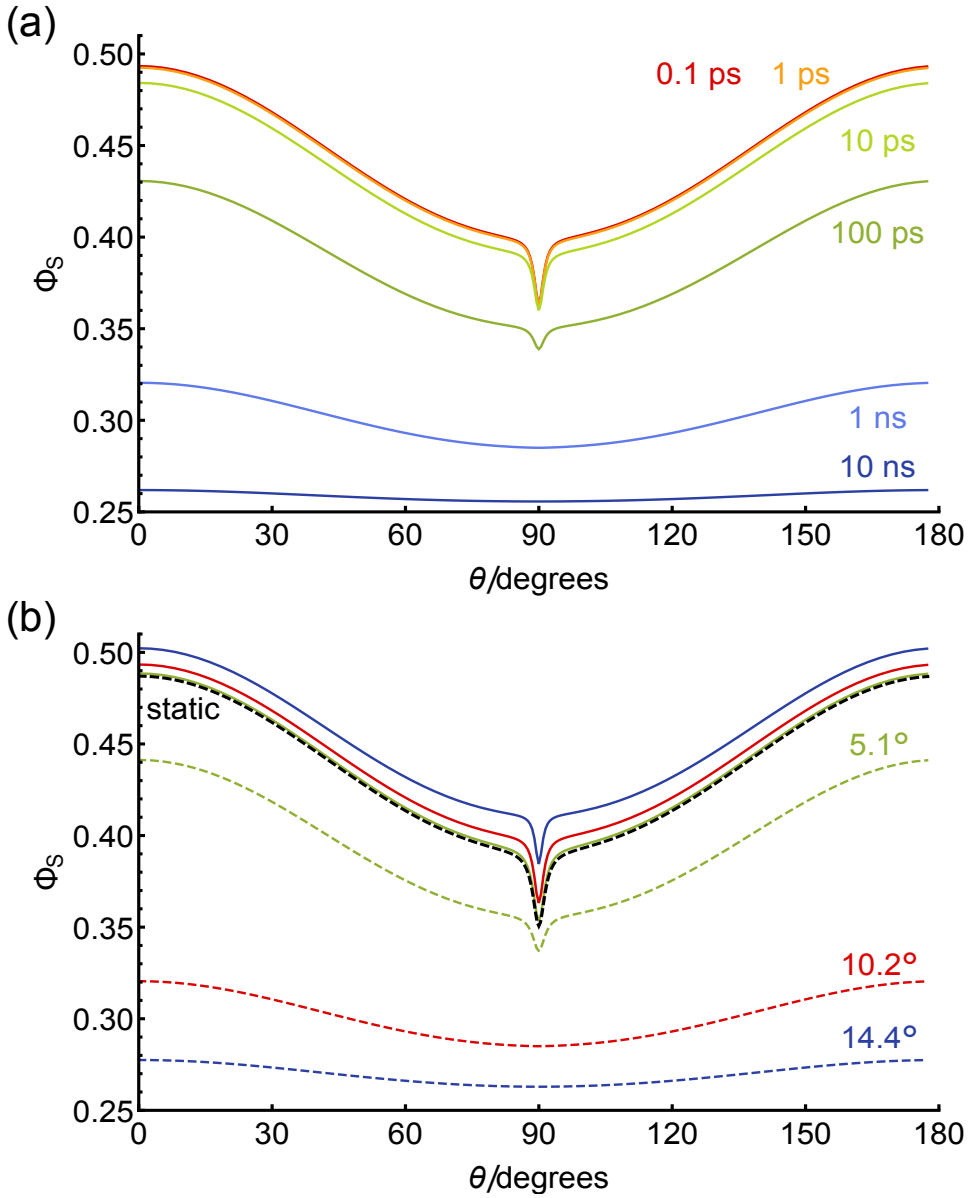


Figure 5.3: Relaxation of a four-spin system. The primary radical contains a spin-1 nucleus with hyperfine components $[A_{xx}, A_{yy}, A_{zz}] = [-0.2, -0.2, 1.7569]$ mT. The secondary radical also contains a spin-1 nucleus, with hyperfine components $[0.0, 0.0, 1.0812]$ mT. The z axes of the two hyperfine tensors are parallel. The radical pair recombination lifetime is 10 μs. The external field strength is 50 μT. (a) The primary radical undergoes isotropic rotational diffusion within a potential that allows tumbling of the z axis with a mean deviation of 10° ($A = 100$). The rotational correlation time increases from 0.1 ps to 10 ns, as indicated. (b) The primary radical undergoes isotropic rotational diffusion within a series of potentials, whose mean deviation is indicated on the graph. Solid lines: $\tau = 0.1$ ps, where the hyperfine couplings are effectively averaged and there is very little relaxation. Dashed lines: $\tau = 1$ ns, at which strong relaxation occurs. The singlet yield profile corresponding to an ensemble of static, aligned radical pairs is shown by the dashed, black line. [*Figure published as figure 2 in Ref. [150].*]

curve gradually recovers and the spike becomes visible. For correlation times as short as 1 ps, there is negligible relaxation. This is consistent with the trends observed using the two-site model in chapter 4 and the established proportionality between relaxation rate and spectral densities (equation(4.18)).

Relaxation rates are also proportional to the mean squared amplitude of the fluctuating magnetic interactions that drive the relaxation. In this case, the relevant fluctuations are in the strength and direction of the field experienced by the electron spin in the moving radical due to the magnetic nuclei to which it is coupled. In less steep potentials, the greater range of orientations sampled by the moving radical leads to larger amplitude fluctuations in the components of the hyperfine tensor in the laboratory frame. Consequently, we observe faster spin relaxation. This is apparent in the increasing gap between the $\tau = 0.1$ ps (solid lines) and $\tau = 100$ ns (dashed lines) traces in figure 5.3(b) as A in equation (5.37) is decreased.

Despite the absence of significant relaxation, the static form of the singlet yield profile is not necessarily recovered in the limit of very fast motion. In the fast motion regime, different orientations of the radical become indistinguishable on the time-scale of the coherent spin evolution. As a result, the singlet yield profile reflects the influence of an effective hyperfine interaction, equivalent to the weighted average of the hyperfine tensor over all the orientations of the moving radical. As the value of A (equation (5.37)) is decreased, a greater range of orientations is sampled by the moving radical, enhancing the difference between the static and motionally averaged hyperfine tensors. This is illustrated in figure 5.3(b) by the difference in the singlet yield profile at $\tau = 0.1$ ps (solid lines) across the three potentials shown. In this case, motional averaging of the hyperfine tensors gradually reduces the length of the spike and the anisotropy of the background. However, this sort of averaging is not necessarily always detrimental. The possibility of improving the hyperfine tensors by averaging will be explored in the next section.

Overall, the results shown in figure 5.3 confirm the trends observed for small model systems using the two-site model in section 4.3. However, the more sophisticated model

of molecular motion used in this chapter provides a more accurate picture of the effect of averaging hyperfine tensors over a wider range of orientations.

5.4.1 Optimisation principles

The capacity for fast molecular motion to alter the form of the effective hyperfine interaction naturally raises the question of whether motion could improve the ability of a radical pair to function as a compass. If we assume, in line with previous studies [68, 101], that optimum compass function is achieved by maximising the singlet yield anisotropy (equation (4.16)), it is most favourable for the hyperfine tensor to have the form $[0, 0, A_{zz}]$, i.e. $T_{xx} = T_{yy} = -T_{zz}/2 = -a_{\text{iso}}$ [68]. For a hyperfine tensor that instead has $|T_{xx}| > |a_{\text{iso}}|$, averaging away some of the anisotropic component via molecular rotation would therefore improve the compass signal. Since some degree of motion is unavoidable in real systems, it could be better to have an ostensibly 'non-optimal' static hyperfine interaction that would be improved by motional averaging than an 'optimal' one that would be degraded.

The potential advantage offered by rotational averaging is offset by the degree of relaxation caused by the motion. This is illustrated in figure 5.4 using the example of a radical pair containing a single spin-1 nucleus. The electron in one radical is coupled to the nuclear spin with one of two different hyperfine tensors. This radical undergoes isotropic rotational diffusion in an ordering potential (equation (5.37)) with an average deviation of 27° ($A = 15$). One hyperfine tensor has been designed to be ideal for a static, aligned system (orange lines). The other has a larger anisotropic component that will produce an ideal *effective* hyperfine tensor when averaged over the potential (blue lines). The isotropic component of both hyperfine tensors is 0.5 mT.

In the limit of very fast rotational diffusion (short correlation times), the highest singlet yield anisotropy is produced by the more anisotropic hyperfine tensor (blue lines), which is favourably averaged by the motion. However, the larger anisotropy also induces faster relaxation [101], which increasingly degrades the singlet yield anisotropy as the correlation

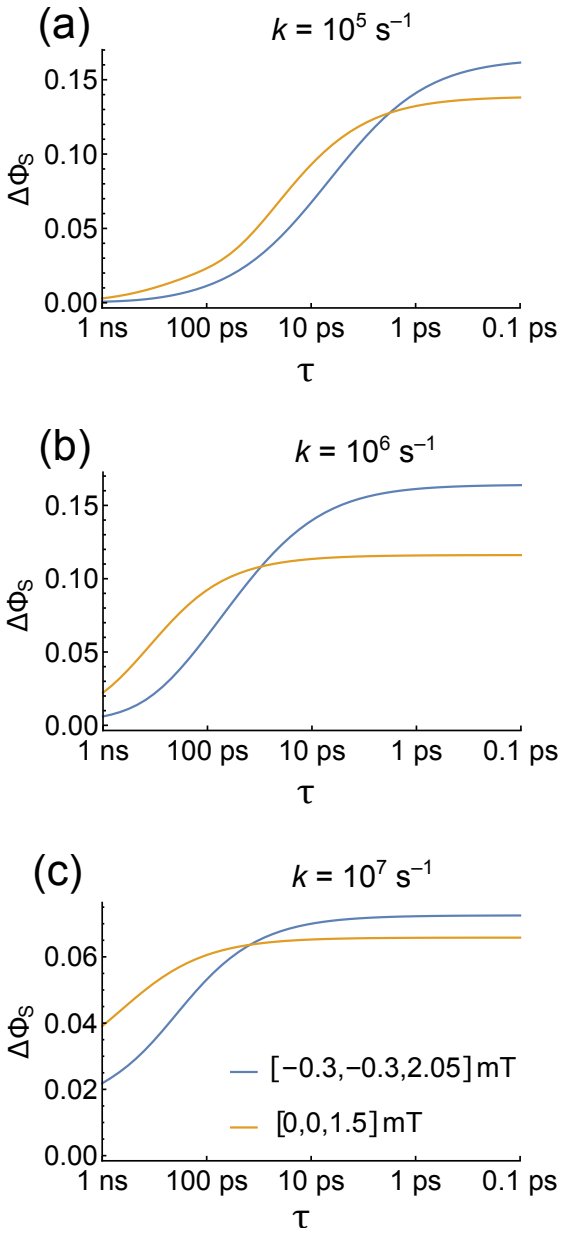


Figure 5.4: Example of constructive rotational averaging for a radical pair containing a single spin-1 nucleus. The radical undergoes isotropic diffusion in a potential with a mean deviation of 27°. The hyperfine coupling for this nucleus is either ideally designed to maximise the singlet yield anisotropy in the absence of motion (orange lines), or is averaged to ideal by the molecular rotation (blue lines). The isotropic component $a_0^{(0)} = 0.5$ mT. The external field strength is 50 μT and the field is applied in the yz plane of the primary radical such that $\phi = \pi/2$. (a) $k = 10^5$ s^{-1}. (b) $k = 10^6$s^{-1}. (c) $k = 10^7$ s^{-1}. [*Figure published as figure 3 in Ref. [150].*]

time gets longer. The point at which the less anisotropic hyperfine tensor (orange lines) becomes more favourable is strongly dependent on the rate constant for radical pair recombination, which dictates how much time is available for relaxation to occur.

When a spike in the singlet yield is taken to be an essential feature of the compass, the picture changes completely. The sensitivity of the compass is measured by the length of the spike, rather than by the singlet yield anisotropy. In addition, the spike should have a narrow width to maximise the compass precision. To maximise the sensitivity of the compass, the spike should be as large as possible, whilst still remaining narrow enough to provide the required compass precision. It was shown in section 4.3.4 that an 'ideal' spike would likely have a width of about 5°. In a static system, with a recombination lifetime of 10 μs, the flavin radical produces a spike roughly 5° wide, making it very well-suited to its role as a component of a sensitive, precise compass. Previous studies have also found that flavin radicals are almost ideally designed to produce a large singlet yield anisotropy when radical pair recombination is faster and spikes are not observable [68]. This suggests that there is little scope for improving the hyperfine tensors in flavin by rotational averaging. The evidence presented in the next section adds further strength to this conjecture.

5.5 Flavin-tryptophan radical pair

A tractable model of FAD-TrpH

In chapter 4, a number of larger model spin systems were used to investigate the effects of motion of different radicals. At this point, I will introduce a single, reduced model of cryptochrome that will be used throughout the rest of the thesis. This cryptochrome model contains 8 nuclear spins (see figure 5.5), which is the maximum number that can be processed in a reasonable time for many of the calculations. The primary radical contains the three largest hyperfine couplings from $FAD^{\bullet -}$ (N5, N10, H6), whilst the secondary radical consists of the N1, H1, H4, H7 and Hβ nuclei of $TrpH^{\bullet +}$ (Appendix A). These

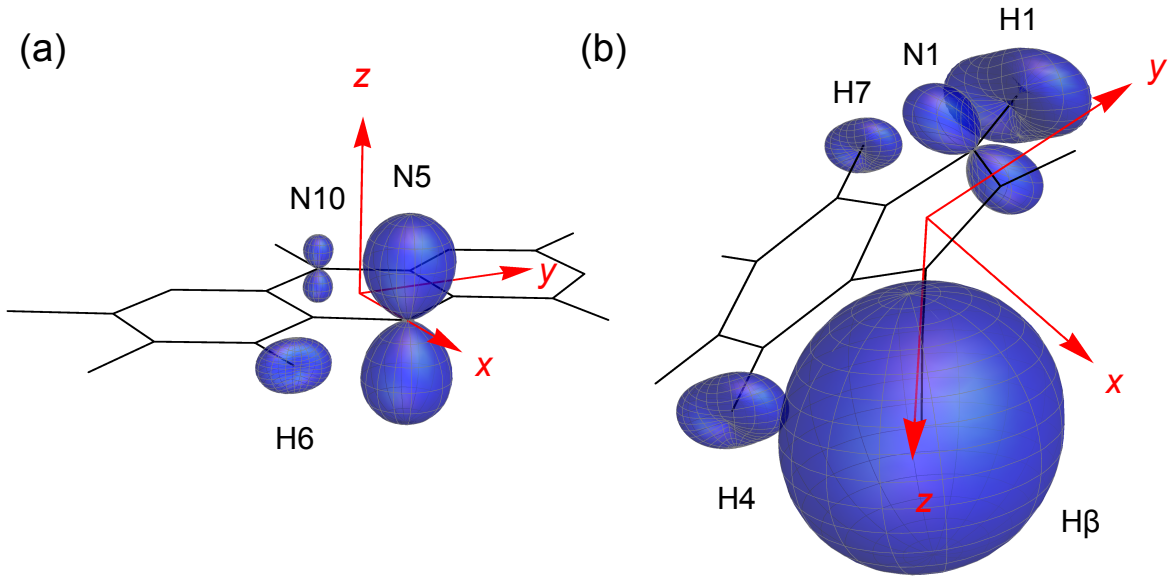


Figure 5.5: Representations of the hyperfine interactions included in (a) the flavin radical $FAD^{\bullet-}$ and (b) the tryptophan radical $TrpH^{\bullet+}$. The corresponding hyperfine tensors are given in appendix A. The relative orientation of the two radicals is taken to be that of FAD and Trp-342 (the terminal tryptophan of the Trp-triad) in the crystal structure of *Drosophila melanogaster* cryptochrome [158, 159]. [*Figure published as part of figure 5 in Ref. [150].*]

nuclei have previously been identified as dominating both the static singlet yield profile of the flavin-tryptophan radical pair [68] and many of its relaxation pathways [157]. In the flavin radical the principal (z) axis is defined as the axis perpendicular to the plane of the aromatic ring system. In the tryptophan radical, the z axis is defined by the C3-Cβ bond, which joins the indole group to the rest of the amino acid side-chain. In most calculations the z axis of the ordering potential is aligned with the z axis of the moving radical before motion is included.

In all of the calculations presented in this chapter, the singlet yield is calculated as a function of the angle θ between the molecular z axis and the Earth's magnetic field, which is applied in the yz plane of the primary radical ($\phi = \pi/2$). This cross-section was chosen because of the clear separation of the small spike at $\theta \approx 30° - 40°$, attributed to N1 in the tryptophan radical, and the larger spike at $\theta = 90°$, created by the N5 and N10 hyperfine interactions in the flavin radical (see figure 5.6(a)). The spike at $\theta \approx 30° - 40°$

is sensitive to the number of nuclei included in the simulation and consequently I have focused on the effect of motion on the spike at $\theta = 90°$. A full 3D representation of the singlet yield for a static flavin-tryptophan radical pair can be found in Ref. [61].

Simulation results

Figure 5.6(b) shows the impact of constrained isotropic rotational diffusion of the model flavin radical on the singlet yield anisotropy. The recombination lifetime is 1 μs, which is too short to allow spikes to develop. In the limit of very fast motion, the system is effectively in a regime of static order, with a set of motionally averaged hyperfine tensors. For $A = 100$ and $A = 400$, the motionally averaged interactions yield a marginally stronger compass signal, whilst averaging over larger amplitude motions degrades the signal. As for small spin systems, the relaxation rate increases with the amplitude of the wobbling such that the optimal size of motion depends on the diffusion rate.

For longer-lived radical pairs, figure 5.6(c) shows that motional averaging of the flavin hyperfine tensors, even within highly restricted potentials, reduces the length of the spike. The spike, as well as the overall anisotropy, is further attenuated by relaxation as the correlation time is increased from $\tau = 0.1$ ps to $\tau = 1$ ns, although the width of the spike is unchanged. In the $A = 400$ potential shown in figure 5.6(d), the spike is barely visible for $\tau = 100$ ps and has completely disappeared for $\tau = 1$ ns. As A is reduced, the rate of relaxation increases and the spike disappears more rapidly. The uniaxial nature of the N5 and N10 hyperfine interactions in the flavin radical means that the observed relaxation is primarily caused by the wobbling motion of the molecular z axis, rather than diffusion around the z axis itself. To demonstrate this, figure 5.6(d) includes a trace corresponding to $D_z = 1.67 \times 10^8$ s^{-1} and $D_x = D_y = 1.67 \times 10^{12}$ s^{-1} (i.e. $\eta = 10^{-4}$). Although substantial relaxation occurs when all three diffusion rate constants equal 1.67×10^8 s^{-1}, the signal is only slightly degraded compared to the limit of fast isotropic diffusion when only D_z has this value.

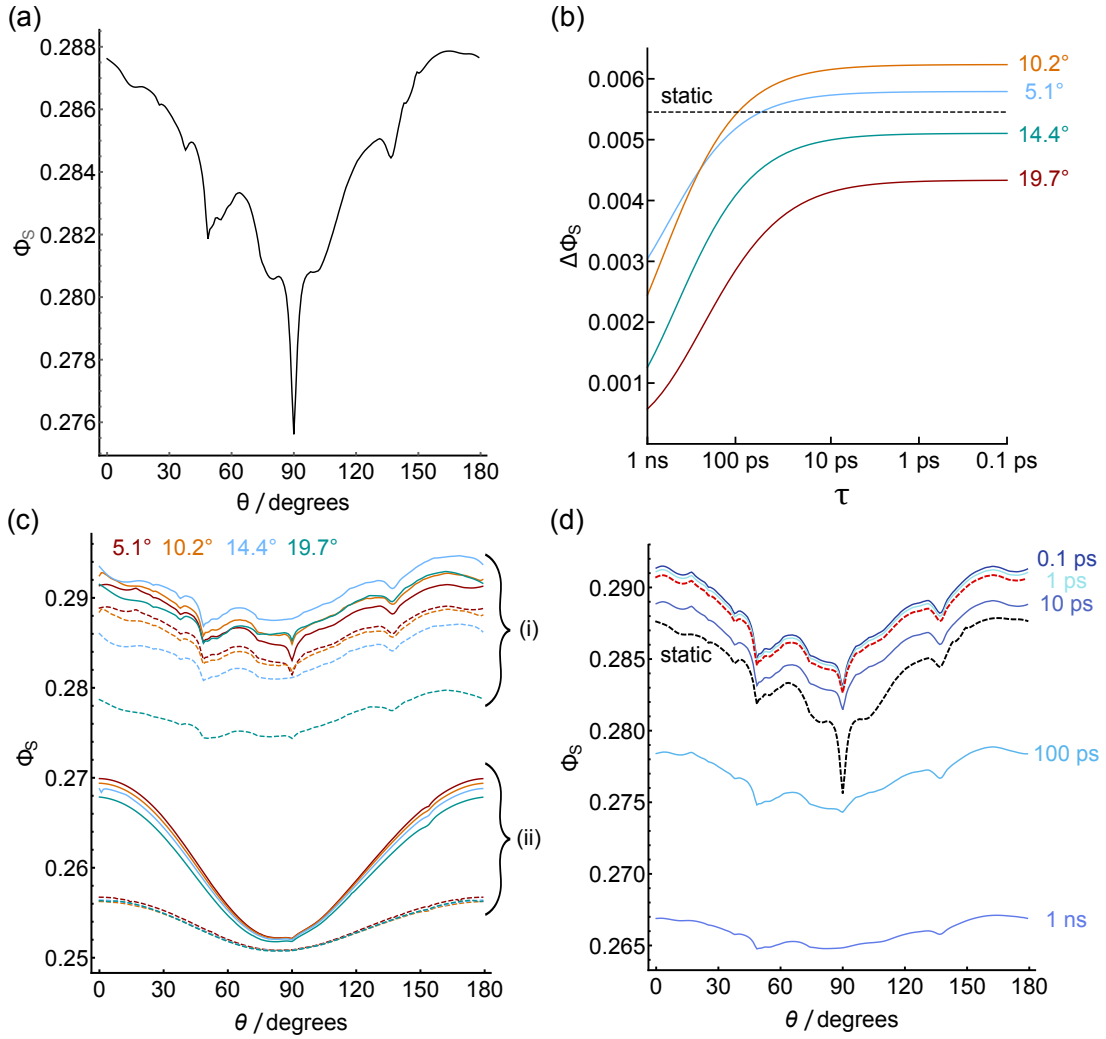


Figure 5.6: Relaxation of a ten-spin system. The primary radical contains the N5, N10 and H6 nuclei from $FAD^{\bullet-}$. The secondary radical consists of N1, H1, H4, H7 and Hβ from $TrpH^{\bullet+}$. The external field strength is 50 μT and the field is applied in the yz plane of the primary radical such that $\phi = \pi/2$. (a) Singlet yield profile for an ensemble of static, aligned radical pairs. (b) Isotropic rotational diffusion of the primary radical in a series of potentials of different mean deviation (see table 5.1). The radical pair recombination lifetime is 1 μs, so no spikes are observable. Only the singlet yield anisotropy, equation (4.17), is reported. The dashed, black line indicates the singlet yield anisotropy produced by a static, aligned ensemble of radical pairs. (c) Isotropic rotational diffusion of (i) the flavin radical and (ii) the tryptophan radical in a series of potentials of different mean deviation, as indicated. Solid lines indicate a rotational correlation time of 0.1 ps, for which there is no significant relaxation. Dashed lines indicate a rotational correlation time of 10 ps. The radical pair recombination lifetime is 10 μs. (d) Isotropic rotational diffusion of the primary radical within a potential that allows tumbling of the z axis with a mean deviation of 5°. The rotational correlation time increases from 0.1 ps to 1 ns, as indicated. The black, dashed line indicates the reaction yield for a static, aligned ensemble of radical pairs. The red line shows the reaction yield when the diffusion is anisotropic, with $D_x = D_y = 1.67 \times 10^{12}$ s^{-1} and $D_z = 1.67 \times 10^{8}$ s^{-1}. The radical pair recombination lifetime is 10 μs. [*Parts (b), (c) and (d) published as part of figure 6 in Ref. [150].*]

These simulations support the prediction made in section 5.4.1 that there is little scope for improving the hyperfine tensors in flavin by rotational averaging and that even highly restricted molecular tumbling degrades the length of the spike and the overall anisotropy of the singlet yield. For optimal compass function, motion of the flavin radical should be as constrained as possible to minimize the detrimental effects of spin relaxation.

Fortunately, the location of FAD, buried inside cryptochrome, means that it is well-placed to have its motion constrained by the surrounding sections of the protein. Molecular dynamics simulations of cryptochrome 1 from *Arabidopsis thaliana* suggest that librations of the flavin radical are restricted to approximately 5° [147], which appears to be compatible with a functioning compass when the rotational correlation time is 100 ps or less and the recombination lifetime is 10 μs. For longer-lived radical pairs, relaxation processes have more time to take effect and are consequently more damaging. To maintain a functioning compass with longer-lived radicals, the correlation time for flavin wobbling would need to be shorter. Alternatively, the loss of some anisotropy or 'spikiness' could be compensated for by amplification further down the signalling pathway [64].

The hyperfine interactions in a static tryptophan radical do not have the same mutually parallel uniaxial symmetry as do N5 and N10 in the flavin radical. Consequently, diffusion of tryptophan around the C3-Cβ bond is associated with large fluctuations in the electron-nuclear interactions, driving fast relaxation. Motional averaging around this bond also greatly reduces the anisotropy of the hyperfine interactions (figure 5.7). The resulting singlet yield profile has a more strongly anisotropic background but the spike is barely visible, even in a regime of very slow relaxation (figure 5.6(c)).

By contrast, averaging the hyperfine interactions around an axis perpendicular to the plane of the indole ring produces a set of hyperfine tensors with a uniaxial symmetry that is missing from their static counterparts, whilst still preserving the anisotropy of the N1 hyperfine tensor. The increased symmetry of the interactions greatly enhances the spike (figure 5.8).

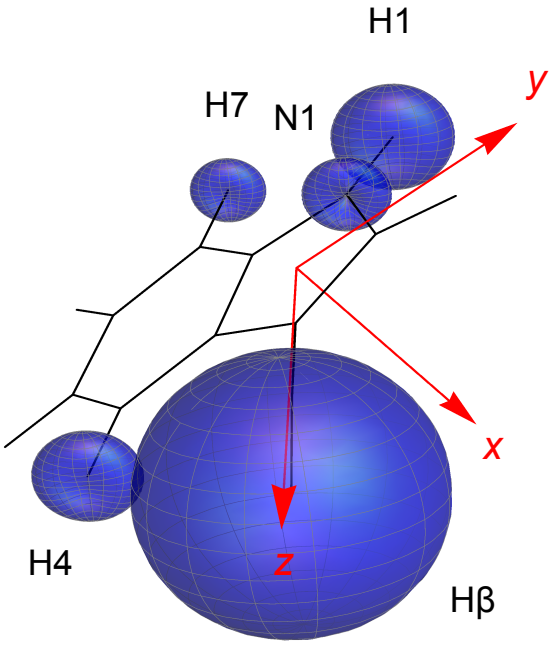


Figure 5.7: Hyperfine interactions in the tryptophan radical after rotational averaging within a potential with $A = 100$ and the symmetry axis (z axis) defined by the C3–Cβ bond. [*Figure published as part of figure 5 in Ref. [150].*]

5.6 Extension to biaxial potentials

Uniaxial potentials that allow free diffusion around one axis do not realistically describe the motion of radicals in restricted protein environments. For radicals, such as FAD, that are highly symmetric around one axis, allowing free motion around the symmetry axis has little to no effect. However, for more asymmetrical radicals, such as tryptophan, the unrestricted motion around one axis dominates both the relaxation behaviour and the shape of the singlet yield. To better understand the effect that motion of the tryptophan radical has on the compass, a biaxial potential can be used to restrict the motion of the radical around all three axes.

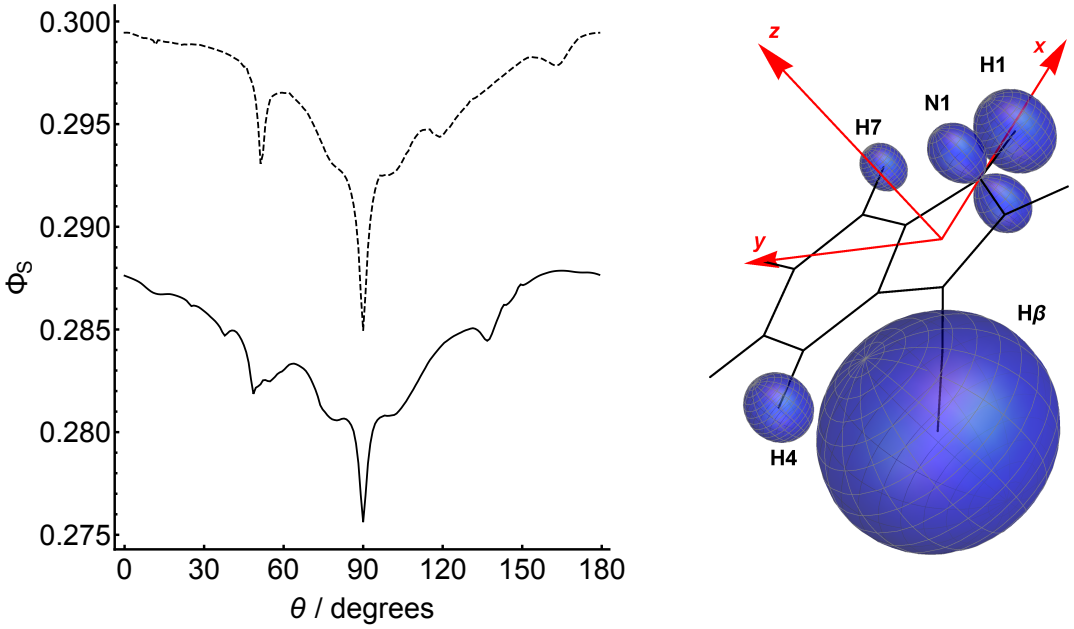


Figure 5.8: Left: Singlet yield profile for the flavin-tryptophan radical pair when it is static (solid line) and when the tryptophan radical diffuses freely, within an ordering potential, around an axis perpendicular to the plane of the indole ring with $\tau = 0.1$ ps (dashed line). $B_0 = 50$ μT; $k = 10^5$ s^{-1}; $A = 100$. Right: Rotationally averaging hyperfine interactions in the tryptophan radical. The averaged hyperfine tensors were calculated by numerical integration over the allowed orientations within a potential with an average deviation of 10°: i.e. $\langle A \rangle_{\text{av}} = \frac{1}{4\pi} \int_0^{\pi} \int_0^{2\pi} [\exp(-100 \cos^2(\beta/2)) \mathbf{R}^{-1} \mathbf{A} \mathbf{R} \sin(\beta)] d\gamma d\beta$ where $\mathbf{R}$ is given by equation (3.6) with α set to zero. [*Figure published in Supplementary Information of Ref. [150].*]

5.6.1 Defining the potentials

A simple biaxial potential was chosen that limits both motion around the molecular z-axis and tumbling of the z-axis, whilst also being easy to expand as a linear combination of low order Wigner functions. The potential,

$$U(\alpha, \beta, \gamma) = A \cos^2\left(\frac{\beta}{2}\right) \cos(\alpha + \gamma) \tag{5.54}$$

$$= \frac{A}{2} \left(\mathfrak{D}^{(1)}_{1,1} + \mathfrak{D}^{(1)}_{-1,-1} \right), \tag{5.55}$$

has a very similar form to the uniaxial potential used in the previous sections. The dependence on $(\alpha+\gamma)$, rather than α and γ separately, makes it harder to visualise. Figure

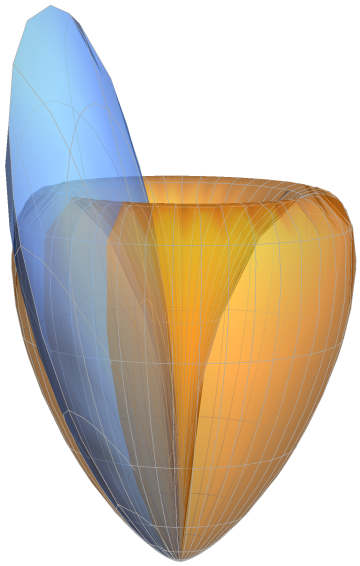


Figure 5.9: Comparison of biaxial and uniaxial potentials. The orange surface represents the probability of a particular orientation being adopted within the uniaxial potential used in sections 5.4 and 5.5. The blue surface shows a snapshot of the same for the biaxial potential in equation (5.54), with a set value of α. Both potentials have $A = -15$.

5.9 shows one possible graphical representation. It could be interpreted as describing a collection of molecules whose director (z-axis) initially has an equal probability of lying anywhere in the xy-plane of the lab frame. However, a molecule with any given position within the lab frame can only wobble between a small range of orientations around its own z-axis.

5.6.2 Calculating correlation functions

As before, correlation functions can be found by solving a rotational diffusion equation in a basis of normalised Wigner functions $\mathfrak{D}^{(L)}_{m,n}$. In contrast to uniaxial potentials, however, we now expect to see coupling between basis functions with different m. This is a computationally more challenging problem, but certain simplifications can be used to make it manageable. The first simplication is that the rates of diffusion around the molecular

x and y axes are always chosen to be equal, such that

$$\epsilon = \frac{D_x - D_y}{D_x + D_y} = 0. \tag{5.56}$$

The general equations for the matrix elements of the rotational diffusion operator $\langle \mathfrak{D}^{(L')}_{m',n'} | \Gamma | \mathfrak{D}^{(L)}_{m,n} \rangle$ are given in Berggren *et al.* (1995). When $\epsilon = 0$, only the following five equations need to be used [160]:

$$\Gamma = -\nabla^2 - \frac{1}{2}\nabla^2 \frac{U(\omega)}{k_\mathrm{B}T} + \frac{1}{4}\left(L_+ \frac{U(\omega)}{k_\mathrm{B}T}\right)\left(L_- \frac{U(\omega)}{k_\mathrm{B}T}\right) + \frac{1}{4}\eta\left(L_z \frac{U(\omega)}{k_\mathrm{B}T}\right)^2; \tag{5.57}$$

$$\left\langle \mathfrak{D}^{(L')}_{m',n'} \right| - \nabla^2 \left| \mathfrak{D}^{(L)}_{m,n} \right\rangle = \left[-L'(L'+1) - n'^2(\eta - 1)\right] \delta_{L'L}\delta_{m'm}\delta_{n'n}; \tag{5.58}$$

$$\begin{aligned}
&\left\langle \mathfrak{D}^{(L')}_{m',n'} \right| - \frac{1}{2}\nabla^2 \frac{U(\omega)}{k_\mathrm{B}T} \left| \mathfrak{D}^{(L)}_{m,n} \right\rangle \\
&\quad = \frac{-\sqrt{2L+1}}{\sqrt{2L'+1}} \times \sum_{Jpq} a_{Jpq}\left[J(J+1) + q^2(\eta - 1)\right] \\
&\quad \times C^{L',m'}_{L,m'-p,J,p} C^{L',n'}_{L,n'-q,J,q} \delta_{m,m'-p}\delta_{n,n'-q};
\end{aligned} \tag{5.59}$$

$$\begin{aligned}
&\left\langle \mathfrak{D}^{(L')}_{m',n'} \right| \frac{1}{4}\left(L_+ \frac{U(\omega)}{k_\mathrm{B}T}\right)\left(L_- \frac{U(\omega)}{k_\mathrm{B}T}\right) \left| \mathfrak{D}^{(L)}_{m,n} \right\rangle \\
&\quad = \frac{\sqrt{2L+1}}{4\sqrt{2L'+1}} \sum_{Jpq}\sum_{J'p'q'} a_{Jpq} a_{J'p'q'} \sqrt{J(J+1) - q(q+1)}\sqrt{J'(J'+1) - q'(q'-1)} \\
&\quad \times \sum_{J''=|J-J'|}^{J+J'} C^{J'',p+p'}_{J,p,J',p'} C^{J'',q+q'}_{J,q+1,J',q'-1} C^{L',m'}_{L,m'-p-p',p+p'} C^{L',m'}_{L,n'-q-q',J'',q+q'} \\
&\quad \times \delta_{m,m'-p-p'}\delta_{n,n'-q-q'};
\end{aligned} \tag{5.60}$$

$$\begin{aligned}
&\left\langle \mathfrak{D}^{(L')}_{m',n'} \right| \frac{1}{4}\eta\left(L_z \frac{U(\omega)}{k_\mathrm{B}T}\right)^2 \left| \mathfrak{D}^{(L)}_{m,n} \right\rangle \\
&\quad = \frac{\eta\sqrt{2L+1}}{4\sqrt{2L'+1}} \sum_{Jpq}\sum_{J'p'q'} a_{Jpq} q q' \\
&\quad \times \sum_{J''=|J-J'|}^{J+J'} C^{J'',p+p'}_{J,p,J',p'} C^{J'',q+q'}_{J,q,J',q'} C^{L',m'}_{L,m'-p-p',p+p'} C^{L',m'}_{L,n'-q-q',J'',q+q'} \\
&\quad \times \delta_{m,m'-p-p'}\delta_{n,n'-q-q'}.
\end{aligned} \tag{5.61}$$

In equations (5.57) – (5.61), a_{Jpq} is the coefficient of the Wigner function $\mathfrak{D}^J_{pq}$ in the expansion of the potential and $C^{lm}_{l_1m_1l_2m_2}$ are Clebsch-Gordan coefficients.

The fact that $p = q$ for both Wigner functions in the expansion of the potential offers an advantage when setting up and solving the rotational diffusion equation. Examination of the delta functions in equations (5.58) – (5.61) reveals that, when $p = q$, the criterion for non-zero matrix elements is $(m' - n') = (m - n)$. This rule can be used to rearrange the rotational diffusion matrix into blocks that can be individually formed and solved, greatly reducing the size of the problem.

The eigenvectors of the rotational diffusion matrix can be used to analytically calculate correlation functions of the form

$$g^{LL'}_{mm'nn'}(t) = \langle D^{L*}_{mn}(0) D^{L'}_{m'n'}(t) \rangle \tag{5.62}$$

using the expression given in Berggren et al. (1995), equation 23:

$$\begin{aligned} g^{LL'}_{mm'nn'}(t) = \sum_k \Bigg[\sum_{Jpq} \sum_{J'p'q'} \sum_{J''J'''} \left(\frac{(2J+1)(2J'+1)}{(2J''+1)(2J'''+1)} \right)^{\frac{1}{2}} \\ \times X_{Jpq;k} X_{J'p'q';k} X_{J'',m-p,n-q;0} X_{J''',m'-p',n'-q';0} \\ \times C^{J'',m-p}_{L,m,J,-p} C^{J'',n-q}_{L,n,J,-q} C^{J''',m'-p'}_{L',m',J',-p'} C^{J''',n'-q'}_{L',n',J',-q'} \Bigg] \\ \times \exp(tD_x r_k) - \langle \mathfrak{D}^L_{mn}(0) \rangle_{\text{av}} \langle \mathfrak{D}^L_{m'n'}(t) \rangle_{\text{av}} \qquad (5.63) \\ = A(k,m,n,m',n') \exp(tD_x r_k) - \langle \mathfrak{D}^L_{mn}(0) \rangle_{\text{av}} \langle \mathfrak{D}^L_{m'n'}(t) \rangle_{\text{av}} \,. \qquad (5.64) \end{aligned}$$

Here, $X_{Jpq;k}$ is the coefficient of the basis function $\mathfrak{D}^J_{pq}$ in the k^{th} eigenvector. The corresponding eigenvalue is r_k.

Hence, the spectral density is

$$J^{ij}_{mm'}(\omega) = \sum_{nn'} \int_0^\infty \phi_{n,i}\phi^*_{n',j} g_{mm'nn'}(t) e^{i\omega t} dt \tag{5.65}$$

$$= \sum_{k,n,n'} \frac{-D_x r_k \phi_{n,i}\phi^*_{n',j} A(k,m,n,m',n')}{(D_x r_k)^2 + (\omega)^2}; r_k \neq 0 \text{ if } \omega = 0, \tag{5.66}$$

which is derived in the same way as equation (5.50).

The averages of the two Wigner functions can be identified by factorising $A(0,m,n,m',n')$ into two identically formed components. The resulting expression is

$$\langle \mathfrak{D}^L_{mn}(t) \rangle_{\text{av}} = \sum_k \sum_{Jpq,J''} \left(\frac{(2J+1)}{(2J''+1)} \right)^{\frac{1}{2}} X_{Jpq;0} X_{J'',m-p,n-q;0} C^{J'',m-p}_{L,m,J,-p} C^{J'',n-q}_{L,n,J,-q}. \tag{5.67}$$

In contrast to the case of uniaxial potentials, $\langle \mathfrak{D}^L_{mn}(t) \rangle_{\text{av}}$ can now be non-zero for any value of m. This increases the number of non-zero contributions to the static Hamiltonian

$$\hat{H}_0 = \gamma_{\text{e}} \mathbf{B_0} \cdot (\hat{\mathbf{S}}^{(1)} + \hat{\mathbf{S}}^{(2)}) + \sum_k a_k \hat{\mathbf{S}}^{(1/2)} \cdot \hat{\mathbf{I}}^{(k)}$$
$$+ \sum_{i \in \text{static}} \left(\sum_{n=-2}^{2} \hat{T}^{(2)}_{n,i} \phi_{n,i} \right) + \sum_{j \in \text{moving}} \left(\sum_{m=-2}^{2} \sum_{n=-2}^{2} \hat{T}^{(2)}_{m,j} \phi_{n,j} \langle \mathfrak{D}^{(2)}_{mn}(t) \rangle_{\text{av}} \right). \tag{5.68}$$

5.6.3 Motion of flavin and tryptophan

Due to the size of the calculations, only the weakest biaxial potential ($A = 27$) was considered.

Figure 5.10 compares the effect of restricting the motion of the flavin radical with a biaxial or uniaxial potential of the same strength. The high degree of symmetry of the flavin radicals means that very little difference is expected between the singlet yields generated in each of the two potentials. Comparing the traces in figure 5.10, we see that the singlet yield profile for the biaxial case retains fractionally more similarity to the static case than that for the uniaxial potential. However, this is a small change and the system

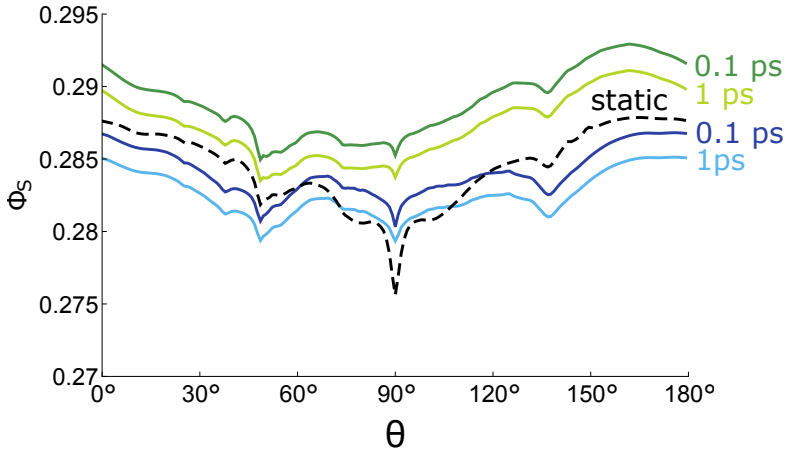


Figure 5.10: Comparison of the singlet yield profiles for the 10-spin model of FAD-Trp when the flavin radical is allowed to move freely within a uniaxial (green lines) or biaxial (blue lines) potential. The uniaxial potential is described by equation (5.37) with $A = 27$. The biaxial potential is given by equation (5.55), also with $A = 27$. The correlation time for the motion (indicated on graph) is assumed to be the same around each axis. i.e. $D_x = D_y = D_z$. The singlet yield of the fully static, oriented radical pair is shown for reference (black, dashed line). The radical recombination lifetime is 10 μs.

otherwise behaves in the same way as described in section 5.5.

By contrast, the relaxation behaviour of tryptophan, which has a large number of rhombic hyperfine interactions, is strikingly different when motion is confined around all three axes. Even in the weak biaxial potential that was treated, the shape of the singlet yield profile is only weakly affected by motion of the tryptophan radical with correlation times of 10 ps or less (figure 5.11). This implies both that relaxation induced by the tryptophan motion is slow and that motional averaging of the hyperfine interactions in the tryptophan radical has little effect on the shape of the singlet yield profile. If it were possible to treat stronger potentials (e.g. the $A = 100$ potential, which allows an average deviation of 10° from the static orientation), we would expect even slower relaxation, with the spike feature possibly remaining visible for correlation times of 100 ps or even 1 ns.

This is in keeping with the observations made in chapter 4 that the shape and size of the spike is dictated primarily by the hyperfine interactions in the flavin radical. Interestingly, the background anisotropy, which appears to be more strongly associated with the hyperfine interactions in tryptophan, is also preserved in the traces in figure 5.11. This

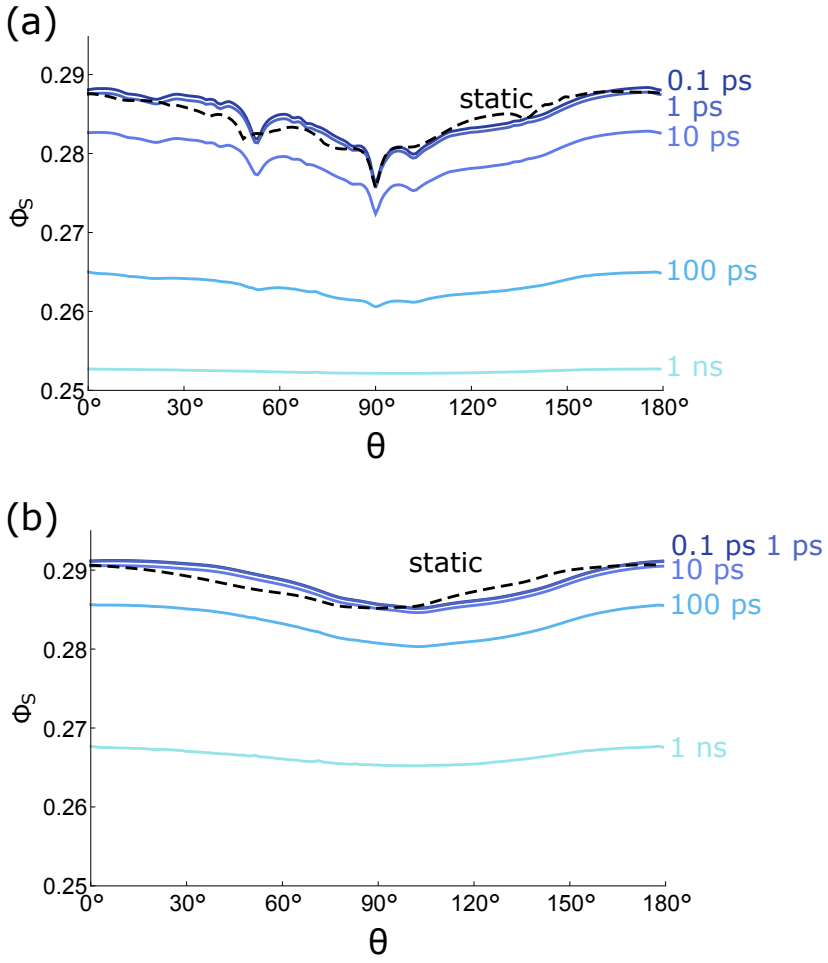


Figure 5.11: Singlet yield profiles for the 10-spin model of FAD-Trp when the tryptophan radical is allowed to move freely within a biaxial potential. The potential is given by equation (5.55) with $A = 27$. The correlation time for the motion (indicated on graph) is assumed to be the same around each axis. i.e. $D_x = D_y = D_z$. The singlet yield of the fully static, oriented radical pair is shown for reference (black, dashed line). The radical recombination lifetimes are (a) 10 μs and (b) 1 μs.

suggests that the singlet yield is not sensitive to small changes to the hyperfine interactions in tryptophan, provided the degree of asymmetry is not significantly altered.

Overall, these results demonstrate that motion of the tryptophan radical is less detrimental to the compass signal than motion of the flavin radical. This means that there is less requirement for tryptophan to be as tightly constrained, in keeping with its position nearer the surface of the protein.

5.7 Conclusions

In this chapter, I have developed and validated a more realistic model of internal rotations of the radical pair and used it to confirm and extend the conclusions made in chapter 4 about the effect of fast molecular motion.

As with the two-site hopping model, calculations on the toy radical pair have shown that the rate of relaxation increases when the correlation times for rotation are decreased towards 10 ns. Relaxation is also faster when the radicals are more weakly constrained and deviate further, on average, from their equilibrium orientation. In contrast to the two-site model, the approach used in this chapter provided a realistic description of the motion over a wide rage of ordering potentials and was most easily applied to weak potentials that allowed a large average deviation.

Building on the results of chapter 4, it was shown how motion alters the criteria for compass design. A balance must always be struck between optimising the singlet yield in the static limit and minimising the potentially destructive effects of relaxation. Furthermore, in regimes of slow relaxation, rotational averaging can potentially be beneficial, if it brings the hyperfine interactions closer to their optimal static values. In particular, motional averaging can increase the cylindrical symmetry of the effective hyperfine interactions, which tends to improve the anisotropy of the singlet yield. The exact balance of all these effects and hence the definition of an ideal hyperfine interaction depends strongly on the lifetime of the radical pair, the amplitude and frequency of its wobbling motion and the desired shape of the singlet yield. As none of these parameters are definitely known for the avian compass, it is impossible to make precise judgements about the exact types of motion that would be most beneficial.

However, the simulations of the flavin-tryptophan radical pair in cryptochrome indicate that the hyperfine interactions in the flavin radical are already close to optimal. Rotational averaging of the hyperfine tensors therefore offers no advantage and librational motion of the flavin ring should be as constrained as possible to minimise relaxation. Within the

5° ordering potential predicted by molecular dynamics simulations, the compass signal is preserved over a range of physically realisable diffusion rates.

By contrast, rotational diffusion of tryptophan causes fast relaxation unless the correlation time is short. However, as predicted at the end of chapter 4, the dimensions of the spike are relatively insensitive to small changes in the hyperfine tensors caused by librational motion of the indole ring, particularly when motion is constrained around more than one axis. The tryptophan radical could therefore be allowed less restricted motion than the flavin radical, in keeping with its position close to the surface of the cryptochrome. Based on the observations in this chapter and chapter 4, a secondary radical with fewer, smaller and more symmetric hyperfine tensors could provide a better alternative to tryptophan in forming a radical pair compass with a flavin radical.

It is worth noting that the simulations performed here only consider the effects of internal rotation of one radical at a time. In reality, both radicals will be moving, which will likely compound the detrimental effects of relaxation. In addition, there will be other types of motion that have not been considered here, including fluctuations in the dihedral angles between different parts of the radical and electron-hopping between the tryptophan (and possibly tyrosine) residues in the electron transport chain [117, 147]. It is possible that some of these types of motion could improve the immunity of the system to relaxation or even amplify the anisotropy of the compass signal [117].

Overall, the results of this investigation suggest that, under a set of stringent but feasible conditions, a cryptochrome compass could still function in the presence of spin relaxation caused by internal rotations of the two radicals. However, if other sources of relaxation are also considered, it becomes difficult to see how a sufficiently strong signal could be preserved within our current model of the radical pair compass.

Chapter 6

Interaction of the compass with polarized light

The requirement for a high degree of ordering, as discussed at the start of chapter 4 makes the compass inherently sensitive to polarized light. Studies to experimentally probe the effect of polarized light on birds' orientation behaviour have begun to appear in the literature [50]. This chapter will briefly consider the problems that arise from this polarization sensitivity and then look at how they could be avoided by careful arrangement of the cells that contain the magnetoreceptors.

6.1 Skylight polarization

Skylight is naturally polarized by scattering off particles as it passes through the atmosphere [161, 162]. The dominant features of the polarization pattern produced by these scattering events are shown in figure 6.1. The isolines for the degree of polarization form concentric circles around the position of the sun, with a band of maximum polarization passing through the sky at 90° to the sun. Hence, the polarization pattern shifts as the sun moves through the sky. In a clear sunlit sky, the maximum degree of polarization

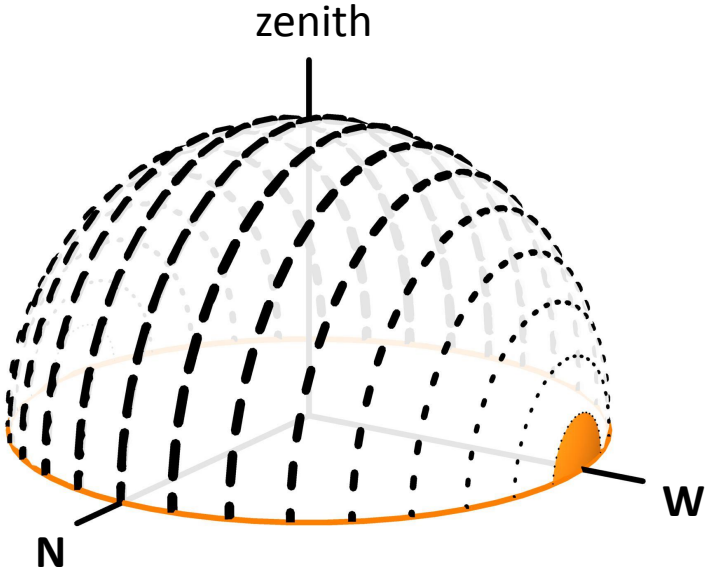


Figure 6.1: Representation of skylight polarization according to the Rayleigh sky model when the sun is on the horizon (orange) in the west. The directions and weights of the short black lines represent the e-vectors of light perceived by an observer at the centre of the celestial hemisphere. [*Figure published as part of figure 1 in Ref. [165].*]

is ≈ 0.75 [162–164]. The electric vector of the light from any given point in the sky is polarized along an axis tangential to the polarization isoline.

These features are captured by the Rayleigh model of skylight polarization [166–168], which assumes that all scattering events are elastic. Using the Rayleigh model, the degree of polarization of a ray of light detected by an observer is

$$\Lambda = \frac{\Omega \sin^2 a}{1 + \cos^2 a}, \tag{6.1}$$

where a is the angle between the line of sight $\boldsymbol{s}_\mathrm{g}$ of the observer and the position of the sun. The electric vector of the polarized light ray is oriented perpendicular to the scattering plane that passes through the observer, the sun and the observed point in the sky. It can be calculated as

$$\boldsymbol{e}_\mathrm{g} = \boldsymbol{s}_\mathrm{g} \times \boldsymbol{p}_\mathrm{sun}, \tag{6.2}$$

where $\boldsymbol{p}_\mathrm{sun}$ is the position vector of the sun.

Many of the bird species used to study the avian magnetic compass are night-migratory

songbirds so it is the polarization of the evening and night sky that is the most relevant. Moonlight is already weakly polarized before it enters the Earth's atmosphere. The degree of polarization depends on the angle between the sun, moon and Earth, with the maximum degree of polarization (8.7%) occuring when the moon is towards the end of its first quarter [162, 169, 170]. When it enters the atmosphere, moonlight is scattered in exactly the same way as sunlight. Polarization through scattering dominates the natural polarization. Consequently, the polarization pattern of a moonlit sky is the same as for a sunlit sky, with the sun in the equivalent position [162]. However, the degree of polarization of a moonlit sky is 'expected to be less' than for a sunlit sky [171]. As moonlight is much dimmer, the night-time polarization pattern is 'about a million' times weaker than in a sunlit sky [172] and is hence more easily corrupted by artificial light sources [171].

Furthermore, skylight polarization is not generally considered to be particularly robust to hazy or cloudy conditions as light is rapidly depolarized by multiple scattering events off ice crystals and water droplets in the clouds [171, 173]. Although the polarization of overcast skies is very similar to that of clear skies, the pattern is much noisier and the degree of polarization is significantly reduced (from ∼20-30% to ∼5-6% in ref. [173]). UV light maintains a higher degree of polarization under cloudy conditions than visible light [167]. This is perhaps significant in light of the fact that most known examples of polarized light sensitivity are mediated by UV receptors [174].

6.2 Polarization vision and polarization sensitivity

6.2.1 The photoselection effect

The probability p of a molecule absorbing a photon of light depends on the relative orientation ω of the electric vector $\boldsymbol{e}$ of the light and the transition dipole moment $\boldsymbol{t}_{\mathrm{m}}$ of

the molecule in the following way:

$$p = [\boldsymbol{t}_{\mathrm{m}} \cdot \boldsymbol{e}]^2 = |\boldsymbol{t}_{\mathrm{m}}|^2 |\boldsymbol{e}|^2 \cos^2 \omega. \tag{6.3}$$

This phenomenon is known as photoselection. Light is maximally absorbed when the electric vector lies parallel to the transition dipole moment. When $\boldsymbol{e}$ and $\boldsymbol{t}_{\mathrm{m}}$ are perpendicular, no light is absorbed. The electric vector $\boldsymbol{e}$ always lies in a plane perpendicular to the direction of propagation of the light ray $\boldsymbol{v}$. For 100% linearly polarized light, $\boldsymbol{e}$ has a unique orientation in this plane whereas for unpolarized light all orientations of $\boldsymbol{e}$ perpendicular to $\boldsymbol{v}$ occur with equal probability.

6.3 Birds' eyes

Birds rely heavily on vision and have (relatively) some of the largest eyes in the animal kingdom, particularly compared to the size of their brains [175]. The shape of their eyes can be divided into three categories: flat, globose and tubular [176, 177]. All three shapes are based on a (distorted) hemisphere and are distinguished by the increasing length of the anterior-posterior axis. None of these shapes resemble typical near-spherical mammalian eyes but are thought to minimize the weight of the eye whilst maintaining the focal length [176].

The most important parameter describing the shape and size of the eye is the (anterior) focal length: the distance from the posterior nodal point in the lens to the posterior focal point on the back of the retina [175, 176]. With a larger focal length the image is spread over a greater area of the retina (and hence a greater number of photoreceptors). The size of the image on the retina can also be adjusted by varying the refractive index of the cornea and the lens [176].

When light enters the eye, it passes through the cornea, anterior chamber, lens and vitreous body before it hits the retina, all of which are transparent to wavelengths going

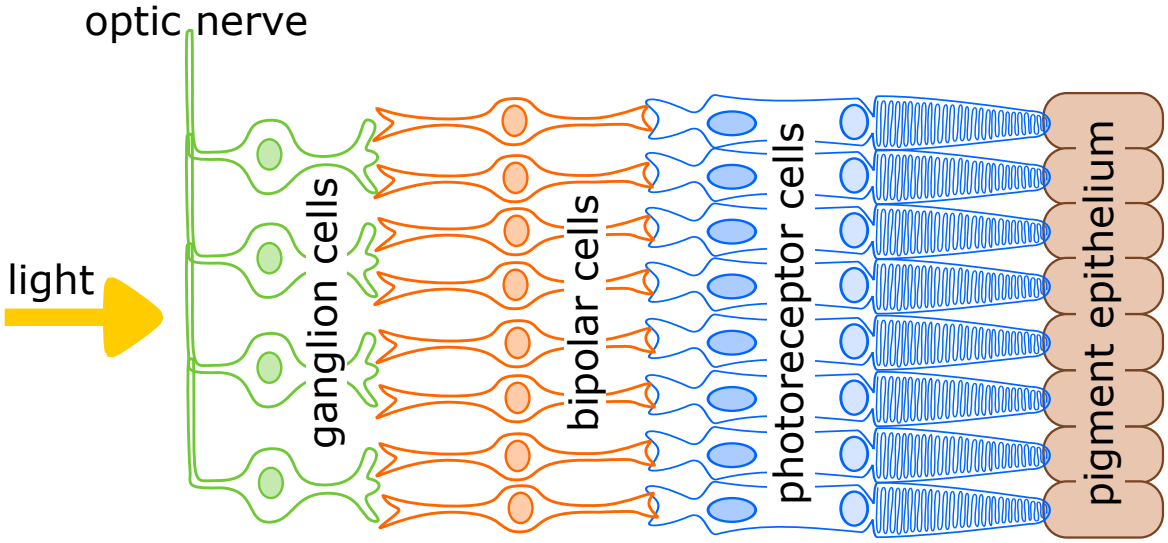


Figure 6.2: Structure of the retina. Light must pass through a layer of ganglion cells and a layer of bipolar cells before it reaches the photoreceptor cells. The ganglion cells, whose axons lead to the optic nerve, may receive input from different numbers of photoreceptor cells to tailor the resolution and light sensitivity of the retina.

down to the near-UV region (130 nm) [175]. They are also thought not to alter the polarization of light before it reaches the retina [178]. At the retina, light travels through layers of bipolar and ganglion cells before it reaches the photoreceptor cells attached to the pigment epithelium at the back of the retina (figure 6.2) [59, 175, 177, 179]. The retina has no veins, to prevent shadows and light-scattering [175]. Oxygen is instead served to the retina by a structure called the pecten; a pleated mass of blood vessels protruding out of the surface of the retina that is extremely effective at providing oxygen and nutrients to the retinal cells [175, 177, 180]. The densities of different types of cells dictate how well-adapted the eye is to perform different tasks. The ability of the eye to detect objects under very low light conditions can be maximized by increasing the density of photoreceptor cells and having several photoreceptors feed into each ganglion cell. By contrast, reducing the number of photoreceptors per ganglion cell improves the resolution of the image at the expense of light sensitivity [176, 177].

The ratio of photoreceptor to ganglion cells is not uniform across the retina. Regions with a higher density of ganglion cells reveal one way that birds are adapted to their

environments. These may occur in a long horizontal strip (visual streak) across the centre of the retina, for birds that need to detect predators or threats along the horizon [177], or in one or more circular regions (area centralis) for focusing on smaller details, like food in front of the bird [175, 179]. High densities of ganglion cells may even be associated with small depressions in the retina (fovea) that further enhance image resolution. This is common in raptors, which have two foveae (within a visual streak) that can resolve incredible detail (e.g. a 2 mm insect from the top of an 18 m high tree [175]).

Photoreceptor cells come in several varieties (figure 6.3) [181, 182], including rods, which are active under low light; cones, which are active in daytime light levels and are tuned to different wavelengths, and double cones, which make up to 50% of the cone population of some birds [59, 179, 182]. In birds, cones are associated with an oil droplet in their inner segment [175, 177, 183], which can be coloured or clear [184]. They act as a cut-off filter to tune the wavelength sensitivity of the cone and offer protection from high-energy UV radiation. It is also thought that they may help focus light onto the visual pigments within the cell [183].

The outer segments of rod and cone cells contain ordered stacks of free-floating (rods) or folded (cones) membrane discs [181], which house a range of visual pigments, such as rhodopsin. Combined with the oil droplets, the presence of different pigments tunes the cell to different wavelengths of light, equipping birds with sensitively gradated colour vision [175, 183]. Like image resolution, colour sensitivity may vary across the retina.

Despite the obvious complexity and variation in birds' eyes, the work in this chapter assumes a relatively simple model of the eye. Although it cannot capture the exact way that particular parts of the image may be magnified, focused or blurred out, it captures the information that is available to the birds without making any unjustifiable assumptions about how that information might be processed. The retina is modelled as a hemisphere (figure 6.4) with the pupil at its centre. The photoreceptor cells form a grid across the whole retina, with cells equally spaced in two positioning Euler angles, θ and ϕ. (Note that this results in a greater cell density at the centre of the retina.) The third Euler

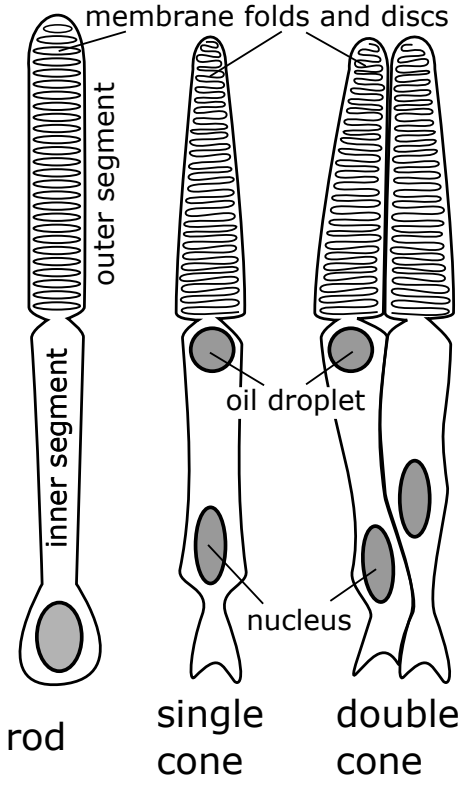


Figure 6.3: Varieties and structure of photoreceptor cells.

angle, η, is used to rotate the cells so that they have a uniform orientation relative to their line of sight. This prevents a discontinuity in the centre of the retina. All the cells are assumed to have their long cylindrical cell axis directed towards the pupil [185–188].

6.3.1 Known mechanisms of polarization sensitivity

When discussing polarized-light sensitivity, a distinction should be drawn between 'polarization-sensitivity-mediated behaviour' and true polarization vision [189]. The first refers to behaviours (commonly observed in navigation) where the animal locks onto or aligns themselves to a specific polarization pattern or signal. True polarization vision requires more complex processing to discriminate between e.g. e-vector angle and intensity and then respond to these signals. To separately detect all properties of polarized light (e-vector angle, degree of polarization and intensity), signals would need to be integrated from three receptors that each preferentially absorb different polarizations

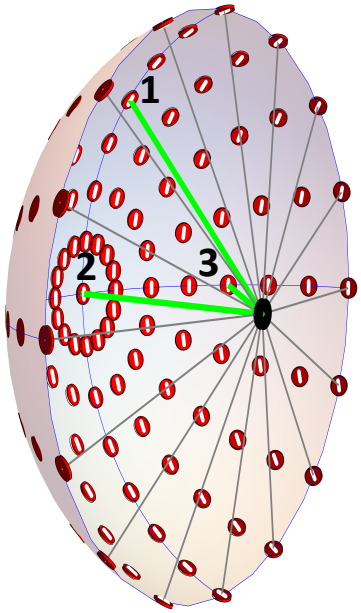


Figure 6.4: Schematic representation of an eye showing representative AB pairs of photoreceptor cells (red discs) distributed around the retina, modelled as a hemisphere with the pupil (black spot) at its centre. The white line through each of the red discs indicates the direction of the transition dipole moment in the two cells. Three rays of light (green) are shown entering the eye through the pupil and hitting the retina at points 1, 2 and 3. [*Figure published as part of figure 3 in Ref. [165].*]

of light. With the exception of a recently studied species of bee [190], all currently known polarization-sensitive systems are simpler than this with only two orthogonal e-vector sensitivities [189]. Thus far, land animals with polarization sensitivity have largely shown 'polarization-sensitivity-mediated behaviour', often responding to the celestial polarization pattern, whilst most known cases of true polarization vision have been found in underwater animals [189, 191].

In insects (invertebrates) polarized light sensitivity is mediated by UV receptors. UV-sensitive photoreceptor cells in the insects' eyes are found in pairs with perpendicularly arranged microvilli (rhabdomeres) [189, 192]. Photopigment molecules are fixed on the microvilli and are consequently held in a highly ordered arrangement. When exposed to polarized light, the members of each pair of perpendicularly arranged receptor cells have 90° shifted responses, which act antagonistically on the rate of neuron firing to create an integrated signal [191]. Combining the signals in this way gives increased sensitivity and

filters out light intensity changes [192].

Insects use a simple method to navigate using polarized light. The photoreceptors in each eye segment are arranged in a pattern that roughly matches the polarization pattern of the sky [189, 192]. To orient, the insect then scans the sky by rotating about its vertical body axis [192]. This is reminiscent of the head scans performed by birds when orienting themselves. The signals from all the cell pairs are summed by large integrative neurons. When this summed response is at a maximum, the insect is aligned with the symmetry plane of the sky. This mechanism can be predictably disrupted by light with only one or a few e-vector alignments [192]. Only a small part of the retina, containing less than 10% of all the photoreceptors is needed for the polarized light compass. In this region the photoreceptors remain straight, rather than twisting as they pass through the retina to preserve the orientation of the photopigments [192].

Of particular pertinence to the consideration of night-migratory birds, is one species of dung beetle that has been found to use the moonlight polarization pattern to navigate in a straight line away from a dung heap [172]. This is the first (and possibly only) known example of an animal using the moonlight polarization pattern for navigation. These beetles have wider rhabdoms (the light-sensitive part of the eye segment, containing the photopigments) than similar diurnal species, to enhance light collection [193]. In addition, electrophysiology experiments have demonstrated that the retinal cells of the nocturnal species have a polarization sensitivity approximately 10 times higher than in the diurnal species [194]. Laboratory experiments on certain species of crickets have found that they can detect highly polarized light at light intensities even lower than that of a clear, moonless night sky [193]. These two examples demonstrate that moonlight polarization is detectable by certain animals and therefore has the potential to interfere with the functioning of the avian magnetic compass, which must necessarily be sensitive to very low photon densities [59].

In vertebrates, photoreceptor cells contain membrane stacks rather than microvilli [189]. Photopigments in the membrane stacks are not held in such a rigid arrangement and can be

disordered around the membrane normal [195]. For this reason, most vertebrates appear to be insensitive to polarized light [196]. As for invertebrates, polarization sensitivity requires that signals from adjacent cells are compared [189].

Double cones have generally been considered to play a role in polarized light sensitivity in vertebrates. In pigeons, particularly large numbers of double cones are found in the polarization-sensitive part of the retina (the part that looks at the sky) [177, 183]. Current theory suggests that (in fish at least), the ellipsoidal partitions of the inner segments of double cones act as partial dielectric mirrors that preferentially reflect, refract and scatter particular polarizations, leading to a variation in the intensity of light incident on the outer segments of neighbouring cones [197, 198]. This theory is supported by the observation that these partitions have a higher lipid and protein content than the surrounding cytoplasm and hence a higher refractive index (i.e. they possess the characteristics of a dielectric mirror). For this mechanism to work, it is important that the inner segment partitions are tilted or asymmetric with respect to the optic axis of the eye. Notably, in polarization-insensitive fish species, the paired cone partitions are straight rather than curved so this condition is not met. In addition, neighbouring UV cones (polarization sensitivity in fish also occurs only in the UV region) are displaced such that their outer segments are in line with the inner segments of the double cones [197].

In polarization-sensitive fish, the double cones are arranged in square mosaics with the long axis of the inner segment rotated by 90° around each side of the square. UV single cones in the corners of the square would receive the same light intensity if they weren't preferentially illuminated by reflected polarized light from the double cone inner segment partitions. By comparing the signals from the corner cells, polarization and light intensity effects can be separated [197].

All the mechanisms of polarized light sensitivity in vertebrates and invertebrates involve the comparison of signals from multiple populations of receptors with different responses to a polarized light cue. Different responses can only be achieved if some component of the system is highly ordered. The receptors furthermore need to share a visual field,

have the same wavelength-sensitivity, and cooperate to produce a shared output that is independent of light intensity [191].

6.3.2 Can birds perceive polarized light?

In vertebrates, polarized light vision has only ever been observed in species that have photoreceptor mosaics made up of regularly-spaced, orthogonally oriented double cones [199]. Double cones are the most common cone type in the avian retina [59, 200] and currently their function is not well understood. However, it is possible that they are arranged in a way that would facilitate polarization sensitivity.

The photoreceptor mosaics in chicken retinas have been studied in some detail [182, 201]. It was found that all cone types show some type of long-range order. This arises naturally from the observation that cones of the same type seem to 'repel' each other. Around each cone is an 'exclusion zone' in which other cones of the same type are highly unlikely to be found [182]. Packing the photoreceptors whilst obeying the boundaries of the exclusion zones automatically creates some degree of order. The spatial correlation function for any given cone type shows decaying concentric rings, reminiscent of hydration spheres in aqueous solutions. Double cones show a higher degree of topological order than any of the single cone types [182]. Similarly ordered distributions of cones have also been observed in woodpeckers, house sparrows and pigeons [182].

Within the global pattern of rod and cone cells, double cones are locally arranged in a number of recognisable patterns.[1] One of the most common patterns to find is a 'Cross' pattern, in which two opposite double cones point towards each other and the other two point away from each other. Also common is a 'Ring' pattern that looks very similar to the square arrangement responsible for polarized light sensitivity in fish.

Despite apparently being well-equipped to detect polarized light, true polarization vision has not been reliably demonstrated in birds. Initially successful attempts [202, 203] to

[1] Some beautiful images of these patterns may be found in reference [201].

train homing pigeons to respond to polarized light cues in an operant conditioning experiment were not reproducible and are thought to have been confounded by light intensity artefacts [200, 204].

The most convincing evidence that birds respond in any way to polarized light comes from cue conflict experiments testing migratory birds' use of skylight polarization patterns and the Earth's magnetic field as cues for navigation [200]. By allowing birds to view the sky naturally, through a depolarizing filter or not at all, it was shown that birds will only change their preferred orientation relative to the magnetic field if they are able to see the polarization pattern across the sky [45–49]. A full view of the sky through a depolarizing filter does not elicit a change in preferred orientation, suggesting that the birds are not able to use other visual cues, like the position of the sun [45, 49], to recalibrate their compass. Birds appear to calibrate their magnetic compass twice a day, at sunrise and sunset, using the polarization patterns around the horizon [48]. Regular recalibration means that the compass continues to work accurately even in areas of magnetic anomaly and in instances where birds migrate across the equator and need to transition from heading 'equatorwards' to 'polewards' [47, 204]. It also allows the compass to adapt to secular variation of the magnetic field. Pigeons are similarly thought to use celestial polarization patterns at twilight to calibrate their sun compass ([205] cited in [46, 177])

A very recent study by Muheim *et al.* (reference [50]) has attempted to unravel exactly how polarized light cues interact with the magnetic compass: whether the birds detect the two stimuli as independent pieces of information that jointly inform their choice of preferred direction, or whether polarized light directly modulates the magnetic compass, creating a combined signal from which a heading can be identified. The authors concluded that polarized light does interact directly with the magnetic compass. However, unlike cue conflict experiments, which can be performed in a natural arena, these experiments were conducted under entirely artificial conditions in a four-arm Plexiglas maze inside a tent of matt white sheeting. In this and other artificial experiments it becomes much harder to control for the possibility of light intensity artefacts that are created when surfaces

preferentially reflect light of a certain polarization - a problem that has undermined the validity of many studies investigating responses to polarized light [200, 204]. Whereas birds with a view of the sky receive light directly from the source of polarization (i.e. the scattering event that polarized the light), the birds in the Plexiglas maze mainly receive reflected light, making the exact polarization difficult to control. In addition, the matt fabric surrounding the clear maze is a diffuse reflector, which would likely depolarize any light reflected off it. As such, the polarization conditions to which the birds were exposed are unclear.

The position of the bird in the maze was tracked throughout the experiment and at regular intervals it was noted which arm the bird was in. Each bird was then assigned a preferred direction based on a vector sum of unit vectors describing the direction of the arm occupied by the bird at each interval. The preferred direction could lie in any direction, creating a set of continuous data that was analysed using standard circular statistical methods. This was arguably not an accurate reflection of an experiment where birds were forced to choose between only four discrete directions [206].

The lack of control over the experimental conditions or an appropriate statistical analysis suggests that further experiments may be needed to validate the conclusion that polarized light interacts directly with the magnetic compass. As simultaneous detection of the two stimuli seems likely to cause problems (discussed in the next section), I will assume that it would be preferable to have a magnetic compass system that is insensitive to polarized light and focus on ways that this could be achieved through careful ordering of the cells.

6.3.3 The problem with polarization sensitivity

In the radical pair mechanism, the strength of the signal produced by a population of aligned magnetoreceptor molecules (e.g. the cryptochromes in a single cell) in response to a magnetic stimulus depends not only on the direction and intensity of the magnetic

field but also on the number of radical pairs responsible for the signal. The fact that the radical pairs are created photochemically means that changes in light intensity would affect the output of a single cell in a manner that would be indistinguishable from a change in the direction of the magnetic field experienced by the cell. This can be understood by considering a simple example. Suppose that when a field is applied in one direction, 10% of the radical pairs in a single receptor cell react to form the signalling state and that when the field is applied in a perpendicular direction, 20% of radical pairs end up in the signalling state. If the incident light entering the receptor cells excites 100 cryptochrome molecules to produce 100 radical pairs, there will be 10 molecules of signalling state produced when the field is in direction 1 and 20 molecules of signalling state produced when the field is in direction 2. Now suppose that the cell is exposed to more intense light, such that 200 cryptochrome molecules are excited to produce 200 radical pairs. When the field is in direction 1, 20 molecules of signalling state will be produced, exactly the same as if the field were in direction 2 under the lower light intensity.

It is worth noting that this argument applies even if the magnetically sensitive radical pair is produced in a light-independent reaction subsequent to the initial photoexcitation, as has been suggested in a recent study [28]. The number of radical pairs (and hence of signalling state molecules) depends on the concentration of the photochemically produced precursor state and therefore still depends on the number of photons absorbed.

A closely related problem is encountered in colour vision, where a single photoreceptor cell cannot distinguish a change in colour (increased intensity at some wavelengths at the expense of others) from a change in brightness (a uniform increase of intensity across all wavelengths). The problem is resolved by detecting the relative stimulation of neighbouring photoreceptor cells containing pigments tuned to different wavelengths [207]. Thus, the retina is capable of integrating signals from neighbouring photoreceptor cells. It has recently been suggested that magnetic sensing could work in a similar fashion, by detecting the ratio of signals from neighbouring receptor cells that have different orientations within the retina and hence different magnetic responses (see figure 9 in Ref. [59]).

Double-cone photoreceptor cells, the most common cone type in the avian retina [182], seem particularly appealing in this context: the two member-cones would be exposed to very similar light intensities and could house populations of magnetoreceptor molecules with well-defined orientations [59].

Although comparing the signals generated by two populations of ordered magnetoreceptor molecules seems an obvious and elegant solution to the light-intensity problem, it raises questions about the effect of linearly polarized light on the operation of the compass sensor. As described in section 6.3.1, this set up exactly describes a mechanism for detecting polarized light. Vertebrate photoreceptor cells are normally insensitive to polarization because the opsin photoreceptor proteins in the membrane discs are free to rotate around the direction of the incoming light, so that, taken together, the opsins within a photoreceptor cell absorb all polarizations of light with equal probability [208, 209]. However, for the compass to work, the magnetoreceptors must be at least partially aligned [58]. Due to the photoselection effect, aligned populations of magnetoreceptors will preferentially absorb light of a particular polarization [210]. Under natural skylight conditions, this recreates the 'light intensity problem' described above - that differences in the signals produced by cells in different parts of the retina may be as much due to the difference in photon absorption as to a difference in magnetic field direction. Furthermore, small differences in the magnetic field signal are easily overwhelmed by much larger variations in the polarization pattern across the sky (see figure 6.5). In the following section, I derive conditions under which the signals from two populations of ordered magnetoreceptor molecules can be used to give a pure magnetic signal, independent of light intensity and polarization.

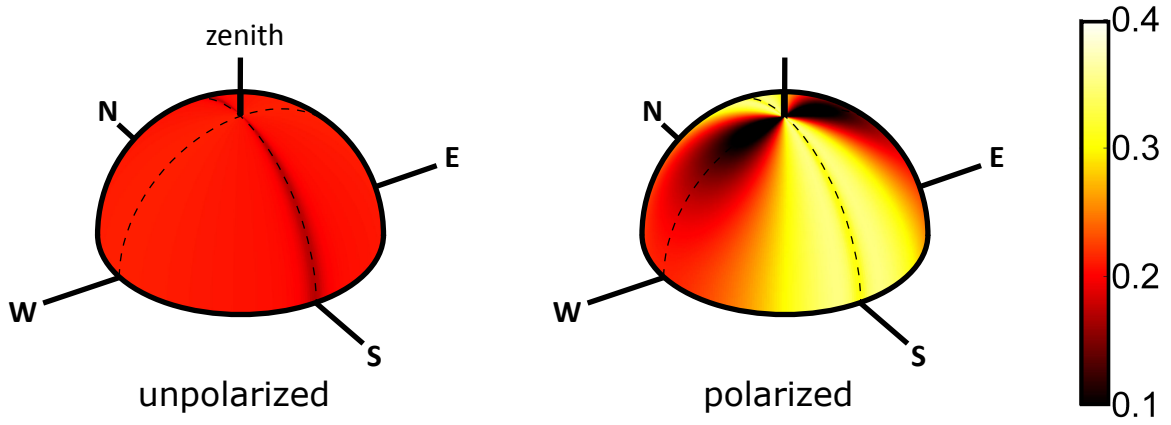


Figure 6.5: Signal from a cell containing a magnetoreceptor molecule with $\alpha = 0°$, $\beta = 90°$, $\gamma = \pi/2°$ (see section 6.5.1). The hemispheres represent the signal received by the cell as the eye scans across the sky. The skylight is either completely unpolarized (left) or 75% polarized by Rayleigh scattering (right), with the sun setting in the west. The magnetic field is pointing North, with an inclination of 66° ($I = 66°$, $D = 0°$). The dark stripe (North-South direction) in the magnetic signal can be clearly seen under unpolarized light but it completely hidden by the skylight polarization pattern when the light is polarized.

6.4 Geometric requirements

6.4.1 Relative orientation of magnetoreceptor cells

For the ratio of signals from two adjacent cells, A and B, in the retina to contain only information about the magnetic field, light-induced radical pairs must be formed with identical probability in the two cells but the magnetic field effects on the receptors in A and B must differ. This imposes certain restrictions on the relative orientations of the magnetoreceptor molecules in A and B, the external magnetic field and the direction of propagation of the incoming light. Using simple geometric and biological arguments, these restrictions can be translated into a set of conditions for the orientation of the magnetoreceptors within the cells and the cells within the retina.

Initially, three assumptions are made. The first is that A and B, being side-by-side in the retina, receive equal numbers of photons per second. The second is that the orientations of the magnetoreceptor molecules contained in each cell are identical. The only difference

between the two cells is that one is rotated relative to the other by an angle, and around an axis, to be determined.

Note that it is not necessary to assume that the cells contain equal numbers of photoreceptor molecules. For example, if cell A contains twice as many photoreceptors as cell B, the probability of a photon being absorbed will always be twice as high in cell A compared to cell B, regardless of changes in light intensity or polarization. Therefore the ratio of signals A/B will be multiplied by a constant factor of 2. The important thing is that the probability per photoreceptor of absorbing a photon is identical in the two cells. However, for simplicity, equal numbers of photoreceptor molecules in each cell are assumed for all the simulations presented here.

The third assumption is that the magnetoreceptor molecules have perfect rotational order within the cells. The implications of this will be discussed in section 6.6.2. The eye is imagined to operate as a pinhole camera. Rays of light are assumed to enter the eye via the pinhole (the pupil) and to strike the retina at a position determined simply by their direction, without refraction or scattering.

To convert identical numbers of cryptochromes from the resting state to the radical pair state, the probability of photon absorption by the flavin chromophores should be the same in the two cells. The absorption probability (equation (6.3)) is proportional to $\cos^2\omega$, where ω is the angle between the transition dipole moment $\boldsymbol{t}_{\mathrm{m}}$ of the magnetoreceptor and the electric vector $\boldsymbol{e}$ of the incoming light [60]. For 100% linearly polarized light, $\boldsymbol{e}$ has a unique orientation in the plane perpendicular to the light-propagation direction, $\boldsymbol{v}$, whereas for unpolarized light all orientations of $\boldsymbol{e}$ perpendicular to $\boldsymbol{v}$ occur with equal probability. In cryptochrome, $\boldsymbol{t}_{\mathrm{m}}$ for the $S0 \rightarrow S1$ transition lies approximately parallel to the long in-plane axis of the isoalloxazine ring system of the flavin chromophore, labelled $\boldsymbol{y}_{\mathrm{m}}$ in 6.6(a) [60, 211, 212]. This dipole moment is responsible for the absorption of blue light. The transition dipole moment for the $S0 \rightarrow S2$ transition (UV region) lies at an angle within the plane of the ring system.

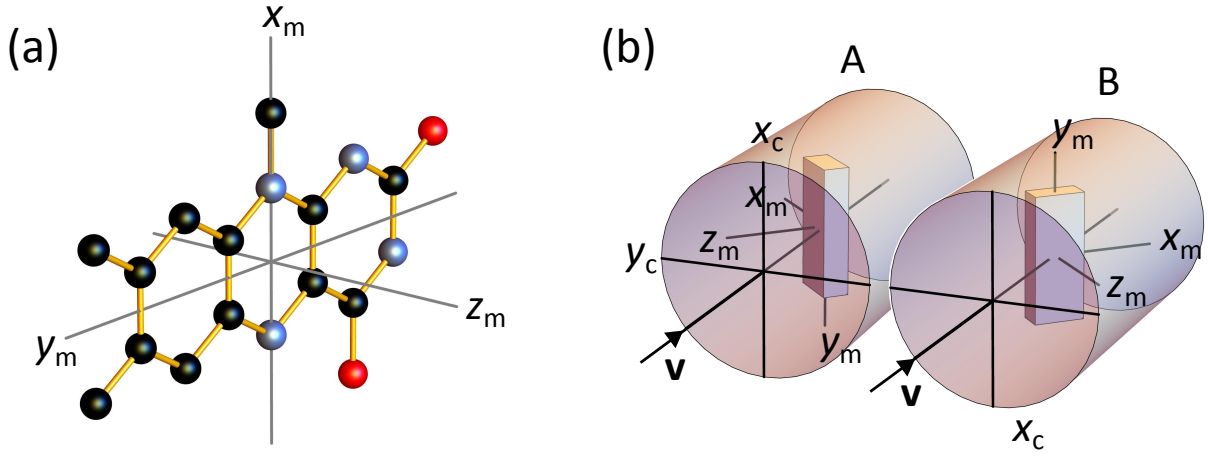


Figure 6.6: (a) Structure of the tricyclic flavin component of the flavin adenine dinucleotide chromophore in cryptochrome including the molecular axis system, $(\boldsymbol{x}_\mathrm{m}, \boldsymbol{y}_\mathrm{m}, \boldsymbol{z}_\mathrm{m})$. The transition dipole moment is approximately parallel to $\boldsymbol{y}_\mathrm{m}$, the long, in-plane axis of the aromatic ring system. The approximate symmetry axis of the magnetic response of a flavin-containing radical pair is parallel to $\boldsymbol{z}_\mathrm{m}$. Black, blue and red balls indicate carbon, nitrogen and oxygen atoms. Hydrogen atoms are not shown. (b) Schematic representation of two adjacent cylindrical photoreceptor cells, A and B, in the retina. The direction of propagation of the incoming light, $\boldsymbol{v}$, is parallel to $\boldsymbol{z}_\mathrm{c}$, the long symmetry axis of the cells. A and B are identical apart from a 180° rotation around $\boldsymbol{v}$. Both cells are considered to contain populations of aligned flavin chromophores, one of which is shown in each cell as a cuboid with approximately the same aspect ratios as the flavin structure in (a). The TDM vectors ($\boldsymbol{y}_\mathrm{m}$) are parallel in A and B and both are perpendicular to $\boldsymbol{z}_\mathrm{c}$. The magnetic symmetry axes ($\boldsymbol{z}_\mathrm{m}$) form an angle β with $\boldsymbol{z}_\mathrm{c}$ and lie in the $y_\mathrm{c}z_\mathrm{c}$-plane. [*Figure published as part of figure 1 in Ref. [165].*]

For the remainder of this chapter the 'transition dipole moment of cryptochrome' will refer only to that for the $S0 \rightarrow S1$ transition. However, it should be noted that, as the following derivation makes no assumption about the orientation of cryptochrome or its transition dipole moment, in relation to the cell or the magnetically sensitive axis, the resulting criteria are completely general and hold for absorption in the UV as well.

For the separation mechanism to work for all possible polarizations, the cell rotation needs to preserve ω for an e-vector with an arbitrary direction in the plane perpendicular to $\boldsymbol{v}$. The conditions for this to occur can be deduced using elementary vector algebra.

Taking $\boldsymbol{v}$ as the z-axis, the electric vector $\boldsymbol{e}$ must lie in the xy-plane and has the general

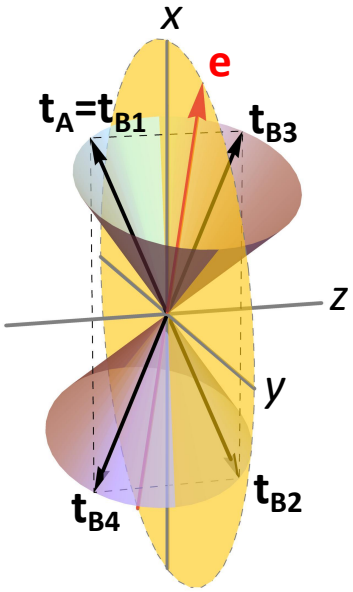


Figure 6.7: Representation of the transition dipole moment vectors in equation (6.7). The incoming light propagates along the z-axis. $\boldsymbol{e}$ is an arbitrarily chosen electric vector (red) in the xy plane (yellow) and is the axis of the two cones. $\boldsymbol{t}_{\mathrm{A}}$ is the TDM of an arbitrarily oriented magnetoreceptor molecule in cell A. For the particular $\boldsymbol{e}$-vector shown in the figure, any molecule in cell B whose TDM vector points from the origin to any point on the surface of one of the two cones has the same probability of absorbing a photon as does the molecule whose TDM vector is $\boldsymbol{t}_{\mathrm{A}}$ (because all such vectors have the same value of $\cos^2(\omega)$ (equation (6.3))). However, only four of these vectors, $\boldsymbol{t}_{\mathrm{B1}}$, $\boldsymbol{t}_{\mathrm{B2}}$, $\boldsymbol{t}_{\mathrm{B3}}$ and $\boldsymbol{t}_{\mathrm{B4}}$ (all in the xz plane) give the same probability of photon absorption as $\boldsymbol{t}_{\mathrm{A}}$ for *any* direction of $\boldsymbol{e}$ in the xy plane. $\boldsymbol{t}_{\mathrm{B1}}$ is identical to $\boldsymbol{t}_{\mathrm{A}}$. $\boldsymbol{t}_{\mathrm{B2}} = -\boldsymbol{t}_{\mathrm{B1}}$ (i.e. $\boldsymbol{t}_{\mathrm{B1}}$ exactly inverted). $\boldsymbol{t}_{\mathrm{B3}}$ and $\boldsymbol{t}_{\mathrm{B4}}$ are, respectively, the reflections of $\boldsymbol{t}_{\mathrm{B1}}$ and $\boldsymbol{t}_{\mathrm{B2}}$ in the xy plane. Only $\boldsymbol{t}_{\mathrm{B4}}$ is related to $\boldsymbol{t}_{\mathrm{A}}$ by a rotation around the z-axis. [*Figure published as part of figure 1 in Ref. [165].*]

form

$$\boldsymbol{e} = (e_x, e_y, 0). \tag{6.4}$$

If the transition dipole moment (TDM) of the receptor molecules in cell A is defined, without loss of generality, by the unit vector

$$\boldsymbol{t}_{\mathrm{A}} = (t_x, 0, t_z), \tag{6.5}$$

then $\cos^2(\omega)$ is equal to the square of the scalar product of vectors $\boldsymbol{e}$ and $\boldsymbol{t}_{\mathrm{A}}$:

$$\cos^2(\omega) = (\boldsymbol{e} \cdot \boldsymbol{t}_{\mathrm{A}})^2 = e_x^2 t_x^2. \tag{6.6}$$

For the particular e-vector shown in figure 6.7, a molecule in cell B whose TDM vector points from the origin to any point on the surface of one of the two cones satisfies $\cos^2(\omega_{\mathrm{A}}) = \cos^2(\omega_{\mathrm{B}})$, i.e. has the same probability of absorbing a photon as does the molecule in cell A whose TDM vector is $\boldsymbol{t}_{\mathrm{A}}$. However, only the four vectors in equation (6.7) give the same probability of photon absorption as does $\boldsymbol{t}_{\mathrm{A}}$ for any direction of $\boldsymbol{e}$ in the xy plane (i.e. any polarization of the light):

$$\boldsymbol{t}_{\mathrm{B1}} = (t_x, 0, t_z), \quad \boldsymbol{t}_{\mathrm{B2}} = (-t_x, 0, -t_z), \quad \boldsymbol{t}_{\mathrm{B3}} = (t_x, 0, -t_z), \quad \boldsymbol{t}_{\mathrm{B4}} = (-t_x, 0, t_z). \tag{6.7}$$

That is, to satisfy equation (6.6), the rotation that relates A and B must either invert the x-component or the z-component of the TDM or invert both or leave both unchanged.

The next stage is to use biological arguments to eliminate three of the four TDM orientations in equation (6.7). The most probable location of the magnetoreceptors is inside rod or cone photoreceptor cells [23]. Cryptochromes have been found in several types of photoreceptor cells [102–104], and of all the cells in the retina the photoreceptors are the only ones known to contain multiple highly ordered structures - the membrane discs - that could provide an ideal scaffold for aligning and immobilizing magnetoreceptor molecules [106]. Both rod and cone photoreceptors are roughly pencil-shaped [181] with approximate cylindrical symmetry (see figure 6.3); they connect to the layer of horizontal and bipolar cells at one end and to the pigment epithelium at the other (see section 6.3 and figure 6.2). It therefore seems most likely that the A↔B rotation would be around the long symmetry axis of the cell which, in vertebrate eyes, points directly at the pupil irrespective of the cell's position in the retina [185–188]. We therefore infer that the A↔B rotation should be around the direction of the incoming light, $\boldsymbol{v}$ (defined above as the z-axis) in our pinhole-camera eye.

Returning to equation (6.7), this conclusion immediately excludes $\boldsymbol{t}_{\mathrm{B2}}$ and $\boldsymbol{t}_{\mathrm{B3}}$ because a z-rotation of a vector leaves its z-component unchanged. $\boldsymbol{t}_{\mathrm{B1}}$, which is identical to $\boldsymbol{t}_{\mathrm{A}}$,

may also be ruled out on the basis that the TDM would have to be parallel to the rotation axis (i.e. $\boldsymbol{v}$), in which case $\cos^2(\omega_\mathrm{A})$ and $\cos^2(\omega_\mathrm{B})$ would both equal zero (equation (6.3)) and no light would be absorbed by the magnetoreceptors in either cell. Thus (figure 6.7), we are left with $\boldsymbol{t}_\mathrm{B4}$. Because $\boldsymbol{t}_\mathrm{A}$ and $\boldsymbol{t}_\mathrm{B4}$ differ only in the sign of their x-components, the rotation around the z-axis that relates the two cells, i.e. converts $\boldsymbol{t}_\mathrm{A}$ into $\boldsymbol{t}_\mathrm{B4}$, must be 180°. For the rest of this chapter, the cells will be assumed to be related in this way.

It is only possible to single out the solution above by making the (biologically sensible) assumption that the rotation axis of the cell lies parallel to the direction of travel of incoming light rays. However, if this assumption proved false, the analysis above can be extended to derive the appropriate rotation.

To transform $\boldsymbol{t}_\mathrm{A}$ onto any of the vectors $\boldsymbol{t}_\mathrm{B2}$, $\boldsymbol{t}_\mathrm{B3}$ or $\boldsymbol{t}_\mathrm{B4}$, the cell rotation axis needs to lie in the plane bisecting the angle between them. The details of the rotation and the biological feasibility of each case is briefly outlined below:

1. $\boldsymbol{t}_\mathrm{A}\rightarrow\boldsymbol{t}_\mathrm{B2}$: *Inversion of the TDM*

   The transformation can be effected by a 180° rotation around any axis perpendicular to the TDM ($\boldsymbol{t}_\mathrm{m}$). This solution has the advantage that the position of the rotation axis is not defined relative to the direction of the light rays. Consequently, pairs of cells across the retina could be oriented relative to the retina surface rather than the pupil or the incoming light.

2. $\boldsymbol{t}_\mathrm{A}\rightarrow\boldsymbol{t}_\mathrm{B3}$

   The axis for this rotation must lie in the plane of e-vectors, which bisects $\boldsymbol{t}_\mathrm{A}$ and $\boldsymbol{t}_\mathrm{B3}$. The is equivalent to saying that incoming light rays have to hit the receptor cells side-on, which will prevent the cells collecting any light at all and is clearly impractical.

3. $\boldsymbol{t}_\mathrm{A}\rightarrow\boldsymbol{t}_\mathrm{B4}$

   Defining a physically motivated axis system, spanned by $\boldsymbol{t}_\mathrm{m}$, the vector $(\boldsymbol{t}_\mathrm{A}\times\boldsymbol{t}_\mathrm{B4})$ (which lies in the plane of e-vectors) and the vector $(\boldsymbol{t}_\mathrm{m}\times(\boldsymbol{t}_\mathrm{A}\times\boldsymbol{t}_\mathrm{B4}))$, $\boldsymbol{t}_\mathrm{m}$ can ini-

tially be expressed as (1,0,0) and, after the rotation as (cos(2χ),0,sin(2χ)), where χ is the angle between $\boldsymbol{t}_{\mathrm{m}}$ and $\boldsymbol{v}$. The rotation axis in this coordinate frame is (cos(χ) sin(ψ),cos(ψ),sin(χ) sin(ψ)), where ψ is the angle between the rotation axis and ($\boldsymbol{t}_{\mathrm{A}}\times\boldsymbol{t}_{\mathrm{B4}}$). Using the Rodrigues' formula (equation(3.1)), the rotation axis and angle α and the orientation of $\boldsymbol{t}_{\mathrm{m}}$ can be shown to be related by

$$\sin(\chi)\sin(\alpha) + \cos(\psi)\cos(\chi)(1-\cos(\alpha)) = 0. \tag{6.8}$$

When $\chi = 90°$, the solution becomes equivalent to inversion of the TDM, described above. Similarly, when $\psi = 90°$, the situation collapses into the original case where the rotation axis is parallel to $\boldsymbol{v}$. The closer ψ is to 90°, the more light the cell will be able to collect.

6.4.2 Orientation of magnetoreceptor molecules

Having determined the required cell rotation, we now use a similar analysis to identify and hence exclude those orientations of magnetoreceptor molecules that lead to the same magnetic signals from the two cells. Theoretical treatments of the anisotropy of the magnetic field effect on flavin-containing radical pairs in cryptochrome have found that the yield of the putative signalling state of the protein approximates to [60, 61, 68]

$$\Phi_{\mathrm{S}}(\xi) = \sum_{n=0,1,2,\ldots} a_n(\sin^2(\xi))^n, \tag{6.9}$$

where the a_n coefficients are constants for a given magnetic field strength and ξ is the angle between the magnetic-field vector and the z_{m}-axis of the flavin in the radical pair (figure 6.6a). $\Phi_{\mathrm{S}}(\xi)$ is cylindrically symmetric around $\boldsymbol{z}_{\mathrm{m}}$ and invariant to inversion of the magnetic field direction ($\xi \to 180° - \xi$), consistent with the *axial* nature of the avian compass [23]. If the lifetime of the spin-coherence in the radical pair is less than about a microsecond, the terms with $n = 0$ and $n = 1$ dominate and $\Phi_{\mathrm{S}}(\xi)$ has a broad,

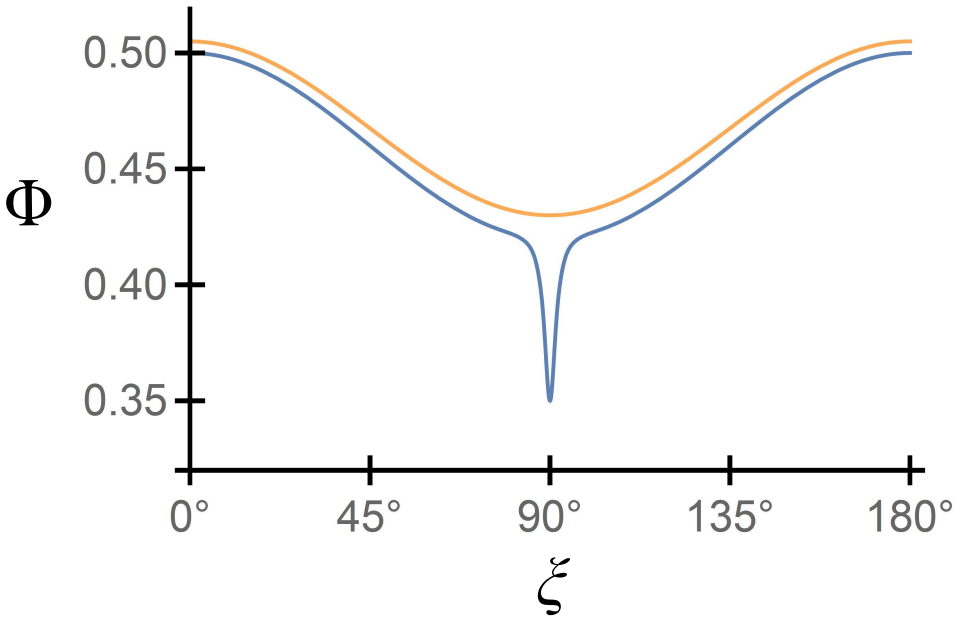


Figure 6.8: Idealized orientation-dependence of the yield of the signalling state of cryptochrome formed from the flavin-tryptophan radical pair state of the protein. $\Phi_{\mathrm{S}}(\xi)$ is modelled (equation (6.9)) so as to resemble the results of calculations presented in Ref. [61] using $a_0 = 0.5$, $a_1 = -0.08$, $a_{128} = -0.01$, $a_{512} = -0.03$, $a_{2048} = -0.03$. ξ is the angle between the magnetic field axis and the z_{m} axis of the flavin structure shown in figure 6.6(a). The orange and blue traces are appropriate for radical pairs with short and long lifetimes, respectively. The former, which includes just the a_0 and a_1 terms, has been shifted vertically by +0.015 for clarity. [*Figure published as part of figure 1 in Ref. [165].*]

shallow minimum at $\xi = 90°$ (because $a_1 < 0$, figure 6.8). For longer coherence lifetimes, the flavin-tryptophan radical pair shows, additionally, a strong, narrow 'spike' [61] (see section 4.3.1 and 6.8), that can be modelled by higher order terms ($n \geq 2$) in equation (6.9).

The magnetic signals (equation (6.9)) from cells A and B will only be identical when $\sin^2(\xi_{\mathrm{A}}) = \sin^2(\xi_{\mathrm{B}})$. Writing the two magnetic symmetry axes (related, as above, by a 180° z-rotation) as the unit vectors $\boldsymbol{z}_{\mathrm{mA}} = (m_x, m_y, m_z)$ and $\boldsymbol{z}_{\mathrm{mB}} = (-m_x, -m_y, m_z)$, and the magnetic field axis as the unit vector $\boldsymbol{b} = (b_x, b_y, b_z)$, gives:

$$\begin{aligned}\sin^2(\xi_{\mathrm{A}}) &= 1 - \cos^2(\xi_{\mathrm{A}}) = 1 - (\boldsymbol{b} \cdot \boldsymbol{z}_{\mathrm{mA}})^2 = 1 - (b_x m_x + b_y m_y + b_z m_z)^2, \\ \sin^2(\xi_{\mathrm{B}}) &= 1 - \cos^2(\xi_{\mathrm{B}}) = 1 - (\boldsymbol{b} \cdot \boldsymbol{z}_{\mathrm{mB}})^2 = 1 - (-b_x m_x - b_y m_y + b_z m_z)^2. \end{aligned} \tag{6.10}$$

The only way that $\sin^2(\xi_A) = \sin^2(\xi_B)$ for an arbitrary direction of the magnetic field, $\boldsymbol{b}$, is when either $m_z = 0$ or $m_x = m_y = 0$, i.e. when the two z_m-axes are either perpendicular or parallel to the cell rotation axis. In both cases, the two cells would deliver identical magnetic information and the ratio of their outputs would be independent of the magnetic field. In practice, therefore, orientations of the magnetoreceptor molecules that are not too close to either of these extremes should lead to significantly different signals from A and B.

In summary, for axially symmetric receptor cells with the symmetry axis parallel to the incoming light, the ratio of the signals from two adjacent cells will provide pure magnetic information if their orientations are related by a 180° rotation around the cell axis. Within the cell, the cryptochromes should be positioned so that their z_m-axes are neither approximately parallel nor approximately perpendicular to the cell axis (figure 6.6b).

6.5 Visualising the signal

6.5.1 Reference frames

Table 6.1: Summary of reference frames.

Basis vectors	Description
$\boldsymbol{x}_m$, $\boldsymbol{y}_m$,$\boldsymbol{z}_m$	Molecular frame. $\boldsymbol{z}_m$ is perpendicular to the plane of flavin ring system. $\boldsymbol{x}_m$ is parallel to the short in-plane axis. $\boldsymbol{y}_m$ is parallel to the long in-plane axis.
$\boldsymbol{x}_c$, $\boldsymbol{y}_c$, $\boldsymbol{z}_c$	Cell frame. $\boldsymbol{z}_c$ is parallel to the long symmetry axis of cell. $-\boldsymbol{z}_c$ points towards pupil.
$\boldsymbol{x}_r$, $\boldsymbol{y}_r$, $\boldsymbol{z}_r$	Retina frame. $\boldsymbol{z}_r$ points from the pupil to the centre of the retina directly opposite across the eyeball.
$\boldsymbol{x}_g$, $\boldsymbol{x}_g$, $\boldsymbol{z}_g$	Geo frame. $\boldsymbol{z}_g$ points north. $\boldsymbol{y}_g$ points East. $\boldsymbol{x}_g$ points up.

The signal generated at any given point on the retina depends on the relative orientations of the magnetoreceptor, the Earth's magnetic field and the electric vector of the incident light at that location. To describe the orientations of all three entities in the most intuitive manner, a number of different reference frames are used. In the following sections, the different reference frames (summarised in Table 6.1) are defined and transformations are given between them. The angles defining the orientations of various objects in the appropriate reference frame are summarised in Table 6.2.

Table 6.2: Summary of angles.

Angles	Frame	Description
σ, τ	Geo	Polar angles describing the line of sight.
I, D	Geo	Inclination and declination of the magnetic field.
ϕ, θ, η	Retina	Euler angles describing the position of the cell in the retina.
α, β, γ	Cell	Euler angles describing the orientation of the magnetoreceptor molecule in the cell.
κ, λ	Molecular	Polar angles describing the direction of the transition dipole moment.
ξ, δ	Molecular	Polar angles describing the direction of the magnetic field.

Geo Frame

The Geo frame is defined by the three perpendicular vectors ($\boldsymbol{x}_\mathrm{g}$, $\boldsymbol{y}_\mathrm{g}$, $\boldsymbol{z}_\mathrm{g}$). The vector $\boldsymbol{z}_\mathrm{g}$ points North, $\boldsymbol{y}_\mathrm{g}$ points East and $\boldsymbol{x}_\mathrm{g}$ points vertically up.

Within this frame, the orientation of the magnetic field is described by its inclination I and declination D (see figure 6.9(a)). Using these two angles, the magnetic field vector

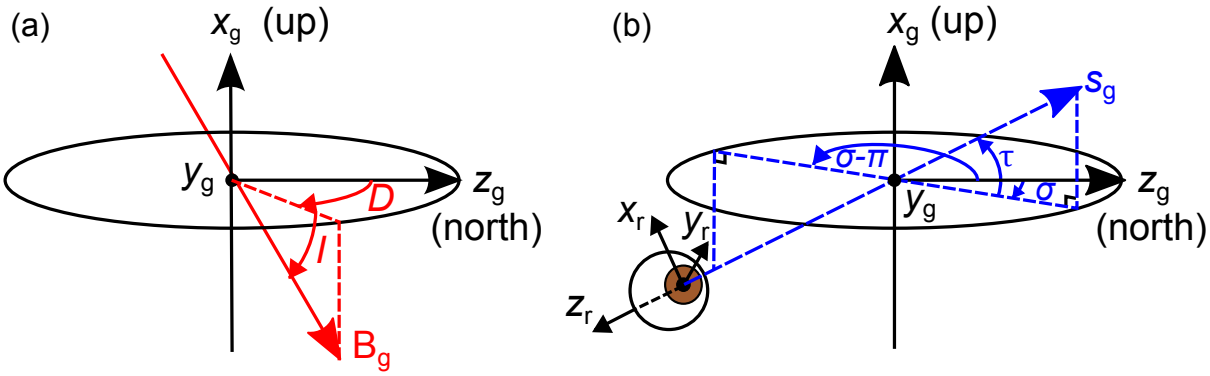


Figure 6.9: (a) Orientation of the magnetic field in the geo frame. The inclination (I) and declination (D) angles are shown in red. (b) Polar angles specifying the direction of the line of sight ($\boldsymbol{s}_g$) in the geo frame. In both images, the y_g axis is coming directly out of the page.

is

$$\boldsymbol{B}_g = \begin{pmatrix} -\sin(I) \\ \cos(I)\sin(D) \\ \cos(I)\cos(D) \end{pmatrix}. \tag{6.11}$$

The line of sight ($\boldsymbol{s}_g$) of the bird is similarly defined using the two polar angles σ and τ (see figure 6.9(b)), such that

$$\boldsymbol{s}_g = \begin{pmatrix} \sin(\tau) \\ \cos(\tau)\sin(\sigma) \\ \cos(\tau)\cos(\sigma) \end{pmatrix}. \tag{6.12}$$

When the bird is looking horizontally north, $\sigma = \tau = 0$.

Retina Frame

Within the eye, magnetoreceptors cells are assumed to be found spread across the retina, as described in section 6.3. The retina frame, spanned by the perpendicular vectors ($\boldsymbol{x}_r$, $\boldsymbol{y}_r$, $\boldsymbol{z}_r$), is used as a reference to describe the positions of individual cells within the eye. The pupil is defined as the centre of the retina frame axis system, with $\boldsymbol{z}_r$ pointing towards the centre of the retina, directly opposite the pupil. The $\boldsymbol{x}_r$ axis is aligned vertically within

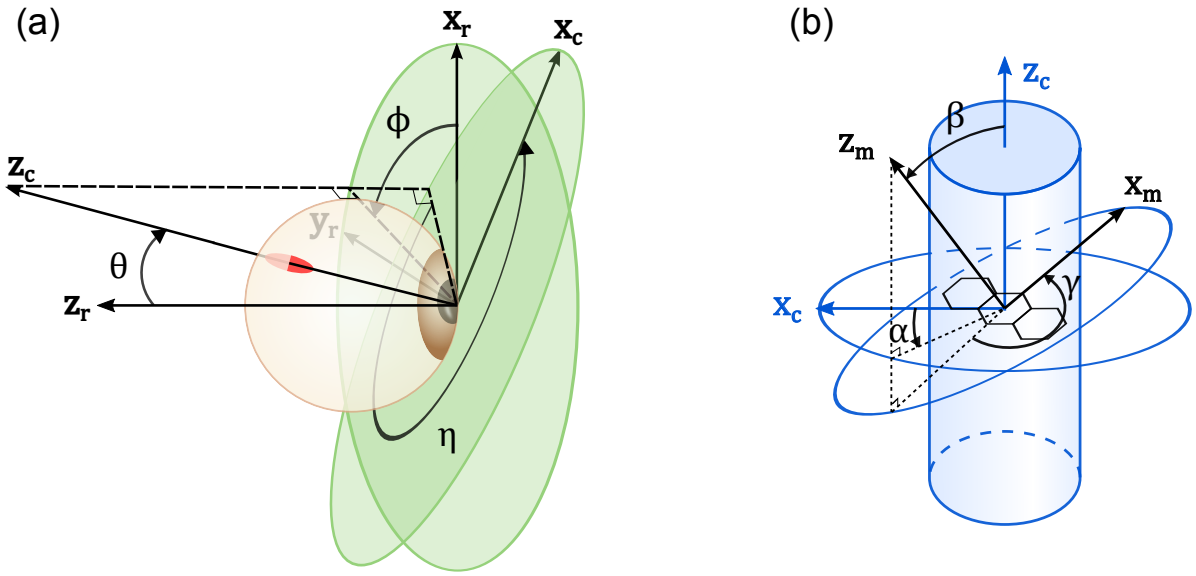


Figure 6.10: (a) Euler angles (ϕ, θ, η) defining the position and orientation of a cell (red oval) on the retina. (b) Euler angles (α, β, γ) defining the orientation of the magnetoreceptor within the cell.

the eye, such that, when $\sigma = \tau = 0$, $(\boldsymbol{x}_\mathrm{r}, \boldsymbol{y}_\mathrm{r}, \boldsymbol{z}_\mathrm{r})$=$(\boldsymbol{x}_\mathrm{g}, -\boldsymbol{y}_\mathrm{g}, -\boldsymbol{z}_\mathrm{g})$.

The position of any cell within the retina can be described by three Euler angles (ϕ, θ, η), (see figure 6.10(a)).

Cell Frame

In the same way that the retina frame is defined to allow for easy positioning of cells within the eye, the cell frame $(\boldsymbol{x}_\mathrm{c}, \boldsymbol{y}_\mathrm{c}, \boldsymbol{z}_\mathrm{c})$ is defined as a reference by which the orientation of the magnetoreceptor molecule can be defined. $\boldsymbol{z}_\mathrm{c}$ is chosen as the symmetry axis of the cylindrical cell, with the $-\boldsymbol{z}_\mathrm{c}$ axis pointing towards the pupil. The orientation of the magnetoreceptor is specified by the three Euler angles (α, β, γ), (see figure 6.10(b)).

Molecular Frame

Using the molecular frame the orientation of objects can be described relative to the important features of the radical pair, such as it's transition dipole moment. The three axes defining the molecular frame are chosen such that $\boldsymbol{z}_\mathrm{m}$ is perpendicular to the plane

of the aromatic ring system in the flavin cofactor, $\boldsymbol{y}_{\mathrm{m}}$ is parallel to the long in-plane axis of the ring system and $\boldsymbol{x}_{\mathrm{m}}$ is parallel to the short in-plane axis (see figure 6.6).

The transition dipole moment (TDM) is defined in the molecular frame by the polar angles κ and λ as

$$\boldsymbol{t}_{\mathrm{m}} = \begin{pmatrix} \sin(\kappa)\cos(\lambda) \\ \sin(\kappa)\sin(\lambda) \\ \cos(\kappa) \end{pmatrix}. \tag{6.13}$$

In the flavin-tryptophan radical pair the TDM is taken to lie along $\boldsymbol{y}_{\mathrm{m}}$, with $\kappa = \lambda = \pi/2$.

The magnetic field can similarly be defined by two polar angles (ξ,δ) in the molecular frame as

$$\boldsymbol{B}_{\mathrm{m}} = \begin{pmatrix} \sin(\xi)\cos(\delta) \\ \sin(\xi)\sin(\delta) \\ \cos(\xi) \end{pmatrix}. \tag{6.14}$$

This definition is useful when discussing the magnetic response of the radical pair.

Transformations between frames

Although it is convenient to discuss the absolute orientation of objects in whichever reference frame is the most intuitive, a common reference frame is needed to determine relative orientations and perform calculations.

The magnetic field, line of sight and TDM vectors can be expressed in any of the four reference frames using the following transformations:

$$\boldsymbol{W}_{\mathrm{c}} = R_z(\alpha)R_y(\beta)R_z(\gamma)\boldsymbol{W}_{\mathrm{m}} \tag{6.15}$$

$$\boldsymbol{W}_{\mathrm{r}} = R_z(\phi)R_y(\theta)R_z(\eta)\boldsymbol{W}_{\mathrm{c}} \tag{6.16}$$

$$\boldsymbol{W}_{\mathrm{g}} = R_x(\pi - \sigma)R_y(-\tau)\boldsymbol{W}_{\mathrm{r}} \tag{6.17}$$

$$\tag{6.18}$$

where $\boldsymbol{W}_{\mathrm{m}}$, $\boldsymbol{W}_{\mathrm{c}}$, $\boldsymbol{W}_{\mathrm{r}}$ and $\boldsymbol{W}_{\mathrm{g}}$ are general vectors in the molecular, cell, retina and geo frames respectively and $R_q(\Omega)$ are rotation matrices, defined as in section 3.1.2.

6.5.2 Simulation method

The signal received from a single magnetoreceptor cell is simply the magnetic field response Φ_{S} modulated by the probability that the magnetoreceptors within that cell can absorb a photon of polarized (p_{pol}) or unpolarized (p_{unpol}) light,

$$S = (\Lambda p_{\mathrm{pol}} + (1 - \Lambda) p_{\mathrm{unpol}})\, \Phi_{\mathrm{S}}. \tag{6.19}$$

The fraction of light that is polarized is given by the constant Λ (see section 6.1).

In the following simulations[2], the singlet yield profile for the 'toy' radical pair (section 4.3.2) is used to model the magnetic field response of spike-producing radical pairs. The dependence of the singlet yield on the angle ξ between the magnetic field and the $\boldsymbol{z}_{\mathrm{m}}$ axis can be described by

$$\Phi_{\mathrm{S}} = 0.5 - 0.08 \sin^2(\xi) - 0.01 \sin^{256}(\xi) - 0.03 \sin^{1024}(\xi) - 0.03 \sin^{4096}(\xi), \tag{6.20}$$

which has the form of equation (6.9). A second model with the higher order terms removed was used to compare the behaviour of spike and non-spike producing radical pairs. The singlet yield of this second model is

$$\Phi_{\mathrm{S}} = 0.5 - 0.08 \sin^2(\xi). \tag{6.21}$$

Equations (6.20) and (6.21) are illustrated in figure 6.8.

To calculate ξ for a given cell, the global magnetic field vector (equation (6.11)) is trans-

[2]The methods used here closely follow those in ref. [213], which also contains a number of preliminary simulations of different arrangements of cell pairs. These simulations inspired the more thorough, algebraic investigation made in this chapter.

formed into the molecular frame of the magnetoreceptors inside the cell using

$$\boldsymbol{B}_{\mathrm{m}} = R_z(-\gamma)R_y(-\beta)R_z(-\alpha-\eta)R_y(-\theta)R_z(-\phi)R_y(\tau)R_x(\sigma-\pi)\boldsymbol{B}_{\mathrm{g}}, \tag{6.22}$$

as described by equations (6.15) - (6.17). The angle ξ is then given by

$$\xi = \cos^{-1}\left(\frac{\boldsymbol{B}_{\mathrm{m,z}}}{|\boldsymbol{B}_{\mathrm{m}}|}\right). \tag{6.23}$$

To calculate the absorption probability for individual magnetoreceptors (equation (6.3)), one needs to know the orientation of the electric vector of the light as it hits any given receptor. According to the Rayleigh model (section 6.1), the fraction of light that is polarized and the orientation of the electric vector depend on where in the sky the light comes from relative to the position of the sun or moon (equation (6.2)). In the following calculations, the sun is positioned on the $-\boldsymbol{y}_{\mathrm{g}}$ axis to model the sun setting in the west (figure 6.9). As birds appear to calibrate their compass using polarized cues at sunrise and sunset, this was considered as the most relevant set of polarization conditions. The line of sight $\boldsymbol{s}_{\mathrm{g}}$ can be positioned relative to the sun in the geo frame using the angle a between $\boldsymbol{s}_{\mathrm{g}}$ and $\boldsymbol{p}_{\mathrm{sun}}$, and a second angle b, which acts as an azimuthal angle in the plane perpendicular to $\boldsymbol{p}_{\mathrm{sun}}$. Using these two angles, the line of sight vector is

$$\boldsymbol{s}_{\mathrm{g}} = \begin{pmatrix} \sin(a)\cos(b) \\ -\cos(a) \\ \sin(a)\sin(b) \end{pmatrix}. \tag{6.24}$$

The electric vector of the light is therefore expressed in the geo frame as

$$\boldsymbol{e}_{\mathrm{g}} = \begin{pmatrix} \sin(a)\cos(b) \\ -\cos(a) \\ \sin(a)\sin(b) \end{pmatrix} \times \begin{pmatrix} 0 \\ -1 \\ 0 \end{pmatrix} = \begin{pmatrix} \sin(a)\sin(b) \\ 0 \\ -\sin(a)\cos(b) \end{pmatrix}, \tag{6.25}$$

which normalizes to

$$\boldsymbol{e}_{\mathrm{g}} = \begin{pmatrix} \sin(b) \\ 0 \\ -\cos(b) \end{pmatrix}. \tag{6.26}$$

The values of a and b can be calculated for any point (σ, τ) in the sky by equating equation (6.24) and equation (6.12) to give

$$a = \cos^{-1}(-s_{\mathrm{g},y}) = \cos^{-1}(-\sin(\sigma)\cos(\tau)) \tag{6.27}$$

$$b = \tan^{-1}(s_{\mathrm{g},z}/s_{\mathrm{g},x}) = \tan^{-1}(\cos(\sigma)\cot(\tau)). \tag{6.28}$$

Using these relationships, the degree (equation (6.1)) and direction of polarization (equation (6.26)) can be calculated for the light reaching a cell looking at any point in the sky specified by (σ, τ). The probability of the receptors inside the cell absorbing polarized light $(\Lambda(\boldsymbol{e}_{\mathrm{m}} \cdot \boldsymbol{t}_{\mathrm{m}})^2)$ is calculated in the molecular frame after first transforming $\boldsymbol{e}_{\mathrm{g}}$ according to

$$\boldsymbol{e}_{\mathrm{m}} = R_z(-\gamma)R_y(-\beta)R_z(-\alpha-\eta)R_y(-\theta)R_z(\phi)R_y(\tau)R_x(\sigma-\pi)\boldsymbol{e}_{\mathrm{g}}. \tag{6.29}$$

The probability of absorbing unpolarized light does not depend on the line of sight in any way other than that light from different parts of the sky contains different proportions of polarized and unpolarized light. It is therefore easiest to start directly from the cellular frame by considering a ray of light of arbitrary polarization travelling along the $-\boldsymbol{z}_{\mathrm{c}}$ axis, straight through the centre of the cell. In the molecular frame the electric vector can be expressed as

$$\boldsymbol{e}_{\mathrm{m}} = R_z(-\gamma)R_y(-\beta)R_z(-\alpha)\left(\cos(\epsilon)\boldsymbol{x}_{\mathrm{c}} + \sin(\epsilon)\boldsymbol{y}_{\mathrm{c}}\right), \tag{6.30}$$

where ϵ is an angle describing the polarization of the light. Unpolarized light contains a mixture of all values of ϵ so the absorption probability must be averaged over ϵ to give

$$p_{\mathrm{unpol}} = \frac{1}{2\pi}\int_0^{2\pi} [\boldsymbol{t}_{\mathrm{m}} \cdot \boldsymbol{e}_{\mathrm{m}}]^2 d\epsilon. \tag{6.31}$$

Using the method above it is possible to simulate the information received by a single cell (or pair of neighbouring cells) as it looks around at different points in the sky. An alternative approach is to produce a 'visual modulation pattern', which acts as a pictorial representation of the information available across the entire eye when the bird looks in a given direction. This requires a few subtle alterations to the way the electric vector is calculated. First, the line of sight in the geo frame must now include the angles (ϕ, θ), which position each cell in the retina:

$$\boldsymbol{l}_{\mathrm{g}} = R_x(\pi - \sigma)R_y(-\tau)R_z(\phi)R_y(\theta) \begin{pmatrix} 0 \\ 0 \\ -1 \end{pmatrix}. \tag{6.32}$$

The angles a and b are also accordingly redefined by

$$a = \cos^{-1}(-l_{\mathrm{g},y}) \tag{6.33}$$

$$b = \tan^{-1}(l_{\mathrm{g},z}/l_{\mathrm{g},x}) \tag{6.34}$$

Similarly, for unpolarized light the absorption probability is calculated by averaging over all possible polarization angles (ϵ) in the plane perpendicular to $\boldsymbol{l}_{\mathrm{g}}$. We can no longer assume that this plane is spanned by $\boldsymbol{x}_{\mathrm{c}}$ and $\boldsymbol{y}_{\mathrm{c}}$ but rather define the plane by two general vectors, $\boldsymbol{a}_{1\mathrm{g}}$ and $\boldsymbol{a}_{2\mathrm{g}}$, perpendicular to $\boldsymbol{l}_{\mathrm{g}}$, such that

$$\boldsymbol{e}_{\mathrm{g}} = \cos(\epsilon)\boldsymbol{a}_{1\mathrm{g}} + \sin(\epsilon)\boldsymbol{a}_{2\mathrm{g}}. \tag{6.35}$$

The vectors $\boldsymbol{a}_{1\mathrm{g}}$ and $\boldsymbol{a}_{2\mathrm{g}}$ can be calculated using

$$\boldsymbol{a}_{1\mathrm{g}} = \frac{l_{\mathrm{g},y}\boldsymbol{x}_{\mathrm{g}} - l_{\mathrm{g},x}\boldsymbol{y}_{\mathrm{g}}}{(l_{\mathrm{g},y})^2 + (l_{\mathrm{g},x})^2} \tag{6.36}$$

$$\boldsymbol{a}_{2\mathrm{g}} = \boldsymbol{a}_{1\mathrm{g}} \times \boldsymbol{l}_{\mathrm{g}}. \tag{6.37}$$

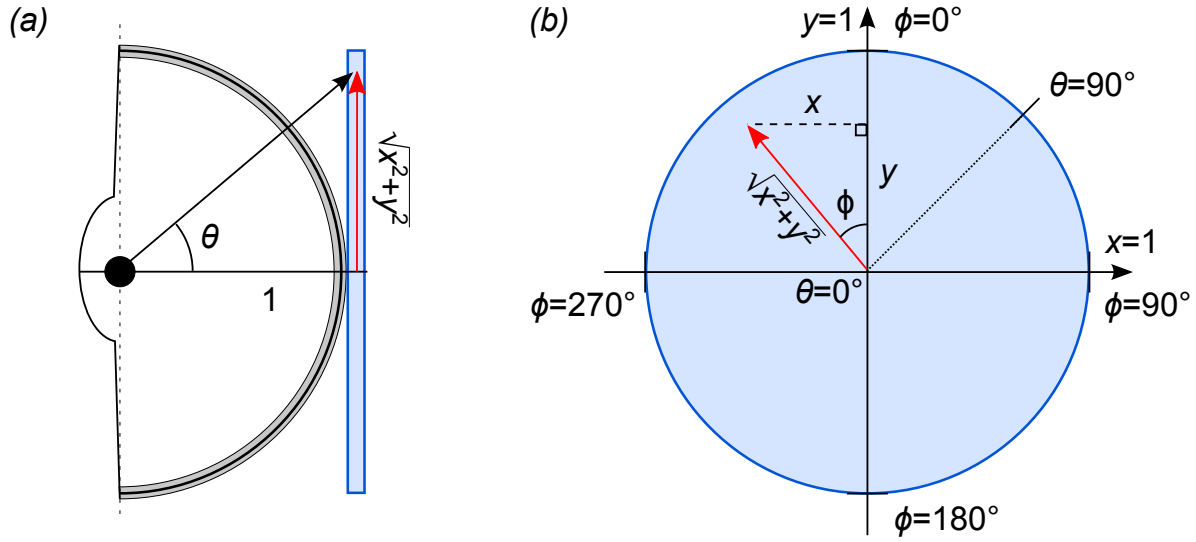


Figure 6.11: Mapping of points on the retina (grey), described by the angles θ and ϕ, onto a flat circular plane (blue) with cartesian x, y coordinates. The angle θ goes from 0° in the centre of the plane to 90° at its edge. (a) Side view of the eye and its mapping onto a plane behind the retina. (b) Relationship between (x, y) and (θ, ϕ).

Using these vectors, the electric vector of a ray of light in the molecular frame is

$$\boldsymbol{e}_{\mathrm{m}} = R_z(-\gamma)R_y(-\beta)R_z(-\alpha-\eta)R_y(-\theta)R_z(-\phi)\left(\cos(\epsilon)\boldsymbol{a}_{1\mathrm{g}} + \sin(\epsilon)\boldsymbol{a}_{2\mathrm{g}}\right). \tag{6.38}$$

This expression can be substituted into equation (6.31) to calculate the probability of absorbing unpolarized light. The total signal from the cell can be calculated using equation (6.19) as before.

To produce a visual modulation pattern, the signal from each cell is mapped onto a circular plane behind the retina. Figure 6.11 illustrates how the cartesian (x, y) coordinates of the plane are related to the positioning angles θ and ϕ. Mathematically, the mapping is described by the relations

$$\theta = 2\tan^{-1}\left(\sqrt{x^2+y^2}\right), \tag{6.39}$$

$$\phi = \tan^{-1}\left(\frac{x}{y}\right), \tag{6.40}$$

with $-1 \leq x, y \leq 1$.

6.5.3 Directional information

In section 6.4, conditions were derived under which the ratio of the signals from two adjacent cells in the retina depends only on the orientation of the cells with respect to the axis of the magnetic field. The methods introduced in section 6.5.2 are now used to explore the directional information conveyed by this arrangement of cells.

First, consider a single pair of cylindrical cells, A and B, located side-by-side in the retina at a position on the optical axis, i.e. diametrically opposite the pupil (figure 6.12). B is rotated relative to A by 180° around the direction of the incoming light, $\boldsymbol{v}$ (which in this case coincides with the optical axis). The cells contain identical magnetoreceptor molecules arranged as in figure 6.6(b) with the TDMs ($\boldsymbol{y}_{\mathrm{m}}$) aligned parallel to the $\boldsymbol{x}_{\mathrm{c}}$-axes of the cells and the magnetic symmetry axes ($\boldsymbol{z}_{\mathrm{m}}$) placed in the $y_{\mathrm{c}}z_{\mathrm{c}}$-plane at an angle of 45° to the symmetry axes of the cells ($\boldsymbol{z}_{\mathrm{c}}$). This arrangement was chosen to maximize the amount of light absorbed when the "eye" looks horizontally due north, under sunset light conditions. The magnetic signal has the form of equation (6.20).

The signals from each cell, $\Phi_{\mathrm{S}}(\xi_{\mathrm{A}})$ and $\Phi_{\mathrm{S}}(\xi_{\mathrm{B}})$, are calculated as the eye scans the sky by means of rotations around two perpendicular axes (pitch and yaw, figure 6.12). As the line of sight changes, each cell registers the spike whenever the $\boldsymbol{z}_{\mathrm{m}}$-axis of its magnetoreceptor molecules is perpendicular to the magnetic field axis, which here points north with an inclination angle of 66° relative to the horizontal. The panels in figure 6.13 show $\Phi_{\mathrm{S}}(\xi_{\mathrm{A}})$ and $\Phi_{\mathrm{S}}(\xi_{\mathrm{B}})$, respectively, projected onto the celestial sphere. The spike in the yield of the signalling state (figure 6.8) appears as a narrow band arcing across the sky and the two cells produce mirror-image patterns. This band pattern can be thought of as a slice through the plane perpendicular to the magnetic field, tilted by the offset between the $\boldsymbol{z}_{\mathrm{m}}$ axis and the line of sight of the cell (or bird). The remainder of the magnetic signal (the $n = 0$ and $n = 1$ terms in equation (6.20)) produces a much broader band that is difficult to detect in these figures.

The bands associated with the spikes are less apparent for the individual cells when the

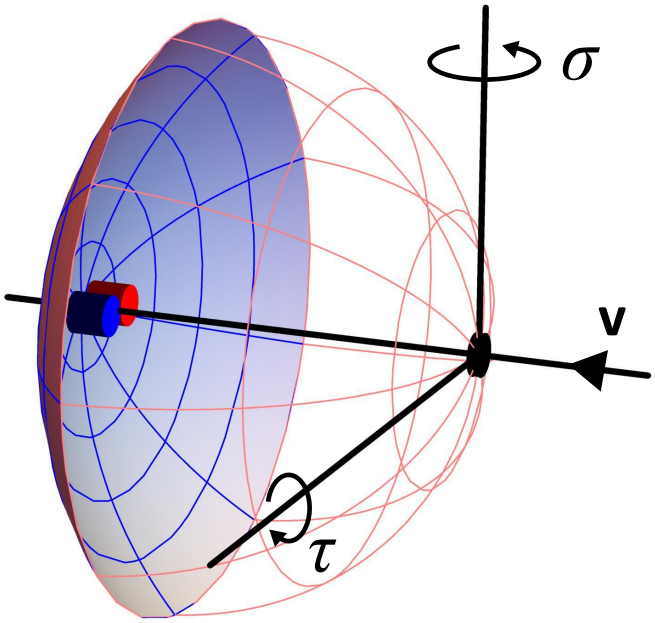


Figure 6.12: Schematic representation of an eye. Cells A and B (small blue and red cylinders) are positioned at the centre of the retina (pink/blue spherical section), diametrically opposite the pupil (black spot). The magnetic responses of A and B are calculated for different 'lines of sight' of the eye, obtained by rotating the eye around the indicated axes. σ and τ are the yaw and pitch angles, respectively. [*Figure published as part of figure 1 in Ref. [165].*]

light is polarized (figure 6.13 (c) and (d)) as the magnetic information is partially obscured by the strong variation in light absorption arising from photoselection. However, the ratio of the two signals, $\Phi_S(\xi_A)/\Phi_S(\xi_B)$, which displays a pattern of two bands, one derived from each cell, is, as expected, identical whether the incoming light is polarized or not (figure 6.13(e)). The two bands cross when the orientation of the eye causes the $\boldsymbol{z}_{mA}$ and $\boldsymbol{z}_{mB}$ axes to be simultaneously perpendicular to the magnetic field, producing a distinct feature that could be used to provide a precise compass bearing. For the geometry used to produce figure 6.13, this crossing marks magnetic north at an elevation angle equal to the complement of the magnetic inclination, i.e. 24°. A different choice of the orientation of the magnetoreceptor molecules in the cells either puts the crossing point at a different point in the sky or causes the two bands not to cross (a crossing point only occurs when the angle between the vector product $(\boldsymbol{t}_{m,A} \times \boldsymbol{t}_{m,B})$ and the $\boldsymbol{y}_c$-axis (figure 1c) is smaller than the inclination of the magnetic field, as shown in section 6.5.4).

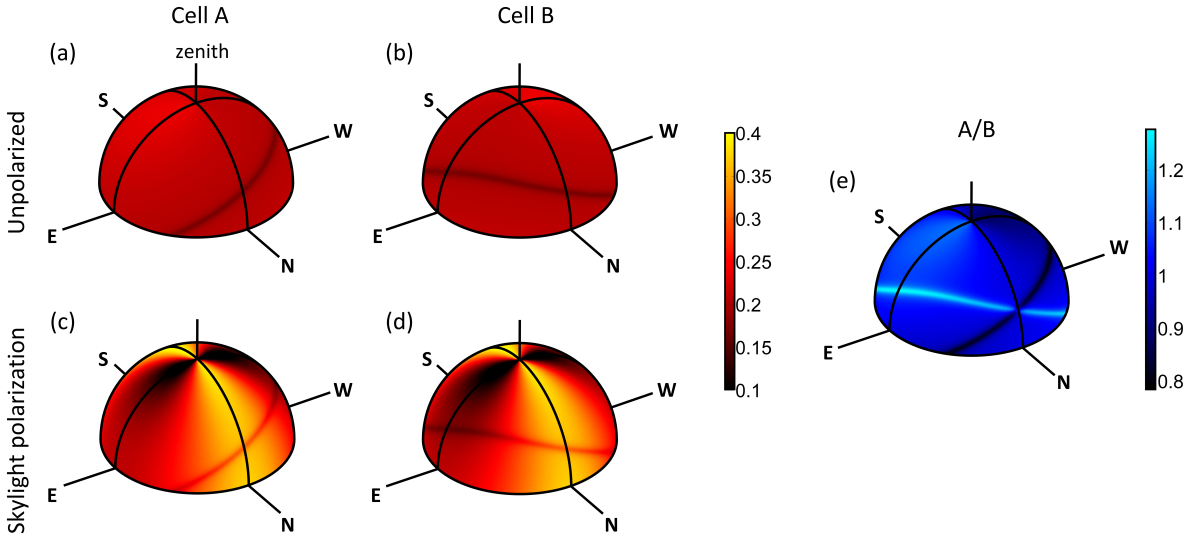


Figure 6.13: Signals generated by a pair of cells in the centre of the retina as the eye scans the sky. The radical pairs are oriented inside cells A and B using the Euler angles ($\alpha = 90°$, $\beta = 45°$, $\gamma = 0°$) and ($\alpha = 270°$, $\beta = 45°$, $\gamma = 0°$), respectively. Light entering the cells is either completely unpolarized, (a) and (b), or is polarized according to the Rayleigh sky model, (c) and (d), with a maximum polarization of 75%. (e) The ratio of the signals from the two cells; this pattern is identical whether the light is polarized or not.

Figure 6.14 shows the result of a related calculation. Instead of a single pair of magnetoreceptor cells positioned on the optical axis of an eye that scans the sky, it shows the visual modulation pattern (see figure 6.11) produced by an array of paired cells distributed around the retina (using the eye model introduced in section 6.3) when the eye looks towards different points in the sky. The resulting image shows the same information as in figure 6.13, although it appears slightly distorted due to the difference in projecting the image onto the retina rather than the celestial sphere. These patterns demonstrate how the magnetic information perceived by the bird changes smoothly as it scans its head around the horizon or looks up and down. Using these images, the bird should be able to clearly identify North as the position at which the cross appears centrally (looking left to right) in its vision. When the bird looks directly along the magnetic field lines, the visual modulation pattern is even more plainly distinct as the 'spike bands' vanish altogether. The band and cross pattern reappear when the bird shifts its gaze 2-3° away from the magnetic field lines, which is consistent with the observation that their compass is precise

to within approximately 5° [65, 66, 214].

Simulations similar to figure 6.13 suggest that the optimum orientation of the cryptochrome molecule occurs when its magnetic symmetry axis (z_m) lies in the $y_\mathrm{c}z_\mathrm{c}$ plane of the cell and makes an angle of 60-70° with respect to the cell's symmetry axis (z_c). With this geometry, the two bands that arise from the spike (figure 6.13) have close to their maximum amplitude and cross at an angle of ca. 90°, arguably affording the clearest indication of the direction of the north-south axis. This was determined by plotting the hemispherical sky patterns on a Mercator projection [215], which preserves the angles and shapes of objects on the surface of a sphere. An example is shown in figure 6.15, with $\beta = 65°$. Furthermore, when $\boldsymbol{z}_\mathrm{m}$ lies in the $y_\mathrm{c}z_\mathrm{c}$ plane, the crossing point exists for any magnetic field inclination (see section 6.5.4).

It is not known whether spin coherence could be preserved long enough in the avian compass to produce a spiked signal of the type modelled above. However, it is still possible to identify a particular bearing (e.g. North) using the proposed receptor setup with radical pairs that do not produce spikes. Figure 6.16 shows an example of this for a radical pair whose singlet yield is described by equation (6.21). In these patterns, North can be identified by the point at which the $\Phi_\mathrm{S}(\xi_\mathrm{A})/\Phi_\mathrm{S}(\xi_\mathrm{B}) = 1$ contours cross.

I have aimed to find conditions under which the ratio of light-induced signals from two adjacent cells is independent of the intensity and polarization of the incident light. However, this is not to say that polarized light no longer has an effect on the output of the compass. If light is polarized parallel to the TDMs of the receptors, more photons will be absorbed than if the light is unpolarized, producing stronger signals from both cells. Although this does not change the size of the A/B ratio, it does lead to an improvement in the signal-to-noise ratio. The example magnetoreceptor orientations used for figures 6.13 and 6.15 have the TDM oriented such that the chromophore preferentially absorbs the maximally polarized light in the band that stretches across the sky from the northern horizon to the southern horizon passing through the zenith (figure 6.1). In other words, the position of the cross coincides with a direction in which the signal-to-noise should be

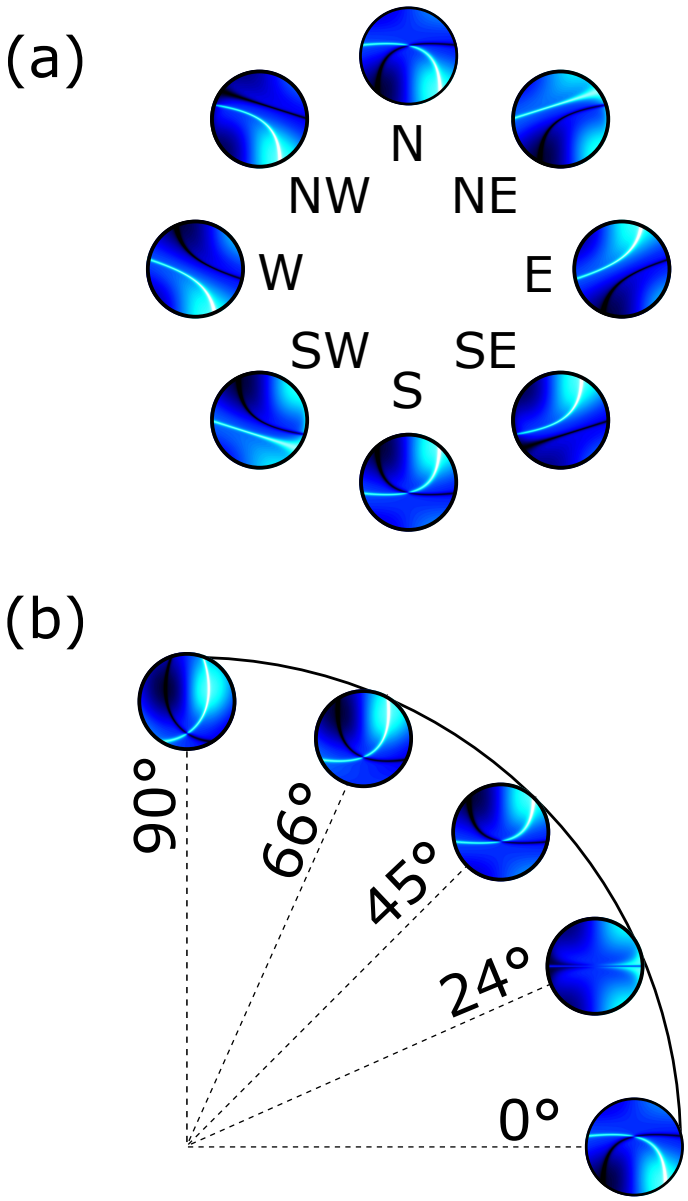


Figure 6.14: Visual modulation patterns, representing the signal $\Phi_S(\xi_A)/\Phi_S(\xi_B)$ as the bird looks towards different points in the sky. The radical pairs are oriented inside cells A and B using the Euler angles ($\alpha = 90°$, $\beta = 45°$, $\gamma = 0°$) and ($\alpha = 270°$, $\beta = 45°$, $\gamma = 0°$), respectively. Note that images produced by a pinhole camera appear upside down and back to front compared to the real object. The images displayed here have been reflected back across both the horizontal and vertical axis so they can be more intuitively understood. (a) Change in visual information as the birds scans its eye along the horizon ($\tau = 0°$). (b) Change in visual pattern as the bird looks up and down the northern longitude line ($\sigma = 0°$; τ is indicated on the figure). Note that $\tau = 24°$ corresponds to the bird looking along the magnetic field lines, which have an inclination of 66°.

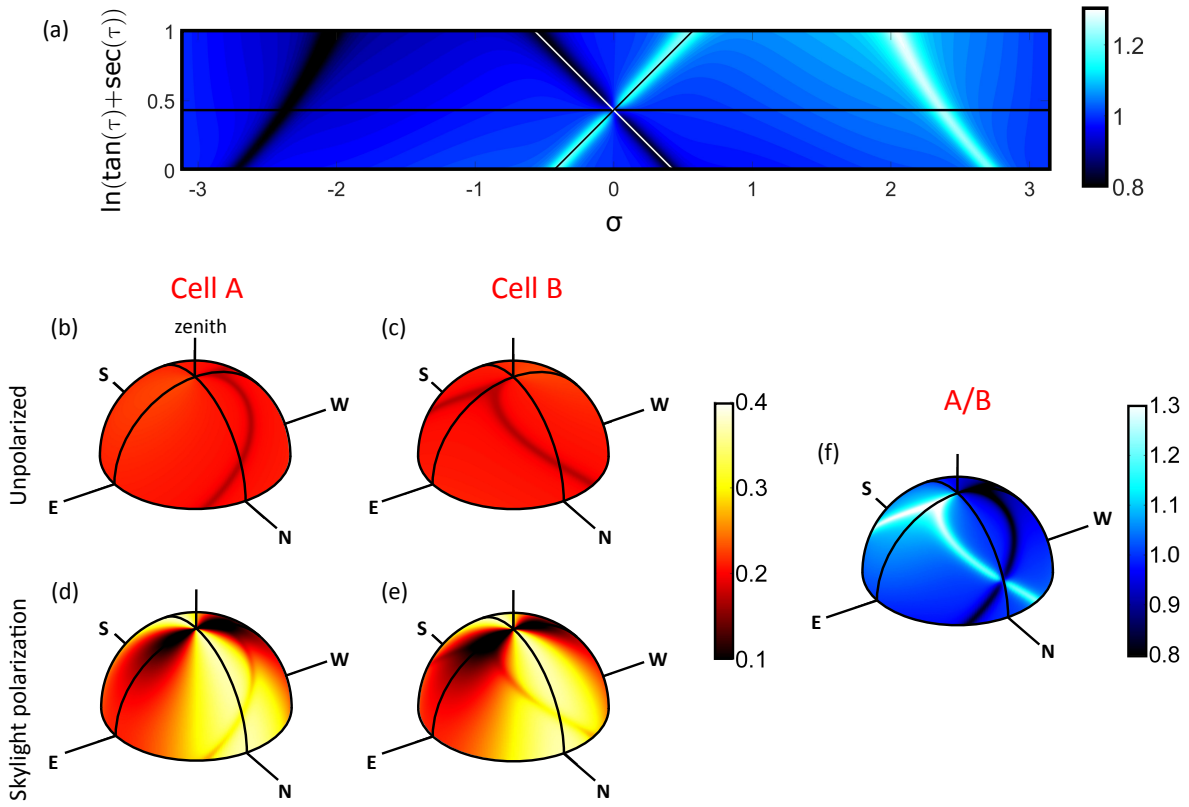


Figure 6.15: Signal from a pair cells at the centre of the retina ($\theta = \phi = 0$) with the radical pair orientation described by the Euler angles ($\alpha = 90°$, $\beta = 65°$, $\gamma = 0°$) and ($\alpha = 270°$, $\beta = 65°$, $\gamma = 0°$) in cells A and B, respectively. (a) Mercator projection of the signal $\Phi_S(\xi_A)/\Phi_S(\xi_B)$ as the eye looks around at different points in the sky The horizontal black line marks the latitude of the crossing point. The diagonal crossed lines are exactly perpendicular with gradients of 1 (black) and -1 (white). (b)-(f) Signals from cells A and B, individually and together, projected onto the celestial hemisphere.

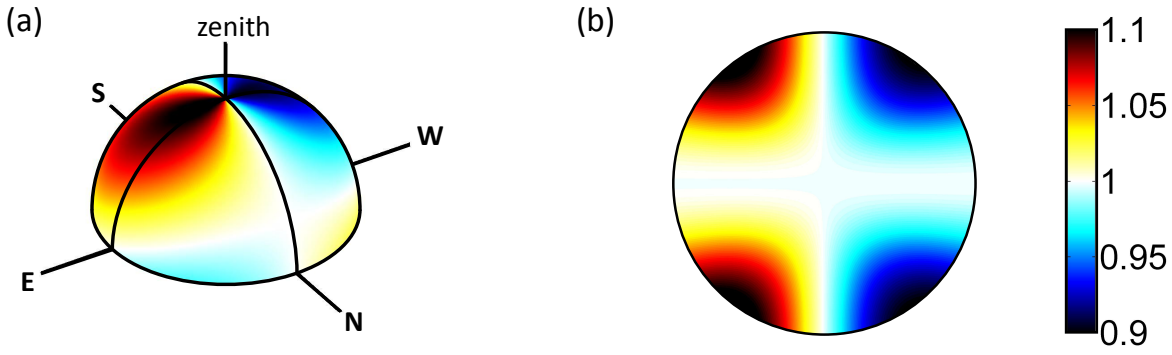


Figure 6.16: Ratio of signals from cells A and B when the magnetic response of the radical pairs is described by equation (6.21). (a) The signals generated by a pair of cells in the centre of the retina as the eye scans the sky. (b) The signal received across a hemispherical retina, with the eye looking directly along the magnetic field lines. [*Figure published as part of figure 2 in Ref. [165].*]

at a maximum.

This is illustrated in figure 6.17, which shows the effect of adding gaussian white noise to each of the signals Φ_S^A and Φ_S^B before the ratio is taken. This type of noise might arise from imperfect amplification or transmission of a signal and is easily modelled by adding a random noise element,

$$\delta = s \times \text{rand} + m; \qquad 0 \leq \text{rand} \leq 1, \tag{6.41}$$

to each pixel in an image, where s and m are, respectively, the standard deviation and mean of the gaussian distribution. Note that this is not the only type of noise that might affect the compass and is used here only as an illustrative example. Under more highly polarized light (figure 6.17), the signal is stronger in regions where the alignment of the magnetoreceptors matches the polarization of the incoming light. In regions of poor matching (in this example, around the azimuth), little to no light is absorbed so no information can be extracted. Provided these 'dark' regions do not overlap with important parts of the magnetic signal, this is a reasonable price to pay for improved signal:noise ratio around more critical features. By contrast, under unpolarized light, the signal:noise ratio is approximately uniform across the celestial hemisphere but is much poorer around

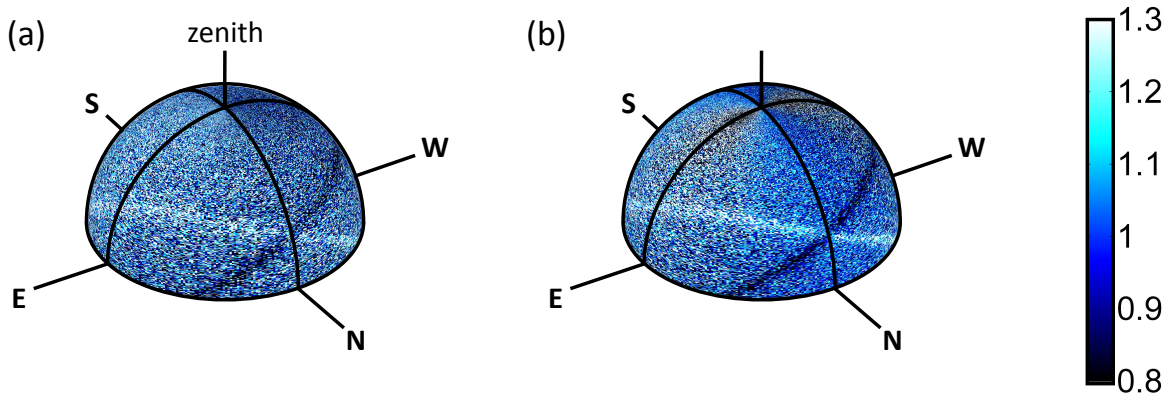


Figure 6.17: Ratio of signals from a pair of cells in the centre of the retina as the eye scans the sky. Gaussian white noise with $m = 0$ and $s = 0.04$ is added to the signal from each individual cell before the ratio taken. The radical pairs are oriented inside cells A and B using the Euler angles ($\alpha = 90°$, $\beta = 45°$, $\gamma = 0°$) and ($\alpha = 270°$, $\beta = 45°$, $\gamma = 0°$), respectively. Light entering the cells is either (a) completely unpolarized, or (b) polarized according to the Rayleigh sky model with $\Lambda = 1$.

the region of the cross than under polarized light.

6.5.4 Cross conditions

For a radical pair that produces a 'spiky' magnetic signal, two rings appear in the final signal A/B as the bird scans its eyes around the sky. When the two rings cross, as in the example shown in figure 6.15, a precise heading can be obtained from the crossing point. A crossing point only exists if the inclination of the magnetic field is less than the angle between ($\boldsymbol{z}_{\mathrm{m}}^{\mathrm{A}} \times \boldsymbol{z}_{\mathrm{m}}^{\mathrm{B}}$) in the pair of cells at the centre of the retina and the axis perpendicular to the line of sight in the horizontal plane ($\boldsymbol{y}_{\mathrm{c}}$ for the pair of cells in the centre of the retina).

This condition can most easily be understood using the diagram in figure 6.18. The 'eyeball' in the middle represents a single pair of cells on the bird's retina. The bird can rotate its eye (or its body) around the vertical retina axis ($\boldsymbol{x}_{\mathrm{r}}$) by any angle $0 \leq \sigma \leq 360°$ so that the pair of cells can look side-to-side around the horizon. The bird can also look up or down in the sky through an angle $-90° \leq \tau \leq 90°$ by rotating its head/eye around

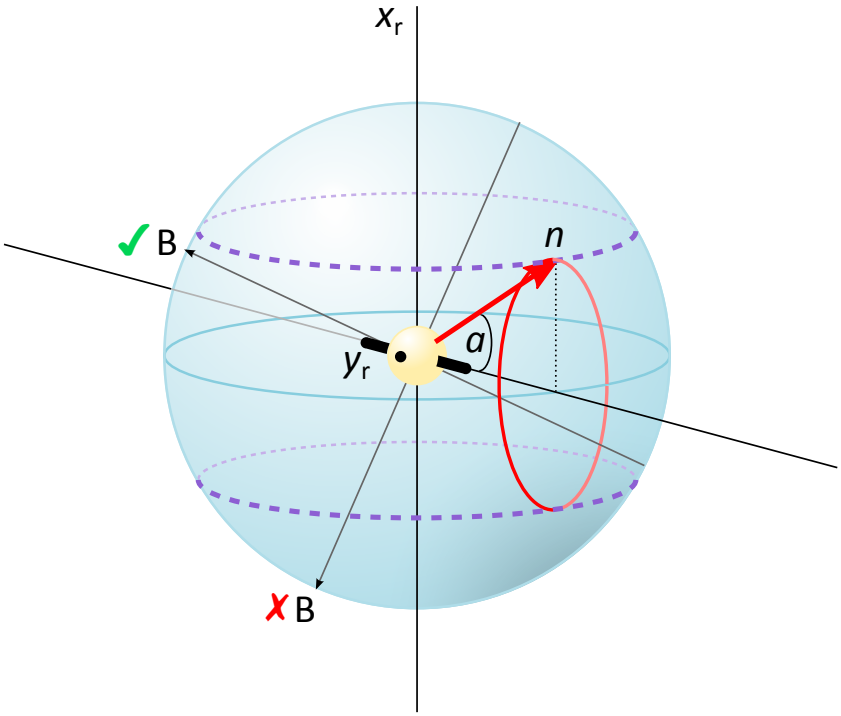


Figure 6.18: Geometric proof of the 'cross condition'.

the horizontal retina axis ($\boldsymbol{y}_r$).

The pair of cells sees a crossing point when the $\boldsymbol{z}_m$ axes of the magnetoreceptors in both cells are simultaneously perpendicular to the magnetic field. This is equivalent to saying that the vector normal to the plane containing both $\boldsymbol{z}_m$ axes is parallel to the magnetic field. This vector is labelled $\boldsymbol{n}$ in figure 6.18. As the bird looks up and down, the vector $\boldsymbol{n}$ sweeps out a circle of different orientations (shown in red). As the bird looks from side to side, the circle of possible $\boldsymbol{n}$ orientations forms a band (purple dashed lines) around the sky/visual field. For $\boldsymbol{n}$ to lie parallel to the magnetic field (i.e. for a crossing point to exist), the magnetic field vector $\boldsymbol{B}$ must lie within this band.

The width of the band is determined by the orientation of the magnetoreceptor within the cell. The smaller the angle a between $\boldsymbol{n}$ and the horizontal retina axis ($\boldsymbol{y}_r$), the narrower the band will be. If the inclination of the field is larger than a, the field vector will lie outside the band and no cross will be observed.

6.6 Cell disorder

6.6.1 Introducing disorder

Previous studies have shown that, whilst orientational disorder of the magnetically-sensitive radical pairs reduces the precision and sensitivity of the compass, it can be counteracted by averaging the signal over larger numbers of radical pairs in a cell [64, 138]. However, these studies did not investigate the effect of the cells themselves being disordered. For the separation mechanism being discussed in this chapter, there are two types of cell disorder to consider.

First, the two cells being compared to form the final signal could deviate from their ideal 180° relative rotation. Second, the pair of cells may be perfectly aligned with each other but not perfectly oriented within the retina, reducing their probability of absorbing light and muddling the visual impression received by the bird. In both cases, disorder may be introduced into any of the three angles $\{\phi, \theta, \eta\}$ that are used to position the cells in the retina.

The effects of the two types of cell disorder were investigated by creating visual modulation patterns with either ϕ, θ or η selected randomly from a gaussian distribution (equation (6.41)) centred on the ideal value of the angle $m = \theta_0$, with a standard deviation s. By increasing the value of s, it is possible to get an impression of how quickly the signal deteriorates in the presence of cell disorder.

However, the complex curve of the 'spike feature' makes it difficult to accurately characterise the rate at which it fades and broadens with increased s. Moreover, a lack of knowledge about how sensitively the bird can detect a signal and how much signal it needs to detect to decide on a bearing, mean that it is impossible to state at what point cell disorder would render the compass non-functional. The following method, illustrated in figure 6.19 was used to assess the rate at which the 'spike features' faded into the background as the cells became increasingly disordered.

Visual modulation patterns (VMPs) were created on a grid of points that were equally spaced in θ and ϕ, as described in section 6.5.2. Before any analysis was carried out on the image, the grid was recentred on the crossing point. The new values of θ' and ϕ' were calculated from the original θ, ϕ grid using the transformations

$$\phi' = \sqrt{\phi^2 + r_0^2 + 2\phi r_0 \cos(a - \theta)}, \tag{6.42}$$

$$\theta' = \arctan\left(\frac{\phi \sin\theta + r_0 \sin a}{\phi \cos\theta + r_0 \cos a}\right), \tag{6.43}$$

where (r_0, a) are the polar coordinates of the crossing point on the original VMP. Note that here (θ, ϕ) and $(\theta'\phi')$ are being used to represent the polar coordinates of points on the original and shifted VMPs, respectively.

The grid was then divided in half along the ϕ' axis. In each half, the maximum and minimum values of the singlet yield Φ_S were located along each line of constant θ'. In this way, each of the four arms of the cross pattern were mapped out. Each θ' isoline was then shifted along the ϕ' dimension so that each arm of the cross in turn was reshaped into a straight line. The shifted grids were summed along the θ' dimension. This gives a set of four profiles in which one each of the four arms of the cross (whichever has been aligned) appears as a strong peak. From these profiles, it is possible to observe how the height of each peak decreases with increased cell disorder.

To aid interpretation of the results, the compass signal was modelled purely by the spike feature with a flattened out background,

$$\Phi_{\mathrm{S}} = 0.5 - 0.01\sin^{256}(\xi) - 0.03\sin^{1024}(\xi) - 0.03\sin^{4096}(\xi). \tag{6.44}$$

Using this model, the final signal $\Phi_{\mathrm{S}}(\xi_{\mathrm{A}})/\Phi_{\mathrm{S}}(\xi_{\mathrm{B}})$ has a constant value of 1, everywhere except at the spike feature. In the alignment procedure outlined above, the height of the peak can be calculated relative to a baseline value equal to the number of grid points in the θ' dimension.

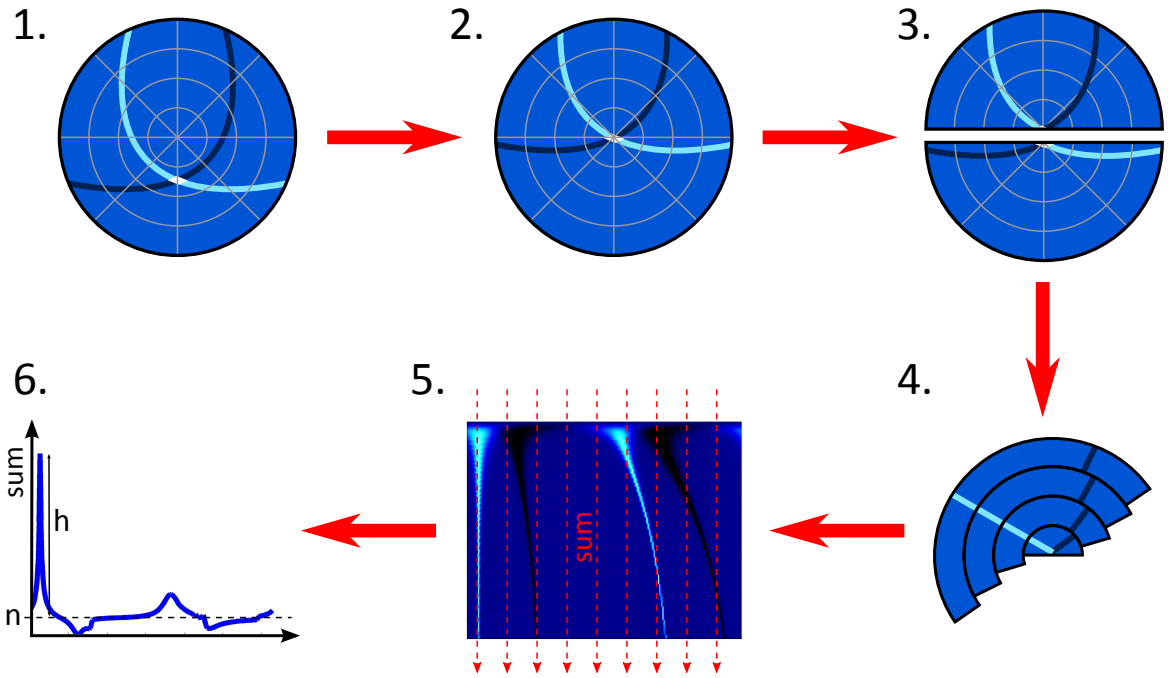


Figure 6.19: Schematic representation of the alignment method used to assess the rate at which the signal is attenuated with increased disorder. 1. A normal VMP pattern is generated using an equal angle (θ, ϕ) grid of cell positions. 2. The (θ, ϕ) grid is recentered on the cross position. 3. The grid is divided in half in the ϕ' dimension. 4. The θ' isolines are shifted to align each arm of the cross in turn. 5. The aligned strips are summed along the θ' dimension. 6. The height of the peak corresponding to each arm of the spike is recorded.

6.6.2 The effect of disorder

Figure 6.20 shows the attenuation of the spike features in $\Phi_S(\xi_A)/\Phi_S(\xi_B)$ as disorder is introduced into each of the Euler angles $\{\phi, \theta, \eta\}$ describing the orientation of a cell pair. An exact relative orientation of 180° is preserved between the two cells A and B. The presence of the spike feature is tracked by measuring the peak height in aligned traces of the type described above.

Two features are immediately obvious. First, the spike feature is rapidly lost in the presence of disorder. The height of the peak is half its original value when $s \approx 5°$ in any angle. This corresponds to a blurring out of the spike features, as shown in figure 6.21. The high sensitivity to disorder is in contrast to the $34 - 50°$ of disorder that could be tolerated in the orientation of individual receptors [64, 101, 106, 138], where the effects

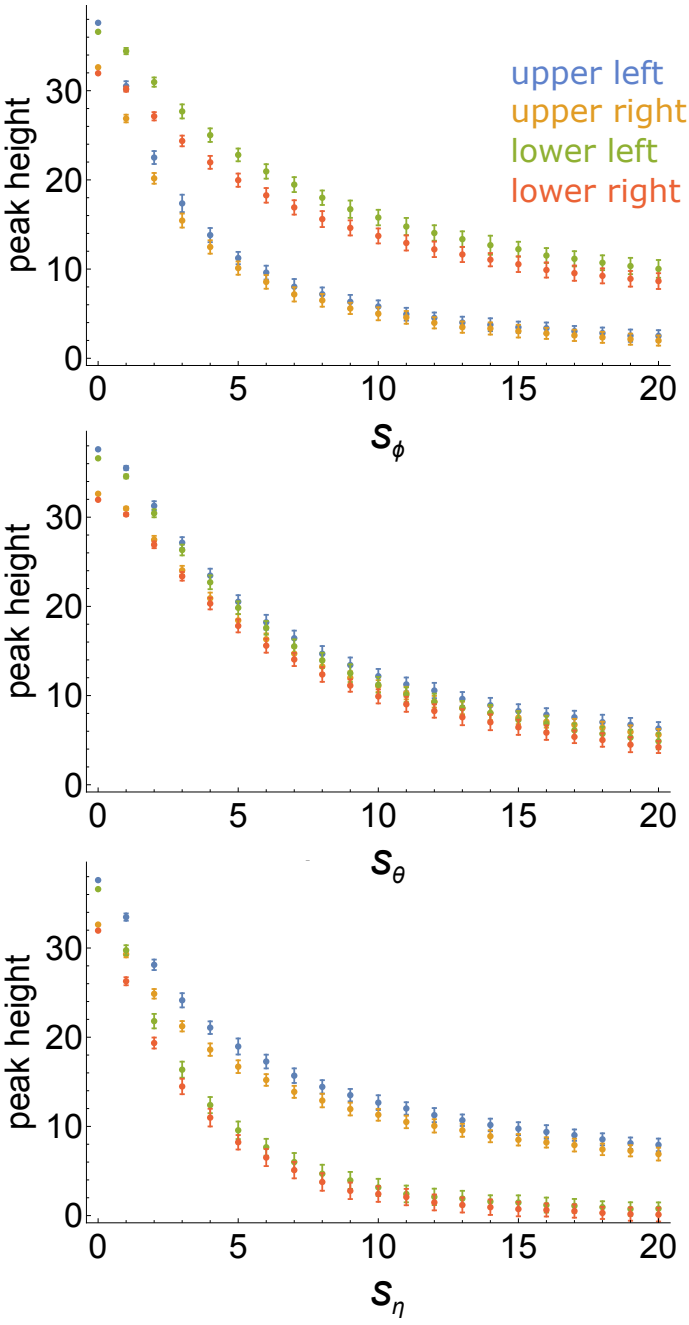


Figure 6.20: Effect of cell disorder. Cells A and B are perfectly aligned relative to each other but disorder is introduced in one of the three angles (ϕ, θ, η) describing the orientation of the pair. The presence of the 'spike feature' in the VMP (for a bird looking horizontally north) is measured using the alignment procedure described in section 6.6.1. The height of the peak corresponding to each arm of the cross pattern is shown as the mean of a sample of 250 instances of random disorder. The error bars indicate the standard deviation of the peak height.

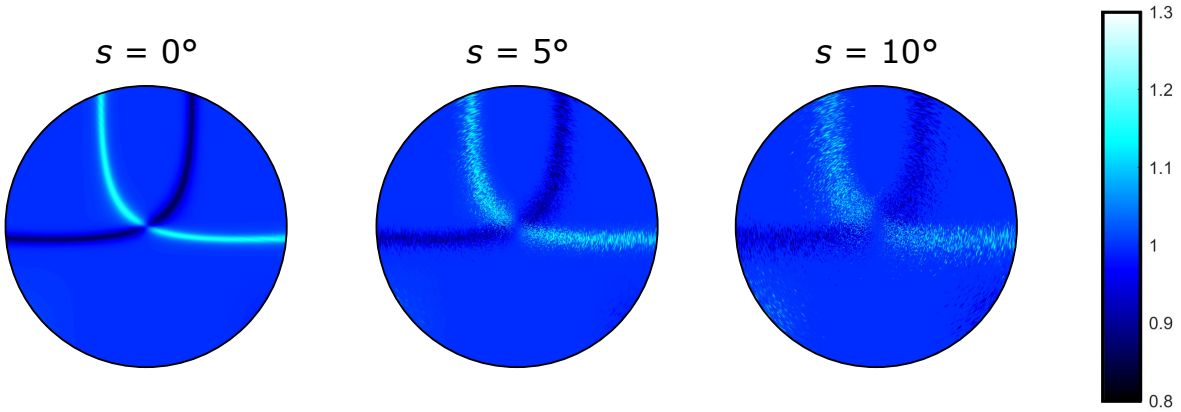


Figure 6.21: Effect of increasing disorder in θ. The visual modulation patterns are calculated with the bird looking horizontally north.

could be counteracted by averaging over larger number of receptors per cell.

Second, different parts of the image (different arms of the cross) do not all respond in the same way to disorder. Given the analysis in section 6.4, this is unsurprising. A region of the visual modulation pattern will be most strongly affected by disorder if small changes in cell orientation lead to large differences in the cell signal. The size of the signal depends on the angles that the cell axes make with the magnetic field vector and the electric field vector of incoming photons. The closer the relevant cellular rotation axis lies to these important vectors, the less the crucial angles, and hence the signal, will change when disorder is introduced.

More interesting, in assessing the proposed separation mechanism, is the case where one cell, A, remains ordered whilst disorder is introduced in ϕ_{B}, θ_{B} or η_{B}. Figure 6.22 shows the decay of the aligned peaks when only cell B is disordered.

It is immediately clear that the peak height cannot be so easily tracked in these examples. After an initial decrease, the peak height plateaus and then increases again as more disorder is introduced. Examination of the aligned traces and visual modulation patterns (figure 6.23) reveals that this is the result of an overall increase in background noise rather than a true reflection of how clearly the spike feature appears above the background.

However, from the decrease in the peak height at small s, we see that the spike features

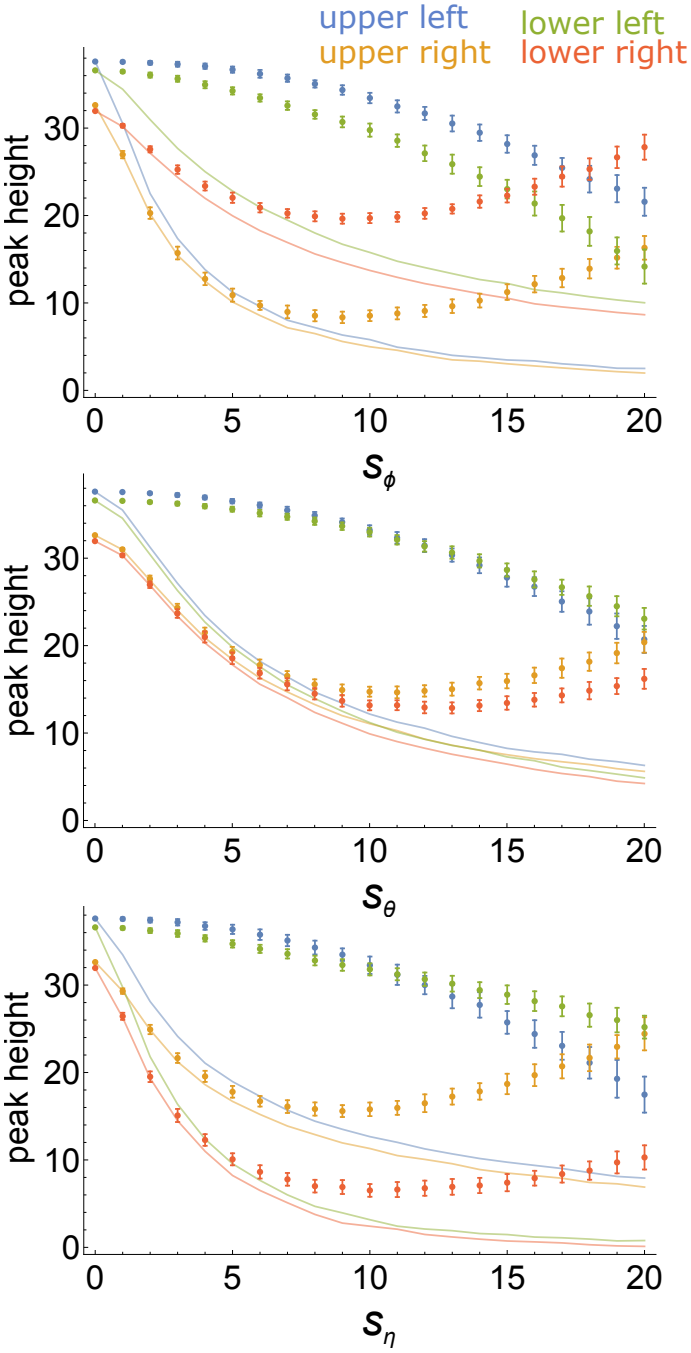


Figure 6.22: Effect of disorder within a cell pair. Cell A is perfectly aligned relative to the retina whilst disorder is introduced in one of the three angles $(\phi_B, \theta_B, \eta_B)$ describing the orientation of the pair. The presence of the 'spike feature' in the VMP (for a bird looking horizontally north) is measured using the alignment procedure described in section 6.6.1. The height of the peak corresponding to each arm of the cross pattern is shown as the mean of a sample of 250 instances of random disorder. The error bars indicate the standard deviation of the peak height. The solid lines in the background show the data from figure 6.20 for comparison.

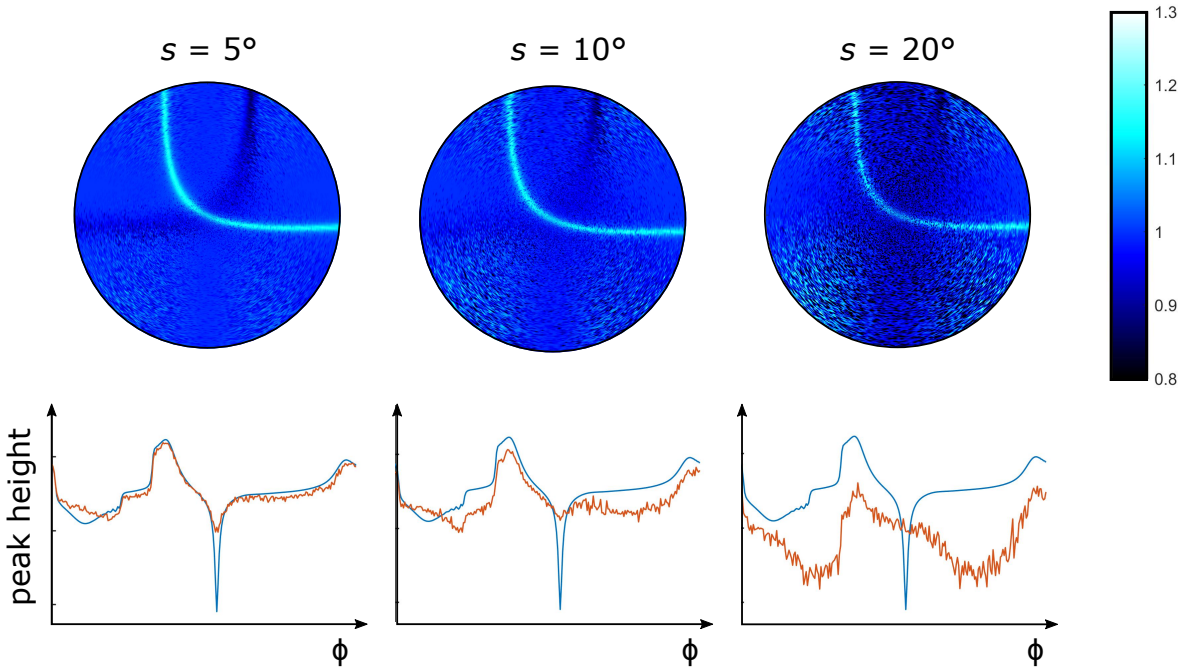


Figure 6.23: Effect of increasing disorder in η_B. The visual modulation patterns (top row) are calculated with the bird looking horizontally north. As s increases (more disorder) the curved 'spike feature' corresponding to cell B is blurred out and difficult to see. However, the feature corresponding to cell A is still clearly visible, even over a noisy background. Aligned traces, mapping the lower right hand arm of the cross pattern are shown below the VMPs. The peak produced by the aligned arm of the cross is clearly visible for an ordered system (blue traces) but disappears quickly when disorder is included (orange traces). The peak height is measured relative to a fixed point on the y axis, making it appear that the height has increased at large values of s.

disappear at very similar rates, regardless of whether disorder is included in the orientation of just one cell or of the cell pair. This suggests that disorder of the cells relative to the retina frame is more damaging than a slightly mismatched orientation within the cell pair. Or, in other words, the limiting factor on the amount of tolerable disorder is maintaining compass precision rather than maintaining the separation mechanism. This hypothesis is borne out by the appearance of the visual modulation patterns (figure 6.23). Even at the largest values of s, the 'spike feature' corresponding to the ordered cell (A) remains clear and precise, although, within each pair, the two cells may be far from the 180° relative orientation needed to perfectly filter out confounding polarized light signals.

6.7 Realising the separation mechanism

6.7.1 Immobilizing the magnetoreceptors

Section 6.4 outlined a number of requirements for arranging two cells such that the ratio of the signals from the two cells provides pure magnetic information. Probably the most stringent geometric constraint is that the magnetoreceptor molecules must have (on average) a single dominant orientation inside the cells. Previous studies have recognised that a high degree of immobilization and some degree of alignment amongst the magnetoreceptors is likely to be required for direction sensing [29, 64, 102, 106]. Proposed ways in which this could be achieved [84, 103, 104, 106] include fixing the magnetoreceptor molecules between the stacked membrane discs in the outer segments of photoreceptor cells, binding to quasi-cylindrical membranes in the inner segments of photoreceptor cells, and attachment to the cytoskeleton in retinal ganglion cells. However, it is difficult to see how any of these interactions would preferentially constrain a magnetoreceptor molecule to a single orientation. For example, consider a cryptochrome hypothetically tethered to a rhodopsin molecule embedded in a membrane disc in the outer segment of a photoreceptor cell. Although the rhodopsin orients with its helices spanning the membrane, it is free to rotate around the axis perpendicular to the membrane surface [106, 208, 209]. A cryptochrome tethered to the rhodopsin would therefore be disordered with respect to rotation around the axis of the cell. Under these circumstances, cells A and B would, on average, give rise to identical magnetic signals.

By contrast, the highly ordered "tracks" of rhodopsin dimers recently discovered in the membrane discs of the outer segments of mouse rod photoreceptors [216] could provide the necessary template for orienting magnetoreceptor proteins [59]. A similar suggestion has previously been made in reference [210] in the context of immobilizing photopigments to detect polarized light. The dimer tracks are uniformly aligned parallel to the incisure of the discs which consist of flattened sacs of bilayer membranes, shown schematically in

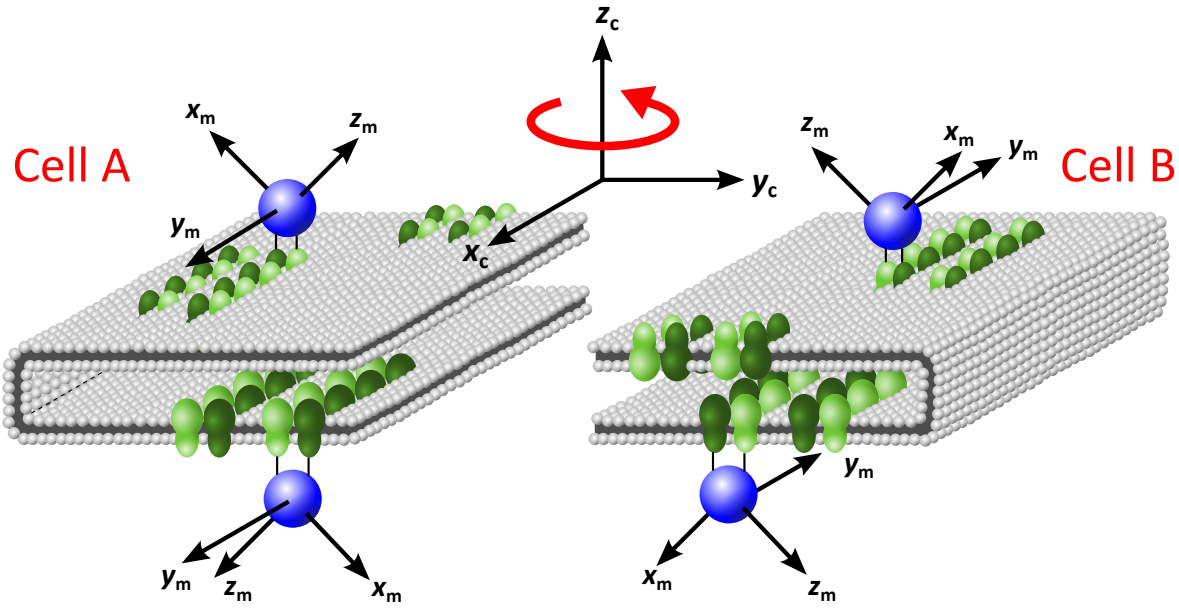


Figure 6.24: Schematic picture of the hypothetical interaction of cryptochrome magnetoreceptors (blue spheres) with aligned tracks of rhodopsin dimers (green) embedded in the membrane discs in the outer segments of photoreceptor cells. The figure shows a small section of one of the discs in two neighbouring cells, A and B, related by a 180° rotation around the cell axis, $\boldsymbol{z}_c$, which coincides with the direction of the incoming light. The cryptochrome molecule is imagined to bind identically to the top and bottom layers of the discs with the same geometry as in figure 6.6b. [*Figure published as figure 4 in Ref. [165].*]

figure 6.24 [216, 217]. Specific binding of a cryptochrome to a rhodopsin dimer would lead to two symmetry-related cryptochrome orientations in each cell. If the geometry of the interaction were as drawn in figure 6.24, the two orientations would have the same absorption probability for polarized light and the same magnetic field effect (because the $\boldsymbol{y}_m$ axes are parallel to one another and the $\boldsymbol{z}_m$ axes are antiparallel). Rotation of the cell and its contents by 180° around its $\boldsymbol{z}_c$ axis, as shown in figure 6.24, would not change the absorption probability but would alter the magnetic field effect (because $\boldsymbol{y}_m$ is still along the $\pm\boldsymbol{x}_c$ axis but $\boldsymbol{z}_m$ now points in a different direction). It is not essential that the cryptochrome binds directly to the rhodopsin dimer, but it is important that the interaction, whether mediated by other molecules or not, substantially restricts the rotational freedom of the cryptochrome molecules.

In addition to a high degree of ordering of the cryptochromes within the cells, the proposed

separation mechanism requires that the cells occur in pairs with a fixed, well-defined relative orientation of the two partners. In this respect, the double-cone photoreceptor cells are a promising location for the magnetic sensors [59]. These cells are aligned in the retina, contain ordered structures on which cryptochromes could be oriented, and could allow magnetic information to be separated from light intensity and polarization effects as described above. Moreover, cone cells are not active at night so that changes in membrane potential generated by magnetic sensors in nocturnal migrants would not have to compete with those generated by visual pigments [59]. Given their pencil-shape morphology, it seems plausible that the two components of the double cones could be related by a (180°) rotation around the cell axis as proposed above.

6.7.2 Potential pitfalls

Although they offer the most obvious way to ensure a fixed relative orientation between two populations of magnetoreceptor molecules, some aspects of double-cone morphology could potentially make them unsuitable for our suggested separation mechanism. First, morphological data indicates that, at least in some bird species, just one member of the double cone is associated with a complete oil droplet, whilst the secondary member either lacks a droplet or possesses a smaller droplet [184]. As these droplets function as filters that narrow the spectrum of light, the assumption that both members of the double cone receive the same light input could be problematic [218, 219]. Note that if the oil droplets caused different amounts of light to enter the two cells in a constant ratio, independent of the intensity and polarization of the incident light, this would be equivalent to having different numbers of receptors inside the two cells and would not prevent the separation mechanism from working. If, on the other hand, the fraction of light passing through the oil droplet did depend on its intensity or polarization, the mechanism would break down at the most fundamental level.

Second, the proposed model requires that the double cones would need to function as

separable units because it is the differential synaptic output that would reflect the magnetic stimuli. However, it appears that at least some double cones are electrically coupled by gap junctions [220] and it is unknown whether these junctions would be functionally 'open' during magnetoreception (meaning that the cells would provide a single, synchronized response). Neither of these morphological issues has been studied in night-migratory songbirds and consequently there are currently too many unknowns to judge whether double cones could really be responsible for magnetoreception, although they are undoubtedly potential candidates. An alternative to comparing the signals from two members of a double cone would be to compare signals coming from two independent neighbouring single or double cones with more similar morphology.

6.8 Alternative mechanisms

Given the potential difficulties with realising strict orientations of the magnetoreceptors it may be that it is not possible to isolate the magnetic information using signal ratios. If this were the case, we would have to conclude that birds have developed a different mechanism for disentangling the effects of the magnetic field, light intensity and photoselection on the amount of signalling state produced.

There are two obvious ways to avoid detecting potentially confusing polarized light signals. The first, which accounts for humans' inability to detect polarized light, is to have populations of magnetoreceptors that are disordered around the propagation vector of the incoming light such that, for any polarization of light, there will be a receptor that is correctly oriented to absorb it. On average, across the whole population, the photon absorption probability, and hence the signal, is then independent of the polarization of the incoming photons. Membrane-embedded proteins are commonly free to rotate around the axis perpendicular to the membrane surface [106] so it is far easier to see how this arrangement could be achieved than one which requires rigidly and uniquely bound magnetoreceptors. However, relying on signal averaging over a large population of mag-

netoreceptors may be incompatible with the low light conditions that birds can navigate under (down to 1 photon per photoreceptor cell per second) [59]. Furthermore, the same disorder that effectively averages away polarization effects also necessarily averages the magnetic signal such that the total magnetic signal from a cell is unaffected by a cell rotation and consequently, intensity can no longer be filtered out by comparing the signals from two neighbouring cells. If magnetic field and polarized light signals are separated using magnetoreceptor disorder, intensity effects must be removed by a different mechanism, such as detection of the difference between optical and magnetic flow during head scanning and/or free flight [139, 140]. For smoothly varying (not spiky) magnetic signals, changes in the magnetic signal could be distinguished from generally sharper transitions in the light intensity using low-pass filtering techniques [139].

Assuming that some such mechanism could be used to separate the magnetic signal from changes in the optical intensity, photoselection effects could also be filtered out by detecting the sum of signals from two cells with a relative orientation of 90°. Since the photon absorption probability is proportional to $\cos^2(\omega)$ (see above) and $\cos^2(\omega)+\cos^2(\omega+90°) = \cos^2(\omega) + \sin^2(\omega) = 1$, the polarization patterns from the two individual cells will sum to a constant value, leaving the weaker magnetic signal visible. An example is shown in figure 6.25, with the $\boldsymbol{x}_\mathrm{m}$ axis of the magnetoreceptors aligned with the long symmetry ($\boldsymbol{z}_\mathrm{c}$) axis of the cell ($\alpha = 0°$, $\beta = 90°$, $\gamma = 0°$).

The second obvious way to prevent skylight polarization patterns overwhelming the magnetic signal would be to depolarize light as it entered the eye or magnetoreceptive cell. This would appear to be at odds with the fact that birds apparently display polarization-sensitive behaviour, specifically that they appear to calibrate their magnetic compass using twilight polarized light cues [45–49]. For the magnetoreceptor to receive depolarized photons without damaging the birds' ability to respond to polarized light cues, the magnetoreceptors could be located in different cells to the polarization-sensitive photoreceptors, with their own depolarising filter. For example, the magnetoreceptors could be located in photoreceptor cells tuned to absorb visible light, with polarization sensitivity mediated

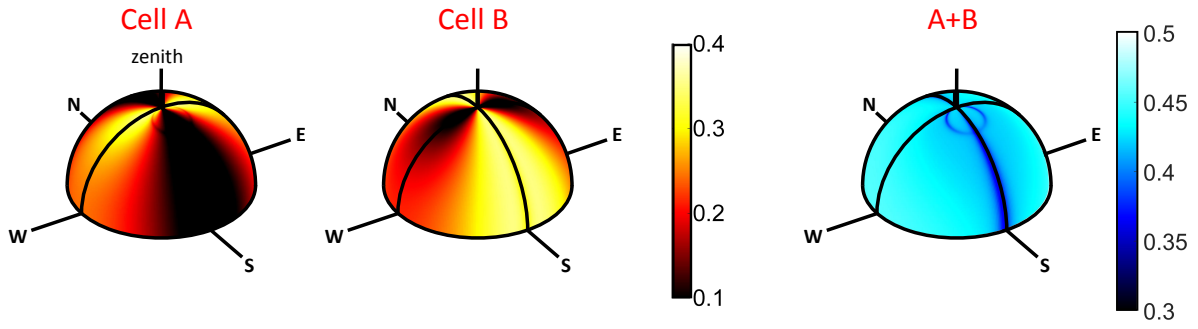


Figure 6.25: Sum of signals from two perpendicularly oriented cells ($\eta = 0$, left, and $\eta = \pi/2$, right) containing a magnetoreceptor molecule with ($\alpha = 0°$, $\beta = 90°$, $\gamma = 0°$). The hemispheres represent the signal received by a pair of cells at the centre of the retina ($\phi = \theta = 0$) as the eye scans across the sky. The skylight is 75% polarized by Rayleigh scattering, with the sun setting in the west. The magnetic field is pointing North, with an inclination of 66° ($I = 66°$, $D = 0°$).

by UV cones, as in other animals (e.g. insects [190, 192] and fish [197, 198]).

Conversely, it is possible that birds do not have a mechanism for separating magnetic field and polarized light signals. The ratio of two 90° rotated cells could be taken to remove light intensity, leaving a combined polarization and magnetic signal, which would be in keeping the observation of Muheim et al. [50] that the polarized light cues seem to interact directly with the magnetic compass. However, if this were the case, the bird would, in addition, need a mechanism for detecting the weakly modulating magnetic signal on top of the potentially large variations in polarization across the sky.

6.9 Conclusions

The ordering of receptors required for a functioning compass makes it inherently sensitive to polarized light. This is potentially problematic as large variations in skylight polarization could obscure the magnetic signal.

In this chapter, I have shown that a pure magnetic signal, independent of light intensity and polarization, can be obtained by taking the ratio of signals from two neighbouring cells with a relative orientation of 180° around the direction of propagation of incoming

light rays, which, for photoreceptor cells pointing towards the pupil for maximum light collection, lies parallel to the long cylindrical symmetry axis of the cell. Inside the cell the magnetoreceptors must be arranged so that the magnetic symmetry axis is neither exactly parallel nor exactly perpendicular to the rotation axis.

The proposed separation mechanism works for both spike- and non-spike- producing radical pairs. However, it is clear that the ability to produce a spike offers a great advantage when it comes to identifying a precise magnetic field direction. To determine a direction from figure 6.16 (no spike) with the same precision as from figure 6.15 (spike), the bird would need to be over ten times more sensitive to changes in the yield of the signalling state. This high sensitivity requirement would make the compass more susceptible to noise and less able to function under low light conditions. The resilience of the compass to noise is also affected by polarized light. The signal:noise ratio is highest when the incident light is highly polarized in the direction preferentially absorbed by the magnetoreceptors.

A high degree of cell order is required for the separation mechanism to function correctly. However, this is no more than is needed to maintain the precision of the compass. More important is the requirement for the magnetoreceptors within the cells to have, on average, a fixed orientation within the cells such that 180° rotation of the cell changes its response to the magnetic field. I have suggested one possible way that this could be achieved, by binding the magnetoreceptor molecules to aligned tracks of rhodopsin dimers embedded in the membrane discs in the outer segments of photoreceptor cells. Housing the magnetoreceptors within double cone cells seems particularly appealing as it offers an obvious way of fixing the relative orientations of the two cells being compared. However, if double cones turned out not to be suitable, the separation mechanism could still be implemented by comparing the signals from two neighbouring single cones (or rods).

Finally, it should be noted that the simulations presented here do not provide any evidence for how the avian compass works in reality, although they offer hints about ways in which it might work. As yet, we cannot even be certain of how the compass interacts with polarized light. However, if it can be demonstrated experimentally that birds can

detect a pure magnetic signal, the work here provides a comprehensive list of criteria and suggestions to narrow the search for a suitable magnetoreceptor.

Chapter 7

Testing the cryptochrome hypothesis

Since it was first demonstrated that birds could use the geomagnetic field as a navigational cue, the quest to uncover the underlying mechanism has been hampered by the lack of an unambiguously identified receptor. Throughout the previous chapters of this thesis, I have focused on the flavin-tryptophan radical pair in cryptochrome, which is currently the best candidate magnetoreceptor. The work in chapters 4 and 5, along with previous theoretical [61, 67, 68] and spectroscopic studies [109, 221], have demonstrated that, in many ways, it is well-suited to fulfil this role [84]. However, while there is appreciable evidence that cryptochrome is involved, at some stage, with magnetoreception [17, 97, 103, 105, 107], we are still far from being able to prove that it can claim the title of 'magnetoreceptor' by producing the magnetically-sensitive radical pair. Furthermore, although the most recent evidence points towards CRY4 [107], little is known about which of the four avian cryptochromes might participate in magnetoreception.

Properly identifying the magnetoreceptor would allow better parameterisation of calculations, better design of behavioural experiments and a directed approach to neurophysiological and spectroscopic experiments. In this chapter, I use ideas from chapters 4 and 5

to design an experiment to test the cryptochrome hypothesis by selectively disabling the magnetic sensitivity of the cryptochrome radical pair.

7.1 Proposed experiment

Selectively probing the magnetoreceptive function of cryptochrome requires an experiment that is carefully designed to perturb its magnetic properties without otherwise affecting its ability to participate in a sensory pathway. Fortunately, detection of magnetic fields via the radical pair mechanism depends on the delicate interplay of magnetic interactions several orders of magnitude smaller than those governing bonding and structure, providing a pathway to gently and selectively disrupt the compass.

One of the key requirements of the radical pair mechanism is that the radicals remain in a coherent, non-equilibrium state long enough for appreciable differences in the (field-dependent) ratio of singlet to triplet products to emerge [12,13]. If the system relaxes to a state of thermal equilibrium too quickly, all information about the direction of the magnetic field will be lost. Here I propose an experiment in which any potential magnetoreceptive behaviour of cryptochrome is selectively disabled by artificially introducing a superparamagnetic nanoparticle into the bird, which would bind to cryptochrome and locally enhance spin relaxation rates.

The key characteristic of superparamagnetic materials is that their magnetic moment is unstable and randomly changes direction. This behaviour means that the nanoparticle is the source of a fluctuating magnetic field, which could provide the driving force for relaxing the radical pair system and destroying the compass function. Additionally, Brownian motion of the nanoparticle may create fluctuations in the net magnetic field experienced by the radicals, which also have the potential to relax the system.

7.2 Magnetic materials: some definitions

Diamagnetism

[1]In diamagnetic materials, all the electrons are paired and therefore the atoms have no net magnetic moment. In the absence of an external field, they have zero magnetisation. Under an applied magnetic field, diamagnetic materials acquire a magnetization that opposes the field. The magnetic susceptibility, which gives the ratio between the magnetic moment induced per unit volume of the material and the strength of the applied field, is negative and temperature-independent.

Paramagnetism

The atoms in paramagnetic materials have a magnetic moment due to unpaired electrons. However, in zero field, the bulk material has no net magnetic moment as the moments of individual atoms do not interact and so are randomly aligned. Application of an external magnetic field can align the magnetic moments of the atoms to give the material a temporary magnetization that disappears when the field is removed. The magnetic susceptibility is temperature-dependent as individual magnetic moments will only be significantly aligned if the energy of the interaction with the external field is comparable to or larger than the thermal energy.

Ferromagnetism

In contrast to paramagnetic materials, the magnetic moments of atoms in ferromagnetic materials are aligned by strong, favourable exchange interactions. This gives the material a permanent magnetic moment, even in the absence of an external magnetic field. At high enough temperatures, the thermal energy can outweigh the exchange energy and randomize the spins of the atoms. Thus the magnetic susceptibility decreases with in-

[1]Useful references for this section are [222] and [223].

creased temperature and drops rapidly to zero above a characteristic temperature, known as the Curie temperature.

Anti-ferromagnetism

Anti-ferromagnetic materials are composed of two interleaved sub-lattices with equal magnetic moments. An antiparallel alignment of the magnetic moments is favoured by a strong, negative exchange interaction so that the material has zero net magnetic moment. In ferrimagnetic materials, which are similarly constructed, the exchange interaction is positive so the magnetic moments of the two sub-lattices are aligned, creating a net magnetic moment.

Magnetic domains

Three magnetic fields are required to characterise the properties of a magnetic material. The fundamental magnetic field, or $\boldsymbol{B}$-field, describes the magnetic flux density at any point inside or outside the material. It obeys Maxwell's equations, of which the first

$$\nabla \cdot \mathbf{B} = 0, \tag{7.1}$$

states that the magnetic field has no source and no sink. In other words, the $\boldsymbol{B}$ field always forms continuous loops.

At a microscopic level, inside the material, the source of any magnetic behaviour is the presence and interaction of the magnetic moments produced by each (paramagnetic) atom. The magnetization field, $\boldsymbol{M}$, is the vector sum of all the individual magnetic moments. It can be thought of as the (local) density of magnetic moments.

At the surface of a material, the magnetization field stops but does not change direction. By contrast, the $\boldsymbol{B}$-field bends as it reaches the edge of a material, to start forming a continuous loop around the material. The discrepancy between the two fields is accounted

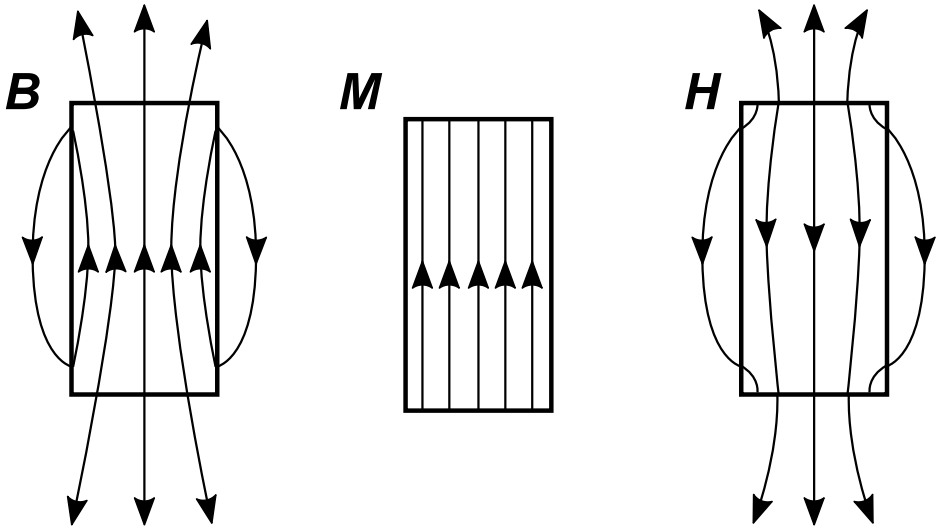


Figure 7.1: Three fields used to describe the magnetism of a material. The demagnetizing field $\boldsymbol{H}$ both alters the shape and reduces the magnitude of the field inside the sample. [*Figure redrawn in part from reference [222].*]

for by an auxilliary field, the $\boldsymbol{H}$-field, also known as the demagnetizing field. The three fields are related by the vector sum

$$\boldsymbol{B} = \mu_0(\boldsymbol{H} + \boldsymbol{M}), \tag{7.2}$$

where μ_0 is the vacuum permeability. As can be seen from figure 7.1, the surface of a material forms a plane of sources or sinks of $\boldsymbol{H}$. It can be useful to think of these sources and sinks as a collection of 'magnetic charges' or 'North and South poles', which are associated with an energy, the magnetostatic energy, in much the same way that electric charges are associated with electrostatic energy. The magnetostatic energy can be minimized by avoiding the formation of these 'magnetic charges' and by keeping opposite 'charges' or 'poles' as far apart as possible. One way to do this is to split the material up into a number of smaller 'domains' that are magnetized in opposite directions.

Creation of domain boundaries is also associated with an energy, as it forces unfavourable exchange interactions between the atoms on either side. The number of domains in a material is determined by the balance between the surface magnetostatic energy and the energy needed to create the domain boundaries. This balance is strongly dependent on

particle size. It is possible to create magnetic particles that are too small to support domain boundaries. These are known as single domain particles.

Superparamagnetism

When a single-domain particle becomes sufficiently small or the temperature is sufficiently high, the magnetization of the domain becomes unstable and can randomly flip between different favourable orientations. The characteristic time between flips is called the Néel relaxation time. In zero field, the magnetization of the bulk material averages to zero when measured over timescales much longer than the Néel relaxation time. A net magnetization can be induced by applying an external field, just as for a paramagnetic material. However, the susceptibility of superparamagnetic materials is much higher.

The Néel relaxation time for a superparamagnetic particle is given by the Néel-Arrhenius equation:

$$\tau_{\mathrm{N}} = \tau_0 \exp\left(\frac{KV}{k_{\mathrm{B}}T}\right), \tag{7.3}$$

where K is an anisotropy constant, V is the volume of the particle and $1/\tau_0$ is an attempt frequency (often referred to as the pre-exponential frequency factor), parameterising how often the system tries to cross the energy barrier between different stable orientations of the magnetization. The height of the energy barrier (KV) depends on the size, shape and structure of the nanoparticle.

At very low temperatures, the system does not have enough energy to cross the energy barrier between local minima (stable orientations of the magnetization). Néel relaxation becomes very slow (on the timescale of the measurement) and a fixed orientation of the magnetization is observed. This is known as a blocked state. The temperature below which the material is in a blocked state is called the blocking temperature.

Magnetic anisotropy

The magnetic anisotropy of a sample describes how difficult it is to induce a magnetization along different axes. The two main sources of anisotropy are the structure (magnetocrystalline anisotropy) and the shape (shape anisotropy of the sample). Magnetocrystalline anisotropy arises when spin-orbit coupling or crystal field splitting creates a preferred direction for spins within the crystal lattice. Shape anisotropy, like the formation of magnetic domains, is a result of minimizing surface magnetostatic energy. An ellipsoidal particle, for example, is most easily magnetized along its long axis, which only produces a small number of magnetic charges at each end of the particle. It is less energetically favourable to magnetize the particle across its short axis, which would result in a larger number of more closely spaced magnetic 'poles' or 'charges'.

The nanoparticles considered in this chapter largely display strong uniaxial anisotropy, meaning that they have a strong preference to be magnetized along a single axis, known as the easy axis.

7.3 Biological applications of magnetic nanoparticles

Like all nanoparticles, magnetic nanoparticles (MNPs) have many interesting properties arising from their small size and enormous surface area to volume ratio [224]. Consequently, they have found applications in fields from information storage to catalysis to biosensing [224–228]. In medicine, MNPs have found multiple uses in imaging and targeted therapies, demonstrating a number of properties that would particularly suit them to the experiment proposed in section 7.1.

MNPs, delivered intravenously or by a localized injection, can be guided to specific locations by an externally applied magnetic field gradient, giving them a role in targeted drug

delivery or gene therapy [224, 229]. Alternatively, they can be functionalised with ligands that target particular cell types, where they act as contrast agents for MRI [224, 226, 230–233] or are used for magnetic hyperthermia treatments. Magnetic hyperthermia involves heating MNPs with an oscillating AC field to kill heat-sensitive cancer cells [224, 226]. Both this and targeted delivery using magnetic field gradients rely on the interaction between a nanoparticle and an extremely strong external magnetic field. This has little bearing on how a magnetic nanoparticle might be used in an experiment where the external field is no more than a few microtesla. Of much more interest is the use of MNPs as MRI contrast agents, which exploits the interaction of the NP's own magnetic field with the spins of water protons (although MRI experiments do, of course, also use large external magnetic fields!).

Contrast agents are substances that are used to increase the relaxation of water protons in their local environment. This decreases the strength of the NMR signal from those protons and therefore increases the contrast between different parts of the image in an MRI scan. As targeted relaxation is exactly what needs to be achieved in the proposed experiment, contrast agents are a good inspiration.

There are three mechanisms by which contrast agents induce relaxation [234–237]. The first, which is based on exchange of water protons in and out of the first and second hydration sphere of the nanoparticle, is fairly specific to water and is unlikely to be applicable to relaxing the radical pairs in cryptochrome.The second is based on Brownian motion of the nanoparticle and the surrounding water molecules. As the nanoparticle tumbles, the magnetic field felt by any single molecule due to the nanoparticle will fluctuate, driving relaxation. Finally, Néel relaxation of a superparamagnetic nanoparticle is also the source of a fluctuating magnetic field that can relax nearby protons. These second two mechanisms, both based on rotations of the nanoparticle's magnetic moment, are very similar to the relaxation processes studied in chapters 4 and 5. Both will be investigated in this chapter using the two-site model.

All medical applications of MNPs require them to be highly localised, biocompatible, non-

toxic and have a controllable shape, stoichiometry, surface structure and size [224, 226]. It is common to use iron oxide nanoparticles, which occur naturally in many biological systems and are largely biocompatible and biodegradable [230, 232] However, other metals and compounds are sometimes used to achieve particular magnetic properties. For example, one of the most common families of contrast agents are those based on Gd^{3+} ions, which have seven unpaired electrons [226, 230, 232]. Gadolinium is toxic, so the ions are chelated to stop them reacting inside the body.

Superparamagnetic iron oxide (SPIO) nanoparticles form another major class of contrast agents. They reach different parts of the body and use different relaxation mechanisms to Gd^{3+} (more Brownian and Néel relaxation and less proton exchange) [230, 232, 235]. They primarily drive transverse relaxation and produce good T_2-weighted images. The first use of SPIOs was in imaging livers, where they are selectively taken up by Kupffer cells. Ultra-small SPIOs can also pass out of the blood vessels and have been used for diagnostic imaging of the lymphatic system [230].

Contrast agents are usually made up of three components: a magnetic core, a biocompatible shell and bioactive labels that allow the particle to target specific substrates [230]. SPIOs have frequently been coated with organic ligands (such as dextran or PEG), trapped in micelles or encapsulated in inorganic (Si or C) shells to improve their biocompatibility, allow for easier functionalisation and prevent them from aggregating inside the body [224, 226, 230, 232, 235].

Traditional syntheses of SPIOs (e.g. co-precipitation, micelle synthesis and thermal decomposition) have focused on achieving a uniform size distribution, although this was only partially successful for the original dextran-coated SPIOs [226, 230, 232]. However, the crystallinity and surface-structure is not well-controlled by these methods. An alternative approach, adopted more recently, is to make use of natural cage structures, such as lipoproteins, viruses and ferritin proteins, to template the synthesis of encapsulated nanoparticles [227, 238]. The biological origin of the protein cages imparts natural biocompatibility, minimises the toxicity of the mineral core, and makes them suitable for

large-scale production [227]. Furthermore, the protein cage provides a versatile platform for functionalising the particle [239] (with e.g. targeting materials) and it confines the growth of the mineral cores to produce uniformly sized particles.

The most commonly used protein templates are the ferritins – a class of spherical iron-storage proteins common to animals, plants and bacteria [227, 238, 240]. Ferritin will be considered as a candidate nanoparticle in section 7.6. Viruses, although they have a natural ability to enter and infect cells, will not be considered due to their larger size (the commonly used cowpea chlorotic mottle virus and tobacco mosaic virus are a 28 nm spheroid and an 18×300 nm rod, respectively) [227, 231].

Independently of their many uses in medicine, a handful of studies have considered how (biogenic or artificial) MNPs might interact with the radical pair mechanism [241–243]. However, they have all focused on ferromagnetic nanoparticles with a permanent magnetic moment that creates a nanoscale field gradient between the two radicals. The field gradients that they suggest are, at best, only achievable if the radical pair sits on the surface of a large, highly magnetized nanoparticle. In this situation, the spins in the radicals experience very different magnetic fields and therefore precess at different rates, providing an additional pathway for singlet-triplet interconversion. This is thought to amplify the magnetic field effect.

A very different scenario is considered in this chapter, where the radical pair interacts with a nearby superparamagnetic nanoparticle. In the absence of an external magnetic field, the average magnetic moment of the nanoparticle is zero. In addition, the distance between the nanoparticle and the radical pair is much larger than the distance between the two radicals, which consequently experience very similar magnetic fields. Field gradients of the type described in references [241–243] will not arise.

7.4 Application of the two-site model

7.4.1 Néel relaxation

The Néel relaxation of a particle with strong uniaxial symmetry consists of virtually instantaneous flips of the particle's magnetic moment between two antiparallel orientations, which lie along what is termed the 'easy axis'. A strong external magnetic field can bias the flipping of the magnetic moment so that it is more often aligned with the field. However, in an Earth-strength field at room temperature, the degree of alignment is on the order of $m \times 10^{-7}$, where m is the instantaneous magnetic moment in Bohr magnetons (μ_{B}) [244]. Therefore, for magnetic moments smaller than a few thousand Bohr magnetons, the flipping can be treated as a random event, with the time between flips taken from an exponential distribution whose mean is given by equation (7.3). This behaviour can intuitively be captured using a two-site model (see section 3.2.1), in which the two sites correspond to each of the two possible orientations of the magnetic moment. Mathematically, the system is described by two coupled Liouville-von Neumann equations:

$$\begin{pmatrix} \dot{\rho}_1(t) \\ \dot{\rho}_2(t) \end{pmatrix} = \begin{pmatrix} -\hat{\hat{L}}_1 - \frac{\mathbb{I}}{\tau_{\mathrm{N}}} & \frac{\mathbb{I}}{\tau_{\mathrm{N}}} \\ \frac{\mathbb{I}}{\tau_{\mathrm{N}}} & -\hat{\hat{L}}_2 - \frac{\mathbb{I}}{\tau_{\mathrm{N}}} \end{pmatrix} \begin{pmatrix} \rho_1(t) \\ \rho_2(t) \end{pmatrix}, \tag{7.4}$$

where $\rho_{1/2}(t)$ are the density matrices of the radical pair subject to each of the two orientations of the magnetic moment, $\mathbb{I}$ is the identity operator, τ_{N} is the Néel relaxation time and $\hat{\hat{L}}_{1/2}$ are Liouville space superoperators that act on the density matrix according to

$$\hat{\hat{L}}_{1/2}\rho(t) = i\left[\hat{H}_{1/2}, \rho(t)\right] + k\rho(t), \tag{7.5}$$

where k is the recombination rate constant (assumed to be the same for singlet and triplet reactions). The spin Hamiltonian in each site $\hat{H}_{1/2}$ contains the Zeeman interaction with the Earth's magnetic field, hyperfine interactions between the unpaired electrons and the nuclei in each radical and the Zeeman interaction between the unpaired electrons and one

orientation of the nanoparticle's magnetic moment:

$$\begin{aligned}\hat{H} =&\gamma_e B_0\Big((S_z^{(1)}+S_z^{(2)})\cos(\theta)+(S_x^{(1)}+S_x^{(2)})\sin(\theta)\cos(\phi)+(S_y^{(1)}+S_y^{(2)})\sin(\theta)\sin(\phi)\Big)\cdots\\ &+\sum_{i=1,2}\sum_n \mathbf{I}_n\cdot\mathbf{A}_{n,i}\cdot\mathbf{S}^{(i)}+\gamma_e\Big(\boldsymbol{B}_{\mathrm{n}}(\mathbf{r}^{(1)})\cdot\mathbf{S}^{(1)}+\boldsymbol{B}_{\mathrm{n}}(\mathbf{r}^{(2)})\cdot\mathbf{S}^{(2)}\Big).\end{aligned} \tag{7.6}$$

The nanoparticle is modelled as a point dipole which produces a field at position $\boldsymbol{r}$

$$\boldsymbol{B}_{\mathrm{n}}(\mathbf{r})=\frac{\mu_0}{4\pi}\left(\frac{3(\mathbf{m}\cdot\mathbf{r})\mathbf{r}}{r^5}-\frac{\mathbf{m}}{r^3}\right), \tag{7.7}$$

where $\boldsymbol{m}$ is the instantaneous magnetic moment of the particle. The point dipole model is a good description of the field around a uniformly magnetized sphere (at points outside the surface of the sphere). As the distance from the centre of the nanoparticle to the radical pair will likely be ≥ 3 times the distance from the centre of the nanoparticle to its surface (see later discussion), the point dipole model provides a good approximation of the nanoparticle field. Deviations from this model might arise from non-uniform composition or structure of the nanoparticle but this will not be treated.

Larger spin systems

In chapter 4, I focused on the regimes of fast and slow motion, where the compass was able to survive relaxation. For the simulations in this chapter, the region of maximum relaxation is of the most interest. For large spin systems, the linear system was handled in a similar way to the slow motion regime in section 4.1.1, with a slight adjustment that proved effective in handling the regime of interest.

Before the gaussian elimination, the top and bottom rows of equation (7.4) are exchanged so that the linear system to be solved is

$$\begin{pmatrix}-\frac{\mathbb{I}}{\tau_{\mathrm{N}}} & \Delta_2\\ \Delta_1 & -\frac{\mathbb{I}}{\tau_{\mathrm{N}}}\end{pmatrix}\begin{pmatrix}x_u\\ x_l\end{pmatrix}=\begin{pmatrix}\rho(0)\\ \rho(0)\end{pmatrix}, \tag{7.8}$$

where

$$\Delta_1 = \hat{\hat{L}}_1 + \frac{\mathbb{I}}{\tau_{\mathrm{N}}} \tag{7.9}$$

$$\Delta_2 = \hat{\hat{L}}_2 + \frac{\mathbb{I}}{\tau_{\mathrm{N}}}. \tag{7.10}$$

After the gaussian elimination step this becomes

$$\begin{pmatrix} -\frac{\mathbb{I}}{\tau_{\mathrm{N}}} & \Delta_2 \\ 0 & -\frac{\mathbb{I}}{\tau_{\mathrm{N}}} + \Delta_1 \tau_{\mathrm{N}} \mathbb{I} \Delta_2 \end{pmatrix} \begin{pmatrix} x_u \\ x_l \end{pmatrix} = \begin{pmatrix} \rho(0) \\ \rho(0) + \Delta_1 \tau_{\mathrm{N}} \mathbb{I} \rho(0) \end{pmatrix}. \tag{7.11}$$

As before, the lower line is solved first, using the BICGSTAB solver with an initial guess of

$$x = (\Delta_1 \tau_{\mathrm{N}} \mathbb{I} \Delta_2)^{-1} (\rho(0) + \Delta_1 \tau_{\mathrm{N}} \mathbb{I} \rho(0)). \tag{7.12}$$

The initial guess is constructed in a stepwise manner, transforming between the eigenbases of Δ_1 and Δ_2 where appropriate. In the region of maximum relaxation, $1/\tau_{\mathrm{N}}$ is a similar size to the eigenvalues of the Hamiltonian. Therefore, $(\Delta_1 \tau_{\mathrm{N}} \mathbb{I} \Delta_2)$, which contains all the possible terms, should be significantly larger than $\mathbb{I}/\tau_{\mathrm{N}}$, making equation (7.12) a very good initial guess. Providing a better initial guess is equivalent to preconditioning the system and greatly reduces the number of iterations performed by the solver.

7.4.2 Brownian motion

In addition to undergoing Néel relaxation, the nanoparticle and radical pair can both move around relative to each other. One of the main ways that MRI contrast agents induce relaxation is through fluctuations in their interaction with neighbouring spins as all the molecules tumble and diffuse in solution. In the proposed experiment, the nanoparticle is imagined to be bound to cryptochrome to ensure that it selectively relaxes its target. This will naturally reduce the amount of relative motion between the two molecules.

However, it is still possible that small motions could add to the relaxation induced by the nanoparticle. To investigate this possibility, the two-site model was extended to a four-site model:

$$\begin{pmatrix} \dot{\rho}_1 \\ \dot{\rho}_2 \\ \dot{\rho}_3 \\ \dot{\rho}_4 \end{pmatrix} = \begin{pmatrix} -\hat{\hat{L}}_1 - \frac{\mathbb{I}}{\tau_{\mathrm{N}}} - k_m\mathbb{I} & \frac{\mathbb{I}}{\tau_{\mathrm{N}}} & k_m\mathbb{I} & 0 \\ \frac{\mathbb{I}}{\tau_{\mathrm{N}}} & -\hat{\hat{L}}_2 - \frac{\mathbb{I}}{\tau_{\mathrm{N}}} - k_m\mathbb{I} & 0 & k_m\mathbb{I} \\ k_m\mathbb{I} & 0 & -\hat{\hat{L}}_3 - \frac{\mathbb{I}}{\tau_{\mathrm{N}}} - k_m\mathbb{I} & \frac{\mathbb{I}}{\tau_{\mathrm{N}}} \\ 0 & k_m\mathbb{I} & \frac{\mathbb{I}}{\tau_{\mathrm{N}}} & -\hat{\hat{L}}_4 - \frac{\mathbb{I}}{\tau_{\mathrm{N}}} - k_m\mathbb{I} \end{pmatrix} \begin{pmatrix} \rho_1(t) \\ \rho_2(t) \\ \rho_3(t) \\ \rho_4(t) \end{pmatrix}. \tag{7.13}$$

Sites 1 and 2 have the same positions of the nanoparticle and the radical but opposing orientations of the nanoparticle's magnetic moment. The same is true for sites 3 and 4. This is the two-site model for Néel relaxation described in section 7.4.1. Sites 1 and 3 have the same orientation of the nanoparticle's magnetic moment but different relative positions of the nanoparticle and the radical pair. For example, in site 3, the nanoparticle might be 2 nm further away from the radical pair than in site 1. Sites 2 and 4 are likewise paired. This creates a two-site model for nanoparticle 'hopping', where k_m is the rate constant for the hopping. In each site, the magnetic field from the nanoparticle at the radical pair is calculated using equation (7.7). Note that N_{sites} in equation 4.2 is now 4.

7.5 Determining the criteria for the nanoparticle

Calculations on small model systems

Applying the two-site model to a representative radical pair, with one spin-1/2 nucleus in one of the radicals and a recombination lifetime of 10 μs, highlights some important criteria for selecting a suitable nanoparticle.

First, the Néel relaxation time needs to be carefully chosen so that the magnetic field from the nanoparticle fluctuates on the right timescale to affect the spin dynamics of

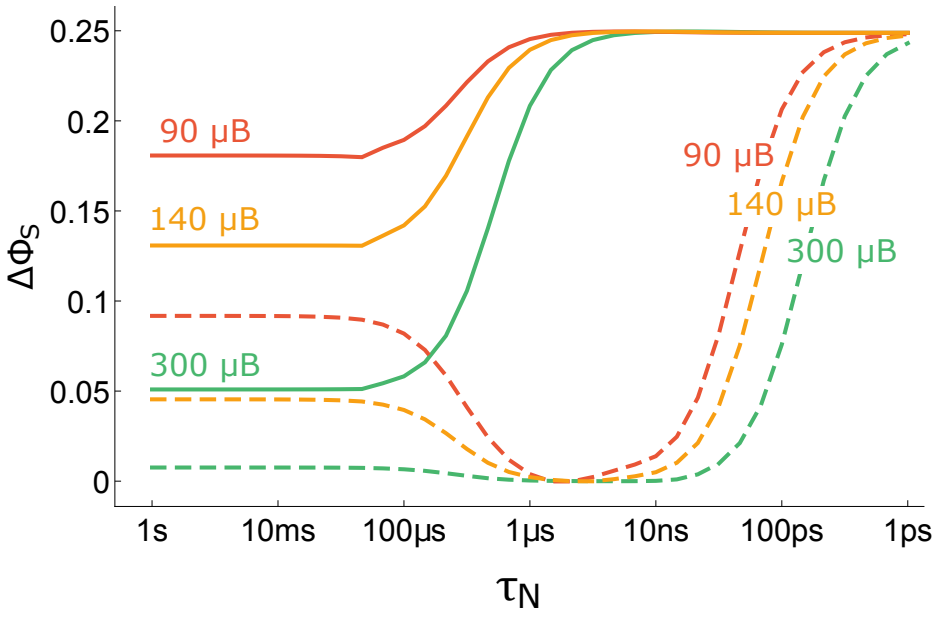


Figure 7.2: Singlet yield anisotropy (equation 4.16) as a function of Néel relaxation time τ_N for a radical pair with a single spin-1/2 nucleus in one of the radicals with HFI [0,0,1.5] mT. The distance between the two radicals is 1.9 nm. A nanoparticle is positioned 12 nm to the left of the radical containing the single magnetic nucleus. Its easy axis is oriented either parallel (solid lines) or perpendicular (dashed lines) to the principal axis of the single hyperfine interaction. The magnetic moment of the nanoparticle (in Bohr magnetons) is indicated in each case (values selected from reference [245]). $k = 10^5$ s^{-1}; $\phi = 0$; $B_0 = 50$ μT.

the radical pair. From chapters 4 and 5, we expect maximum relaxation to occur when $\tau_N \approx 10$ ns. From the dashed lines in figure 7.2, it can be seen that, indeed, at $\tau_N \approx 10$ ns the system is efficiently relaxed to an equilibrium state ($\Delta\Phi_S = 0$). However, relaxation is not the only way to reduce the anisotropy of the compass signal. For much longer τ_N, the Zeeman interaction with the apparently static magnetic moment of the nanoparticle is enough to distort the shape of the compass signal, which, although it is not a relaxation effect, could also fulfil the requirements of the experiment.

Suggestions have previously been made that a nearby magnetic moment (such as a ferromagnetic nanoparticle) would enhance rather than destroy compass anisotropy by amplifying the Earth's magnetic field [82]. This assumes that the magnetic nanoparticle swings round like a compass needle to align itself with the Earth's field. However, here, the interaction between the nanoparticle and the Earth's field is much smaller than the

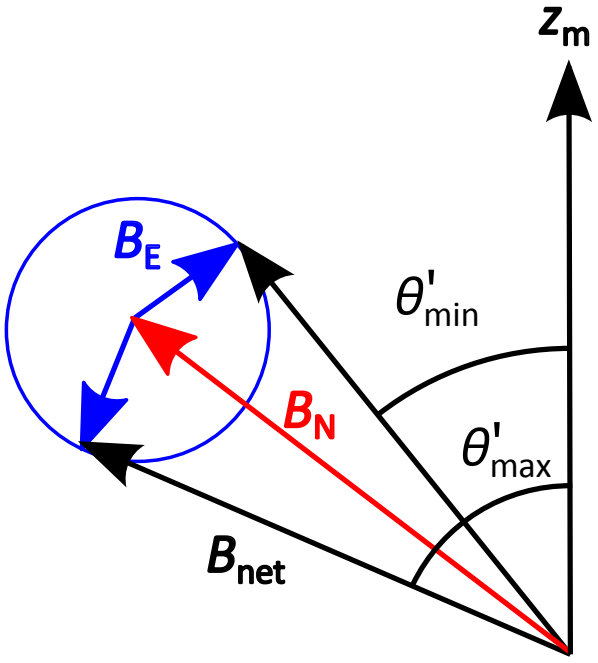


Figure 7.3: The angle θ' between the net field vector $\boldsymbol{B}_{\text{net}}$ and the molecular $\boldsymbol{z}_{\text{m}}$ axis adopts a limited range of values, whereas the angle between the Earth's field $\boldsymbol{B}_{\text{E}}$ and $\boldsymbol{z}_{\text{m}}$ can take any value because the bird can face in any direction.

thermal energy (see above) and hence the angle between the radical pair and the easy axis of the nanoparticle is fixed, regardless of the direction of the Earth's field.

In the limit of slow Néel relaxation, the radical pair experiences a Zeeman interaction with the net magnetic field ($\boldsymbol{B}_{\text{net}} = \boldsymbol{B}_{\text{E}} + \boldsymbol{B}_{\text{N}}$), where $\boldsymbol{B}_{\text{E}}$ is the geomagnetic field and $\boldsymbol{B}_{\text{N}}$ is the field generated by the nanoparticle. As illustrated in figure 7.3, the range of values for θ', the angle between the net field vector $\boldsymbol{B}_{\text{net}}$ and the molecular z axis $\boldsymbol{z}_{\text{m}}$, is always smaller than the range of θ values, where θ is the angle between $\boldsymbol{z}_{\text{m}}$ and $\boldsymbol{B}_{\text{E}}$. The larger $\boldsymbol{B}_{\text{N}}$ is relative to $\boldsymbol{B}_{\text{E}}$, the more closely $\boldsymbol{B}_{\text{net}}$ resembles $\boldsymbol{B}_{\text{N}}$ and the smaller the range of θ' values, invariably reducing the difference between the maximum and minimum singlet yield (the singlet yield anisotropy). Moreover, if $\boldsymbol{B}_{\text{N}}$ is significantly larger than $\boldsymbol{B}_{\text{E}}$, it may alter the dependence of Φ_{S} on θ', further reducing the anisotropy.

When $\boldsymbol{B}_{\text{N}}$ is large, the difference between θ' and θ may also result in the singlet yield profile being shifted along the θ axis. The two opposing orientations of $\boldsymbol{B}_{\text{N}}$ sampled by Néel relaxation shift the singlet yield profile in opposite directions. Subsequently

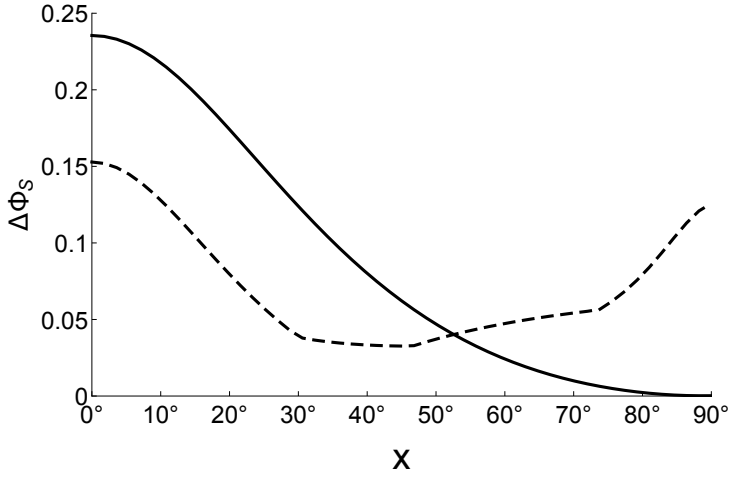


Figure 7.4: Singlet yield anisotropy when the easy axis of the nanoparticle is $[\sin(x), 0, \cos(x)]$. The magnetic moment of the nanoparticle is 140 μ_{B} and the Néel relaxation time is 1 ns (solid line) or 10 ms (dashed line). $k = 10^5$ s^{-1}; $\phi = 0$; $B_0 = 50$ μT.

averaging the singlet yield profile over the two sites in the model produces a broader, flatter minimum.

As the rate of Néel relaxation increases, the field from the nanoparticle is partially averaged away ($\boldsymbol{B}_{\mathrm{N}}$ is smaller). When τ_{N} is very short, $\boldsymbol{B}_{\mathrm{N}}$ averages to zero and the nanoparticle has no effect on the spin dynamics of the radical pair.

In addition to selecting a nanoparticle with an appropriate Néel relaxation time, the size m of the nanoparticle's instantaneous magnetic moment must also be considered. As described above, when τ_{N} is long, a nanoparticle with a larger magnetic moment more effectively flattens out the singlet yield profile to a constant value. Increasing m also leads to more efficient relaxation (see equation (4.18)), reducing the singlet yield anisotropy. However, if m is too large, the nanoparticle field will extend further into the surrounding environment and thus has a greater potential to affect other nearby (non-cryptochrome) radical pairs that may exist, reducing the selectivity of the experiment.

Finally, the orientation of the nanoparticle relative to the radical pair dictates what influence it will have. When τ_{N} is large, the angle θ' between the easy axis of the nanoparticle and the principal axis of hyperfine interaction in the radical pair (z_{m}) determines the

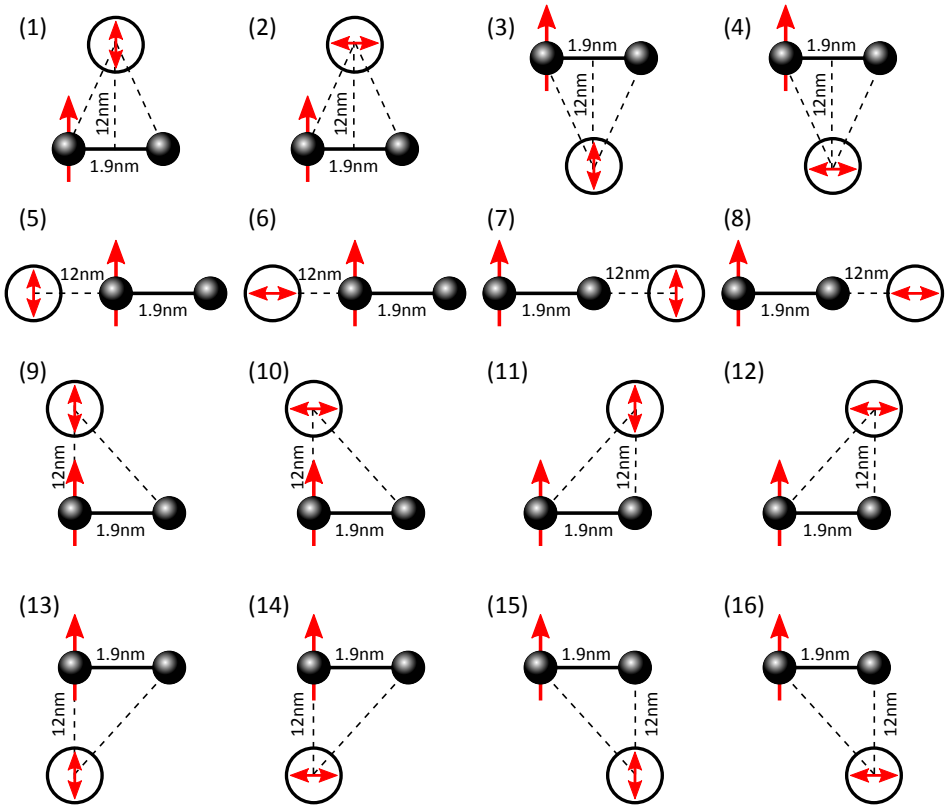


Figure 7.5: Representative arrangements of a nanoparticle bound to a radical pair. The black spheres represent the two radicals, with the red arrow on the left hand sphere indicating the principal axis of the single hyperfine interaction (defined as the z axis). The position of the nanoparticle is shown by the white circle, with the double-headed red arrow marking the orientation of the easy axis. 1.9 nm is the distance between the flavin and tryptophan radicals in cryptochrome. 12 nm is a representative distance based on approximately 6 nm from the flavin radical to the surface of the cryptochrome, plus the 6 nm radius of ferritin (discussed in section 7.6).

value to which the singlet yield will flatten out (see figure 7.4). In addition, for this simple radical pair, the nanoparticle only induces spin relaxation if some component of its magnetic moment lies perpendicular to z_{m}. The larger the perpendicular component, the faster relaxation it induces and the more effect it has on the compass.

Figure 7.2 only shows data for a situation in which the nanoparticle is located 12 nm from the radical containing the hyperfine interaction, along the axis joining the two radicals. In reality, the nanoparticle could be bound in almost any position relative to the radical pair (see figure 7.5). The same effects may be observed in all cases to varying degrees. Figure 7.6 give some illustrative examples.

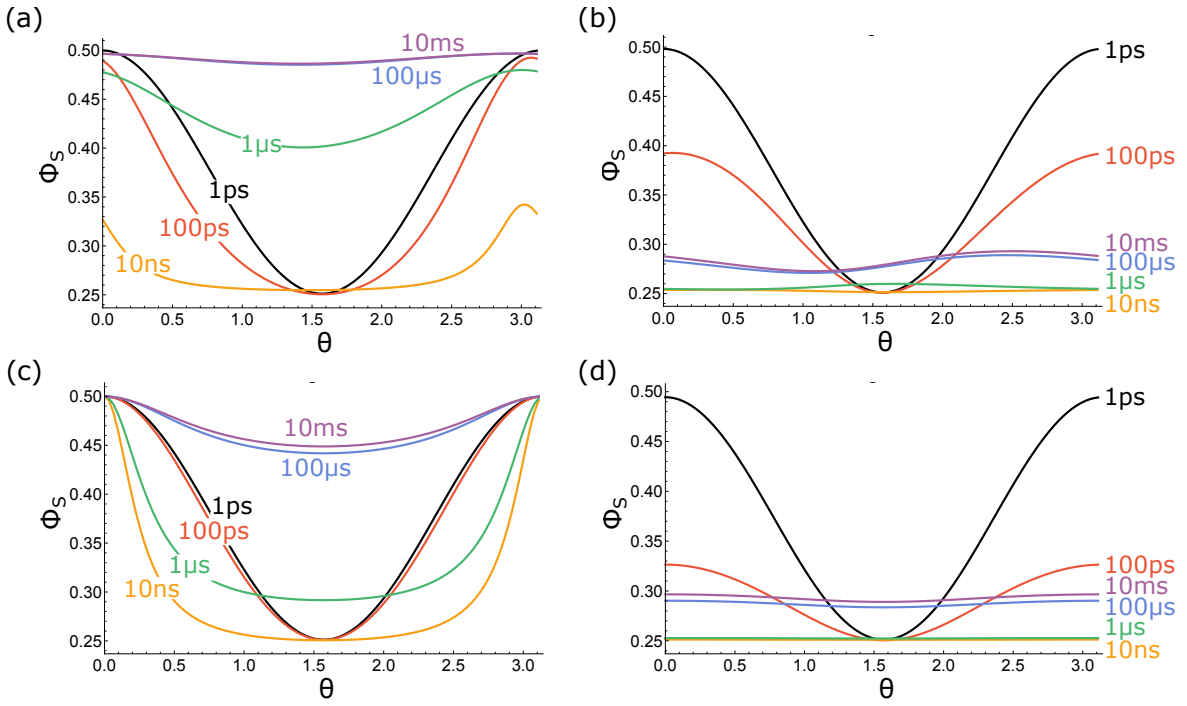


Figure 7.6: Singlet yield profiles for the model radical pair containing a single spin-1/2 nucleus. The radical pair and nanoparticle are organised as shown in (a) arrangement 1, (b) arrangement 2, (c) arrangement 5, (d) arrangement 6 in figure 7.5. The Néel relaxation time of the nanoparticle is indicated on the graph. $k = 10^5$ s^{-1}; $\phi = 0$; $B_0 = 50$ μT.

In arrangement 1 (figure 7.6(a)), the nanoparticle produces a field at the radicals with a large z (parallel) component but a small x (perpendicular) component. The fastest spin relaxation is observed when $\tau_N \sim 1 - 10$ ns. Furthermore, the minimum in the singlet yield profile is broadened and slightly shifted along the θ axis by the interaction with the net field ($\boldsymbol{B}_N + \boldsymbol{B}_E$). For very large τ_N, the strong static field from the nanoparticle completely outweighs the Earth's field and the singlet yield tends to a constant value of 0.5 (corresponding to $\theta = 0°$).

By contrast, in arrangement 2 (figure 7.6(b)), the nanoparticle produces a field at the radicals with a large x component and small z component. Consequently, faster relaxation is observed and the minimum in the singlet yield is more strongly shifted along the θ axis. At large τ_N, the singlet yield tends to a constant value of ≈ 0.3, which corresponds to $\theta = 90°$ for the ~ 0.3 mT field produced by the nanoparticle at the radicals.

Arrangements 5 (figure 7.6(c)) and 6 (figure 7.6(d)) are related in a similar way, although

the minimum in the singlet yield remains centred on the θ axis. When, as here, the field vector $\boldsymbol{B}_{\mathrm{N}}$ at the radicals is exactly inverted by Néel relaxation, the singlet yield profiles corresponding to the two sites are shifted by equal amounts in opposite directions along the θ axis. Averaging the singlet yield profile over the two sites reintroduces the symmetry around $\theta = 90°$.

The other way that a nanoparticle might conceivably drive relaxation of the radical pair is that Brownian motion of the nanoparticle could cause random fluctuations in the field experienced by the radicals. Figure 7.7 demonstrates that small fluctuations in the distance between the nanoparticle and the radical pair do very little to increase the damage already done to the compass by Néel relaxation. Since we wish the nanoparticle to be bound to cryptochrome to maximize the selectivity of the experiment, it cannot move very far relative to the radical pair. Small 'hops', or even small rotations of a tethered nanoparticle will not greatly change the magnetic field experienced by the radical pair, particularly in comparison to the full reversal of $\boldsymbol{B}_{\mathrm{N}}$ that it experiences due to Néel relaxation.

Furthermore, if the motion of the nanoparticles increases the distance to the radical pair, it reduces the strength of the Zeeman interaction and, hence, the amount of spin relaxation driven by Néel relaxation of the nanoparticle. The increased rate of spin relaxation driven by nanoparticle hopping does not compensate for the reduced efficacy of Néel relaxation and overall, more of the compass signal survives.

As Brownian motion seems to have little effect compared to Néel relaxation in the situation where the nanoparticle is tethered to cryptochrome, it will be neglected from the remainder of the simulations in this chapter.

Calculations on the cryptochrome model

More detail about the required magnetic moment and orientation of the nanoparticle can be obtained by considering the more realistic model of cryptochrome introduced in chapter 5.

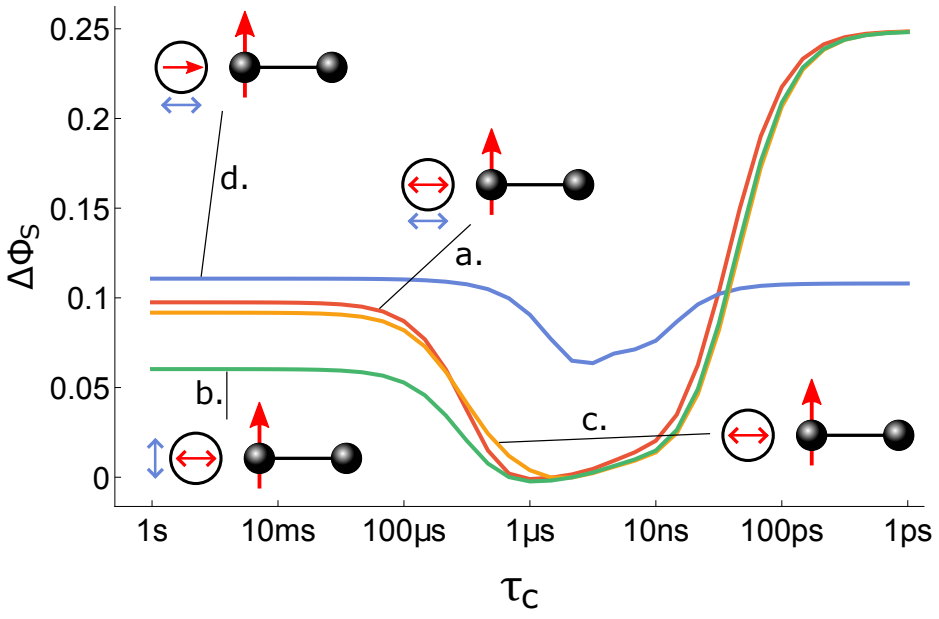


Figure 7.7: Variation in the singlet yield anisotropy (equation (4.16)) as the nanoparticle performs different combinations of hopping motion and Néel relaxation: a. 2 nm horizontal hopping and Néel relaxation with $k_m = 10^9$ s^{-1} and $\tau_N = \tau_c$; b. 2 nm vertical hopping and Néel relaxation with $k_m = 10^9$ s^{-1} and $\tau_N = \tau_c$; c. Néel relaxation only with $\tau_N = \tau_c$; horizontal hopping only with $1/k_m = \tau_c$. (Blue arrows indicate hopping motion of the nanoparticle.) The nanoparticle and radical pair are positioned as in arrangement 6 (see figure 7.5). Hopping motion increases the distance between the nanoparticle and radical pair. The nanoparticle has a magnetic moment of 90 μ_B. $k_S = 10^5$ s^{-1}; $\phi = 0$; $B_0 = 50$ μT.

The optimum magnetic moment of the nanoparticle depends on how closely it is bound to cryptochrome, which may be varied, and how much change must be made to the compass signal to disorient the bird, which is not known. Therefore, rather than attempting to determine a precise magnetic moment, the calculations in figure 7.8 focus on how large $\boldsymbol{B}_N$ must be at the radical pair. Using the two-site model, a periodically reversing field is applied along the x_m axis at each of the radicals, mimicking the Néel relaxation of a nearby nanoparticle. The Néel relaxation time is taken as 1 ns, a value characteristic for ferromagnetic materials [246].

When the radical pair recombination rate is $k = 10^5$ s^{-1}, a spike is present in the singlet yield profile in the absence of a nanoparticle field. When the strength of the nanoparticle field is 0.15 mT or higher, the spike ceases to be visible. I will take this as "sufficiently

altered" that the bird can no longer orient.

When $k = 10^6$ s^{-1} the point where the signal may be considered "sufficiently altered" is harder to pinpoint. However, the singlet yield anisotropy is reduced to approximately 10% of its original value by a 0.4 mT field, which I will take as the target field in the remainder of this chapter.

Figure 7.8(c) shows how close to cryptochrome a nanoparticle with a given magnetic moment would need to be bound to create a 0.15 mT or 0.4 mT field. It assumes that the nanoparticle can be modelled as a point dipole with its easy axis perpendicular to z_{m}. These curves can be used to assess the suitability of candidate nanoparticles. In general, it would be preferable to bind the nanoparticle as close to cryptochrome as possible to minimize the possibility of it interacting with anything else in the surrounding environment. However, the size of the cryptochrome protein and the magnetic nanoparticle place a lower bound on the centre-to-centre distance.

Figure 7.9 demonstrates that, in contrast to the one-nuclear-spin model, when the radical pair contains hyperfine interactions with components along more than one axis, Néel relaxation of the nanoparticle always drives spin relaxation, even when the easy axis is parallel to z_{m}. However, as for the smaller radical pair model, the fastest relaxation is induced by fluctuations in the magnetic field perpendicular to z_{m}.

Overall, the proposed experiment requires a nanoparticle with a Néel relaxation time of at least a few nanoseconds and an instantaneous magnetic moment on the order of a few hundred bohr magnetons.

7.6 Candidate nanoparticles

In addition to the key magnetic characteristics identified above, the nanoparticle that is chosen for the experiment must, ultimately, be suitable for incorporation into a living system. This means it must be non-toxic and stable under physiological conditions. For

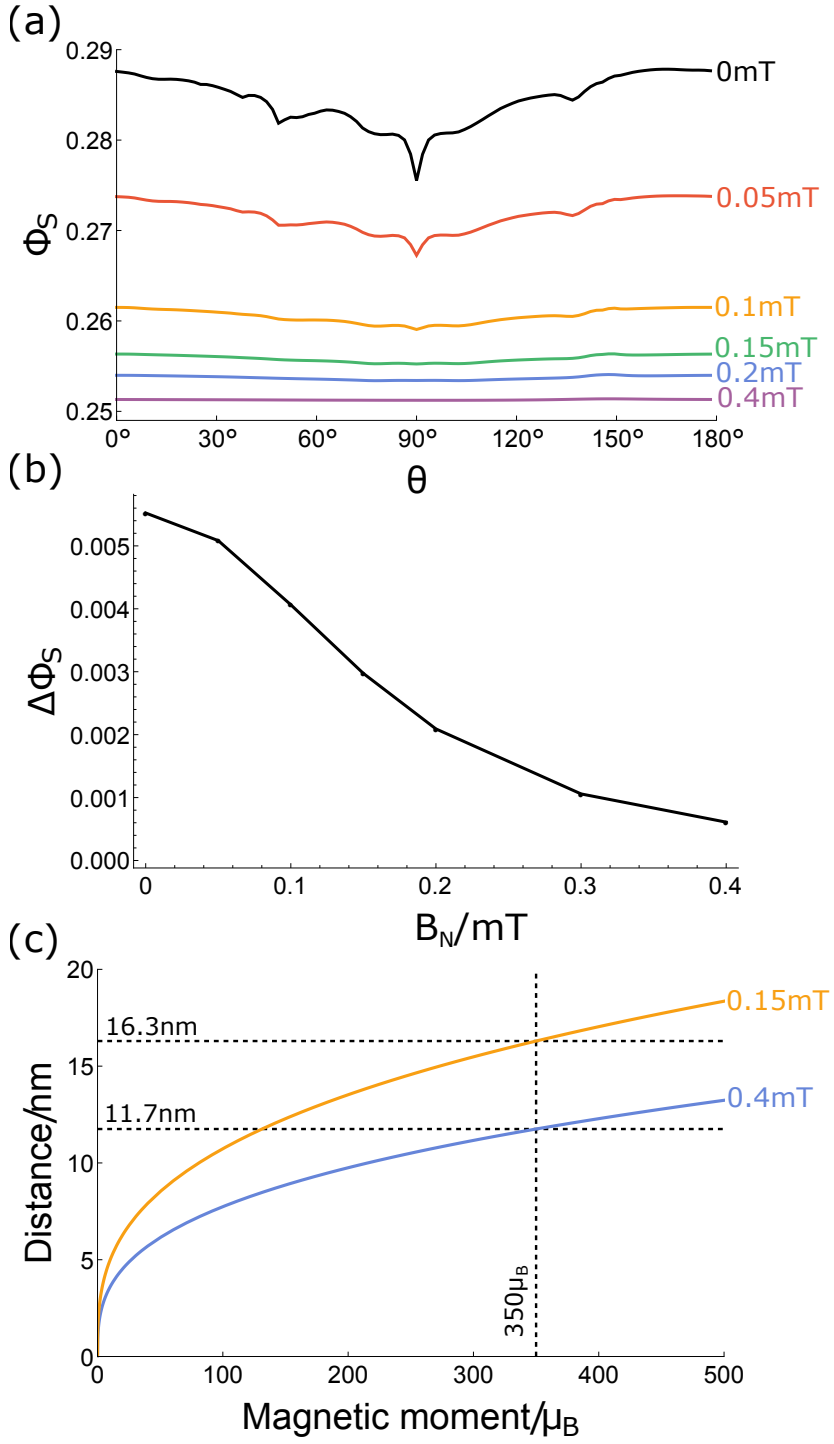


Figure 7.8: (a) Singlet yield profiles of the model flavin-tryptophan radical pair in the presence of a fluctuating magnetic field (from a nearby nanoparticle). The radical pair recombination lifetime is 10 μs. (b) Change in the singlet yield anisotropy as a function of the strength of the nanoparticle field at the radical pair. The radical pair recombination lifetime is 1 μs. For both (a) and (b), the field strength is the same at both radicals and is indicated on the graph. The Néel relaxation time of the nanoparticle is 1 ns. The Earth's field strength is 50 μT and $\phi = \pi/2$. (c) Correlating the magnetic moment of the nanoparticle with the distance it must be from the radical to achieve a given field strength (indicated on the graph). The nanoparticle is assumed to act as a point dipole.

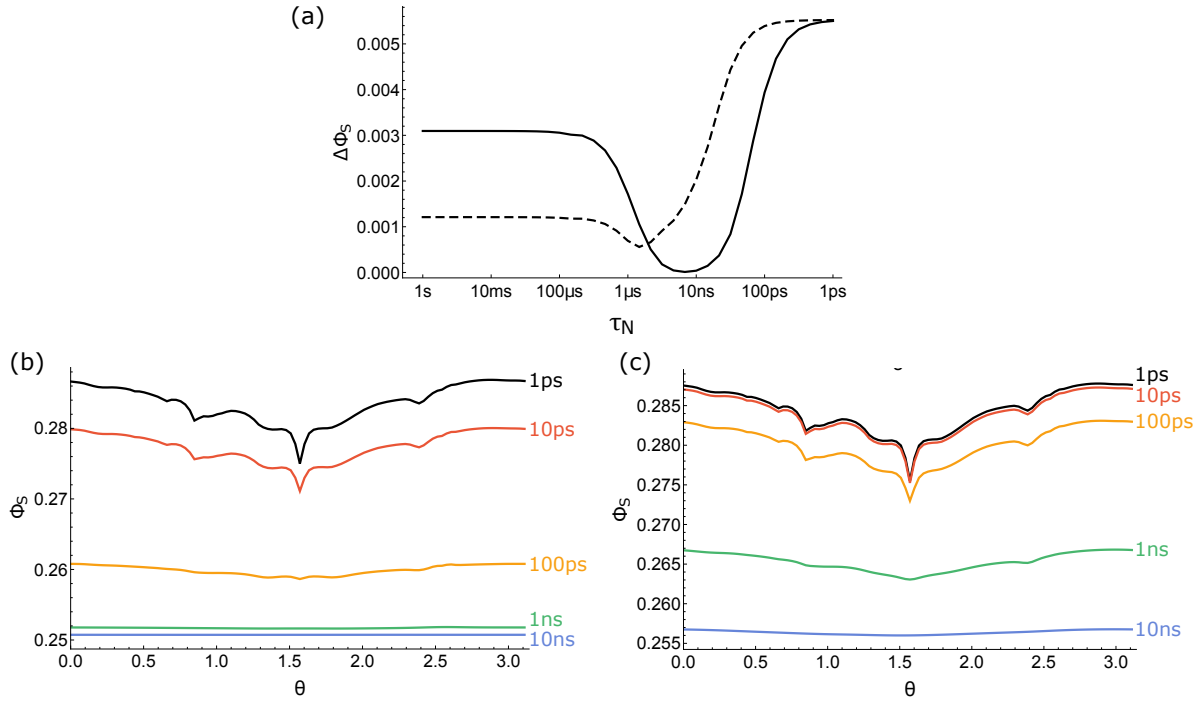


Figure 7.9: (a) Singlet yield anisotropy for the model FAD-Trp radical pair (section 5.5) as a function of the Néel relaxation time of a nearby nanoparticle. The nanoparticle is arranged with its easy axis either parallel (dashed line) or perpendicular (solid line) to the principal axis of the N5 hyperfine tensor in the flavin radical. The radical pair recombination lifetime is 1 μs. (b) and (c): Change in the singlet yield profile with the Néel relaxation time of a nearby nanoparticle. The easy axis of the nanoparticle is either perpendicular (b) or parallel (c) to the principal axis of the N5 hyperfine tensor in the flavin radical. In all cases, the nanoparticle is situated 12 nm away from the flavin radical along the flavin-tryptophan axis (13.9 nm away from the tryptophan radical) and has a magnetic moment of 350 μ_B. The radical recombination lifetime is 10 μs and $\phi = \pi/2$.

good experimental control, the particle size should be uniform and well-defined. These are, in essence, the same requirements that must be met by MRI contrast agents (see section 7.3). Contrast agents based on nanoparticles grown inside a protein or virus template are particularly appealing for their biocompatibility and monodispersity. Due to its small size, ferritin, the most common protein template, was chosen as the initial inspiration for a nanoparticle.

Ferritin

Ferritin is a highly symmetric spherical protein with a hollow centre that houses an iron-based magnetic mineral core [240, 247]. Its main functions are to store iron and regulate the concentration of free radicals in the body. Increased expression of the ferritin protein is consequently observed under high levels of oxidative stress and in areas of high iron concentration [240].

The protein shell of ferritin is made up of 24 subunits of two types: H (heavy) and L (light). Ferritins in different species, or different organs within the same species contain different ratios of H to L subunits; those with more L subunits (found, for example, in the liver and spleen) are capable of storing larger amounts of iron [240].

Ferritin is water-soluble, resistant to denaturation, attracts high affinity antibodies and is 12 nm in diameter, with an 8 nm diameter for the internal cavity [240, 248]. These are all attractive features for an *in vivo* experiment. In particular, the fact that ferritin has a comparable size to cryptochrome means that it should hopefully be able to interact with the radical pair without dominating the immediate environment too much. The same could not be said of Gd^{3+} or other iron oxide nanoparticles, which can have hydrodynamic diameters on the order of 10's – 100's of nanometres [230]. Furthermore, unlike many other nanoparticles, derivatives of human ferritin are capable of crossing a number of biological barriers, including the blood-brain barrier [233].

Natural ferritin has a single-domain, superparamagnetic ferrihydrite ($5Fe_2O_3$-$9H_2O$) core [227, 249], which contains up to 4500 Fe^{3+} ions [247] (and around 2000 on average [250]). The number of iron atoms contained within the mineral core is known as the loading factor and it can be controlled in artificial syntheses of ferritin [238]. The high-spin Fe^{3+} ions contain 5 unpaired electrons but are antiferromagnetically ordered, such that the net magnetic moment should be zero in the absence of an applied field. However, each ferritin core possesses a small magnetic moment due to uncompensated spins at the surface of the core [251, 252]. In a single-domain antiferromagnetic cluster of N spins, it is predicted

that about $N^{1/2}$ spins will be uncompensated [251]. This suggests a magnetic moment in the range $263 - 395$ μ_{B} (based on $2000 - 4500$ iron spins [250] with $S = 5/2$ and $\mu = g_e\sqrt{S(S+1)}$), which is in good agreement with the measured value of ≈ 300 μ_{B} between 20 and 120 K [249, 251]. Above 120 K, the magnetic moment increases slowly with temperature, which may be a result of increasing thermal disorder [251].

Ferritin is considered to be an ideal superparamagnet as the magnetic domains (the individual single-domain cores) are separated by the protein shell, meaning that they do not interact but, rather, behave as isolated magnetic particles [235, 249, 252]. The Néel relaxation time depends on the energy barrier between different orientations of the magnetic moment according to the Néel-Arrhenius equation (equation (7.3)). The size of the energy barrier, $E = KV/k_{\mathrm{B}}$, in turn depends linearly on the volume of the particle. Horse-spleen ferritin has a broad energy-barrier distribution, peaking between 180 and 400 K with a full width at half maximum of 200 K [249]. Combined with an attempt frequency $1/\tau_0 = 10^{12}$ s^{-1}, the Néel relaxation time of ferritin at room temperature is on the order of a few picoseconds. Despite the many otherwise favourable properties of ferritin, its Néel relaxation time makes it unsuitable for the proposed experiment as its magnetic moment will average to zero on the time-scale of the spin dynamics.

Magnetoferritin

Apart from its very short Néel relaxation time ferritin has many appealing properties that could be exploited in an experiment to test the identity of proposed magnetoreceptors. It therefore seems natural to look for nanoparticles based on the ferritin architecture but with improved magnetic properties.

Without its mineral core, the protein shell of ferritin is known as apoferritin. A large number of nanoparticles have been synthesised inside apoferritin [227, 245], which acts a template during synthesis to produce particles with a narrow size distribution. Of particular interest is a compound called magnetoferritin [253], which is synthesised by refluxing

apoferritin with ammonium ferrous sulphate ($(NH_4)_2Fe(SO_4)_2.H_2O$) in a deoxygenated environment [245, 254, 255]. This produces a core with ferrimagnetic maghemite and magnetite phases [246, 256, 257]. The change from antiferromagnetic to ferrimagnetic spin ordering, compared to natural ferritin, reduces the Néel relaxation time to $\tau_N \sim 1$ ns, in good agreement with values measured for pure magnetite [246]. Based on the results in section 7.5, a nanoparticle with $\tau_N \sim 1$ ns should be capable of driving efficient spin relaxation to destroy the functioning of the compass.

By varying the amount of iron reagent available in solution during the synthesis, different amounts of iron may be loaded into the magnetoferritin core, which offers a way of tailoring the magnetic moment. Magnetoferritin has been created with magnetic moments anywhere in the range $13 - 4636\ \mu_B$ [245, 246]. Some of these values are surprisingly small when one considers that a ferrimagnetic core would generally be expected to have a larger magnetic moment than the antiferromagnetic core in natural ferritin. Small magnetic moments are a result of disordered core formation when apoferritin is only partially loaded [245]. During core formation, small pieces of crystal grow around the interior surface of the protein shell (see figure 7.10). Strong exchange interactions mean that the whole core can be treated as a single domain particle. However, the disordered arrangement of individual fragments reduces the size of the net magnetic moment and creates strongly uniaxial magnetic anisotropy [258]. The Néel relaxation of magnetoferritin is consequently very well described by the two-site model in section 7.4.1. As more iron is loaded into the protein, the core becomes increasingly ordered and unified, with larger magnetic moments. An increased fraction of magnetite phase is also observed in larger cores [245].

Although a larger magnetic moment is more likely to guarantee that a nanoparticle could disrupt the spin dynamics of the radical pair compass, it reduces the selectivity of the experiment as the nanoparticle will also be more likely to affect other potential radical pairs in the surrounding environment. Furthermore, loading more iron into the apoferritin shell has other, unwanted effects. Although natural ferritin is relatively stable, the protein

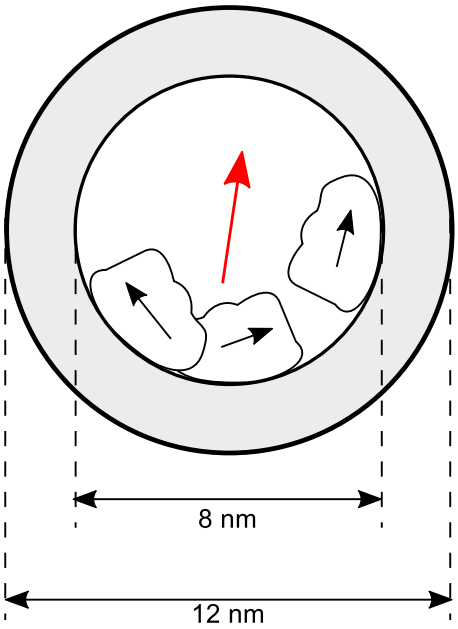


Figure 7.10: Structure of magnetoferritin. The diameter of the protein is 12 nm, whilst the interior diameter of the cavity is 8 nm. The core forms in small disordered chunks (a few of which are shown) on the interior surface but strong coupling between the pieces means that the core can be treated as one single domain particle with a magnetic moment indicated by the red arrow.

shell of magnetoferritin starts to distort as the loading factor is increased [257, 259]. When the loading factor exceeds 600, magnetoferritin has an increasing tendency to form aggregates. At a loading factor of 1000, approximately half of the protein shell has started to disassemble [257]. Where possible, it will therefore be advantageous to avoid overloading the magnetoferritin nanoparticles.

Early attempts to use magnetoferritin as a contrast agent found that it could be removed from the blood-stream in a matter of minutes by the liver and spleen, raising concerns that it would have limited use in imaging [232, 260, 261]. However, the use of magnetoferritin as a targeted contrast agent for imaging tumour cells has since been demonstrated successfully both *in vitro* [233, 239, 262] and *in vivo* [263]. This is encouraging as it suggests that magnetoferritin could similarly be engineered to target a magnetoreceptor. As for contrast agents, this experiment would exploit the natural biocompatibility of magnetoferritin, its ability to cross biological barriers [233] and the versatility of the protein shell for adding targeting ligands.

Other potential problems with the use of magnetoferritin *in vivo* are that the particles might aggregate and that ferritin and magnetoferritin have been shown to have peroxidase activity [240, 264]. Aggregation can be reduced by shaking and filtering the solution of particles before they are injected into the body so that no aggregates are present in the initial solution [257]. The possibility of the nanoparticle interacting chemically with the magnetoreceptor or other important compounds in the environment could be controlled for by repeating the experiment with apoferritin or natural ferritin, which have many of the same chemical properties but very different magnetic properties. The existence of a number of ready-made controls is one of the many appealing features of ferritin-based nanoparticles.

7.7 Practical considerations

There are a number of practical challenges to implementing an experiment that relies on specific binding of a synthetic nanoparticle to an intracellular protein.

First, there are hundreds of thousands of photoreceptor cells in each square millimetre of a bird's retina [182] and each cell contains multiple (potentially a large number of) cryptochrome proteins [265]. We do not know how many cryptochrome proteins would need to be deactivated in order to sucessfully disrupt the compass. This makes it difficult to judge how many nanoparticles need to be injected (or otherwise incorporated) into the bird. If too few nanoparticles are provided the compass may continue to function and the experiment could falsely conclude that cryptochrome is not the magnetoreceptor. Conversely, an excess of nanoparticles increases the risk that they will interact with something other than the intended target or even reach toxic levels that will harm the bird. These problems are exacerbated by the fact that the liver is effective at removing excess magnetoferritin from the blood, suggesting that the eventual number of bound nanoparticle - radical-pair complexes will be signficantly smaller than the original number of nanoparticles that are injected.

Targeted delivery to an intracellular protein is particularly challenging as the nanoparticle needs to first pass through the cell membrane. Increased uptake of magnetoferritin by cells can be achieved by labelling the protein shell with markers that will be recognised by the cell or by exploiting natural interaction pathways [262]. However, it is possible that the level of highly targeted delivery required by the proposed experiment is beyond the reach of current technology.

The problem of targeted delivery could be avoided altogether if the particle could be synthesised *in situ*. Section 7.7.1 will discuss the possibility of synthesising magnetoferritin in the body of a genetically modified animal.

Alternatively, the effect could be measured in a simpler system. Currently, research is underway to measure a magnetic field response directly from an isolated retina by recording electrical activity from a sample of cells using arrays of micro-electrodes [178]. If this technique can be perfected to the point where clear responses to a magnetic field can be recorded, the nanoparticle experiment could be conducted in a sample of retina rather than a whole bird. Delivering nanoparticles is likely to be easier in a system that is smaller, that does not incorporate the body's natural ability to remove foreign objects and where solutions of nanoparticles could possibly even be injected directly into the cells. In addition, the measured magnetic response would not rely on the bird's motivation to orient and would be less susceptible to unwanted side-effects of the nanoparticle's presence. Although no observation is directly made of changes to the birds' behaviour, magnetic field dependent firing of neuronal cells is closely linked to the way that the bird responds to magnetic stimuli.

Similar research is also focused on developing experiments to create spatially-resolved images of magnetic field effects on live cell cultures [113]. This sort of approach would again circumvent many of the problems of delivering the nanoparticles to the intended target. However, it does not involve the observation of any change in animal behaviour or even a change in neuronal firing or signalling, leaving slightly more room to doubt the link between cryptochrome and the magnetic compass. Additionally, the technique requires

the cryptochrome protein to be overexpressed in the cell, which is unlikely to be a good model of natural conditions. Nevertheless, if the nanoparticle experiment could not be performed on live animals, these two approaches could still offer interesting insights into the magnetic behaviour of cryptochrome *in vivo* .

The second practical problem with implementing the proposed experiment is setting it up in such a way that the results can be unambiguously interpreted. It needs to be clear that a change in behaviour (or neuronal firing) is the result of magnetic interactions between the nanoparticle and the target magnetoreceptor (cryptochrome), rather than any other effect of the nanoparticle in the body.

The first step to ensuring that the experiment can be properly interpreted is to fully characterise the interaction of magnetoferritin *in vitro* and demonstrate that the system behaves in the way predicted by the calculations in section 7.5. Suggestions for preliminary experiments of this sort are made in section 7.7.2.

Interpretation of the experimental results can also be aided by performing a set of control experiments for which the ferritin architecture is particularly well suited. The ability to remove or replace the core of natural ferritin creates the opportunity to repeat the experiment with a variety of similar but slightly different properties. In particular, it would be easy and beneficial to repeat the experiment using empty apoferritin and natural ferritin. This would prove that it is the magnetic and not the chemical presence of magnetoferritin that disrupts the compass. It would also confirm the theoretical prediction that the Néel relaxation of ferritin is too fast for it to have any effect on a radical pair compass, which would help to validate other predictions made by the same method.

7.7.1 Biogenic nanoparticles

Possibly the largest barrier to realising the proposed experiment is the need to deliver magnetoferritin nanoparticles in a targeted manner to intracellular cryptochrome proteins. A potentially more achievable alternative would be to genetically engineer a bird or fruit

fly to produce magnetoferritin, or a similar nanoparticle, already bound to cryptochrome. Existing literature suggests three possible routes towards synthesising magnetite nanoparticles in the animal's body.

The best-known example of biogenic magnetite is the crystals found in magnetotactic bacteria [266]. These bacteria produce vesicles called magnetosomes containing nanometre-sized particles of magnetite [228, 266]. The vesicles align to form a 'needle' that is clearly visible inside the body of the bacterium. The needle swings about to align itself with the magnetic field, forcing the bacterium to change its orientation.

Magnetite crystals are formed in magnetosomes by co-precipitating Fe^{2+} with Fe^{3+} ions that have been extracted from natural ferritin cores [267]. Typically, the crystals are large enough to be in the single domain region, although mutant species of bacteria have been engineered to produce superparamagnetic particles [228, 268]. The size of the magnetosomes varies between species but is usually well-controlled and uniform within a species [266]. Some species of bacteria, known as metal-reducing bacteria, produce superparamagnetic magnetite crystals outside their cell walls [269]. In contrast to the particles formed in magnetosomes, these crystals have an irregular morphology and broad size distribution. A poorly controlled synthesis of this sort is undesirable for the proposed experiment.

Magnetotactic bacteria could provide useful inspiration for producing intracellular superparamagnetic magnetite. However, if magnetosomes were to be used in place of magnetoferritin in the proposed experiment, particular care would need to be taken over their size. Not only should the particles be small enough to be superparamagnetic, but they should also be small enough not to show a preferential alignment in a magnetic field. Whereas, in magnetoferritin, magnetite grows on the interior protein surface, the crystal in a magnetosome is not attached to its encapsulating lipid bilayer and can rotate inside the vesicle to align itself with an external field or the contents of another magnetosome vesicle [266]. If the particles were to continually realign themselves with the Earth's field, the effect would be to enhance rather than destroy the compass signal by strengthening

the effective field experienced by the radical pair.

It may also be possible to modify ferritin itself to make naturally occuring magnetoferritin. A number of neurodegenerative diseases have been linked to the presence of mutated or malfunctioning ferritin proteins in the brain. The cores of 'pathological ferritin' contain a higher percentage of maghemite/magnetite phases and therefore more closely resemble magnetoferritin [270]. However, unlike artificial magnetoferritin, magnetite produced in pathological ferritin is poorly crystallised [271].

Furthermore, the protein shell of pathological ferritin does not function correctly and allows large amounts of iron to pass out of the protein into the blood, where it can reach toxic levels [270]. Clearly, we do not wish to engineer an organism to produce ferritin that will malfunction in this way as it would likely be so ill that one could no longer rely on it displaying any normal migratory or orientation behaviour, regardless of the effect on the radical pair mechanism. However, the observation of pathological ferritin suggests that there is scope to engineer 'biogenic magnetoferritin'.

Work by Gajdardziska *et al.* also hints at this possibility. In a paper in 2001, they report measurements of magnetite phases in the cores of plant ferritin (phytoferritin) in samples of grass (*Festuca* family) [272]. Phytoferritin differs structurally in several ways from animal ferritin; it contains only one type of subunit and has a unique N-terminal sequence [273]. The idea that these differences allow a magnetite core to form would be very promising if it could be verified. However, although a handful of papers have cited the original paper by Gajdardziska *et al.*, no further characterization of the magnetic properties of phytoferritin has appeared in the literature.

7.7.2 Suggested preliminary experiments

Performing the proposed experiment exactly as described, in an animal, pushes the boundaries of what may be achievable with current technology. It is conceivable that the technology could exist in the next few years to do this experiment on a cell culture or isolated

retina, which could be a very good alternative. However, before any of these options can be explored or implemented the effect needs to be characterised in a simpler system. Magnetic field effects have been measured on a number of artificial radical pair systems and on isolated proteins in solution [57, 110, 112, 221, 274, 275]. Demonstrating that these effects could be eradicated by the addition of magnetoferritin would be an excellent way to test the principles of the experiment and the choice of nanoparticle.

Previous measurements of magnetic field effects on radical pair reactions have mostly been performed using set-ups where the radicals or proteins are allowed to tumble freely in solution with no fixed orientation. These set-ups do not allow singlet yield profiles, of the sort considered throughout this thesis, to be measured. Rather, they are used to measure a MARY (Magnetically Altered Reaction Yield) curve, which describes the change in the (isotropic) singlet yield as a function of field strength (rather than direction). If relaxation induced by the nanoparticle can visibly alter the MARY curve, it will also necessarily alter the singlet yield anisotropy in an experiment where rotation of the radical pairs is restricted.

In addition, even in the case where magnetoferritin is bound to cryptochrome (or another radical pair model), the orientation of its easy axis inside the spherical protein shell cannot be controlled. The signal measured from an ensemble of magnetoferritin-cryptochrome complexes will contain contributions from complexes with all possible relative orientations between the easy axis and the radical pair.

To get a sense of the effects that might be observed on a spectroscopically measured MARY curve, I simulated the singlet yield of the cryptochrome model introduced in chapter 5, using only the isotropic components of the hyperfine interactions. At each field strength, the singlet yield was averaged over 500 random orientations of the magnetoferritin nanoparticle.

Averaging over nanoparticle orientations

It was assumed that the easy axis of the nanoparticle could adopt any orientation relative to the radical pair with equal probability. The response from an ensemble of magnetoferritin-radical pair complexes was taken as the expectation value

$$E(\Phi_{\mathrm{S}}) = \frac{1}{N}\sum_{i=1}^{N}\Phi_{\mathrm{S}}(\chi_i,\psi_i), \tag{7.14}$$

where χ_i and ψ_i are polar and azimuthal angles describing the orientation of the magnetic moment of the nanoparticle and the number of samples $N = 500$. The orientation $O(\chi_i,\psi_i)$ should be a random variable uniformly distributed on the surface of a sphere.

Sample orientations were chosen using

$$\chi_i = \cos^{-1}(2v-1), \psi_i = 2\pi u, \tag{7.15}$$

where v and u are random variables uniformly distributed on [0,1].

The probability of choosing a value of χ in the range $\chi + d\chi$ is given by the probability density function

$$P(\chi)d\chi = P(v)\frac{dv}{d\chi}d\chi \tag{7.16}$$

$$= \frac{1}{2}\sin\chi d\chi. \tag{7.17}$$

Similarly,

$$P(\psi)d\psi = \frac{d\psi}{2\pi}. \tag{7.18}$$

The probability density function for $O(\chi,\psi)$ is therefore

$$P(\chi)d\chi P(\psi)d\psi = \frac{1}{4\pi}\sin\chi d\chi d\psi, \tag{7.19}$$

which, summed over the surface of a sphere is

$$\int_0^{2\pi}\int_0^{\pi}\frac{1}{4\pi}\sin\chi d\chi d\psi = \int\frac{1}{4\pi}dA = 1, \tag{7.20}$$

where 4π is the surface area of the unit sphere. $P(O(\chi,\psi))dA = dA/4\pi$ is the definition of a uniform distribution on the surface of a unit sphere, as required.[2]

Simulation results

Figure 7.11(a) shows simulated MARY curves (singlet yield as a function of field strength) for the radical pair model introduced in section 5.5 with only the isotropic components of the hyperfine tensors included. The recombination lifetime of the radical pair is 1 μs. Tethered to the radical pair is a nanoparticle that produces an instantaneous field of either 0.15 mT or 0.4 mT at both radicals. The field from the nanoparticle ($\boldsymbol{B}_{\mathrm{N}}$) is oriented either parallel or perpendicular to the Earth's magnetic field ($\boldsymbol{B}_{\mathrm{E}}$), which defines the quantization axis in the absence of any anisotropic hyperfine interactions. For these traces no orientational averaging is included. The Néel relaxation time of the nanoparticle is 1 ns.

In the absence of a nanoparticle, the MARY curve has a characteristic shape. The singlet yield initially shows a sharp decrease with increased field strength due to the Low Field Effect, where the weak external field lifts the degeneracy between coherent spin states, opening up new pathways for singlet-triplet interconversion [119, 276]. As the field strength (B_{E}) increases further, the Zeeman interaction with the external field increases the energy gap between states, reducing the overlap between them and hence the rate of inter-system crossing. The effect plateaus when the field strength is significantly larger than the hyperfine interactions.

[2]The probability density function of continuous uniform distribution is

$$f(x) = \begin{cases} \frac{1}{b-a} & a \le x \le b \\ 0 & x < a \text{ or } x > b. \end{cases} \tag{7.21}$$

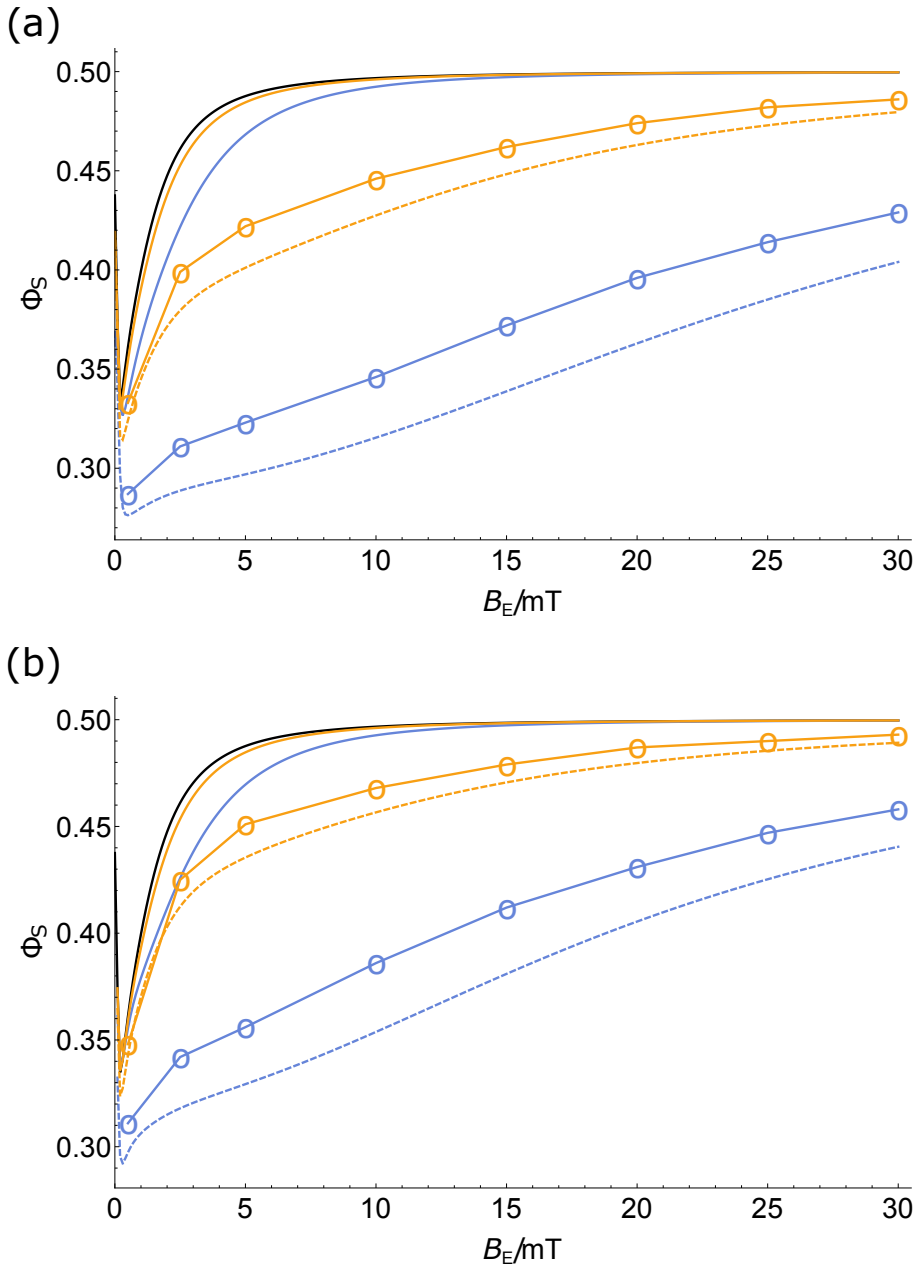


Figure 7.11: Singlet yield as a function of field strength for a model flavin-tryptophan radical pair containing only the isotropic components of the hyperfine tensors. The presence of a nanoparticle creates a 0.15 mT (orange lines) or 0.4 mT (blue lines) field at the radical pair. This field is either parallel (solid lines) or perpendicular (dashed lines) to the Earth's field, or averaged over 500 randomly chosen orientations (circular markers). For the averaged data, the singlet yield was only calculated at the marked points, due to the length of the calculation. In (a), the nanoparticle field is felt by both radicals, whilst in (b) it is only felt by the tryptophan radical. The solid, black line is the singlet yield in the absence of a nanoparticle. The Earth's field strength is 50 μT and the radical pair recombination lifetime is 1 μs. The Néel relaxation time of the nanoparticle is 1 ns.

The presence of the fluctuating field from the nanoparticle induces relaxation, which reduces the singlet yield at all field strengths and increases the field strength at which the plateau value is reached. The position of the turning point does not change so the shape of the MARY curve is significantly altered. As would be expected from the results in section 7.5, these effects are greatest when $\boldsymbol{B}_{\mathrm{N}}$ is large and perpendicular to the quantization axis.

Figure 7.11(a) also shows the effect on the MARY curve when the singlet yield is averaged over a random sample of 500 different orientations of $\boldsymbol{B}_{\mathrm{N}}$, as described above. The resulting curve is considerably closer to that for $\boldsymbol{B}_{\mathrm{N}}$ perpendicular to $\boldsymbol{B}_{\mathrm{E}}$ than that for $\boldsymbol{B}_{\mathrm{N}}$ parallel to $\boldsymbol{B}_{\mathrm{E}}$. This can be understood by considering that only two orientations ($\chi = 0$ and $\chi = \pi$) put $\boldsymbol{B}_{\mathrm{N}}$ parallel to $\boldsymbol{B}_{\mathrm{E}}$ whereas a whole range of orientations ($\chi = \pi/2$, $\psi = 0$ — 2π) place $\boldsymbol{B}_{\mathrm{N}}$ perpendicular to $\boldsymbol{B}_{\mathrm{E}}$. Consequently, we can expect to see an effect on the MARY curve even without being able to control the orientation of the nanoparticle relative to the radical pair.

Figure 7.12 shows how the singlet yield value for a single field strength converges as more sample orientations are included in the average. Although a proper assessment of the error in each value cannot be made without repeating the sampling several times over, the data in figure 7.12 suggests that the averaged values plotted in figure 7.11 can be taken as accurate to at least two (and frequently three) decimal places.

An experimental set-up could also be conceived where the two radicals are not fixed in the same molecule but one or both radicals are allowed to diffuse freely in solution. Figure 7.11(b) addresses this situation by considering the case where only one of the radicals, the tryptophan radical, is exposed to a field from the nanoparticle. Although the effects are less pronounced, the same trends are observed and the MARY curve is noticeably altered by both a 0.15 mT and a 0.4 mT nanoparticle field.

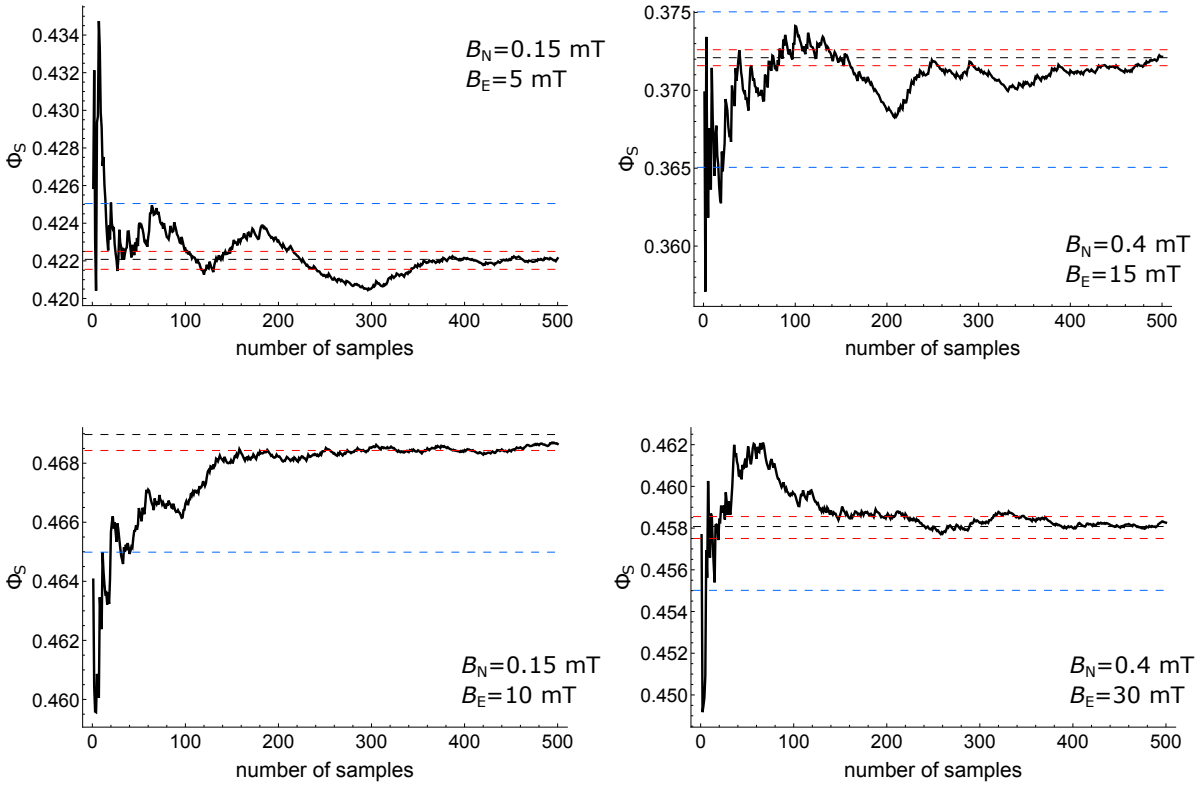


Figure 7.12: Examples of the convergence of the singlet yield values plotted in figure 7.11 (circular markers) as more sample orientations are included in the average. The value at 500 samples, rounded to 3 decimal places, is marked by a black dashed line. Red dashed lines indicate the bounds past which the rounded value would change whereas blue dashed lines show where the rounded value would change if only 2 decimal places were used. The magnitude of $\boldsymbol{B}_{\mathrm{E}}$ and $\boldsymbol{B}_{\mathrm{N}}$ are given on each graph. For the top row, both radicals interact with $\boldsymbol{B}_{\mathrm{N}}$, whereas, for the bottom row, only the tryptophan radical experiences the nanoparticle field. These four examples were chosen to illustrate reasonable to poor convergence.

Experimental procedure

[3]Making a spectroscopic measurement of the effect of a nanoparticle on the radical pair mechanism requires that the desired nanoparticle is first synthesised, magnetically characterised and then linked to the radical pair system. The nanoparticle cannot be left free in solution or the measured result would include the effect of relaxation induced by Brownian motion of the nanoparticle, which would be much more significant than the highly restricted motions modelled in section 7.5.

[3]With thanks to members of the Timmel and Mackenzie groups for helpful discussion about the practicalities of the suggested experiments.

The synthesis of magnetoferritin is well-documented in the literature. The procedure is fairly straightforward and is given in Appendix C. Following Reference [245], the recipe produces nanoparticles with a theoretical loading factor of 1030, which had a measured magnetic moment of 350 μ_B. From figure 7.8, this means the nanoparticle must be bound no more than ∼13 nm from the radical for it to experience a field of 0.4 mT (∼16 nm for a 0.15 mT field). Magnetoferritin has a 6 nm radius, meaning that the length of the linker combined with the distance from the radical to the surface of the molecule should be less than 7 nm (10 nm for a 0.15 mT field).

A standard way to link proteins is using a short organic molecule coupled with EDC (1-ethyl-3-(3-dimethylaminopropyl)carbodiimide), as shown in figure 7.13. EDC activates carboxylic acid groups to form amide bonds with accessible amine groups (particularly the N-terminal amine) in a protein [277]. Although unlikely to be sufficiently selective for an *in vivo* experiment, a linker like the one shown in figure 7.13 could be used in a simpler *in vitro* experiment. The linker would not selectively bind magnetoferritin at one end and cryptochrome (or an alternative radical pair model) at the other. Nor is there any intrinsic reason why more than one linker could not bind to a single magnetoferritin molecule. However, there are ways around these problems. A simple solution would be to mix all the reagents, including magnetoferritin and cryptochrome together, allow them to react and then extract the desired products from the mixture using chromatographic techniques that separate components by weight. This is not likely to be a high yield process. An alternative might be to attach magnetoferritin to linker molecules tethered to a surface (as in reference [277]). Steric factors would prevent more than one linker binding to each magnetoferritin particle. The other end of the linker could then be detached from the surface and allowed to react with cryptochrome.

The theoretical mean magnetic moment of the synthesised nanoparticles can be confirmed by measuring the magnetization M of a bulk sample at different temperatures (T) or field

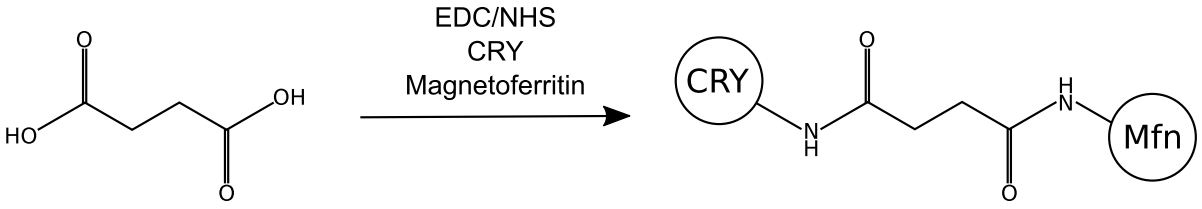


Figure 7.13: Magnetoferritin and cryptochrome could be linked together by succinic acid, activated by EDC (1-ethyl-3-(3-dimethylaminopropyl)carbodiimide) and NHS (N-hydroxysuccinimide) [277].

strengths (B_{app}) and fitting the data to the form

$$M(T, B_{\text{app}}) = \frac{M_s}{x} \ln\left(\frac{\sinh x}{x}\right) - \chi B_{\text{app}}, \quad x = \frac{\mu_0 m B_{\text{app}}}{k_{\text{B}} T}, \tag{7.22}$$

where M_s is the saturation magnetization, μ_0 is the vacuum permeability and χ is the magnetic susceptibility.

Spectroscopic measurements of the magnetoferritin-radical pair complex *in vitro* would provide a very necessary demonstration that a nanoparticle could destroy the compass in the way predicted by theoretical calculations. Ideally, two control experiments would also be performed with the radical pair coupled to an empty apoferritin protein or to normal ferritin.

7.8 Conclusions

In this chapter, I have proposed an experiment to conclusively test the role of cryptochrome as a magnetoreceptor by deactivating the radical pair compass using a superparamagnetic nanoparticle bound to cryptochrome. A superparamagnetic nanoparticle can disable the magnetoreceptive ability of a radical pair if its Néel relaxation time is on the order of 1 ns or longer. When the Néel relaxation is around 1 ns, the nanoparticle relaxes the radical pair, whereas slower Néel relaxation times correspond to the particle creating an approximately static magnetic field that combines with the Earth's magnetic field to create a net magnetic field vector with a reduced range of orientations relative

to the radical pair. The magnetic moment of the nanoparticle needs to be large enough to have an observable effect on the singlet yield of the radical pair reaction but not so large that the selectivity of the experiment is compromised. The exact value that is required depends on how far the nanoparticle is from the radical pair. Brownian motion of a tethered nanoparticle has very little effect on the compass signal.

Magnetoferritin has been identified as a good candidate nanoparticle for the proposed experiment. It combines suitable magnetic properties with a natural biocompatibility, controlled synthesis and offers opportunities to functionalise the nanoparticle and carry out a number of useful control experiments.

There are a number of practical challenges to implementing the proposed experiment, not least of which is delivering the nanoparticles to cryptochrome in a targeted fashion. Possible solutions to this problem include synthesising the nanoparticle *in situ* or, if necessary, carrying out the experiment in a cell culture or isolated sample of retina. However, before the experiment reaches this stage, preliminary investigations must be carried out to confirm the action of the nanoparticle on the radical pair reaction.

Chapter 8

Conclusions

In this thesis I have explored the effects of molecular order and molecular motion on a radical pair compass, with a particular focus on testing the feasibility of cryptochrome as a magnetoreceptor.

Molecular motion has long been considered a major barrier to realising a functional radical pair compass as it drives spin relaxation and introduces dynamic disorder. As ordered receptors and long-lived spin coherence are key requirements of a radical pair compass, molecular motion is expected to be highly detrimental. The work I presented in chapters 4 and 5 suggests that internal rotational motion of the individual radicals will not completely destroy the compass, providing the rotations are fast and highly constrained. In cryptochrome, constraining the motion of the flavin radical is particularly important as it will otherwise average away the highly favourable shape of the N5 and N10 hyperfine interactions. Motion of the tryptophan radical can be less restricted but needs to be very rapid as modulation of the large number of asymmetric hyperfine interactions is potentially a source of very fast spin relaxation. Molecular dynamics simulations of *At*-CRY suggest that the motions of the radicals may be compatible with a functioning compass. However, the compass would be more sensitive and more resilient to motionally-induced relaxation if the tryptophan radical was replaced by a counter-radical with more highly symmetric interactions. This idea resonates with suggestions that the counter-radical

may be based on tyrosine rather than tryptophan [59, 68] and with work showing that an FAD-Z radical pair would better explain radiofrequency experiments [40].

Even with a more symmetrical counter-radical, relaxation induced by molecular motion severely reduces the anisotropy of the compass signal (or the magnitude of the spike for longer-lived radical pairs). Combined with the puzzling observation that birds can use their compass under extremely low levels of light (implying high sensitivity and a strongly anisotropic signal), it seems not unlikely that there are aspects of the radical pair compass that are not captured by the current model. For example, recent work has demonstrated that involvement of a third, scavenging, radical could lead to large amplifications of the compass signal and improve the tolerance of the compass to relaxation [278, 279]. The role of exchange and dipolar coupling in producing favourable decoherence may furthermore be a significant feature [117].

Finding a feasible mechanism by which the compass signal can be either amplified or protected from relaxation will be crucial if the radical pair mechanism is to remain a credible mechanism for the avian compass. A first step may be developing more powerful simulations to capture the interaction between different sources of relaxation and the potential amplification mechanisms that have already been identified. For example, a computational model that included motion of both radicals, the exchange and dipolar coupling between them and its modulation by electron-hopping along the Trp triad would provide valuable information about the ability of this amplification mechanism to counteract relaxation. It could also reveal criteria for the best way to arrange the radicals to give the most advantageous balance of different effects.

A very real barrier to improving our understanding and investigations of the compass mechanism is the lack of a definitely identified magnetoreceptor. The dependence of a radical pair compass on maintaining delicate spin coherences offers an opportunity to probe the role of cryptochrome as a magnetoreceptor. In chapter 7 I described an experiment in which the putative magnetoreceptive function of cryptochrome is disabled by binding a superparamagnetic nanoparticle to cryptochrome. The synthetic nanoparti-

cle magnetoferritin was proposed as a good choice of nanoparticle based on its magnetic properties and natural biocompatibility. There are substantial practical challenges to implementing this experiment *in vivo* but it is conceivable that upcoming technologies and procedures could help to overcome these in the near future. The next step will be to carry out preliminary experiments demonstrating that the presence of magnetoferritin can remove measured magnetic field effects on simple radical pair models *in vitro*. Some suggestions and simulations of such an experiment were given in chapter 7.

Finally, one clear conclusion of molecular motion simulations presented in this thesis is that a high degree of ordering of the magnetoreceptors is necessary within the current model of the radical pair mechanism. This makes the radical pair compass inherently sensitive to polarized light. However, by introducing an additional level of order, it is possible to arrange the cells and receptors in such a way that a pure magnetic signal could be detected. Unwanted information about light intensity and polarization can be filtered out by comparing the signals from two cells that are rotated relative to each other by 180° around the axis connecting the cell to the pupil. Both cells should contain identical populations of magnetoreceptors. I have suggested that this mechanism could be realised by binding the magnetoreceptor to aligned tracks of rhodopsin dimers embedded in membrane discs in the outer segments of double cone photoreceptor cells. Although necessarily speculative, these suggestions, along with the criteria for creating a polarization-independent compass, could provide guidance for future investigations into the identity, location and interactions of the magnetoreceptor.

Before further investigation of the proposed separation mechanism is carried out, additional behavioural and/or electrophysiological experiments will be needed to better characterise the interaction of the compass with polarized light. In the meantime, however, microscopy experiments could be used to probe the orientation and distribution of photoreceptor cells across the retina and look for patterns that might permit the required signal separation. Experiments could also be performed to test the viability of rhodopsin as an interaction partner for cryptochrome.

Bibliography

[1] British Geological Survey. *The Earth's Magnetic Field: An Overview [online].* http://geomag.bgs.ac.uk/education/earthmag.html#_Toc2075559 (2018).

[2] R. F. Butler. *Paleomagnetism: Magnetic Domains to Geologic Terranes.* Blackwells Scientific Publishing, 1st edition (1992). ISBN 9780865420700. doi:10.1108/S0749-742320160000019022.

[3] E. Thébault, C. C. Finlay, C. D. Beggan, P. Alken, J. Aubert, O. Barrois, F. Bertrand, T. Bondar, A. Boness, L. Brocco, E. Canet, A. Chambodut, A. Chulliat, P. Coïsson, F. Civet, A. Du, A. Fournier, I. Fratter, N. Gillet, B. Hamilton, M. Hamoudi, G. Hulot, T. Jager, M. Korte, W. Kuang, X. Lalanne, B. Langlais, J. M. Léger, V. Lesur, F. J. Lowes, S. Macmillan, M. Mandea, C. Manoj, S. Maus, N. Olsen, V. Petrov, V. Ridley, M. Rother, T. J. Sabaka, D. Saturnino, R. Schachtschneider, O. Sirol, A. Tangborn, A. Thomson, L. Tøffner-Clausen, P. Vigneron, I. Wardinski, and T. Zvereva. International geomagnetic reference field: The 12th generation. *Earth, Planets and Space*, 67(1) (2015). doi:10.1186/s40623-015-0228-9.

[4] H. Mouritsen. Magnetoreception in Birds and Its Use for Long- Distance Migration. *Sturkie's Avian Physiology*, chapter 8:113–133 (2015). doi:10.1007/978-3-642-10.

[5] N. Chernetsov, A. Pakhomov, D. Kobylkov, D. Kishkinev, R. A. Holland, and H. Mouritsen. Migratory Eurasian Reed Warblers Can Use Magnetic Declination to Solve the Longitude Problem. *Current Biology*, 1–5 (2017). doi:

10.1016/j.cub.2017.07.024.

[6] I. H. Campbell and D. L. Smith. Physics of Organic Electronic Devices. *Solid State Physics*, 55:1–117 (2001).

[7] F. W. Merkel and W. Wiltschko. Magnetismus und Richtungsfinden zugunruhiger Rotkehlchen (*Erithacus rubecula*). *Vogelwarte*, 23:71–77 (1965).

[8] W. Wiltschko. Über den Einfluß statischer Magnetfelder auf die Zugorientierung der Rotkehlchen (*Erithacus rubecula*). *Zeitschrift für Tierpsychologie*, 25(5):537–558 (1968).

[9] W. Wiltschko and R. Wiltschko. *Magnetic orientation in animals.* Springer Verlag (1995).

[10] P. Berthold. *Bird Migration. A General Survey.* Oxford University Press (2001).

[11] H. Mouritsen, D. Heyers, and O. Güntürkün. The Neural Basis of Long-Distance Navigation in Birds. *Annual Review of Physiology*, 78:133–54 (2016). doi: 10.1146/annurev-physiol-021115-105054.

[12] W. Wiltschko. The influence of magnetic total intensity and inclination on directions preferred by migrating european robins. *NASA Technical Reports Server* (1972).

[13] R. Wiltschko and W. Wiltschko. Magnetoreception. *BioEssays*, 28(2):157–168 (2006). doi:10.1002/bies.20363.

[14] M. Winklhofer, E. Dylda, P. Thalau, W. Wiltschko, and R. Wiltschko. Avian magnetic compass can be tuned to anomalously low magnetic intensities. *Proceedings of the Royal Society B*, 280:20130853 (2013). doi:10.1098/rspb.2013.0853.

[15] R. Blakemore. Magnetotactic Bacteria. *Science*, 190(4212):377–379 (1975). doi: 10.1126/science.170679.

[16] J. L. Kirschvink, M. M. Walker, and C. E. Diebel. Magnetite-based magnetorecep-

tion. *Current Opinion in Neurobiology*, 11(4):462–467 (2001). doi:10.1016/S0959-4388(00)00235-X.

[17] O. Bazalova, M. Kvicalova, T. Valkova, P. Slaby, P. Bartos, R. Netusil, K. Tomanova, P. Braeunig, H.-J. Lee, I. Sauman, M. Damulewicz, J. Provaznik, R. Pokorny, D. Dolezel, and M. Vacha. Cryptochrome 2 mediates directional magnetoreception in cockroaches. *Proceedings of the National Academy of Sciences of the United States of America*, 113(6):1660–1665 (2016). doi:10.1073/pnas.1518622113.

[18] R. Muheim, N. M. Edgar, K. A. Sloan, and J. B. Phillips. Magnetic compass orientation in C57BL/6J mice. *Learning & Behaviour*, 34(4):366–373 (2006). doi:10.3758/BF03193201.

[19] E. P. Malkemper, S. H. K. Eder, S. Begall, J. B. Phillips, M. Winklhofer, V. Hart, and H. Burda. Magnetoreception in the wood mouse (Apodemus sylvaticus): influence of weak frequency-modulated radio frequency fields. *Scientific Reports*, 4:9917 (2015). doi:10.1038/srep09917.

[20] S. T. Emlen and J. T. Emlen. A Technique for Recording Migratory Orientation of Captive Birds. *The Auk*, 83(3):361–367 (1966). doi:10.2307/4083048.

[21] H. Mouritsen, G. Feenders, A. Hegemann, and M. Liedvogel. Thermal paper can replace typewriter correction paper in Emlen funnels. *Journal of Ornithology*, 150(3):713–715 (2009). doi:10.1007/s10336-009-0421-3.

[22] G. Kramer. Über Richtungstendenzen bei der nächtlichen Zugunruhe gekäfigter Vögel. In *Ornithologie als biologische Wissenschaft*, 269–283 (1949).

[23] W. Wiltschko and R. Wiltschko. Magnetic compass of European robins. *Science (New York, N.Y.)*, 176(4030):62–64 (1972). doi:10.1126/science.176.4030.62.

[24] V. Lambinet, M. E. Hayden, C. Reid, and G. Gries. Honey bees possess a polarity-sensitive magnetoreceptor. *Journal of Comparative Physiology A*, 203(12):1029–1036 (2017). doi:10.1007/s00359-017-1214-4.

[25] D. A. Ernst and K. J. Lohmann. Effect of magnetic pulses on Caribbean spiny lobsters: implications for magnetoreception. *Journal of Experimental Biology*, 219:1827–1832 (2016). doi:10.1242/jeb.136036.

[26] W. Wiltschko and R. Wiltschko. Light-dependent magnetoreception in birds: the behaviour of European robins, *Erithacus rubecula*, under monochromatic light of various wavelengths and intensities. *The Journal of experimental biology*, 204:3295–3302 (2001).

[27] R. Wiltschko, K. Stapput, P. Thalau, and W. Wiltschko. Directional orientation of birds by the magnetic field under different light conditions. *Journal of The Royal Society, Interface*, 7:S163–S177 (2010). doi:10.1098/rsif.2009.0367.focus.

[28] R. Wiltschko, M. Ahmad, C. Nießner, D. Gehring, and W. Wiltschko. Light-dependent magnetoreception in birds : the crucial step occurs in the dark. *Journal of The Royal Society, Interface*, 13:20151010 (2016). doi:10.1098/rsif.2015.1010.

[29] T. Ritz, S. Adem, and K. Schulten. A model for photoreceptor-based magnetoreception in birds. *Biophysical Journal*, 78(2):707–718 (2000). doi:10.1016/S0006-3495(00)76629-X.

[30] K. Schulten and P. G. Wolynes. Semiclassical description of electron spin motion in radicals including the effect of electron hopping. *The Journal of Chemical Physics*, 68(7):3292 (1978). doi:10.1063/1.436135.

[31] K. Schulten and A. Windemuth. Model for a Physiological Magnetic Compass. In G. Maret, N. Boccara, and J. Kiepenheuer (eds.), *Biophysical Effects of Steady Magnetic Fields*, 99–106. Springer-Verlag, Berlin (1986).

[32] K. B. Henbest, P. Kukura, C. T. Rodgers, P. J. Hore, and C. R. Timmel. Radio frequency magnetic field effects on a radical recombination reaction: A diagnostic test for the radical pair mechanism. *Journal of the American Chemical Society*, 126(26):8102–8103 (2004). doi:10.1021/ja048220q.

[33] T. Ritz, P. Thalau, J. B. Phillips, R. Wiltschko, and W. Wiltschko. Resonance effects indicate a radical-pair mechanism for avian magnetic compass. *Nature*, 429(6988):177–180 (2004). doi:10.1038/nature02534.

[34] P. Thalau, T. Ritz, K. Stapput, R. Wiltschko, and W. Wiltschko. Magnetic compass orientation of migratory birds in the presence of a 1.315 MHz oscillating field. *Naturwissenschaften*, 92(2):86–90 (2005). doi:10.1007/s00114-004-0595-8.

[35] T. Ritz, R. Wiltschko, P. J. Hore, C. T. Rodgers, K. Stapput, P. Thalau, C. R. Timmel, and W. Wiltschko. Magnetic compass of birds is based on a molecule with optimal directional sensitivity. *Biophysical Journal*, 96(8):3451–3457 (2009). doi:10.1016/j.bpj.2008.11.072.

[36] S. Schwarze, N.-L. Schneider, T. Reichl, D. Dreyer, N. Lefeldt, S. Engels, N. Baker, P. J. Hore, and H. Mouritsen. Weak broadband electromagnetic fields are more disruptive to magnetic compass orientation in a night-migratory songbird (*Erithacus rubecula*) than strong narrow-band fields. *Frontiers in Behavioral Neuroscience*, 10:1–13 (2016). doi:10.3389/fnbeh.2016.00055.

[37] S. Engels, N.-L. Schneider, N. Lefeldt, C. M. Hein, M. Zapka, A. Michalik, D. Elbers, A. Kittel, P. J. Hore, and H. Mouritsen. Anthropogenic electromagnetic noise disrupts magnetic compass orientation in a migratory bird. *Nature*, 509(7500):353–6 (2014). doi:10.1038/nature13290.

[38] A. Pinzon-Rodriguez and R. Muheim. Zebra finches have a light-dependent magnetic compass similar to migratory birds. *The Journal of Experimental Biology*, 220(7):1202–1209 (2017). doi:10.1242/jeb.148098.

[39] M. Vacha, T. Puzova, and M. Kvicalova. Radio frequency magnetic fields disrupt magnetoreception in American cockroach. *Journal of Experimental Biology*, 212(21):3473–3477 (2009). doi:10.1242/jeb.028670.

[40] H. G. Hiscock, H. Mouritsen, D. E. Manolopoulos, and P. J. Hore. Disrup-

tion of Magnetic Compass Orientation in Migratory Birds by Radiofrequency Electromagnetic Fields. *Biophysical Journal*, 113(7):1475–1484 (2017). doi: 10.1016/j.bpj.2017.07.031.

[41] K. V. Kavokin. The puzzle of magnetic resonance effect on the magnetic compass of migratory birds. *Bioelectromagnetics*, 30(5):402–410 (2009). doi: 10.1002/bem.20485.

[42] E. M. Gauger and S. C. Benjamin. Comment on "Quantum Coherence and Sensitivity of Avian Magnetoreception". *Physical Review Letters*, 110(17):178901 (2013). doi:10.1103/PhysRevLett.110.178901.

[43] H. Mouritsen, G. Feenders, M. Liedvogel, K. Wada, and E. D. Jarvis. Night-vision brain area in migratory songbirds. *Proceedings of the National Academy of Sciences of the United States of America*, 102(23):8339–8344 (2005). doi: 10.1073/pnas.0409575102.

[44] M. Liedvogel, G. Feenders, K. Wada, N. F. Troje, E. D. Jarvis, and H. Mouritsen. Lateralized activation of Cluster N in the brains of migratory songbirds. *European Journal of Neuroscience*, 25(4):1166–1173 (2007). doi:10.1111/j.1460-9568.2007.05350.x.

[45] K. P. Able and M. A. Able. Daytime calibration of magnetic orientation in a migratory bird requires a view of skylight polarization. *Nature*, 364(6437):523–525 (1993). doi:10.1038/364523a0.

[46] K. P. Able and M. A. Able. Manipulations of polarized skylight calibrate magnetic orientation in a migratory bird. *Journal of Comparative Physiology A*, 177(3):351–356 (1995). doi:10.1007/BF00192423.

[47] W. W. Cochran, H. Mouritsen, and M. Wikelski. Migrating songbirds recalibrate their magnetic compass daily from twilight cues. *Science*, 304:405–408 (2004). doi: 10.1126/science.1095844.

[48] R. Muheim, J. B. Phillips, and S. Åkesson. Polarized light cues underlie compass calibration in migratory songbirds. *Science*, 313(5788):837–839 (2006). doi: 10.1126/science.1129709.

[49] R. Muheim, S. Åkesson, and J. B. Phillips. Magnetic compass of migratory Savannah sparrows is calibrated by skylight polarization at sunrise and sunset. *Journal of Ornithology*, 148:S485–S494 (2007). doi:10.1007/s10336-007-0187-4.

[50] R. Muheim, S. Sjöberg, and A. Pinzon-Rodriguez. Polarized light modulates light-dependent magnetic compass orientation in birds. *Proceedings of the National Academy of Sciences*, 113(6):1654–1659 (2016). doi:10.1073/pnas.1513391113.

[51] R. Kaptein and J. L. Oosterhoff. Chemically Induced Dynamic Nuclear Polarization II. *Chemical Physics Letters*, 4(4):195–197 (1969). doi: http://dx.doi.org/10.1016/0009-2614(69)80098-9.

[52] R. Kaptein and J. L. Oosterhoff. Chemically Induced Dynamic Nuclear Polarization III. *Chemical Physics Letters*, 4(4):214–216 (1969). doi: 10.1016/j.amjmed.2012.04.013.

[53] G. L. Closs and A. D. Trifunac. Theory of Chemically Induced Nuclear Spin Polarization. III. Effect of Isotropic g Shifts in the Components of Radical Pairs with One Hyperfine Interaction. *Journal of the American Chemical Society*, 92(7):2183–2184 (1970). doi:10.1021/ja00710a092.

[54] P. J. Hore. The Quantum Robin. *Navigation News*, 19–21 (2011).

[55] K. Schulten, C. E. Swenberg, and A. Weller. A biomagnetic sensory mechanism based on magnetic field modulated coherent electron spin motion. *Zeitschrift für Physikalische Chemie*, 111(1):1–5 (1978). doi:10.1524/zpch.1978.111.1.001.

[56] H. J. Hogben, T. Biskup, and P. J. Hore. Entanglement and sources of magnetic anisotropy in radical pair-based avian magnetoreceptors. *Physical Review Letters*, 109(22):1–5 (2012). doi:10.1103/PhysRevLett.109.220501.

[57] E. W. Evans and C. A. Dodson. Magnetic field effects in flavoproteins and related systems. *Interface Focus*, 3:20130037 (2013). doi:10.1098/rsfs.2013.0037.

[58] C. T. Rodgers and P. J. Hore. Chemical magnetoreception in birds: the radical pair mechanism. *Proceedings of the National Academy of Sciences of the United States of America*, 106(2):353–60 (2009). doi:10.1073/pnas.0711968106.

[59] P. J. Hore and H. Mouritsen. The radical-pair mechanism of magnetoreception. *Annual Review of Biophysics*, 45:299–344 (2016). doi:10.1146/annurev-biophys-032116-094545.

[60] J. C. S. Lau, C. T. Rodgers, and P. J. Hore. Compass magnetoreception in birds arising from photo-induced radical pairs in rotationally disordered cryptochromes. *Journal of the Royal Society, Interface*, 9(77):3329–3337 (2012).

[61] H. G. Hiscock, S. Worster, D. R. Kattnig, C. Steers, Y. Jin, D. E. Manolopoulos, H. Mouritsen, and P. J. Hore. The quantum needle of the avian magnetic compass. *Proceedings of the National Academy of Sciences of the United States of America*, 113(17):4634–4639 (2016). doi:10.1073/pnas.1600341113.

[62] O. Efimova and P. J. Hore. Role of exchange and dipolar interactions in the radical pair model of the avian magnetic compass. *Biophysical Journal*, 94(5):1565–74 (2008). doi:10.1529/biophysj.107.119362.

[63] J. L. Kirschvink, M. Winklhofer, and M. M. Walker. Biophysics of magnetic orientation : strengthening the interface between theory and experimental design Biophysics of magnetic orientation : strengthening the interface between theory and experimental design. *Journal of The Royal Society, Interface*, 7:S179–S191 (2010). doi:10.1098/rsif.2009.0491.focus.

[64] E. Hill and T. Ritz. Can disordered radical pair systems provide a basis for a magnetic compass in animals? *Journal of the Royal Society, Interface*, 7:S265–S271 (2010). doi:10.1098/rsif.2009.0378.focus.

[65] R. E. Gill, T. L. Tibbitts, D. C. Douglas, C. M. Handel, D. M. Mulcahy, J. C. Gottschalck, N. Warnock, B. J. McCaffery, P. F. Battley, and T. Piersma. Extreme endurance flights by landbirds crossing the Pacific Ocean: ecological corridor rather than barrier? *Proceedings of the Royal Society B*, 276:447–457 (2009). doi: 10.1098/rspb.2008.1142.

[66] N. Lefeldt, D. Dreyer, N.-L. Schneider, F. Steenken, and H. Mouritsen. Migratory blackcaps tested in Emlen funnels can orient at 85 degrees but not at 88 degrees magnetic inclination. *Journal of Evolutionary Biology*, 218:206–211 (2015). doi: 10.1242/jeb.107235.

[67] F. Cintolesi, T. Ritz, C. W. M. Kay, C. R. Timmel, and P. J. Hore. Anisotropic recombination of an immobilized photoinduced radical pair in a 50-μT magnetic field: A model avian photomagnetoreceptor. *Chemical Physics*, 294(3):385–399 (2003). doi:10.1016/S0301-0104(03)00320-3.

[68] A. A. Lee, J. C. S. Lau, H. J. Hogben, T. Biskup, D. R. Kattnig, and P. J. Hore. Alternative radical pairs for cryptochrome-based magnetoreception. *Journal of the Royal Society, Interface*, 11:20131063 (2014). doi:10.1098/rsif.2013.1063.

[69] M. Winklhofer and J. L. Kirschvink. A quantitative assessment of torque-transducer models for magnetoreception. *Journal of The Royal Society, Interface*, 7:S273–S289 (2010). doi:10.1098/rsif.2009.0435.focus.

[70] J. Shaw, A. Boyd, M. House, R. Woodward, F. Mathes, G. Cowin, M. Saunders, and B. Baer. Magnetic particle-mediated magnetoreception. *Journal of The Royal Society, Interface*, 12:20150499 (2015). doi:http://dx.doi.org/10.1098/rsif.2015.0499.

[71] M. M. Walker, C. E. Diebel, C. V. Haugh, P. M. Pankhurst, J. C. Montgomery, and C. R. Green. Structure and function of the vertbrate magnetic sense. *Nature*, 390:371–376 (1997). doi:10.1038/37057.

[72] G. Fleissner, E. Holtkamp-Rötzler, M. Hanzlik, M. Winklhofer, G. Fleissner, N. Pe-

tersen, and W. Wiltschko. Ultrastructural analysis of a putative magnetoreceptor in the beak of homing pigeons. *Journal of Comparative Neurology*, 458(4):350–360 (2003). doi:10.1002/cne.10579.

[73] J. L. Kirschvink and A. K. Kirschvink. Is geomagnetic sensitivity real? Replication of the Walker-Bitterman magnetic conditioning experiment in honey bees. *Integrative and Comparative Biology*, 31:169–186 (1991). doi:10.1093/icb/31.1.169.

[74] P. Jandacka, B. Kasparova, Y. Jiraskova, K. Dedkova, K. Mamulova-Kutlakova, and J. Kukutschova. Iron-based granules in body of bumblebees. *BioMetals*, 28(1):89–99 (2015). doi:10.1007/s10534-014-9805-9.

[75] N. B. Edelman, T. Fritz, S. Nimpf, P. Pichler, M. Lauwers, R. W. Hickman, A. Papadaki-Anastasopoulou, L. Ushakova, T. Heuser, G. P. Resch, M. Saunders, J. A. Shaw, and D. A. Keays. No evidence for intracellular magnetite in putative vertebrate magnetoreceptors identified by magnetic screening. *Proceedings of the National Academy of Sciences*, 112(1):262–267 (2015). doi:10.1073/pnas.1407915112.

[76] C. D. Treiber, M. C. Salzer, J. Riegler, N. Edelman, C. Sugar, M. Breuss, P. Pichler, H. Cadiou, M. Saunders, M. Lythgoe, J. Shaw, and D. A. Keays. Clusters of iron-rich cells in the upper beak of pigeons are macrophages not magnetosensitive neurons. *Nature*, 484:367–370 (2012). doi:10.1038/nature11046.

[77] M. M. Walker, T. E. Dennis, and J. L. Kirschvink. The magnetic sense and its use in long-distance navigation by animals. *Current Opinion in Neurobiology*, 12(6):735–744 (2002). doi:10.1016/S0959-4388(02)00389-6.

[78] C. D. Treiber, M. Salzer, M. Breuss, L. Ushakova, M. Lauwers, N. Edelman, and D. A. Keays. High resolution anatomical mapping confirms the absence of a magnetic sense system in the rostral upper beak of pigeons. *Communicative and Integrative Biology*, 6(4) (2013). doi:10.4161/cib.24859.

[79] G. Falkenberg, G. Fleissner, K. Schuchardt, M. Kuehbacher, P. Thalau, H. Mourit-

sen, D. Heyers, G. Wellenreuther, and G. Fleissner. Avian magnetoreception: Elaborate iron mineral containing dendrites in the upper beak seem to be a common feature of birds. *PLoS ONE*, 5(2) (2010). doi:10.1371/journal.pone.0009231.

[80] U. Munro, J. A. Munro, J. B. Phillips, R. Wiltschko, and W. Wiltschko. Evidence for a magnetite-based navigational 'map' in birds. *Naturwissenschaften*, 84(1):26–28 (1997). doi:10.1007/s001140050343.

[81] S. Qin, H. Yin, C. Yang, Y. Dou, Z. Liu, P. Zhang, H. Yu, Y. Huang, J. Feng, J. Hao, J. Hao, L. Deng, X. Yan, X. Dong, Z. Zhao, T. Jiang, H.-W. Wang, S.-J. Luo, and C. Xie. A magnetic protein biocompass. *Nature Materials*, 15(2):217–226 (2015). doi:10.1038/nmat4484.

[82] K. Kavokin. Can a hybrid chemical-ferromagnetic model of the avian compass explain its outstanding sensitivity to magnetic noise? *PLoS ONE*, 12(3):1–10 (2017). doi:10.1371/journal.pone.0173887.

[83] D. S. Hsu, X. Zhao, S. Zhao, A. Kazantsev, R. P. Wang, T. Todo, Y. F. Wei, and A. Sancar. Putative human blue-light photoreceptors hCRY1 and hCRY2 are flavoproteins. *Biochemistry*, 35(44):13871–13877 (1996). doi:10.1021/bi962209o.

[84] M. Liedvogel and H. Mouritsen. Cryptochromes–a potential magnetoreceptor: what do we know and what do we want to know? *Journal of the Royal Society, Interface*, 7:S147–162 (2010). doi:10.1098/rsif.2009.0411.focus.

[85] M. Ahmad and A. R. Cashmore. HY4 gene of *A. thaliana* encodes a protein with characteristics of a blue-light photoreceptor. *Letters to Nature*, 366:162–166 (1993).

[86] A. R. Cashmore, J. A. Jarillo, Y.-J. Wu, and D. Liu. Cryptochromes: blue light receptors for plant and animals. *Science*, 284(l):760–765 (1999).

[87] X. Yu, H. Liu, J. Klejnot, and C. Lin. The Cryptochrome Blue Light Receptors. *The Arabidopsis Book*, 1–27 (2011). doi:10.1199/tab.0135.

[88] M. Müller and T. Carell. Structural biology of DNA photolyases and cryp-

tochromes. *Current Opinion in Structural Biology*, 19(3):277–285 (2009). doi: 10.1016/j.sbi.2009.05.003.

[89] T. Biskup, E. Schleicher, A. Okafuji, G. Link, K. Hitomi, E. D. Getzoff, and S. Weber. Direct observation of a photoinduced radical pair in a cryptochrome blue-light photoreceptor. *Angewandte Chemie - International Edition*, 48(2):404–407 (2009). doi:10.1002/anie.200803102.

[90] B. Giovani, M. Byrdin, M. Ahmad, and K. Brettel. Light-induced electron transfer in a cryptochrome blue-light photoreceptor. *Nature Structural Biology*, 10(6):489–490 (2003). doi:10.1038/nsb933.

[91] P. Muller, J. Yamamoto, R. Martin, S. Iwai, and K. Brettel. Discovery and functional analysis of a 4th electron-transferring tryptophan conserved exclusively in animal cryptochromes and (6-4) photolyases. *Chemical Communications*, 51:15502–15505 (2015). doi:10.1039/C5CC06276D.

[92] F. Cailliez, P. Müller, T. Firmino, P. Pernot, and A. de la Lande. Energetics of Photoinduced Charge Migration Within the Tryptophan Tetrad of an Animal (6-4) Photolyase. *Journal of the American Chemical Society*, jacs.5b10938 (2016). doi: 10.1021/jacs.5b10938.

[93] H.-Q. Yang, Y.-J. Wu, R.-H. Tang, D. Liu, Y. Liu, and A. R. Cashmore. The C Termini of Arabidopsis Cryptochromes Mediate a Constitutive Light Response. *Cell*, 103(5):815–827 (2000). doi:10.1016/S0092-8674(00)00184-7.

[94] I. Chaves, R. Pokorny, M. Byrdin, N. Hoang, T. Ritz, K. Brettel, L.-O. Essen, G. T. J. van der Horst, A. Batschauer, and M. Ahmad. The cryptochromes: blue light photoreceptors in plants and animals. *Annual review of plant biology*, 62:335–364 (2011). doi:10.1146/annurev-arplant-042110-103759.

[95] A. K. Michael, J. L. Fribourgh, R. N. Van Gelder, and C. L. Partch. Animal Cryptochromes: Divergent Roles in Light Perception, Circadian Timekeep-

ing and Beyond. *Photochemistry and Photobiology*, 93(1):128–140 (2017). doi: 10.1111/php.12677.

[96] R. Stanewsky. Clock mechanisms in Drosophila. *Cell and Tissue Research*, 309:11–26 (2002). doi:10.1007/s00441-002-0570-7.

[97] R. J. Gegear, A. Casselman, S. Waddell, and S. M. Reppert. Cryptochrome mediates light-dependent magnetosensitivity in *Drosophila*. *Nature*, 454:1014–1018 (2008). doi:10.1038/nature07183.

[98] G. Fedele, E. W. Green, E. Rosato, and C. P. Kyriacou. An electromagnetic field disrupts negative geotaxis in *Drosophila* via a CRY-dependent pathway. *Nature Communications*, 5:4391 (2014). doi:10.1038/ncomms5391.

[99] C. N. Giachello, N. S. Scrutton, A. R. Jones, and R. A. Baines. Magnetic fields modulate blue-light-dependent regulation of neuronal firing by cryptochrome. *Journal of Neuroscience*, 36(42):10742–10749 (2016). doi:10.1523/JNEUROSCI.2140-16.2016.

[100] G. Fedele, M. D. Edwards, S. Bhutani, J. M. Hares, M. Murbach, E. W. Green, S. Dissel, M. H. Hastings, E. Rosato, and C. P. Kyriacou. Genetic analysis of circadian responses to low frequency electromagnetic fields in *Drosophila melanogaster*. *PLoS Genetics*, 10(12):e1004804 (2014). doi:10.1371/journal.pgen.1004804.

[101] J. C. S. Lau, N. Wagner-Rundell, C. T. Rodgers, N. J. B. Green, and P. J. Hore. Effects of disorder and motion in a radical pair magnetoreceptor. *Journal of The Royal Society, Interface*, 7:S257–S264 (2010). doi:10.1098/rsif.2009.0399.focus.

[102] C. Nießner, S. Denzau, J. C. Gross, L. Peichl, H. J. Bischof, G. Fleissner, W. Wiltschko, and R. Wiltschko. Avian ultraviolet/violet cones identified as probable magnetoreceptors. *PLoS ONE*, 6(5):1–8 (2011). doi: 10.1371/journal.pone.0020091.

[103] H. Mouritsen, U. Janssen-Bienhold, M. Liedvogel, G. Feenders, J. Stalleicken, P. Dirks, and R. Weiler. Cryptochromes and neuronal-activity markers colocal-

ize in the retina of migratory birds during magnetic orientation. *Proceedings of the National Academy of Sciences of the United States of America*, 101(39):14294–9 (2004). doi:10.1073/pnas.0405968101.

[104] P. Bolte, F. Bleibaum, A. Einwich, A. Günther, M. Liedvogel, D. Heyers, A. Depping, L. Wöhlbrand, R. Rabus, U. Janssen-Bienhold, and H. Mouritsen. Localisation of the putative magnetoreceptive protein cryptochrome 1b in the retinae of migratory birds and homing pigeons. *Plos One*, 11(3):e0147819 (2016). doi: 10.1371/journal.pone.0147819.

[105] C. Nießner, J. C. Gross, S. Denzau, L. Peichl, G. Fleissner, W. Wiltschko, and R. Wiltschko. Seasonally changing cryptochrome 1b expression in the retinal ganglion cells of a migrating passerine bird. *Plos One*, 11(3):e0150377 (2016). doi: 10.1371/journal.pone.0150377.

[106] I. A. Solov'yov, H. Mouritsen, and K. Schulten. Acuity of a Cryptochrome and Vision-Based Magnetoreception System in Birds. *Biophysical Journal*, 99(1):40–49 (2010). doi:10.1016/j.bpj.2010.03.053.

[107] A. Günther, A. Einwich, E. Sjulstok, R. Feederle, P. Bolte, K.-W. Koch, I. A. Solov'yov, and H. Mouritsen. Double-Cone Localization and Seasonal Expression Pattern Suggest a Role in Magnetoreception for European Robin Cryptochrome 4. *Current Biology*, 28(2):211–223 (2018). doi:10.1016/j.cub.2017.12.003.

[108] P. Müller and M. Ahmad. Light-activated cryptochrome reacts with molecular oxygen to form a flavin-superoxide radical pair consistent with magnetoreception. *Journal of Biological Chemistry*, 286(24):21033–21040 (2011). doi: 10.1074/jbc.M111.228940.

[109] M. Liedvogel, K. Maeda, K. Henbest, E. Schleicher, T. Simon, C. R. Timmel, P. J. Hore, and H. Mouritsen. Chemical magnetoreception: bird cryptochrome 1a is excited by blue light and forms long-lived radical-pairs. *PLoS ONE*, 2(10):e1106 (2007). doi:10.1371/journal.pone.0001106.

[110] K. Maeda, A. J. Robinson, K. B. Henbest, H. J. Hogben, T. Biskup, M. Ahmad, E. Schleicher, S. Weber, C. R. Timmel, and P. J. Hore. Magnetically sensitive light-induced reactions in cryptochrome are consistent with its proposed role as a magnetoreceptor. *Proceedings of the National Academy of Sciences of the United States of America*, 109(13):4774–4779 (2012). doi:10.1073/pnas.1118959109.

[111] H. Mitsui, T. Maeda, C. Yamaguchi, Y. Tsuji, R. Watari, Y. Kubo, K. Okano, and T. Okano. Overexpression in Yeast, Photocycle, and in Vitro Structural Change of an Avian Putative Magnetoreceptor Cryptochrome4. *Biochemistry*, 54(10):1908–1917 (2015). doi:10.1021/bi501441u.

[112] K. B. Henbest, K. Maeda, P. J. Hore, M. Joshi, A. Bacher, R. Bittl, S. Weber, C. R. Timmel, and E. Schleicher. Magnetic-field effect on the photoactivation reaction of Escherichia coli DNA photolyase. *Proceedings of the National Academy of Sciences of the United States of America*, 105(38):14395–9 (2008). doi:10.1073/pnas.0803620105.

[113] Prof. Jonathan Woodward; personal communication.

[114] R. J. Kutta, N. Archipowa, L. O. Johannissen, A. R. Jones, and N. S. Scrutton. Vertebrate Cryptochromes are Vestigial Flavoproteins. *Scientific Reports*, 7:44906 (2017). doi:10.1038/srep44906.

[115] N. M. Atherton. *Electron Spin Resonance*. Ellis Horwood Limited (1973).

[116] A. R. O'Dea, A. F. Curtis, N. J. B. Green, C. R. Timmel, and P. J. Hore. Influence of Dipolar Interactions on Radical Pair Recombination Reactions Subject to Weak Magnetic Fields. *The Journal of Physical Chemistry A*, 109(5):869–873 (2005). doi:10.1021/jp0456943.

[117] D. R. Kattnig, J. K. Sowa, I. A. Solov'yov, and P. J. Hore. Electron spin relaxation can enhance the performance of a cryptochrome-based magnetic compass sensor. *New Journal of Physics*, 18(6):063007 (2016). doi:10.1088/1367-2630/18/6/063007.

[118] J. Cai, G. G. Guerreschi, and H. J. Briegel. Quantum control and entanglement in a chemical compass. *Physical Review Letters*, 104(22):1–4 (2010). doi: 10.1103/PhysRevLett.104.220502.

[119] C. R. Timmel, U. Till, B. Brocklehurst, K. A. Mclauchlan, and P. J. Hore. Effects of weak magnetic fields on free radical recombination reactions. *Molecular Physics*, 95(1):71–89 (1998).

[120] R. Haberkorn. Density matrix description of spin-selective radical pair reactions. *Molecular Physics*, 32(5):1491–1493 (1976). doi:10.1080/00268977600102851.

[121] K. Maeda, P. Liddell, D. Gust, and P. J. Hore. Spin-selective recombination reactions of radical pairs: Experimental test of validity of reaction operators. *The Journal of Chemical Physics*, 139(23):234309 (2013). doi:10.1063/1.4844355.

[122] D. M. Brink and G. Satchler. *Angular Momentum*. Oxford University Press, 3rd edition (2002).

[123] I. Kuprov. *Module II, Lecture 03: Formal Theory of Rotations*. http://spindynamics.org/Spin-Dynamics—Part-II—Lecture-03.php (2013).

[124] J. C. S. Lau. *Spin-selective chemical reactions in radical pair magnetoreception*. Thesis, University of Oxford (2013).

[125] C. J. Taylor and D. J. Kriegman. Minimization on the Lie Group and Related Manifolds Minimization on the Lie Group SO(3) and Related Manifolds. *Technical Report No. 9405*, (3):10 (1994).

[126] B. Baragiola. *Notes: Tensor Operators [online]*. http://info.phys.unm.edu/~ideutsch/Classes/Phys531F11/SphericalTensors.pdf (2011).

[127] D. A. Varshalovich, A. N. Moskalev, and V. K. Khersonskii. *Quantum Theory of Angular Momentum*. World Scientific Publishing Co Pte Ltd (1988).

[128] R. Tarroni and C. Zannoni. On the rotational diffusion of asymmetric molecules

in liquid crystals. *The Journal of chemical physics*, 95:4550–4564 (1991). doi: doi.org/10.1063/1.461833.

[129] M. E. Rose. *Elementary Theory of Angular Momentum*. John Wiley & Sons Inc. (1957).

[130] H. J. Hogben, M. Krzystyniak, G. T. P. Charnock, P. J. Hore, and I. Kuprov. Spinach - A software library for simulation of spin dynamics in large spin systems. *Journal of Magnetic Resonance*, 208(2):179–194 (2011). doi: 10.1016/j.jmr.2010.11.008.

[131] D. Abergel and A. G. Palmer. On the use of the stochastic liouville equation in nuclear magnetic resonance: Application to R1p relaxation in the presence of exchange. *Concepts in Magnetic Resonance Part A: Bridging Education and Research*, 19(2):134–148 (2003). doi:10.1002/cmr.a.10091.

[132] William J. Stewart. Probability, Markov Chains, Queues and Simulation. Princeton University Press (2009).

[133] D. Abergel and A. G. Palmer. A Markov model for relaxation and exchange in NMR spectroscopy. *Journal of Physical Chemistry B*, 109(11):4837–4844 (2005). doi:10.1021/jp0458304.

[134] A. G. Redfield. On the Theory of Relaxation Processes. *IBM Journal of Research and Development*, 1(1):19–31 (1957). doi:10.1147/rd.11.0019.

[135] M. Goldman. Formal theory of spin–lattice relaxation. *Journal of Magnetic Resonance*, 149(2):160–87 (2001). doi:10.1006/jmre.2000.2239.

[136] C. P. Slichter. *Principles of Magnetic Resonance*. Springer-Verlag, Berlin, Heidelberg, New York, 3rd edition (1996).

[137] M. H. Levitt. *Spin Dynamics*. John Wiley & Sons Ltd (2001).

[138] M. Winklhofer. The physics of geomagnetic-field transduction in ani-

mals. *IEEE Transactions on Magnetics*, 45(12):5259–5265 (2009). doi: 10.1109/TMAG.2009.2017940.

[139] T. Ritz, M. Ahmad, H. Mouritsen, R. Wiltschko, and W. Wiltschko. Photoreceptor-based magnetoreception: optimal design of receptor molecules, cells, and neuronal processing. *Journal of the Royal Society, Interface*, 7:S135–S146 (2010). doi: 10.1098/rsif.2009.0456.focus.

[140] H. Mouritsen and T. Ritz. Magnetoreception and its use in bird navigation. *Current Opinion in Neurobiology*, 15(4):406–414 (2005). doi:10.1016/j.conb.2005.06.003.

[141] C. T. Rodgers. *Magnetic Field Effects in Chemical Systems*. Thesis, University of Oxford (2007).

[142] M. Procopio and T. Ritz. Inhomogeneous ensembles of radical pairs in chemical compasses. *Scientific Reports*, 6(1):35443 (2016). doi:10.1038/srep35443.

[143] E. M. Gauger, E. Rieper, J. J. L. Morton, S. C. Benjamin, and V. Vedral. Sustained Quantum Coherence and Entanglement in the Avian Compass. *Physical Review Letters*, 106(4):040503 (2011). doi:10.1103/PhysRevLett.106.040503.

[144] J. Cai, F. Caruso, and M. B. Plenio. Quantum limits for the magnetic sensitivity of a chemical compass. *Physical Review A - Atomic, Molecular, and Optical Physics*, 85(4):1–5 (2012). doi:10.1103/PhysRevA.85.040304.

[145] J. Cai and M. B. Plenio. Chemical compass model for avian magnetoreception as a quantum coherent device. *Physical Review Letters*, 111(23):1–6 (2013). doi: 10.1103/PhysRevLett.111.230503.

[146] A. M. Lewis, D. E. Manolopoulos, and P. J. Hore. Asymmetric recombination and electron spin relaxation in the semiclassical theory of radical pair reactions. *Journal of Chemical Physics*, 141(4):044111 (2014). doi:10.1063/1.4890659.

[147] D. R. Kattnig, I. A. Solov'yov, and P. J. Hore. Electron spin relaxation in

cryptochrome-based magnetoreception. *Physical Chemistry Chemical Physics*, 18:12443–12456 (2016). doi:10.1039/c5cp06731f.

[148] E. Sjulstok, J. M. H. Olsen, and I. A. Solov'yov. Quantifying electron transfer reactions in biological systems: what interactions play the major role? *Scientific Reports*, 5(1):18446 (2016). doi:10.1038/srep18446.

[149] K. Chen. *Matrix Preconditiong Techniques and Applications*. Cambridge University Press (2005). doi:http://dx.doi.org/10/1017/CB09780511543258.

[150] S. Worster, D. R. Kattnig, and P. J. Hore. Spin relaxation of radicals in cryptochrome and its role in avian magnetoreception. *The Journal of Chemical Physics*, 145(3):035104 (2016). doi:10.1063/1.4958624.

[151] R. Leenders, M. Kooijman, A. van Hoek, C. Veeger, and A. J. W. G. Visser. Flavin dynamics in reduced flavodoxins. *European Journal of Biochemistry*, 211:37–45 (1993).

[152] E. W. Evans, J. Li, J. G. Storey, K. Maeda, K. B. Henbest, C. A. Dodson, P. J. Hore, S. R. Mackenzie, and C. R. Timmel. Sensitive fluorescence-based detection of magnetic field effects in photoreactions of flavins. *Phys. Chem. Chem. Phys.*, 17:18456–18463 (2015). doi:10.1039/C5CP00723B.

[153] P. L. Nordio and P. Busolin. Electron Spin Resonance Line Shapes in Partially Oriented Systems. *The Journal of Chemical Physics*, 55(12):5485 (1971). doi: 10.1063/1.1675713.

[154] I. Kuprov, N. Wagner-Rundell, and P. Hore. Bloch-Redfield-Wangsness theory engine implementation using symbolic processing software. *Journal of Magnetic Resonance*, 184(2):196–206 (2007). doi:10.1016/j.jmr.2006.09.023.

[155] P. L. Nordio and U. Segre. *The Molecular Physics of Liquid Crystals*. Academic, New York (1979).

[156] E. Berggren, R. Tarroni, and C. Zannoni. Rotational diffusion of uniaxial probes

in biaxial liquid crystal phases. *The Journal of Chemical Physics*, 99(8):6180–6200 (1993). doi:doi.org/10.1063/1.465912.

[157] D. R. Kattnig, E. W. Evans, V. Déjean, C. A. Dodson, M. I. Wallace, S. R. Mackenzie, C. R. Timmel, and P. J. Hore. Chemical amplification of magnetic field effects relevant to avian magnetoreception. *Nature Chemistry*, 8(4):384–391 (2016). doi: 10.1038/nchem.2447.

[158] C. Levy, B. D. Zoltowski, A. R. Jones, A. T. Vaidya, D. Top, J. Widom, M. W. Young, N. S. Scrutton, B. R. Crane, and D. Leys. Updated structure of *Drosophila* cryptochrome. *Nature*, 495(7441):E3–E4 (2013). doi:10.1038/nature11995.

[159] B. D. Zoltowski, A. T. Vaidya, D. Top, J. Widom, M. W. Young, and B. R. Crane. Structure of full-length *Drosophila* cryptochrome. *Nature*, 480(7377):396–9 (2011). doi:10.1038/nature10618.

[160] E. Berggren and C. Zannoni. Rotational diffusion of biaxial probes in biaxial liquid crystal phases. *Molecular Physics*, 85(2):299–333 (1995). doi: 10.1080/00268979500101121.

[161] J. Tyndall. On the Blue Colour of the Sky, the Polarization of Skylight, and on the Polarization of Light by Cloudy Matter Generally. *Proceedings of the Royal Society of London*, 17:223–233 (1868). doi:10.1098/rspl.1868.0033.

[162] J. Gál, G. Horváth, A. Barta, and R. Wehner. Polarization of the moonlit clear night sky measured by full-sky imaging polarimetry at full Moon: Comparison of the polarization of moonlit and sunlit skies. *Journal of Geophysical Research*, 106:22647–22653 (2001). doi:10.1029/2000JD000085.

[163] J. Gal, G. Horvath, V. B. Meyer-Rochow, and R. Wehner. Polarization patterns of the summer sky and its neutral points measured by full-sky imaging polarimetry in Finnish Lapland north of the Arctic Circle. *Proceedings of the Royal Society A*, 457:1385–1399 (2001). doi:10.1098/rspa.2000.0726.

[164] U. Homberg, S. Heinze, K. Pfeiffer, M. Kinoshita, and B. el Jundi. Central neural coding of sky polarization in insects. *Philosophical Transactions of the Royal Society B*, 366:680–687 (2011). doi:10.1098/rstb.2010.0199.

[165] S. Worster, H. Mouritsen, and P. J. Hore. A light-dependent magnetoreception mechanism insensitive to light intensity and polarization. *Journal of The Royal Society, Interface*, 14:20170405 (2017). doi:10.1098/rsif.2017.0405.

[166] H. J. W. Strutt. On the light from the sky , its polarization and colour. *Philosophical Magazine Series 4*, 41(271):107–120 (1871). doi:10.1080/14786447108640452.

[167] M. L. Brines and J. L. Gould. Skylight polarization patterns and animal orientation. *Journal of Experimental Biology*, 96(1):69–91 (1982).

[168] I. Pomozi, G. Horváth, and R. Wehner. How the clear-sky angle of polarization pattern continues underneath clouds: full-sky measurements and implications for animal orientation. *The Journal of Experimental Biology*, 204:2933–2942 (2001).

[169] L. Nowinszky, S. Szabó, G. Toth, I. Ekk, and M. Kiss. The effect of the moon phases and of the intensity of polarized moonlight on the light-trap catches. *Zeitschrift für Angewandte Entomologie*, 88:337–353 (1979). doi:10.1111/j.1439-0418.1979.tb02512.x.

[170] J. J. Hopfield. Mechanism of lunar polarization. *Science*, 151:1380–1381 (1966). doi:10.1126/science.151.3716.1380.

[171] T. W. Cronin and J. Marshall. Patterns and properties of polarized light in air and water. *Philosophical Transactions of the Royal Society B*, 366(1565):619–626 (2011). doi:10.1098/rstb.2010.0201.

[172] M. Dacke, D.-E. Nilsson, C. H. Scholtz, M. Byrne, and E. J. Warrant. Insect orientation to polarized moonlight: An African dung beetle uses the moonlit sky to make a swift exit after finding food. *Nature*, 424(6944):33–34 (2003). doi: http://dx.doi.org/10.1038/424033a.

[173] R. Hegedüs, S. Åkesson, and G. Horváth. Polarization patterns of thick clouds: overcast skies have distribution of the angle of polarization similar to that of clear skies. *Journal of the Optical Society of America A*, 24(8):2347 (2007). doi: 10.1364/JOSAA.24.002347.

[174] T. W. Cronin and M. J. Bok. Photoreception and vision in the ultraviolet. *The Journal of Experimental Biology*, 219(18):2790–2801 (2016). doi:10.1242/jeb.128769.

[175] O. Güntürkün. Sensory Physiology: Vision. In G. C. Whittow (ed.), *Sturkie's Avian Physiology,*, chapter 1, 1–19. ACADEMIC PRESS, 5th edition (2000).

[176] G. R. Martin. Producing the Image. In H. P. Zeigler and H.-J. Bischof (eds.), *Vision, Brain and Behaviour in Birds*, chapter 1, 5–24. The MIT Press (1993).

[177] J. A. Waldvogel. The Bird' s Eye View. *American Scientist*, 78(4):342–353 (1990).

[178] Prof. Dr. Henrik Mouritsen and Dr. Arndt Meyer; personal communication.

[179] H.-O. Nalbach, F. Wolf-Oberhollenzer, and M. Remy. Exploring the Image. In H. P. Zeigler and H.-J. Bischof (eds.), *Vision, Brain and Behaviour in Birds*, chapter 2, 25–46. The MIT Press (1993).

[180] C. A. Wood. *The Fundus Oculi of Birds*. Chicago, The Lakeside Press (1917). doi:10.2307/3221706.

[181] R. W. Young. An hypothesis to account for a basic distinction between rods and cones. *Vision Research*, 11(1):1–5 (1971). doi:10.1016/0042-6989(71)90201-X.

[182] Y. A. Kram, S. Mantey, and J. C. Corbo. Avian cone photoreceptors tile the retina as five independent, self-organizing mosaics. *PLoS ONE*, 5(2):e8992 (2010). doi: 10.1371/journal.pone.0008992.

[183] S. R. Young and G. R. Martin. Optics of retinal oil droplets: A model of light collection and polarization detection in the avian retina. *Vision Research*, 24(2):129–137 (1984). doi:10.1016/0042-6989(84)90098-1.

[184] E. J. Maier and J. K. Bowmaker. Colour vision in the passeriform bird, Leiothrix lutea: correlation of visual pigment absorbance and oil droplet transmission with spectral sensitivity. *Journal of Comparative Physiology A*, 172(3):295–301 (1993). doi:10.1007/BF00216611.

[185] A. M. Laties. Histological techniques for study of photoreceptor orientation. *Tissue & Cell*, 1(1):63–81 (1969). doi:10.1016/S0040-8166(69)80006-6.

[186] A. M. Laties and J. M. Enoch. An analysis of retinal receptor orientation. *Investigative Ophthalmology & Visual Science*, 10:69–77 (1971).

[187] H. S. Smallman, D. I. A. MacLeod, and P. Doyle. Realignment of cones after cataract removal. *Nature*, 412:604–605 (2001). doi:10.1038/35088126.

[188] G. Westheimer. Directional sensitivity of the retina: 75 years of Stiles-Crawford effect. *Proceedings of the Royal Society B*, 275:2777–2786 (2008). doi:10.1098/rspb.2008.0712.

[189] J. Marshall and T. W. Cronin. Polarisation vision. *Current Biology*, 21(3):R101–R105 (2011). doi:10.1016/j.cub.2010.12.012.

[190] G. J. Taylor, W. Ribi, M. Bech, A. J. Bodey, C. Rau, A. Steuwer, E. J. Warrant, and E. Baird. The dual function of orchid bee ocelli as revealed by X-ray microtomography. *Current Biology*, 26(10):1319–1324 (2016). doi:10.1016/j.cub.2016.03.038.

[191] T. Labhart. Can invertebrates see the e-vector of polarization as a separate modality of light? *Journal of Experimental Biology*, 219(24):3844–3856 (2016). doi:10.1242/jeb.139899.

[192] R. Wehner. Neurobiology of polarization vision. *Trends in Neurosciences*, 12(9):353–359 (1989). doi:10.1016/0166-2236(89)90043-X.

[193] M. Dacke, M. J. Byrne, E. Baird, C. H. Scholtz, and E. J. Warrant. How dim is dim? Precision of the celestial compass in moonlight and sunlight. *Philosophical Transactions of the Royal Society B*, 366(1565):697–702 (2011). doi:10.1098/rstb.2010.0191.

[194] M. Dacke, M. J. Byrne, C. H. Scholtz, and E. J. Warrant. Lunar orientation in a beetle. *Proceedings of the Royal Society B*, 271:361–5 (2004). doi: 10.1098/rspb.2003.2594.

[195] D. A. Cameron and E. N. Pugh. Double cones as a basis for a new type of polarization vision in vertebrates. *Nature*, 353:161–164 (1991). doi:10.1038/353161a0.

[196] T. W. Cronin, N. Shashar, R. L. Caldwell, J. Marshall, A. G. Cheroske, and T.-H. Chiou. Polarization vision and its role in biological signaling. *Integrative and Comparative Biology*, 43(4):549–558 (2003). doi:10.1093/icb/43.4.549.

[197] I. Novales Flamarique, C. W. Hawryshyn, and F. I. Hárosi. Double-cone internal reflection as a basis for polarization detection in fish. *Journal of the Optical Society of America A*, 15(2):349–358 (1998). doi:10.1364/JOSAA.15.000349.

[198] C. W. Hawryshyn. Ultraviolet polarization vision in fishes: possible mechanisms for coding e-vector. *Philosophical Transactions of the Royal Society B*, 355(1401):1187–1190 (2000). doi:10.1098/rstb.2000.0664.

[199] N. S. Hart and D. M. Hunt. Avian visual pigments: Characteristics, spectral tuning, and evolution. *American Naturalist*, 169:S7–S26 (2007). doi:10.1086/510141.

[200] R. Muheim. Behavioural and physiological mechanisms of polarized light sensitivity in birds. *Philosophical Transactions of the Royal Society B*, 366(1565):763–771 (2011). doi:10.1098/rstb.2010.0196.

[201] V. B. Morris. Symmetry in a receptor mosaic demonstrated in the chick from the frequencies, spacing and arrangement of the types of retinal receptor. *The Journal of Comparative Neurology*, 140(3):359–398 (1970). doi:10.1002/cne.901400308.

[202] M. L. Kreithen and W. T. Keeton. Detection of changes in atmospheric pressure by the homing pigeon, *Columba livia*. *Journal of Comp. Physiol.*, 89:73–82 (1974). doi:10.1007/BF00696165.

[203] J. D. Delius, R. J. Perchard, and J. Emmerton. Polarized light discrimination by

pigeons and an electroretinographic correlate. *Journal of Comparative and Physiological Psychology*, 90(6):560–571 (1976). doi:10.1037/h0077223.

[204] S. Åkesson. The Ecology of Polarisation Vision in Birds. In G. Horváth (ed.), *Polarized Light and Polarization Vision in Animal Sciences Springer Series in Vision Research*, chapter 12, 275–292. Springer-Verlag, Berlin Heidelberg (2014). ISBN 978-3-642-54717-1. doi:10.1007/978-3-642-54718-8.

[205] J. B. Phillips and J. A. Waldvogel. Reflected Light Cues Generate the Short-Term Deflector-Loft Effect. In F. Papi and H. G. Wallraff (eds.), *Avian Navigation*, 190–202. Springer Berlin (1982).

[206] E. Batschelet. *Circular Statistics in Biology*. ACADEMIC PRESS INC. (LONDON) LTD. (1981).

[207] M. F. Land and D.-E. Nilsson. *Animal Eyes*. Oxford University Press, 2nd edition (2012).

[208] R. A. Cone. Rotational Diffusion of Rhodopsin in the Visual Receptor Membrane. *Nature New Biology*, 236:39–43 (1972). doi:10.1038/newbio236039a0.

[209] R. A. Cone and M. Poo. Lateral diffusion of rhodopsin in the photoreceptor membrane. *Nature*, 247:438–441 (1974). doi:10.1038/252497a0.

[210] N. W. Roberts, M. L. Porter, and T. W. Cronin. The molecular basis of mechanisms underlying polarization vision. *Philosophical Transactions of the Royal Society B*, 366:627–637 (2011). doi:10.1098/rstb.2010.0206.

[211] W. A. Eaton, J. Hofrichter, M. W. Makinen, R. D. Andersen, and M. L. Ludwig. Optical spectra and electronic structure of flavine mononucleotide in flavodoxin crystals. *Biochemistry*, 14(10):2146–2151 (1975). doi:10.1021/bi00681a016.

[212] T. Climent, R. González-Luque, M. Merchán, and L. Serrano-Andrés. Theoretical insight into the spectroscopy and photochemistry of isoalloxazine, the flavin

core ring. *Journal of Physical Chemistry A*, 110(50):13584–13590 (2006). doi: 10.1021/jp065772h.

[213] B. Graves. *Polarized light effects in radical pair compass magnetoreception*. Master's thesis, University of Oxford (2016).

[214] S. Akesson, J. Morin, R. Muheim, and U. Ottosson. Avian orientation at steep angles of inclination: experiments with migratory white-crowned sparrows at the magnetic North Pole. *Proceedings of the Royal Society B*, 268:1907–1913 (2001). doi:10.1098/rspb.2001.1736.

[215] WolframMathWorld. *Mercator Projection [online]*. http://mathworld.wolfram.com/MercatorProjection.html (2018).

[216] M. Gunkel, J. Schöneberg, W. Alkhaldi, S. Irsen, F. Noé, U. B. Kaupp, and A. Al-Amoudi. Higher-order architecture of rhodopsin in intact photoreceptors and its implication for phototransduction kinetics. *Structure*, 23(4):628–638 (2015). doi: 10.1016/j.str.2015.01.015.

[217] D. Fotiadis, B. Jastrzebska, A. Philippsen, D. J. Müller, K. Palczewski, and A. Engel. Structure of the rhodopsin dimer: a working model for G-protein-coupled receptors. *Current Opinion in Structural Biology*, 16(2):252–259 (2006). doi: 10.1016/j.sbi.2006.03.013.

[218] N. S. Hart. The visual ecology of avian photoreceptors. *Progress in Retinal and Eye Research*, 20(5):675–703 (2001). doi:10.1016/S1350-9462(01)00009-X.

[219] N. S. Hart and M. Vorobyev. Modelling oil droplet absorption spectra and spectral sensitivities of bird cone photoreceptors. *Journal of Comparative Physiology A: Neuroethology, Sensory, Neural, and Behavioral Physiology*, 191(4):381–392 (2005). doi:10.1007/s00359-004-0595-3.

[220] R. L. Smith, Y. Nishimura, and G. Raviola. Interreceptor junction in the double cone of the chicken retina. *Journal of Submicroscopic Cytology*, 17(2):183–186 (1985).

[221] D. M. W. Sheppard, J. Li, K. B. Henbest, S. R. T. Neil, K. Maeda, J. Storey, E. Schleicher, T. Biskup, R. Rodriguez, S. Weber, P. J. Hore, C. R. Timmel, and S. R. Mackenzie. Millitesla magnetic field effects on the photocycle of an animal cryptochrome. *Scientific Reports*, 7:42228 (2017). doi:10.1038/srep42228.

[222] J. M. D. Coey. *Magnetism and Magnetic Materials*. Cambridge University Press, 1st edition (2010).

[223] B. M. Moskowitz. Hitchhiker's Guide to Magnetism. *Environmental Magnetism Workshop*, 279(1):48 (1991). doi:10.1038/nm1005-1051.

[224] B. Issa, I. M. Obaidat, B. A. Albiss, and Y. Haik. Magnetic nanoparticles: Surface effects and properties related to biomedicine applications. *International Journal of Molecular Sciences*, 14(11):21266–21305 (2013). doi:10.3390/ijms141121266.

[225] A. G. Kolhatkar, A. C. Jamison, D. Litvinov, R. C. Willson, and T. R. Lee. Tuning the magnetic properties of nanoparticles. *International Journal of Molecular Sciences*, 14(8):15977–16009 (2013). doi:10.3390/ijms140815977.

[226] S. Laurent, D. Forge, M. Port, A. Roch, C. Robic, L. Vander Elst, and R. N. Muller. Magnetic iron oxide nanoparticles: Synthesis, stabilization, vectorization, physicochemical characterizations and biological applications. *Chemical Reviews*, 108(6):2064–2110 (2008). doi:10.1021/cr068445e.

[227] M. T. Klem, M. Young, and T. Douglas. Biomimetic magnetic nanoparticles. *Materials Today*, 8(9):28–37 (2005). doi:10.1016/S1369-7021(05)71078-6.

[228] C. Lang, D. Schüler, and D. Faivre. Synthesis of magnetite nanoparticles for bio- and nanotechnology: Genetic engineering and biomimetics of bacterial magnetosomes. *Macromolecular Bioscience*, 7(2):144–151 (2007). doi:10.1002/mabi.200600235.

[229] M. Arruebo, R. Fernández-Pacheco, M. R. Ibarra, and J. Santamaría. Magnetic nanoparticles for drug delivery. *Nano Today*, 2(3):22–32 (2007). doi:10.1016/S1748-0132(07)70084-1.

[230] H. B. Na, I. C. Song, and T. Hyeon. Inorganic nanoparticles for MRI contrast agents. *Advanced Materials*, 21(21):2133–2148 (2009). doi:10.1002/adma.200802366.

[231] D. P. Cormode, P. A. Jarzyna, W. J. M. Mulder, and Z. A. Fayad. Modified natural nanoparticles as contrast agents for medical imaging. *Advanced Drug Delivery Reviews*, 62(3):329–338 (2010). doi:10.1016/j.addr.2009.11.005.

[232] J. W. M. Bulte and D. L. Kraitchman. Iron oxide MR contrast agents for molecular and cellular imaging. *NMR in Biomedicine*, 17(7):484–499 (2004). doi:10.1002/nbm.924.

[233] C. Cao, X. Wang, Y. Cai, L. Sun, L. Tian, H. Wu, X. He, H. Lei, W. Liu, G. Chen, R. Zhu, and Y. Pan. Targeted in vivo imaging of microscopic tumors with ferritin-based nanoprobes across biological barriers. *Advanced Materials*, 26(16):2566–2571 (2014). doi:10.1002/adma.201304544.

[234] Y. Gossuin, R. N. Muller, and P. Gillis. Relaxation induced by ferritin: A better understanding for an improved MRI iron quantification. *NMR in Biomedicine*, 17(7):427–432 (2004). doi:10.1002/nbm.903.

[235] Y. Gossuin, P. Gillis, A. Hocq, Q. L. Vuong, and A. Roch. Magnetic resonance relaxation properties of superparamagnetic particles. *Nanomedicine and Nanobiotechnology*, 1:299–310 (2009). doi:10.1002/wnan.036.

[236] M. A. Boss. The Role of Diffusion in NMR Proton Relaxation Enhancement by Ferritin. *Dissertation presented in the Graduate School of The Ohio State University* (2010).

[237] S.-H. Chung, A. Hoffmann, K. Guslienko, S. D. Bader, C. Liu, B. Kay, L. Makowski, and L. Chen. Biological sensing with magnetic nanoparticles using Brownian relaxation. *Journal of Applied Physics*, 97(10):10R101 (2005). doi:10.1063/1.1853694.

[238] S. Gider, D. D. Awschalom, T. Douglas, K. Wong, S. Mann, and G. Cain. Classical

and quantum magnetism in synthetic ferritin proteins. *Journal of Applied Physics*, 79(8):5324 (1996). doi:10.1063/1.361366.

[239] M. Uchida, M. L. Flenniken, M. Allen, D. A. Willits, B. E. Crowley, S. Brumfield, A. F. Willis, L. Jackiw, M. Jutila, M. J. Young, and T. Douglas. Targeting of cancer cells with ferrimagnetic ferritin cage nanoparticles. *Journal of the American Chemical Society*, 128(51):16626–16633 (2006). doi:10.1021/ja0655690.

[240] P. Arosio, R. Ingrassia, and P. Cavadini. Ferritins: A family of molecules for iron storage, antioxidation and more. *Biochimica et Biophysica Acta*, 1790(7):589–599 (2009). doi:10.1016/j.bbagen.2008.09.004.

[241] A. E. Cohen. Nanomagnetic control of intersystem crossing. *Journal of Physical Chemistry A*, 113(41):11084–11092 (2009). doi:10.1021/jp907113p.

[242] J. Cai. Quantum probe and design for a chemical compass with magnetic nanostructures. *Physical Review Letters*, 106(10):1–4 (2011). doi:10.1103/PhysRevLett.106.100501.

[243] V. Binhi. Do naturally occurring magnetic nanoparticles in the human body mediate increased risk of childhood leukaemia with EMF exposure? *International Journal of Radiation Biology*, 84(7):569–579 (2008). doi:10.1080/09553000802195323.

[244] M. Meister. Physical limits to magnetogenetics. *eLife*, 5 (2016). doi:10.7554/eLife.17210.

[245] M. J. Martínez-Pérez, R. de Miguel, C. Carbonera, M. Martínez-Júlvez, A. Lostao, C. Piquer, C. Gómez-Moreno, J. Bartolomé, and F. Luis. Size-dependent properties of magnetoferritin. *Nanotechnology*, 21(46):465707 (2010). doi:10.1088/0957-4484/21/46/465707.

[246] B. M. Moskowitz, R. B. Frankel, S. A. Walton, D. P. E. Dickson, K. K. W. Wong, T. Douglas, and S. Mann. Determination of the preexponential frequency factor for

superparamagnetic maghemite particles in magnetoferritin. *Journal of Geophysical Research*, 102(97):22671 (1997). doi:10.1029/97JB01698.

[247] P. M. Harrison and P. Arosio. The ferritins: Molecular properties, iron storage function and cellular regulation. *Biochimica et Biophysica Acta - Bioenergetics*, 1275(3):161–203 (1996). doi:10.1016/0005-2728(96)00022-9.

[248] P. Allen, T. St Pierre, W. Chua-anusorn, V. Ström, and K. Rao. Low-frequency low-field magnetic susceptibility of ferritin and hemosiderin. *Biochimica et Biophysica Acta*, 1500(2):186–196 (2000). doi:10.1016/S0925-4439(99)00104-0.

[249] P. F. Vohralik and S. K. H. Lam. NanoSQUID detection of magnetization from ferritin nanoparticles. *Superconductor Science and Technology*, 22(6):064007 (2009). doi:10.1088/0953-2048/22/6/064007.

[250] J. G. E. Harris, J. E. Grimaldi, D. D. Awschalom, A. Chiolero, and D. Loss. Excess Spin and the Dynamics of Antiferromagnetic Ferritin. *Physical Review B*, 60(5):4 (1999). doi:10.1103/PhysRevB.60.3453.

[251] S. Kilcoyne and R. Cywinski. Ferritin: a model superparamagnet. *Journal of Magnetism and Magnetic Materials*, 140-144:1466–1467 (1995). doi:10.1016/0304-8853(94)00626-1.

[252] G. C. Papaefthymiou. The Mössbauer and magnetic properties of ferritin cores. *Biochimica et Biophysica Acta*, 1800(8):886–897 (2010). doi:10.1016/j.bbagen.2010.03.018.

[253] F. C. Meldrum, B. R. Heywood, and S. Mann. Magnetoferritin : In Vitro Synthesis of a Novel Magnetic Protein. *Science*, 257:522–523 (1992). doi:10.1126/science.1636086.

[254] K. K. W. Wong, T. Douglas, S. Gider, D. D. Awschalom, and S. Mann. Biomimetic Synthesis and Characterization of Magnetic Proteins (Magnetoferritin). *Chemistry of Materials*, 10(1):279–285 (1998). doi:10.1021/cm970421o.

[255] C. Cao, L. Tian, Q. Liu, W. Liu, G. Chen, and Y. Pan. Magnetic characterization of noninteracting, randomly oriented, nanometer-scale ferrimagnetic particles. *Journal of Geophysical Research: Solid Earth*, 115(7):1–10 (2010). doi: 10.1029/2009JB006855.

[256] D. Dickson, S. Walton, S. Mann, and K. Wong. Properties of magnetoferritin: a novel biomagnetic nanoparticle. *Nanostructured Materials*, 9(1-8):595–598 (1997). doi:10.1016/S0965-9773(97)00133-5.

[257] L. Melníková, V. I. Petrenko, M. V. Avdeev, V. M. Garamus, L. Almásy, O. I. Ivankov, L. A. Bulavin, Z. Mitróová, and P. Kopĉanský. Effect of iron oxide loading on magnetoferritin structure in solution as revealed by SAXS and SANS. *Colloids and Surfaces B: Biointerfaces*, 123:82–88 (2014). doi:10.1016/j.colsurfb.2014.08.032.

[258] F. Moro, R. De Miguel, M. Jenkins, C. Gómez-Moreno, D. Sells, F. Tuna, E. J. L. McInnes, A. Lostao, F. Luis, and J. Van Slageren. Magnetic anisotropy of polycrystalline magnetoferritin investigated by SQUID and electron magnetic resonance. *Journal of Magnetism and Magnetic Materials*, 361:188–196 (2014). doi: 10.1016/j.jmmm.2014.02.053.

[259] L. Melníková, Z. Mitróová, M. Timko, J. Kováĉ, M. V. Avdeev, V. I. Petrenko, V. M. Garamus, L. Almásy, and P. Kopĉanský. Structural characterization of magnetoferritin. *Mendeleev Communications*, 24(2):80–81 (2014). doi: 10.1016/j.mencom.2014.03.004.

[260] J. W. M. Bulte, T. Douglas, S. Mann, J. Vymazal, P. G. Laughlin, and J. A. Frank. Initial assessment of magnetoferritin biokinetics and proton relaxation enhancement in rats. *Academic Radiology*, 2(10):871–878 (1995). doi:10.1016/S1076-6332(05)80064-9.

[261] L. X. Tiefenauer, A. Tschirky, G. Kühne, and R. Y. Andres. In vivo evaluation of magnetite nanoparticles for use as a tumor contrast agent in MRI. *Magnetic Resonance Imaging*, 14(4):391–402 (1996). doi:10.1016/0730-725X(95)02106-4.

[262] K. Fan, C. Cao, Y. Pan, D. Lu, D. Yang, J. Feng, L. Song, M. Liang, and X. Yan. Magnetoferritin nanoparticles for targeting and visualizing tumour tissues. *Nature Nanotechnology*, 7(7):459–464 (2012). doi:10.1038/nnano.2012.90.

[263] Y. Zhao, M. Liang, X. Li, K. Fan, J. Xiao, Y. Li, H. Shi, F. Wang, H. S. Choi, D. Cheng, and X. Yan. Bioengineered Magnetoferritin Nanoprobes for Single-Dose Nuclear-Magnetic Resonance Tumor Imaging. *ACS Nano*, 10(4):4184–4191 (2016). doi:10.1021/acsnano.5b07408.

[264] L. Melníková, K. Pospiskova, Z. Mitróová, P. Kopĉanský, and I. Safarik. Peroxidase-like activity of magnetoferritin. *Microchimica Acta*, 181(3-4):295–301 (2014). doi: 10.1007/s00604-013-1105-5.

[265] H. Mouritsen and P. Hore. The magnetic retina: light-dependent and trigeminal magnetoreception in migratory birds. *Current Opinion in Neurobiology*, 22(2):343–352 (2012). doi:10.1016/j.conb.2012.01.005.

[266] D. Schüler and R. B. Frankel. Bacterial magnetosomes: Microbiology, biomineralization and biotechnological applications. *Applied Microbiology and Biotechnology*, 52(4):464–473 (1999). doi:10.1007/s002530051547.

[267] D. Faivre, L. H. Böttger, B. F. Matzanke, and D. Schüler. Intracellular Magnetite Biomineralization in Bacteria Proceeds by a Distinct Pathway Involving Membrane-Bound Ferritin and an Iron(II) Species. *Angewandte Chemie*, 46(44):8495–8499 (2007). doi:10.1002/anie.200700927.

[268] Y. Ding, J. Li, J. Liu, J. Yang, W. Jiang, J. Tian, Y. Li, Y. Pan, and J. Li. Deletion of the ftsZ-like gene results in the production of superparamagnetic magnetite magnetosomes in Magnetospirillum gryphiswaldense. *Journal of Bacteriology*, 192(4):1097–1105 (2010). doi:10.1128/JB.01292-09.

[269] J.-H. Lee, Y. Roh, and H.-G. Hur. Microbial Production and Characterization of

Superparamagnetic Magnetite Nanoparticles by *Shewanella* sp. HN-41. *Journal of Microbiology and Biotechnology*, 18(9):1572–1577 (2008).

[270] C. Quintana, J. M. Cowley, and C. Marhic. Electron nanodiffraction and high-resolution electron microscopy studies of the structure and composition of physiological and pathological ferritin. *Journal of Structural Biology*, 147(2):166–178 (2004). doi:10.1016/j.jsb.2004.03.001.

[271] Y. Gossuin, D. Hautot, R. N. Muller, Q. Pankhurst, J. Dobson, C. Morris, P. Gillis, and J. Collingwood. Looking for biogenic magnetite in brain ferritin using NMR relaxometry. *NMR in Biomedicine*, 18(7):469–472 (2005). doi:10.1002/nbm.983.

[272] M. Gajdardziska-Josifovska, R. G. McClean, M. A. Schofield, C. V. Sommer, and W. F. Kean. Discovery of nanocrystalline botanical magnetite. *European Journal of Mineralogy*, 13(5):863–870 (2001). doi:10.1127/0935-1221/2001/0013/0863.

[273] X. Liao, S. Yun, and G. Zhao. Structure, function, and nutrition of phytoferritin: a newly functional factor for iron supplement. *Critical reviews in food science and nutrition*, 54(10):1342–52 (2014). doi:10.1080/10408398.2011.635914.

[274] E. W. Evans, D. R. Kattnig, K. B. Henbest, P. J. Hore, S. R. Mackenzie, and C. R. Timmel. Sub-millitesla magnetic field effects on the recombination reaction of flavin and ascorbic acid radicals. *The Journal of Chemical Physics*, 145(8):085101 (2016). doi:10.1063/1.4961266.

[275] K. Maeda, K. B. Henbest, F. Cintolesi, I. Kuprov, C. T. Rodgers, P. A. Liddell, D. Gust, C. R. Timmel, and P. J. Hore. Chemical compass model of avian magnetoreception. *Nature*, 453(7193):387–390 (2008). doi:10.1038/nature06834.

[276] B. Brocklehurst. Spin Correlation in the Geminate Reconibination of Radical Ions in hydrocarbons. *J. Chem. Soc. Faraday Trans II*, 72:1869–1884 (1976). doi:10.1039/f29767201869.

[277] S. K. H. Lam, W. Yang, H. T. R. Wiogo, and C. P. Foley. Attachment of mag-

netic molecules on a nanoSQUID. *Nanotechnology*, 19(28):285303 (2008). doi: 10.1088/0957-4484/19/28/285303.

[278] D. R. Kattnig and P. J. Hore. The sensitivity of a radical pair compass magnetoreceptor can be significantly amplified by radical scavengers. *Scientific Reports*, 7(1):1–12 (2017). doi:10.1038/s41598-017-09914-7.

[279] D. R. Kattnig. Radical-Pair-Based Magnetoreception Amplified by Radical Scavenging: Resilience to Spin Relaxation. *The Journal of Physical Chemistry B*, 121(44):10215–10227 (2017). doi:10.1021/acs.jpcb.7b07672.

[280] M. J. Frisch, G. W. Trucks, H. B. Schlegel, G. E. Scuseria, M. A. Robb, J. R. Cheeseman, J. A. Montgomery, Jr., K. N. Vreven, T.; Kudin, J. C. Burant, J. M. Millam, S. S. Iyengar, J. Tomasi, V. Barone, B. Mennucci, M. Cossi, G. Scalmani, N. Rega, G. A. Petersson, H. Nakatsuji, M. Hada, M. Ehara, K. Toyota, R. Fukuda, J. Hasegawa, M. Ishida, T. Nakajima, Y. Honda, O. Kitao, H. Nakai, M. Klene, X. Li, J. E. Knox, H. P. Hratchian, J. B. Cross, V. Bakken, C. Adamo, J. Jaramillo, R. Gomperts, R. E. Stratmann, O. Yazyev, A. J. Austin, R. Cammi, C. Pomelli, J. W. Ochterski, P. Y. Ayala, K. Morokuma, G. A. Voth, P. Salvador, J. J. Dannenberg, V. G. Zakrzewski, S. Dapprich, A. D. Daniels, M. C. Strain, O. Farkas, D. K. Malick, A. D. Rabuck, K. Raghavachari, J. B. Foresman, J. V. Ortiz, Q. Cui, A. G. Baboul, S. Clifford, J. Cioslowski, B. B. Stefanov, G. Liu, A. Liashenko, P. Piskorz, I. Komaromi, R. L. Martin, D. J. Fox, T. Keith, M. A. Al-Laham, C. Y. Peng, A. Nanayakkara, M. Challacombe, P. M. W. Gill, B. Johnson, W. Chen, M. W. Wong, C. Gonzalez, and J. A. Pople. Gaussian 03 (2004).

[281] G. G. Slabaugh. *Computing Euler angles from a rotation matrix [online]*. http://www.staff.city.ac.uk/˜sbbh653/publications/euler.pdf (1999).

Appendix A

Hyperfine interaction tensors

Hyperfine Interactions and Atom Numbering Schemes for $FAD^{\bullet-}$ and $TrpH^{\bullet+}$

Table A.1: Hyperfine tensors for the $FAD^{\bullet-}$ radical.$^{\heartsuit}$

Nucleus	**A**	a_{iso}/mT$^{\diamondsuit}$	T_{qq}/mT$^{\clubsuit}$
N5	$\begin{pmatrix} -0.0995 & 0.0029 & 0.0 \\ 0.0029 & -0.0875 & 0.0 \\ 0.0 & 0.0 & 1.7569 \end{pmatrix}$	0.5233	1.2336 −0.6101 −0.6234
N10	$\begin{pmatrix} -0.0149 & -0.0021 & 0.0 \\ -0.0021 & -0.0237 & 0.0 \\ 0.0 & 0.0 & 0.6046 \end{pmatrix}$	0.1887	0.4159 −0.2031 −0.2128
H6	$\begin{pmatrix} -0.2009 & -0.0328 & 0.0 \\ -0.0328 & -0.5271 & 0.0 \\ 0.0 & 0.0 & -0.4336 \end{pmatrix}$	−0.3872	0.1896 −0.0464 −0.1432
H8 (×3)	$\begin{pmatrix} 0.4399 & 0.0 & 0.0 \\ 0.0 & 0.4399 & 0.0 \\ 0.0 & 0.0 & 0.4399 \end{pmatrix}$	0.4399	0.0 0.0 0.0
Hβ (×2)	$\begin{pmatrix} 0.4070 & 0.0 & 0.0 \\ 0.0 & 0.4070 & 0.0 \\ 0.0 & 0.0 & 0.4070 \end{pmatrix}$	0.4070	0.0 0.0 0.0
H7 (×3)	$\begin{pmatrix} -0.1416 & 0.0 & 0.0 \\ 0.0 & -0.1416 & 0.0 \\ 0.0 & 0.0 & -0.1416 \end{pmatrix}$	−0.1416	0.0 0.0 0.0

♡ Calculated by Dr Ilya Kuprov, Department of Chemistry, University of Southampton, using density functional theory in Gaussian-03 [280] at the UB3LYP/EPR-III level [141]. The calculation was done for the radical anion of 7,8,10-trimethyl isoalloxazine (lumiflavin) *in vacuo*. The atom numbering scheme is shown below.

♢ Isotropic hyperfine interactions.

♣ Principal anisotropic components of the hyperfine tensors (arranged in descending order of magnitude for each nucleus).

Notes:

H8 methyl group. The anisotropic components are small (< 0.08 mT) and were not included in the spin dynamics simulations. The average of the three isotropic couplings, $(0.6493 + 0.6493 + 0.0212)/3$ mT, was used for all three methyl protons on the assumption that methyl group rotation is fast enough to average the three interactions.

H7 methyl group. The anisotropic components are small (< 0.05 mT) and were not included in the spin dynamics simulations. The average of the three isotropic couplings, $(0.2011 + 0.2011 + 0.0225)/3$ mT, was used for all three methyl protons on the assumption that methyl group rotation is fast enough to average the three interactions.

Hβ. The anisotropic components are small (< 0.09 mT) and were not included. The β protons were assigned isotropic hyperfine couplings equal to the largest of the three calculated for the N(10) methyl group in lumiflavin (0.4070, 0.4070, -0.0189 mT).

Choice of nuclei. The cryptochrome model included the following 3 nuclei: N5, N10, H6.

The DFT calculations were performed separately for the two radicals on the assumption that the 1.9 nm centre-to-centre distance between them in the protein is large enough that the hyperfine interactions should be very similar in the radical pair.

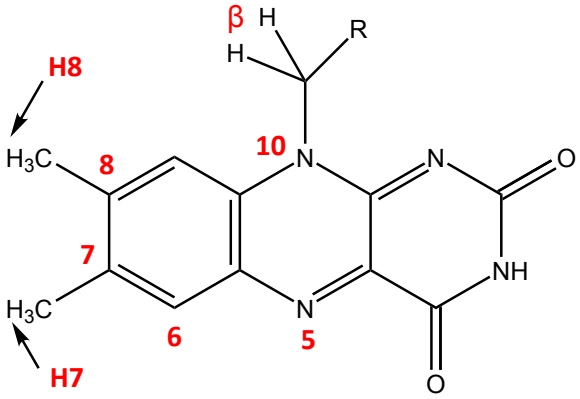


Figure A.1: Atom numbering scheme for $FAD^{\bullet -}$.

Table A.2: Hyperfine tensors for the $TrpH^{\bullet+}$ radical.[♡]

Nucleus	$\mathbf{A}^{\spadesuit}$	$a_{\mathrm{iso}}/\mathrm{mT}^{\diamondsuit}$	$T_{qq}/\mathrm{mT}^{\clubsuit}$
N1	$\begin{pmatrix} -0.0336 & 0.0924 & -0.1354 \\ 0.0924 & 0.3303 & -0.5318 \\ -0.1354 & -0.5318 & 0.6680 \end{pmatrix}$	0.3215	0.7596 −0.3745 −0.3851
H1	$\begin{pmatrix} -0.9920 & -0.2091 & -0.2003 \\ -0.2091 & -0.2631 & 0.2803 \\ -0.2003 & 0.2803 & -0.5398 \end{pmatrix}$	−0.5983	0.5914 −0.1071 −0.4843
H2	$\begin{pmatrix} -0.2843 & 0.1757 & 0.1525 \\ 0.1757 & -0.2798 & 0.0975 \\ 0.1525 & 0.0975 & -0.2699 \end{pmatrix}$	−0.2780	0.2855 −0.0919 −0.1936
H4	$\begin{pmatrix} -0.5596 & -0.1956 & -0.1657 \\ -0.1956 & -0.4020 & 0.0762 \\ -0.1657 & 0.0762 & -0.5021 \end{pmatrix}$	−0.4880	0.3001 −0.0480 −0.2520
H6	$\begin{pmatrix} -0.0506 & 0.0622 & 0.0889 \\ 0.0622 & -0.3100 & -0.0297 \\ 0.0889 & -0.0297 & 0.2642 \end{pmatrix}$	−0.2083	0.1979 −0.0494 −0.1485
H7	$\begin{pmatrix} -0.4355 & -0.1541 & -0.1239 \\ -0.1541 & -0.2777 & 0.0864 \\ -0.1239 & 0.0864 & -0.3770 \end{pmatrix}$	−0.3636	0.2540 −0.0594 −0.1945
Hβ1	$\begin{pmatrix} 1.5808 & -0.0453 & -0.0506 \\ -0.0453 & 1.5575 & 0.0988 \\ -0.0506 & 0.0988 & 1.6752 \end{pmatrix}$	1.6046	0.1521 −0.0456 −0.1065
Hα	$\begin{pmatrix} -0.0601 & 0.0037 & 0.0331 \\ 0.0037 & -0.0251 & 0.0111 \\ 0.0331 & 0.0111 & -0.1940 \end{pmatrix}$	−0.0931	−0.1092 0.0395 0.0698
N*	$\begin{pmatrix} 0.1295 & -0.0134 & 0.0075 \\ -0.0134 & 0.1729 & -0.0249 \\ 0.0075 & -0.0249 & 0.1371 \end{pmatrix}$	0.1465	−0.0224 −0.0207 0.0431
Hβ2	$\begin{pmatrix} 0.1634 & -0.0230 & -0.0064 \\ -0.0230 & -0.0082 & 0.0158 \\ -0.0064 & 0.0158 & -0.0182 \end{pmatrix}$	0.0457	−0.0758 −0.0454 0.1211
H5	$\begin{pmatrix} 0.0051 & 0.0616 & 0.0694 \\ 0.0616 & -0.0665 & 0.0391 \\ 0.0694 & 0.0391 & -0.0586 \end{pmatrix}$	−0.0400	−0.0632 −0.0616 0.1248

♡ Calculated by Dr Ilya Kuprov, Department of Chemistry, University of Southampton, using density functional theory in Gaussian-03[280] at the UB3LYP/EPR-III level[141]. The calculation was done for the radical cation of tryptophan *in vacuo*. The atom numbering scheme is shown below.

♠ Full hyperfine tensors in the same axis system as $FAD^{\bullet-}$ (Table A.1). The relative orientation of the two radicals was taken to be that of the FAD cofactor and Trp-342 (the terminal tryptophan of the Trp-triad) in the crystal structure of *Drosophila melanogaster* cryptochrome (*Dm*Cry, PDB entry 4GU5[158, 159]).

♢ Isotropic hyperfine interactions.

♣Principal anisotropic components of the hyperfine tensors (arranged in descending order of magnitude for each nucleus).

* The nitrogen of the NH_2 group.

Notes:

Choice of nuclei. The cryptochrome model included the following 5 nuclei: N1, H1, H4, H7, Hβ1.

The DFT calculations were performed separately for the two radicals on the assumption that the 1.9 nm centre-to-centre distance between them in the protein is large enough that the hyperfine interactions should be very similar in the radical pair.

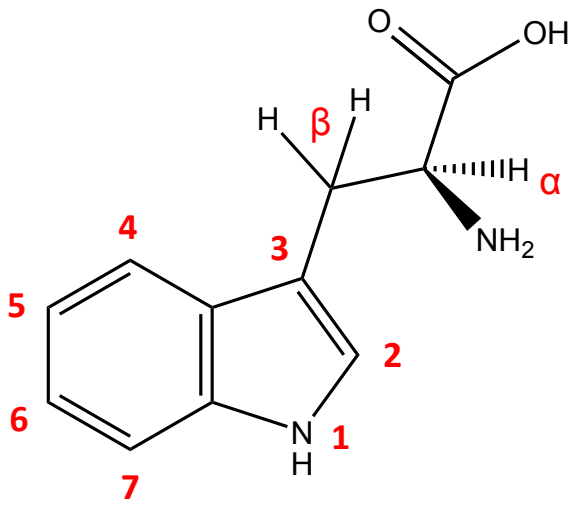


Figure A.2: Atom numbering scheme for $TrpH^{\bullet+}$.

Relative Orientation of $FAD^{\bullet-}$ and $TrpH^{\bullet+}$

The relative orientation of the two radicals was taken to be that of FAD and Trp-342 in *Drosophila melanogaster* cryptochrome (PDB entry 4GU5, A chain) [158, 159].

In each radical, the z axis is usually defined as the normal to the plane of the aromatic ring system. The angle between the two z axes is 39.2°. The rotation matrix that maps the (x, y, z) axes of the tryptophan indole group onto those of the FAD isoalloxazine group is:

$$\mathbf{R} = \begin{pmatrix} -0.3454 & 0.6869 & -0.6395 \\ -0.8269 & 0.0995 & 0.5535 \\ 0.4438 & 0.7199 & 0.5336 \end{pmatrix}. \tag{A.1}$$

For the majority of the calculations presented in this paper, an alternative z axis for the tryptophan radical was defined along the C3-Cβ bond (figure 5.5). The rotation matrix

that maps the axes of the flavin radical into this coordinate system is:

$$\mathbf{R} = \begin{pmatrix} 0.1488 & 0.6102 & -0.7781 \\ 0.5662 & 0.5925 & 0.5730 \\ 0.8107 & -0.5258 & -0.2573 \end{pmatrix}. \tag{A.2}$$

Appendix B

Calculating Euler angles to position hyperfine interactions

The hyperfine interaction tensors listed in Appendix A are given in the coordinate frame of the flavin radical [68]. The Redfield theory calculations presented in chapter 5 instead require a set of Euler angles describing the orientation of the tensor in the molecular frame, along with values for the axiality, rhombicity and isotropic component.

Using the definition of the Euler angles introduced in section 3.1.1, the full rotation matrix describing the orientation of the tensor has the general form

$$\mathbf{R}(\alpha,\beta,\gamma) = \begin{pmatrix} \cos\alpha\cos\beta\cos\gamma - \sin\alpha\sin\gamma & -\cos\alpha\cos\beta\sin\gamma - \sin\alpha\cos\gamma & \cos\alpha\sin\beta \\ \sin\alpha\cos\beta\cos\gamma + \cos\alpha\sin\gamma & -\sin\alpha\cos\beta\sin\gamma + \cos\alpha\cos\gamma & \sin\alpha\sin\beta \\ -\sin\beta\cos\gamma & \sin\beta\sin\gamma & \cos\beta \end{pmatrix}. \tag{B.1}$$

The second euler angle β can be found directly from equation (B.1) as [281]

$$\beta = \cos^{-1}(R_{33}); \qquad 0 \geq \beta \leq \pi. \tag{B.2}$$

The values of α and γ can be found from

$$\frac{R_{32}}{R_{31}} = \tan\gamma; \tag{B.3}$$

$$\frac{R_{23}}{R_{13}} = \tan\alpha. \tag{B.4}$$

More accurately, if the β dependence is removed from the relevant elements of the rotation matrix, the four-quadrant inverse tan function can be used to select the correct values of α and γ:

$$\gamma = \text{atan2}\left(\frac{R_{32}}{\sin\beta}, -\frac{R_{31}}{\sin\beta}\right); \tag{B.5}$$

$$\alpha = \text{atan2}\left(\frac{R_{23}}{\sin\beta}, \frac{R_{13}}{\sin\beta}\right). \tag{B.6}$$

Equations (B.5) and (B.6) have a singularity at $\sin\beta = 0$ (see section 3.1.1 and ref. [123]). This occurs when $\beta = 0$ or π. When $\beta = 0$, $R_{33} = 1$, giving

$$\cos(\gamma + \alpha) = R_{11}; \tag{B.7}$$

$$\sin(\gamma + \alpha) = R_{21}. \tag{B.8}$$

Any values of α and γ that satisfy these conditions will be valid, so we can set $\gamma = 0$ without loss of generality and calculate α as

$$\alpha = \text{atan2}(R_{21}, R_{11}). \tag{B.9}$$

Similarly, when $\beta = \pi$, $R_{33} = -1$ and we choose

$$\gamma = 0; \tag{B.10}$$

$$\alpha = \text{atan2}(-R_{21}, -R_{11}). \tag{B.11}$$

The rotation we wish to consider is from the axis system of each individual hyperfine tensor **A**, which we take as the eigenvector matrix of the hyperfine tensor, to the molecular axis system, which can be identified as the Identity matrix.

$$\mathbf{RA} = \mathbb{I} \tag{B.12}$$

$$\mathbf{R} = \mathbf{A}^{-1} \tag{B.13}$$

This, however, is not a robust way of defining the rotation matrix due to the possibility that axes may be swapped over or reflected during the process of finding the eigenvectors. To ensure that this does not happen the following checking procedure was used:

1. The signs of the diagonal elements of the eigenvector matrix were checked. If they were negative, the whole column was multiplied by -1. This ensured that the rotation has not been made into an improper rotation.

2. When searching for α and γ, solutions from all four quadrants of the $\tan^{-1}$ function were calculated as it was not known whether the signs in the rotation matrix were correct. This resulted in 8 sets of ϕ parameters (see section 5.1).

3. Each set of ϕ values was used to calculate the interaction Hamiltonian for a single spin (RHS below). This was compared to the result calculated using the original hyperfine tensor (LHS below):

$$\hat{\mathbf{L}}^{(1)} \cdot \mathbf{A} \cdot \hat{\mathbf{L}}^{(2)} = a_0^{(0)} \hat{T}_0^{(0)} + \sum_{m=-1}^{1} \phi_m^{(1)} \hat{T}_m^{(1)} + \sum_{m=-2}^{2} \phi_m^{(2)} \hat{T}_m^{(2)}. \tag{B.14}$$

4. The set of ϕ parameters that gave the closest match between the two methods was used to define the hyperfine interaction in the Hamiltonian.

Appendix C

Recipe for magnetoferritin

The procedure given here is based on those outlined in references [254] and [245].

Ingredients

- 100 mg apoferritin
- 500 mL 50 mM AMPSO buffer solution (3-[(1,1-dimethyl-2-hydroxyethyl)amino]-2-hydroxy-propanesulfonic acid)
- 2.0 M sodium hydroxide (NaOH)
- 5 mL ammonium ferrous sulphate ($(NH_4)_2Fe(SO4)_2.H_2O$) solution
- (In reference [254] only: 114 mg Me_3NO)
- Supply of Ar
- Distilled water

Method

1. Make up 500 mL of a 50 mM AMPSO buffer solution: 5.682 g of solid AMPSO dissolved in 500 mL of distilled water. Buffer the solution to pH 8.6 using 2.0 M

NaOH.

2. Make up a solution of 0.1 M $(NH_4)_2Fe(SO4)_2.H_2O$: 600 mg of solid in 15 mL of distilled water. De-aerate the solution with Ar for a minimum of 30 minutes.

3. (If following reference [254], also make up a 0.07 M solution of Me_3NO: 114 mg of solid in 15 mL of distilled water. De-aerate with Ar for a minimum of 30 minutes.)

4. Stir the AMPSO buffer solution with a magnetic stirrer and de-aerate with Ar for a minimum of 1 hour. (Gently bubble Ar through the solution for 1 hour – this removes excess oxygen to minimize formation of non-magnetic ferric oxides).

5. Keep stirring the solution under Ar and heat to 65°C. This temperature needs to be maintained using a water/oil bath.

6. Add 100 mg of apoferritin and leave to stir for 30 minutes (10 minutes in reference [245]).

7. Following reference [245]: Add 66 μL of the 0.1 M $(NH_4)_2Fe(SO4)_2.H_2O$. This corresponds to a theoretical load of 50 iron atoms per protein. Every 15 minutes add a further 185 μL of 0.1 M $(NH_4)_2Fe(SO4)_2.H_2O$. (In reference [254], each of these subsequent aliquots is followed by addition of a stoichiometric amount of Me_3NO solution). This corresponds to a theoretical load of 140 iron atoms per protein. After seven 185 μL aliquots, the theoretical load will be 1030 iron atoms per protein. In reference [245], this produced nanoparticles with an average moment of 350 μB.

8. Dialyze the final solution against distilled water. Concentrate the solution to the desired concentration (concentrated from 100 ml to 5 ml samples in reference [245]).

9. The sample may be freeze-dried for storage. It can be kept at 4°C or at 20°C for longer term storage (up to a year).